

**NMR Spectroscopic Investigation of Lanthanide,
Actinide, and Selenium Containing Complexes Related
to the Environment or Nuclear Waste Disposals**

D I S S E R T A T I O N

zur Erlangung des akademischen Grades

Doctor rerum naturalium
(Dr. rer. nat.)

vorgelegt

dem Bereich Mathematik und Naturwissenschaften
der Technischen Universität Dresden

von

Diplom-Chemiker Jérôme Kretzschmar
geboren am 12.03.1987 in Wurzen

Tag der Einreichung: 06.03.2019

Tag der Verteidigung: 08.05.2019

Gutachter:

Prof. Dr. phil.-nat. habil. Thorsten Stumpf

Prof. Dr. rer. nat. habil. Eike Brunner

Die Dissertation wurde in der Zeit von Oktober 2011 bis Juli 2015 am Institut für
Ressourcenökologie des Helmholtz-Zentrum Dresden-Rossendorf angefertigt.

Betreuer:

Prof. Dr. phil.-nat. habil. Thorsten Stumpf

Prof. Dr. rer. nat. Vinzenz Brendler

Dr. rer. nat. Astrid Barkleit

MEINEN ELTERN

DANKSAGUNG

Zum Gelingen dieser Arbeit haben eine Vielzahl von Personen innerhalb und außerhalb des Helmholtz-Zentrum Dresden-Rossendorf beigetragen, bei denen ich mich im Folgenden bedanken möchte.

Außerordentlicher Dank gilt Professor Dr. Thorsten Stumpf, Direktor des Instituts für Ressourcenökologie, sowie seinem Vorgänger, Professor Dr. Gert Bernhard, unter deren Ägide ich meine Promotion angefertigt habe. Größter Dank gebührt dem Leiter der Abteilung Grenzflächenprozesse und gleichzeitig direktem Betreuer der Arbeit, Professor Dr. Vinzenz Brendler, für den stets konstruktiven Dialog und die fortwährende Motivation. Allen drei zuvor genannten Herren verdanke ich es, größtmögliche Freiheiten genossen zu haben, meinen eigenen Forschungsinteressen nachgehen und mein Thema in Eigenverantwortung wählen und bearbeiten zu können. Ganz herzlich danke ich auch Dr. Astrid Barkleit als zweiter Betreuerin der Arbeit sowie als Diskussions- und Ansprechpartnerin in allen Belangen.

Besonders danken möchte ich Professor Dr. Eike Brunner, Professur Bioanalytische Chemie der Technischen Universität Dresden, für die Erstellung des Zweitgutachtens und wertvolle Diskussionen zur NMR-Spektroskopie. Ihm und Dr. Silvia Paasch bin ich für die zahlreichen, mess- und arbeitsintensiven Festkörper-NMR-Messungen überaus dankbar.

Dr. Erica Brendler, Institut für Analytische Chemie der Technischen Universität Bergakademie Freiberg, bin ich auf alle Zeit zu tiefstem Dank verpflichtet, ist sie es nämlich gewesen, die in mir die Begeisterung für die NMR-Spektroskopie geweckt und mich schon früh während des Studiums bestmöglich gefördert hat. Weiterhin bedanke ich mich für fortgesetzte Kooperation mit zahlreichen NMR-Messungen und stetige Bereitschaft zu konstruktivem Austausch.

Dr. Norbert Jordan hat mit seiner Expertise zur Chemie des Selens und zahlreichen wertvollen Diskussionen und unterstützenden IR/Raman-Messungen wesentlich zum Gelingen der Arbeit beigetragen.

Ein besonderer Dank gilt Professor Dr. Satoru Tsushima für vielfältige Quantenchemische Berechnungen, die eine wertvolle Ergänzung zu den experimentellen Ergebnissen dieser Arbeit darstellen, sowie den damit verbundenen Gedankenaustausch.

Für die kollegiale Zusammenarbeit und unkomplizierte gemeinsame Nutzung der NMR-Spektrometer möchte ich mich bei Dr. Constantin Mamat, Institut für Radiopharmazeutische Krebsforschung, recht herzlich bedanken.

Dr. René Hübner, Institut für Ionenstrahlphysik und Materialforschung, danke ich für die vielen TEM-Messungen und dazugehörigen Analysen, die wertvoller Bestandteil dieser Arbeit sind.

Weiterhin danke ich Alexander Strobel, der im Rahmen eines Praktikums und anschließender Bachelorarbeit mit seinen erzielten Ergebnissen auch meine Arbeit tatkräftig unterstützt

hat. Ausgesprochener Dank gilt Toni Haubitz, der für diese Arbeit ein Mitarbeiter von unschätzbarem Wert war. Nicht nur für sein Engagement und seinen Fleiß, sondern auch für seinen wissenschaftlichen Beitrag möchte ich ihm hiermit persönlich Danke sagen.

Dr. Erik Hennings, seinerzeit am Institut für Anorganische Chemie der Technischen Universität Bergakademie Freiberg, danke ich für die unkomplizierte Anfertigung verschiedener Analysen.

Für tatkräftige Unterstützung in zahlreichen Laborbelangen präparativer und analytischer Natur sei Stephan Weiß, für IR-Messungen Karsten Heim, für die Unterstützung in EXAFS-Fragen Dr. André Rossberg, für weitere Analysen und Zuarbeit Christa Müller, Annette Rumpel, Carola Eckardt, Aline Chlupka, Sabrina Beutner, Annegret Krzikalla und Sandra Strehle, sowie für diversen Support Jana Gorzitze und Ronny Berndt gedankt.

Für anregende wissenschaftliche Diskussionen jederzeit und wertvollen Input während der Erstellung der Arbeit danke ich Dr. Michael Patzschke und insbesondere Dr. Peter Kaden und Dr. Harald Foerstendorf.

Abschließend möchte ich besonders Katharina Müller, Robin Steudtner und Carola Franzen meinen tiefsten Dank aussprechen, da sie nicht nur in wissenschaftlichen, sondern auch persönlichen Angelegenheiten für mich von unschätzbarem Wert waren und sind. Meinen Mitstreitern und Freunden Constanze Richter, Juliane Schott, Richard Husar und Björn Drobot danke ich für ihre Beiträge zu gemeinsamen wissenschaftlichen Projekten sowie die gemeinsame Zeit außerhalb von Labor und Büro.

Während der Durchführung der experimentellen Arbeiten und Anfertigung der vorliegenden Dissertation haben auch zahlreiche Kooperationen innerhalb des Instituts für Ressourcenökologie stattgefunden. Aus verschiedenen Gründen sind die gemeinsam erzielten Ergebnisse zwar nicht Bestandteil der vorliegenden Dissertationsschrift, wurden bzw. werden jedoch in Peer-Review-Zeitschriften publiziert. Die im Rahmen der Promotionszeit entstandenen Veröffentlichungen sind nachfolgend aufgelistet.

A. Barkleit, J. Kretzschmar, S. Tsushima, M. Acker, *Americium(III) and europium(III) complex formation with lactate at elevated temperatures studied by spectroscopy and quantum chemical calculations*, ***Dalton Trans.*** **2014**, 43, 11221.

J. Schott, J. Kretzschmar, M. Acker, S. Eidner, M. U. Kumke, B. Drobot, A. Barkleit, S. Taut, V. Brendler, T. Stumpf, *Formation of a Eu(III) borate solid species from a weak Eu(III) borate complex in aqueous solution*, ***Dalton Trans.*** **2014**, 43, 11516.

J. Kretzschmar, N. Jordan, E. Brendler, S. Tsushima, C. Franzen, H. Foerstendorf, M. Stockmann, K. Heim, V. Brendler, *Spectroscopic evidence for selenium(IV) dimerization in aqueous solution*, ***Dalton Trans.*** **2015**, 44, 10508.

J. Schott, J. Kretzschmar, S. Tsushima, M. Acker, A. Barkleit, S. Taut, V. Brendler, T. Stumpf, *Interaction of Eu(III) with organoborates – a further approach to understand the complexation in the An/Ln(III)-borate system*, ***Dalton Trans.*** **2015**, 44, 11095.

Ch. Franzen, J. Kretzschmar, C. Franzen, S. Weiss, *Staining on heritage building stone identified by NMR*, ***Environ. Earth Sci.*** **2015**, 74, 5275.

C. Hennig, S. Weiss, W. Kraus, J. Kretzschmar, A. C. Scheinost, *Solution species and crystal structure of Zr(IV) acetate*, ***Inorg. Chem.*** **2017**, 56, 2473.

J. Kretzschmar, T. Haubitz, R. Hübner, S. Weiss, R. Husar, V. Brendler, T. Stumpf, *Network-like arrangement of mixed-valence uranium oxide nanoparticles after glutathione-induced reduction of uranium(VI)*, ***Chem. Commun*** **2018**, 54, 8697.

J. Kretzschmar, A. Barkleit, R. Steudtner, V. Brendler, T. Stumpf, *Multi-spectroscopic characterization of aqueous glutathione and glutathione disulfide complexes with Eu(III)*, ***Dalton Trans.***, to be submitted.

J. Kretzschmar, T. Haubitz, A. Strobel, A. Barkleit, R. Steudtner, V. Brendler, T. Stumpf, *Glutathione and glutathione disulfide complexes of uranium(VI) forming in aqueous solution*, ***Inorg. Chem.***, to be submitted.

J. Kretzschmar, S. Tsushima, C. Lucks, E. Jäckel, R. Meyer, R. Steudtner, A. Rossberg, K. Schmeide, V. Brendler, T. Stumpf *On the molecular structure of dimeric and trimeric uranyl(VI)-citrate complexes in aqueous solution*, ***Chem. Sci.***, to be submitted.

J. Kretzschmar, S. Tsushima, R. Steudtner, E. Jäckel, A. Rossberg, S. Weiss, B. Drobot, V. Brendler, T. Stumpf, *Uranyl(VI)-Citrate Photodegradation: New Insight into the Reaction Mechanism upon In-Situ Deuteration*, ***Angew. Chem.***, in preparation.

E. Attia, S. Tsushima, J. Kretzschmar, M. Patzschke, K. Fahmy, *Photoreduction of Quercetin-bound Uranyl in Liposomes*, ***Environ. Sci. Technol.***, to be submitted.

K. Müller et al., *Interdisciplinary round-robin test on molecular spectroscopy of the U(VI) acetate system*, ***ACS Omega*** **2019**, 4, 8167.

CONTENTS

SYMBOLS AND ABBREVIATIONS	V
SUMMARY.....	XI
ZUSAMMENFASSUNG	XIV
1 INTRODUCTION AND OBJECTIVES	1
2 FUNDAMENTALS	4
2.1 LANTHANIDES.....	4
2.1.1 <i>Natural Abundance and Distribution of the Rare Earth Elements</i>	4
2.1.2 <i>Electronic Structure and Oxidation State</i>	4
2.1.3 <i>Coordination Compounds and Solution Chemistry</i>	5
2.1.4 <i>Spectroscopic Properties</i>	5
2.2 ACTINIDES	6
2.2.1 <i>Natural Abundance and Distribution of the Actinides</i>	6
2.2.2 <i>Electronic Structure</i>	6
2.2.3 <i>Oxidation States</i>	7
2.2.4 <i>Solution Chemistry</i>	7
2.2.5 <i>Spectroscopic Properties</i>	9
2.3 GLUTATHIONE.....	9
2.4 CITRATE.....	11
2.5 SELENIUM	12
2.6 NUCLEAR MAGNETIC RESONANCE SPECTROSCOPY	13
2.6.1 <i>General Considerations</i>	13
2.6.2 <i>NMR Spectroscopy of Paramagnetic Molecules</i>	15
2.6.3 <i>⁷⁷Se NMR Spectroscopy</i>	16
3 RESULTS AND DISCUSSION.....	17
3.1 GLUTATHIONE/GLUTATHIONE DISULFIDE TOPIC	17
General considerations	17
3.1.1 <i>Glutathione–Lanthanide System</i>	19
3.1.2 <i>Glutathione–Uranium System under Oxidizing Conditions</i>	26
3.1.2.1 <i>Solution studies</i>	26
3.1.2.2 <i>Precipitate studies</i>	32

3.1.3	<i>Glutathione–Uranium System under Reducing Conditions</i>	36
3.1.3.1	Solution studies	37
3.1.3.2	Precipitate studies.....	46
3.1.3.3	Redox studies	48
3.1.4	<i>Comparison of Lanthanide– and Uranium–Glutathione System</i>	61
3.2	CITRATE TOPIC.....	62
	General considerations.....	62
3.2.1	<i>Uranium–Citrate Complex Structures</i>	63
3.2.1.1	Uranyl–Citrate Dimer	65
3.2.1.2	Uranyl–Citrate Trimer.....	77
3.2.2	<i>Photoinduced Reactions in the Uranium–Citrate System</i>	82
3.2.2.1	State of knowledge	82
3.2.2.2	Proposed and DFT-calculated reaction mechanism	83
3.2.2.3	NMR-spectroscopic proof of the reaction mechanism.....	87
3.2.2.4	Multispectroscopic examination of uranium reduction.....	93
3.2.2.5	Recapitulation.....	99
3.3	SELENIUM TOPIC	101
3.3.1	⁷⁷ Se NMR Spectroscopy.....	101
3.3.2	Se ^{IV} Dimerization in Aqueous Solution.....	103
3.3.3	Temperature Impact on Se ^{IV} and Se ^{VI} Speciation.....	107
3.3.4	Interaction of Se ^{IV} and Se ^{VI} with Mg ²⁺ and Ca ²⁺	112
4	CONCLUSIONS AND OUTLOOK	116
5	EXPERIMENTAL DETAILS	120
5.1	SAMPLE PREPARATION.....	120
5.1.1	General remarks.....	120
5.1.2	<i>Glutathione–Lanthanide System</i>	120
5.1.3	<i>Glutathione–Uranium System</i>	121
5.1.3.1	Oxidizing conditions	121
5.1.3.2	Reducing conditions	122
5.1.4	<i>Citrate – Uranium System</i>	124
5.1.4.1	Complex structure studies	124
5.1.4.2	Photoreaction studies.....	124
5.1.5	<i>Selenium</i>	125

5.2 INSTRUMENTATION	126
5.2.1 <i>Solution NMR</i>	126
5.2.2 <i>Solid-State NMR</i>	127
5.2.3 <i>UV-Vis-NIR</i>	127
5.2.4 <i>IR/Raman</i>	127
5.2.5 <i>TRLFS</i>	127
5.2.6 <i>XANES + EXAFS</i>	128
5.2.7 <i>DLS</i>	128
5.2.8 <i>TEM</i>	128
5.2.9 <i>Quantum Chemical Calculations</i>	128
5.3 DATA PROCESSING AND ANALYSES	129
6 REFERENCES	130
7 LIST OF FIGURES AND SCHEMES	138
8 LIST OF TABLES.....	144
9 APPENDIX	145
9.1 GLUTATHIONE/GLUTATHIONE DISULFIDE TOPIC	145
9.1.1 <i>Ligand-specific information</i>	145
9.1.2 <i>Lanthanide-related studies</i>	149
9.1.3 <i>Uranium-related studies</i>	154
9.2 CITRATE TOPIC	181
9.3 SELENIUM TOPIC.....	185

SYMBOLS AND ABBREVIATIONS

Chemical terms

^1H	hydrogen-1, protium, only nucleon is the proton
^{13}C	carbon-13, carbon isotope with 7 neutrons
^{17}O	oxygen-17, oxygen isotope with 9 neutrons
^{77}Se	selenium-77, selenium isotope with 43 neutrons
AcAc	acetoacetate
Ace	acetone
AMP	adenosine-monophosphate
An	actinide element
An^{III}	actinide, trivalent (generic)
An^{V}	actinide, pentavalent (generic)
AnO_2^+	actinyl ion, pentavalent
AnO_2^{2+}	actinyl ion, hexavalent
Ca^{2+}	calcium ion
CN	coordination number
Cit	citrate, citric acid (generic)
Cys	L-cysteinyl residue (GSH/GSSG)
D^+	deuterium (heavy hydrogen) ion, deuteron
D_2O	deuterium oxide (heavy water)
DCI	deuterium chloride
DSS	3-(trimethylsilyl)propane-1-sulfonic acid (water soluble NMR reference)
EDTA	ethylenediaminetetraacetate
Eu^{III}	europium, trivalent
Eu^{3+}	europium ion
Glu	L-glutamyl residue (GSH/GSSG)
Gly	glycyl residue (GSH/GSSG)
GSH	glutathione, γ -L-glutamyl-L-cysteinylglycine
GSSG	glutathione disulfide, oxidized (dimerized) GSH
H^+	protium (light hydrogen) ion, proton
H_2O	water, (protic)
Hb(s)	hydrogen bond(s)
HDO	semiheavy water (as by exchange of H_2O and D_2O)
H_2SeO_3	selenous acid

H_2SeO_4	selenic acid
HClO_4	perchloric acid
HSeO_3^-	hydrogen selenite ion
$(\text{HSeO}_3^-)_2$	hydrogen selenite ion dimer
HSeO_4^-	hydrogen selenate ion
La^{III}	lanthanum, trivalent
La^{3+}	lanthanum ion
Ln	lanthanide element
Ln^{III}	lanthanide, trivalent (generic)
Mg^{2+}	magnesium ion
N_2	nitrogen gas
NaCl	sodium chloride
NaClO_4	sodium perchlorate
NaOD	sodium deuterioxide
Nd:YAG	neodymium-doped yttrium aluminum garnet
REE	rare earth element
Se	selenium (generic)
Se^0	selenium, zerovalent
Se^{IV}	selenium, tetravalent
Se^{VI}	selenium, hexavalent
SeO_3^{2-}	selenite ion
SeO_4^{2-}	selenate ion
U^{4+}	uranous ion
U^{IV}	uranium, tetravalent (generic)
U^{V}	uranium, pentavalent (generic)
U^{VI}	uranium, hexavalent (generic)
UO_2^+	uranyl ion of U^{V}
UO_2^{2+}	uranyl ion of U^{VI}
$\beta\text{-KG}$	β -ketoglutarate (3-oxoglutarate)

Methodological terms

APT	attached proton test (NMR)
ATR	attenuated total reflection (IR)
CCD	charge-coupled device
COSY	correlation spectroscopy (NMR)

CP	cross polarization (NMR)
CPCM	conductor-like polarizable continuum model
CSA	chemical shift anisotropy
DFT	density functional theory
DLS	dynamic light scattering
DQF	double quantum filter (NMR)
EDX	energy-dispersive X-ray (spectroscopy)
EFG	electric field gradient
EXAFS	extended X-ray absorption fine structure (spectroscopy)
ESI-MS	electrospray ionization mass spectrometry
FT	FOURIER transform
HMBC	heteronuclear multiple-bond correlation (NMR)
HSQC	heteronuclear single-quantum coherence (NMR)
IR	infrared (vibrational spectroscopy)
lb	line broadening factor (exponential function multiplication prior to FT (NMR))
LIS	lanthanide-induced shift
LWCC	liquid waveguide capillary cell
MAS	magic angle spinning (NMR)
MP2	MØLLER – PLESSET perturbation theory
NIR	near-infrared (spectrophotometry)
NMR	nuclear magnetic resonance (spectroscopy)
PARAFAC	parallel factor analysis
PCS	photon correlation spectroscopy
S/N	signal-to-noise ratio
SAED	selected area electron diffraction
SP	single pulse (NMR)
TEM	transmission electron microscopy
TRLFS	time-resolved laser-induced fluorescence spectroscopy
UV-Vis	ultraviolet-visible light absorption (spectrophotometry)
XANES	X-ray absorption near-edge spectroscopy
XAS	X-ray absorption spectroscopy

Symbols and Units

(<i>R</i>)	<i>R</i> (<i>rectus</i>) stereocenter with sense of rotation clockwise
(<i>S</i>)	<i>S</i> (<i>sinister</i>) stereocenter with sense of rotation counterclockwise
°C	degree centigrade
Å	Ångström, <i>i.e.</i> , 10^{-10} m
a.u.	arbitrary units
B_0	magnetic field strength
C_q	quaternary carbon (central carbon of Cit)
d	length of light-path through cuvette
d_n	n -fold deuteration
E	half-cell potential
e^-	electron
E°	half-cell potential for standard conditions
f	femto, <i>i.e.</i> , 10^{-15}
F	FARADAY constant, <i>i.e.</i> , $96.485 \text{ kJ V}^{-1} \text{ mol}^{-1}$
g	grams
g	gravitational acceleration, <i>i.e.</i> , 9.81 m s^{-1}
Hz	Hertz, <i>i.e.</i> , s^{-1}
I	spin quantum number
I	ionic strength
$I(t)$	signal intensity as a function of time
I_0	signal intensity at time $t = 0$
J	Joule
nJ	scalar spin-spin coupling constant <i>via n</i> bonds
K	Kelvin
K	equilibrium constant according to mass law
k	kilo, <i>i.e.</i> , 10^3
k	wavenumber of the photo-electron (EXAFS)
k_{ass}	rate constant of association
k_{dis}	rate constant of dissociation
k_{ex}	exchange rate
$\log \beta^\circ$	logarithmic (base 10) cumulative stability constant for standard conditions
M	molar, <i>i.e.</i> , mol per liter
m	meter
M/L	metal-to-ligand ratio

mM	millimolar, <i>i.e.</i> , 10^{-3} mol per liter
mol	unit of measurement for amount of substance according to the number of atoms in 12 g of C-12, <i>i.e.</i> , $6.022\ 140\ 857 \times 10^{23}$ mol ⁻¹
n	nano, <i>i.e.</i> , 10^{-9}
pD	negative decadic logarithm of deuteron activity
pH	negative decadic logarithm of hydrogen ion activity
pH _c	ionic strength-corrected negative decadic logarithm of hydrogen ion concentration
pK _a	negative decadic logarithm of acid dissociation constant
ppb	parts per billion
ppm	parts per million
Q	electric quadrupole moment
R	universal gas constant, <i>i.e.</i> , 8.31447 J K ⁻¹ mol ⁻¹
r	distance
$R + \Delta R$	phase shift corrected distance (EXAFS)
R^2	coefficient of determination
s	second
T	Tesla
T	temperature
t	time
T_1	longitudinal relaxation time
T_2	transversal relaxation time
V	volt
z	number of electrons
γ	gyromagnetic ratio
δ	deformation vibration
δ^+	(positive) partial charge
δ_i	chemical shift of isotope i in NMR spectra
δ_{obs}	observed (apparent) chemical shift
ΔE	electromotive force
$\Delta_M \delta_i$	metal ion (M)-induced change of the observed chemical shift of isotope i as compared to a corresponding metal ion-free (blank) NMR spectrum
M = Eu, La, U i = H, C	
$\Delta_R G$	change in GIBBS free energy of a chemical reaction
$\Delta_T pK_a$	temperature-induced change of acid dissociation constant
$\Delta_T \delta$	temperature-induced change of chemical shift, <i>i.e.</i> , temperature coefficient of chemical shift (NMR)

$\Delta\nu$	frequency difference
$\Delta\nu_{1/2}$	line width (of an NMR signal), <i>i.e.</i> , full width at half amplitude
ε	molar absorptivity
λ	wavelength
μ	micro, <i>i.e.</i> , 10^{-6}
μ_j	bridging ligand between j metals
ν	frequency
$\tilde{\nu}$	wavenumber (IR)
ν_1	symmetric stretching vibration of the uranyl unit
ν_3	antisymmetric stretching vibration of the uranyl unit
ν_{as}	antisymmetric stretching vibration (generic)
ν_s	symmetric stretching vibration (generic)
π	180° (NMR pulse) according to $2\pi \text{ rad} = 360^\circ$
ρ	in-plane bending (rocking) vibrational mode
σ	shielding tensor (NMR)
τ	lifetime (TRLFS)
χ^{bulk}	bulk susceptibility
$\chi(k)$	normalized oscillatory part of absorption coefficient (EXAFS)

Miscellaneous

CCDC	The Cambridge Crystallographic Data Centre
HSAB	hard and soft acids and bases concept according to R. G. PEARSON
HOMO	highest occupied molecular orbital
IAEA	International Atomic Energy Agency
ICDD	International Center for Diffraction Data
ICSD	Inorganic Crystal Structure Database
LUMO	lowest unoccupied molecular orbital
MLCT	metal-to-ligand charge transfer
NEA TDB	Nuclear Energy Agency Thermochemical Database
SIT	specific ion interaction theory

SUMMARY

The ultimate goal of this work is providing insights into fundamental (physico-) chemical (redox) behavior of hexavalent uranium (U^{VI}), trivalent europium (Eu^{III}) and selenium (Se), and upon their interaction with ubiquitous small biomolecules (in case of U^{VI} and Eu^{III}) or alkaline earth metal ions (in case of Se^{IV} and Se^{VI}) by application of Nuclear Magnetic Resonance (NMR) spectroscopy. NMR spectroscopy is a powerful method providing its usefulness also to environmental and nuclear waste related studies in aqueous solutions by determination of (potential) binding sites, molecular structures (even conformation and configuration) as well as intra- and intermolecular dynamics, (redox) reaction pathways and mechanisms.

The present work comprises extensive NMR spectroscopic investigations in aqueous (D_2O) solutions on (i) glutathione (GSH) and glutathione disulfide (GSSG) interactions with trivalent lanthanides (Ln^{III} , particularly Eu^{III}) and U^{VI} , (ii) molecular structures of citrate (Cit) complexes of U^{VI} , and their reactions upon light-irradiation, as well as (iii) pH- and temperature-dependent speciation of selenium oxyanions, *i.e.*, Se^{VI} (selenate) and Se^{IV} (selenite and, notably, hydrogen selenite) as well as Se^{VI} and Se^{IV} interaction with alkaline earth metal ions. These investigations are supported by time-resolved laser-induced fluorescence spectroscopy (TRLFS), ultraviolet-visible-near infrared (UV-Vis-NIR), IR/Raman, and extended X-ray absorption fine structure (EXAFS) spectroscopy, transmission electron microscopy (TEM), as well as quantum chemical calculations on density functional theory (DFT) level.

For NMR spectroscopic data on GSH/GSSG complexation towards both Eu^{III} and U^{VI} are lacking, the herein presented results are new, and nicely complement other spectroscopic studies. Ln^{III} complexes of GSH are characterized by their high solubility at least up to 300 mM and pD 5. However, the formation constant of the Eu^{III} -GSH 1:1 complex is quite low with $\log K = 1.71 \pm 0.01$ as determined by Eu^{III} TRLFS. The diamagnetic La^{III} and Lu^{III} showed only little effect on the NMR spectra (< 2 ppm) while analogous Eu^{III} solutions revealed hyperfine shifts up to 40 ppm. Eu^{III} -induced 1H chemical shift changes are solely upfield and attributed to be predominantly due to *pseudocontact contribution* caused by dipolar interaction. In contrast, Eu^{III} -induced ^{13}C chemical shift changes of adjacent atoms – at least for the carboxyl and α -carbons – show alternating signs, indicating spin polarization effects owing to *contact contribution*. As expected for hard LEWIS acids and shown by other spectroscopies, complexation facilitates by the carboxyl groups. Qualitative differences between the glutamyl and glycyl carboxylate in metal ion complexation are ascribed to COULOMB repulsion due to the positively charged NH_3^+ in direct vicinity.

Investigations of the U^{VI} -GSH system covered experiments under both oxidizing and reducing conditions, performed with GSH's oxidized form, GSSG, at ambient conditions, while samples with reduced GSH were handled under N_2 atmosphere. For either condition, U^{VI} showed interaction in aqueous (D_2O) solution with both GSH and GSSG as determined

by U^{VI}-induced ¹H and ¹³C chemical shift changes and U^{VI} TRLFS, the latter comprising measurements at 25 °C and –120 °C. In principle, the interactions are stronger as compared to the Ln^{III} system, and the speciation in both solution and solid is more complex owing to the aqueous chemistry of uranium. Observed binary GSH complexes are [UO₂(H₂GSH)]²⁺ for pD values up to ≈ 2.3, and [UO₂(HGSH)]⁺ predominating for pD > 2.3. Complementary to the Eu^{III} results, whenever net neutral binary GSH/GSSG or ternary hydroxo GSH/GSSG U^{VI} complexes form in solution, both these U^{VI} systems revealed extensive precipitation because of the low solubility of these complexes. Binary U^{VI} GSSG and ternary U^{VI} hydroxo GSSG complexes yield solid phases from pD 2 through 8, even in carbonatic media. The largest quantities of aqueous GSSG–U^{VI} complexes are observed for pD ≈ 3.5, with the association constant for pH 3 determined by TRLFS as log *K* = 4.81 ± 0.08 for a 1:1 complex. GSH cannot compete with hydroxo ligands for complexation as of pD 6, whereas GSSG can at least partially compete with hydroxo and carbonate ligands upon formation of both quaternary U^{VI} hydroxo carbonate GSSG, and ternary U^{VI} carbonate GSSG (poly-)anionic species of high solubility.

Under reducing and near-neutral conditions (pD 6 – 9) GSH immediately reduced U^{VI} with subsequent formation of nanocrystalline UO_{2+x}. After centrifugation of the starting material and allowing the decanted supernatant to age, the dissolved nanocrystals assemble network-like as disclosed by TEM, and further analysed by selected-area electron diffraction (SAED), energy-dispersive X-ray (EDX) and UV-Vis spectroscopy, revealing hyperstoichiometric UO_{2+x} phases. Such network-like assembled actinide containing nanocrystals, with the arrangement most likely provoked by the presence of GSSG, have never been shown before. Complementary, the precipitate that has also been allowed to age as a wet paste, showed color changes from yellow *via* olive to black, indicating a reaction to proceed. The repeatedly probed and dissolved material exhibited GSSG in NMR spectra, and UV-Vis-NIR absorption bands attributed to U^{IV} and, notably, U^V, the latter implying a one-electron transfer with subsequent disproportionation of U^V to U^{IV} and U^{VI}. Therefore, obtained results advance the understanding of both fundamental redox behavior of uranium and the role of GSH (and related molecules) in U^{VI} detoxification processes *in vivo*.

Although investigated for over 70 years, there are still controversial discussions on both speciation and structures of U^{VI}–Cit complexes. By means of NMR's strength in both structure determination and sensitivity to dynamic processes, studies regarding the U^{VI}–Cit system allowed further fundamental insights into the structures of the formed complexes on a molecular level. Upon complexation a chiral center is induced in Cit's central carbon, resulting in the formation of two diastereomeric pairs of enantiomers, whereupon the dimeric complexes exhibit *syn* and *anti* configured isomers. In fact, the combination of ¹⁷O NMR (note: at natural abundance) and quantum chemical calculations allowed an unambiguous decision on complex geometry and overall configurations. It is evidenced for the first time that the *syn* isomer is favored in aqueous solution in contrast to the preferably crystallizing *anti* isomer. Both isomers coexist and interconvert among one another, with a rate estimated to be in the order of 10² s⁻¹ at 25 °C in acidic media, and a corresponding

activation energy of approximately 60 kJ mol^{-1} . Moreover, clear indications for uranium chirality is observed for U^{4+} , with the 1:1 $\text{U}^{\text{IV}}\text{-Cit}$ complexes also forming two diastereomeric pairs of enantiomers. Comprehensive spectroscopic experiments combined with quantum chemical calculations improved basic understanding of the photo-reaction mechanism in the $\text{U}^{\text{VI}}\text{-Cit}$ system. Regardless of sample conditions, Cit is degraded to β -ketoglutarate, acetoacetate, and acetone, while U^{VI} was reduced to U^{IV} at pD 2 and U^{V} at pD 5, suggesting a two- and a one-electron transfer, respectively. NMR signals observed for pD 5 samples at remarkable ^1H chemical shift values between 25 and 53 ppm, in combination with UV-Vis-NIR absorptions at about 750 and 930 nm, are assigned to U^{V} complexes of citrate. With regard to reported pH dependence on reaction rate and yield in the literature combined with observations in this work, H^+/D^+ are considered mechanistically crucial constituents. Furthermore, the photoreaction proceeds *intermolecularly*, requiring for free Cit to be present in solution.

In consideration of both the $\text{U}^{\text{VI}}\text{-Cit}$ *photoreaction* and the $\text{U}^{\text{VI}}\text{-GSH}$ *chemical* redox reaction, regardless of the particular mechanism, in both cases the process is *intermolecular*. This is not only a highly interesting, but the more a very important result, rendering the reductants not required to be bound to U^{VI} in order to reduce it.

Owing to the suitability of ^{77}Se as NMR-active but non-radioactive Se isotope, this spectroscopy was also applied to study chemical behavior of the nuclear waste related long-lived ^{79}Se . For the first time spectroscopic evidence is given for hydrogen selenite dimerization in aqueous solution upon formation of homo-dimers by hydrogen bonding that are stable up to $60 \text{ }^\circ\text{C}$ and so are other selenium oxyanionic species. Additionally, a remarkably higher ^{77}Se chemical shift temperature coefficient of the dimer – as compared to corresponding selenite and selenous acid – was found. These findings are attributed to a significant deshielding upon heating due to remarkably different rovibrational modes upon stretching the dimer as a whole instead of its dissociation into monomers owing to the rather strong hydrogen bonds. Interaction of selenium oxyanions with ubiquitous alkaline earth metals, *i.e.*, Ca^{2+} and Mg^{2+} , showed formation of weak aqueous complexes of both selenite and hydrogen selenite dimer for excessive selenium, however, at high ionic strength (5.6 M) for equimolar Ca^{2+} and Se^{IV} even at pH_c 5 crystalline calcium selenite is formed.

ZUSAMMENFASSUNG

Ziel der Arbeit ist es, das Verständnis um das (physiko-) chemische (Redox-) Verhalten sechswertigen Urans (U^{VI}), dreiwertigen Europiums (Eu^{III}) und Selens (Se) allgemein und unter Wechselwirkung der Metallionen mit ubiquitären Biomolekülen bzw. des Se^{IV} und Se^{VI} mit Erdalkalimetallionen grundlegend zu vertiefen. Kernspinresonanzspektroskopie (NMR) ist eine sehr leistungsfähige Methode, die ihre Anwendbarkeit auf umwelt- und endlagerrelevante aquatische Systeme unter Beweis stellt, indem (potentielle) Bindungsstellen und Molekülstrukturen (bisher zu Konformationen und Konfigurationen) bestimmt, sowie intra- und intermolekulare dynamische Prozesse, (Redox-) Reaktionswege und Mechanismen nachvollzogen werden können.

Die vorliegende Arbeit umfasst umfangreiche NMR-spektroskopische Untersuchungen in D_2O Lösungen zur (i) Wechselwirkung von Glutathion (GSH) und Glutathiondisulfid (GSSG) mit sowohl dreiwertigen Lanthaniden (Ln^{III} , insbesondere Eu^{III}) als auch sechswertigem Uran (U^{VI}), (ii) molekularen Struktur der Citrat (Cit)– U^{VI} -Komplexe und den in diesem System ablaufenden Reaktionen infolge der Bestrahlung mit sichtbarem Licht, sowie (iii) pH- und temperaturabhängigen Speziation der Oxoanionen des sechs- und vierwertigen Selens, d. h. Selenat (Se^{VI}) und (Hydrogen-) Selenit (Se^{IV}) sowie der Wechselwirkung von Se^{VI} und Se^{IV} mit den ubiquitären Erdalkalimetallionen Mg^{2+} und Ca^{2+} . Unterstützend wurden weitere Messungen mit zeitaufgelöster Laser-induzierter (U^{VI} und Eu^{III}) Fluoreszenzemissionsspektroskopie (TRLFS), Elektronenabsorptionsspektroskopie im Bereich des ultravioletten, sichtbaren und nahen infraroten Lichts (UV-Vis-NIR), Schwingungsspektroskopie (IR/Raman) und erweiterte Röntgen-Absorption-Feinstruktur-Spektroskopie (EXAFS), Transmissionselektronenmikroskopie (TEM), sowie quantenchemische Berechnungen auf Grundlage der Dichtefunktionaltheorie (DFT) durchgeführt.

Bisherige GSH–Metallionen-Komplexierungsstudien konzentrierten sich vornehmlich auf Übergangsmetalle, unter den Lanthaniden blieb Eu^{III} unberücksichtigt, bei U^{VI} -Untersuchungen interessierten die gebildeten Präzipitate. Sowohl der Fokus auf das Komplexierungsverhalten in wässriger Lösung als auch die erstmalige Anwendung der NMR-Spektroskopie auf diese Systeme ergänzen die bisherige Literatur und liefern wertvolle Referenzdaten. Ln^{III} –GSH Komplexe zeigten eine gute Löslichkeit bis mindestens 300 mM bei pD 5. Die mittels TRLFS bestimmte Bildungskonstante des Eu^{III} –GSH 1:1 Komplex ist mit $\log K = 1.71 \pm 0.01$ vergleichsweise niedrig. Während die diamagnetischen Ionen La^{III} und Lu^{III} nur geringe Auswirkungen auf die NMR Spektren zeigten (< 2 ppm), betrug die Signalverschiebung für Eu^{III} , ceteris paribus, eine Hyperfeinverschiebung von über 40 ppm. Sämtliche Eu^{III} -induzierten 1H NMR-Signalverschiebungen waren zu höherem Feld, die der ^{13}C -Signale sowohl hochfeld- als auch tieffeldverschoben. Während erstere vornehmlich durch dipolare Wechselwirkung hervorgerufen werden (FERMI-Pseudokontakt), zeigen die ^{13}C -Signale benachbarter Molekülpositionen – zumindest für Carboxyl- und α -Kohlenstoff – alternierende Vorzeichen, was auf Polarisierungseffekte aufgrund Elektronendichteverteilung entlang der Molekülkette (FERMI-Kontakt) zurückzuführen ist. Erwartungsge-

mäß binden Ln^{III} als harte LEWIS-Säuren an den Carboxylgruppen. Der qualitative Unterschied der Glutamyl- und Glycyl-Carboxylat-Komplexierung resultiert aus der COULOMB-Abstoßung mit den Metallionen aufgrund der benachbarten protonierten Glutamyl- α -aminogruppe.

Untersuchungen zum U^{VI} -GSH-System erfolgten sowohl unter atmosphärischen Bedingungen mit der oxidierten Form des GSH, dem Glutathiondisulfid (GSSG), als auch mit reduziertem GSH unter N_2 -Schutzgasatmosphäre. In beiden Fällen war anhand U^{VI} -induzierter NMR-Signalverschiebung bzw. TRLFS-Messungen bei 25 °C und -120 °C eine Wechselwirkung erkennbar. Prinzipiell sind die GSH- bzw. GSSG-Wechselwirkungen mit U^{VI} deutlich ausgeprägter als mit Eu^{III} . Für GSH konnten zwei binäre Komplexe beobachtet werden: bis pH 2.3 war $[\text{UO}_2(\text{H}_2\text{GSH})]^{2+}$ vorherrschend, und ab pH 2.3 $[\text{UO}_2(\text{HGSH})]^+$. Im Gegensatz zum Eu^{III} -GSH/GSSG-System kam es mit U^{VI} zur Bildung binärer und ternärer, netto-neutraler und somit schwerlöslicher Komplexspezies. Im untersuchten pD-Bereich (2 bis 8) präzipitierten binäre U^{VI} -GSSG- bzw. ternäre U^{VI} -GSSG-Hydroxo-Komplexe, letztere sogar aus carbonathaltiger Lösung. Die größten Mengen gelöster binärer U^{VI} -GSSG-Komplexe lagen zwischen pD 3 und 4 vor. Mittels TRLFS wurde die Assoziationskonstante bei pH 3 für den 1:1 Komplex zu $\log K = 4.81 \pm 0.08$ bestimmt. Während GSH ab pD 6 infolge U^{VI} -Hydrolyse praktisch keine Komplexierung mehr zeigt, kann GSSG zumindest teilweise mit Hydroxo- und Carbonatliganden konkurrieren. Demnach bilden sich quaternäre U^{VI} -GSSG-Hydroxo-Carbonat- bzw. ternäre U^{VI} -GSSG-Carbonat-Komplexe guter Löslichkeit infolge der hohen negativen Ladung.

Unter sauerstofffreien und nah-neutralen Bedingungen (pD 6 bis 9) war eine sofortige U^{VI} -Reduktion anhand gefundener UO_{2+x} -Nanokristalle feststellbar. Versuche, in denen sowohl der dekantierte Überstand als auch das zentrifugierte Präzipitat über Wochen unter Schutzgas altern konnten, zeigten interessante Veränderungen. Einerseits agglomerierten die kolloidalen Nanokristalle zu netzwerkartigen Strukturen, die aus hyperstöchiometrischen UO_{2+x} -Phasen bestanden, wie TEM in Verbindung mit Elektronenfeinbereichsbeugung (SAED) und energiedispersiver Röntgenspektroskopie (EDX), sowie UV-Vis nach Wiederauflösung offenbarten. Eine derartige netzwerkartige Morphologie ist bisher für keine Actinidoxidphase beobachtet worden, hat somit Einzigartigkeitscharakter. Höchstwahrscheinlich ruft hier das GSSG die besondere Anordnung hervor. Andererseits reagierte der feuchte Niederschlag unter Farbveränderung (von anfänglich gelb über oliv zu schwarz) weiter. Nach Auflösung waren im NMR GSSG-Signale und im UV-Vis-NIR deutliche U^{IV} und U^{V} zugeschriebene Absorptionen beobachtbar, was die Reduktion zu U^{IV} belegt, sowie auf einen ein-Elektron-Transfer mit anschließender Disproportionierung des U^{V} zu U^{VI} und U^{IV} hindeutet. Folglich vertiefen die in den U^{VI} -GSH-Studien erhaltenen Ergebnisse das Verständnis zum grundlegenden Redoxverhalten des Urans, sowie zur Rolle des GSH (und verwandten Molekülen) in Entgiftungsmechanismen *in vivo*.

Experimente zum U^{VI} -Cit System erweitern die Kenntnisse um die molekularen Strukturen der gebildeten Komplexe. Unter besonderer Berücksichtigung der durch Komplexbildung im Citrat induzierten Stereozentren wurden zum ersten Mal auf spektroskopischem Wege die Strukturen der *syn*- und *anti*-konfigurierten Isomere des 2:2 U^{VI} -Cit- Komplexes

beschrieben. Die Kombination aus ^{17}O -NMR (beachte: bei natürlicher Häufigkeit) und quantenchemischen Berechnungen erlaubte die zweifelsfreie Bestimmung der Komplexgeometrie und Konfiguration. Es wurde zum ersten Mal gezeigt, dass in wässriger Lösung das *syn* Isomer deutlich begünstigt ist, während in Kristallstrukturen nahezu ausschließlich das *anti* Isomer vorkommt. Beide Formen existieren gleichzeitig und wandeln sich bei 25 °C in saurer Lösung mit einer Rate in der Größenordnung von 10^2 s^{-1} ineinander um. Die entsprechende Aktivierungsenergie wurde mit 60 kJ mol^{-1} approximiert. Darüber hinaus wurden im ^1H -NMR Hinweise auf zwei diastereomere Enantiomerenpaare des U^{IV} -Cit 1:1 Komplexes gefunden, was chirales U^{4+} impliziert. Außerdem konnten anhand umfangreicher spektroskopischer und quantenchemischer Methoden beachtliche Kenntnisse zum Reaktionsmechanismus der Photoreaktion im U^{VI} -Cit-System erlangt werden. Unabhängig von den untersuchten pH- und Konzentrationsbedingungen wurden als Cit-Abbauprodukte β -Ketoglutarat, Acetylacetonat und Aceton gefunden, während U^{VI} bei pD 2 mittels *zwei*-Elektronen-Transfer zu U^{IV} , jedoch bei pD 5 vermittels *ein*-Elektron-Transfer zu U^{V} reduziert wurde. Für Cit-Komplexe des U^{V} gibt es Hinweise sowohl im UV-Vis-NIR (Absorptionen bei 750 und 930 nm), als auch im NMR anhand bemerkenswert tieffeldverschobener ^1H -NMR-Signale (zwischen 25 und 53 ppm). Basierend auf Literaturdaten und Beobachtungen in dieser Arbeit bezüglich Geschwindigkeit und Umsatz der Photoreaktion, sind sowohl H^+/D^+ als auch nicht- U^{VI} -komplexiertes Cit mechanistisch essentiell.

Unabhängig vom jeweiligen Mechanismus findet die Elektronenübertragung sowohl für die photo-induzierte Reaktion im U^{VI} -Cit- als auch die chemisch-induzierte Redoxreaktion im U^{VI} -GSH-System *intermolekular* statt, was nicht nur interessant, sondern wichtig ist mit Blick auf U^{VI} -Reduktion zu U^{IV} in Prozessen zur Entgiftung *in vivo* oder Anwendungen zu Immobilisierungs- bzw. Sanierungskonzepten.

Weiterhin konnte, auch mittels ^{77}Se -NMR, die Hydrogenselenit-Dimerisierung durch Wasserstoffbrücken erstmalig spektroskopisch bewiesen werden. Diese, wie auch die anderen Se-Oxoanionen unterlagen bis 60 °C keiner signifikanten Speziationsänderung. Darüber hinaus zeigte das Dimer im Vergleich zu anderen Se^{IV} -Spezies eine deutlich höhere Temperaturabhängigkeit der ^{77}Se chemischen Verschiebung, was auf veränderte Rotations-Schwingungs-Moden infolge stärkerer Wasserstoffbrücken zurückgeführt wird. Bei Temperaturerhöhung wird das Dimer infolge der Molekülschwingungen als Ganzes gestreckt, ohne dabei in seine Monomere zu dissoziieren, woraufhin sich die mittlere Elektronendichte am Kernort deutlich reduziert. Das Hydrogenselenit-Dimer bzw. Selenat zeigten bei Überschuss nur schwache Wechselwirkungen mit Ca^{2+} bzw. Mg^{2+} in Lösung, jedoch wurde bei hoher Ionenstärke (5.6 M) und equimolaren Mengen Se^{IV} (Dimer) und Ca^{2+} selbst bei vergleichsweise niedrigem pH_c 5 kristallines Calciumselenit gebildet.

1 INTRODUCTION AND OBJECTIVES

Energy production by nuclear fission of uranium is considered an attractive alternative to the combustion of fossil fuels. As of 02/2019, 453 nuclear power plants are operating in 30 countries worldwide, further 55 are under construction [1]. After the nuclear power plant incident of Fukushima Daiichi in 2011, German government decided to abandon energy production by nuclear fission. The seven German nuclear power plants still in operation (by 02/2019) will be shut down until 2022. All nuclear waste being produced in the past and until then still has to be treated and stored appropriately. Radioactive wastes contain radioactive isotopes that decay to non-radioactive isotopes over time, often *via* several steps and very long timescales. In the process of decay, these wastes emit alpha, beta, and gamma radiation, being harmful to biological tissues. Proper disposal is to isolate radioactive wastes from humans and the environment until the radionuclides in the waste have decayed to safe levels [2]. In many countries it is agreed that these wastes should be stored in deep geological formations (salt, argillaceous rock, crystalline rock). Safety and risk assessment of a nuclear waste repository has to consider the case of water ingress, which would initiate corrosion and dissolution processes of the stored inventory (container material, radioactive waste), the backfill and host rock components. Not only for adequate management of nuclear waste itself, but also regarding operation and remediation of uranium mines and waste piles as well as in the case of a nuclear incident, comprehensive examination of radionuclide interaction with the environment is mandatory for detailed knowledge on how radionuclides can be restrained once they are mobilized. On the one hand, naturally occurring radioactive material (NORM) such as thorium, uranium, and radium in rocks, soil, and natural uranium bearing minerals, can dissolve into ground water simply upon geological alteration. On the other hand, technologically enhanced naturally occurring radioactive material (TENORM) arising from drinking and wastewater treatment, oil and gas production, geothermal engineering, fertilizer production, as well as uranium mining and processing, containing these constituents, can migrate into the environment.

Related and in addition to the latter, uranium is still the most important source for electrical power supply by its use as the main component of nuclear fuel [3-4] and, therefore, major part of the uranium processing cycle comprising mining, excavation material dumping, metallurgy, reprocessing treatment and nuclear waste disposal [5]. Uranium by its widespread occurrence in general, and in (spent) nuclear fuel in particular, is thus a key element considered throughout this work. Under aqueous aerobic conditions, it typically occurs as hexavalent uranium, U^{VI} , commonly forming water soluble, mobile species. In contrast, tetravalent uranium, U^{IV} , is considered hardly soluble and much less mobile. Consequently, reduction to U^{IV} , especially as UO_2 , is seen as an attractive approach for its immobilization in sediments and *in vitro* [6-7]. For environmental science, the most important U^{IV} formation routes are abiotic reduction by redox active minerals [8-10] or biogenic formation by means of microorganisms [11-15], both paths yielding nanocrystalline UO_2 .

Owing to their chemical relationship by being both *f*-elements, rare earth elements (REE) and particularly thorium and, to a lesser extent but because of the quantity produced still significant, uranium, are often commonly found in geological deposits and minerals such as monazites, and thus inevitably mined and, at least in part, processed together. REE represent a growing market and have expanding applications in markets as diverse as rechargeable batteries, advanced ceramics, permanent magnets, optical data storage, laser, fiber optics, glass, phosphors, and superconductors. Rare earth phosphors have been extensively used in color television screens, computer monitors, fluorescent lighting, and medical X-ray photography. Permanent magnets are found in a great variety of industrial and commercial applications [16].

Even though or just because actinides have no specific role in normal biochemistry – since organisms have no regulatory mechanisms for sensing them – the *raison d'être* for studying actinide metabolism and biochemistry is to understand actinide interactions so that predictions can be made concerning retention and distribution in the entire environment, comprising biotic and abiotic components. In the environment and *in vivo* the chemical speciation of actinides is, to a large extent, stabilized by complexing ligands, ranging from water molecules to low molecular-mass ligands to proteins, also including surface complexation. Therefore, an important thrust of actinide bio- and environmental chemistry is to understand and elucidate the thermodynamics and kinetics of actinide binding to complexing groups [17]. In addition to the protein-bound fraction, *viz.* metal-transferrin complexes in the case of actinides, there is also a low molecular-mass fraction in which metal ions are bound to, and transported with, ligands such as anions of amino and carboxylic acids. For the hard cations of the actinide elements, these complexing agents are predominantly carboxylic acids from the citric acid cycle [18-20]. For studies concerning trivalent actinides in general, and Am^{III} in particular (being one of the minor actinides generated by successive neutron capture in spent fuel), Eu^{III} is often used as an isoelectronic, non-radioactive analogue.

Therefore, glutathione as a highly concentrated intracellular redox active tripeptide being involved in various cell regulation and detoxification mechanisms as well as citrate, eponymous for the citrate cycle as the paramount metabolic pathway in aerobic organisms, are employed for studying actinide interaction owing to not only their biological importance and abundance, but also their suitability for spectroscopic investigations as model molecules. Only by means of a sound understanding of the physical and chemical fundamentals determining actinide interaction by studying small model systems in a controlled simple environment, the influence of the various contributing factors can be evaluated individually so that robust results then can be used for, *e.g.*, safety and risk assessment or transformed into effective applications.

Against this background, the fundamentals of U^{VI} redox reaction, *i.e.* electron transfer to U^{VI}, are studied by means of easily facilitated photo-excitation [21-24] of the uranyl ion. After irradiation, the uranyl–citrate system is examined by multiple spectroscopic methods

well suited for obtaining complementary information on both the metal and the ligand. So far, most investigations performed are black-box experiments presenting final products and therefrom assumed reaction pathways. In the present work the validity of a proposed reaction mechanism is proven by both DFT calculation and experiment. In addition, a kind of combinatorial approach is applied upon which each degradation product undergoes deuteration reactions *in situ* and, hence, exhibits all possible forms of deuterated isotopomers, unambiguously distinguishable by NMR spectroscopy thus providing mechanistic traceability of complex degradation.

The third key element in this work is selenium. It is a naturally occurring trace element, essential for plants, animals and the human body, but at high concentration, it becomes toxic [25]. The natural background is remarkably varying and there are various anthropogenic influxes such as coal combustion, processing of copper, or use of phosphate fertilizers [26]. Additionally, the selenium isotope Se-79 is a long-lived (3.27×10^5 a) [27] fission product significantly contributing to the potential radiation dose from nuclear waste repositories [28-30]. High-level and long-lived radioactive wastes increase the temperature in the vicinity of the waste disposal site for about 500 years [31]. Thus, it is important to understand to what extent this temperature increase influences the aqueous speciation of the selenium itself and, hence, its sorption behavior onto mineral phases. Owing to its biological function, bioavailable radioactive selenium, once incorporated in the organism, can develop its full radiotoxic potential. For risk assessment the understanding of the mobility properties of selenium, including redox and sorption processes, is essential. Before running experiments investigating sorption behavior, knowledge about the aqueous speciation is mandatory. Utilising NMR spectroscopy to the non-radioactive isotope Se-77 provides a further, powerful tool to obtain valuable thermodynamic, kinetic, and structural reference data, hence strengthen fundamental knowledge on (physico-) chemical behavior of this critical element. Concomitantly, the methodological NMR scope is extended to ^{77}Se studies yet rarely applied to Se oxoanions in general, and in aqueous solution in particular. For improved understanding of both abiotic and biotic redox-mediated processes, the impact of high temperatures due to decay heat, high ionic strengths as associated with salt and clay as potential host rock materials, as well as pH values on chemical speciation is essential and, therefore, considered in this work.

The present work is mainly written from an NMR spectroscopic point of view, on account of its application to selected chemical systems, supported by further spectroscopies, microscopies, and quantum chemical calculations. Therefore, interactions of lanthanides, actinides, and selenium within these systems of interest are primarily described from the perspective of the (^1H , ^{13}C , ^{77}Se) NMR-active components, *i.e.* glutathione, citrate and its degradation products, and selenium itself.

2 FUNDAMENTALS

In order to provide or remind some basics, concise sections addressing chemical properties and (NMR) spectroscopic peculiarities of the elements associated with this work are given beforehand, excerpting sections from highly recommendable introductory literature.

2.1 LANTHANIDES

REE are a series of chemical elements of the periodic table, comprising the elements with atomic numbers 57 (lanthanum) through 71 (lutetium) – commonly denoted as the lanthanides (Ln) – and, additionally, including yttrium (element no. 39) for ample reasons and, but more controversial, scandium (element no. 21).

Unless stated otherwise, most parts of the following section are adopted from Z. ZHENG AND J. E. GREEDAN, *Rare Earth Elements and Materials* [16], a chapter from the Encyclopedia of Physical Science and Technology.

2.1.1 Natural Abundance and Distribution of the Rare Earth Elements

The rare earths are very widely distributed in the earth's crust and exhibit a great diversity in the geological type of the deposits. In spite of the great mineralogical diversity only a very few REE-bearing minerals occur in sufficient concentration to justify commercial exploitation as an ore. These are, roughly in order of current commercial importance, bastnasite, REEFCO₃; monazite, REEPO₄; and xenotime, YPO₄ (the same chemical formula as monazite but contains mostly yttrium). In addition, apatites (Ca,RE)₅(PO₄)₃F and uranium-bearing minerals such as uraninite (pitchblende), UO_{2+x}, and uranothorite, (Th,U)SiO₄, contain significant quantities.

2.1.2 Electronic Structure and Oxidation State

Although the different REEs are distinguished by different numbers of 4*f*-electrons, there is almost no correlation between the extent of filling the 4*f* level and chemical properties. This is because the outer 5*p* and 5*s* sub-shells shield the inner 4*f*-electrons from outer interactions, which determine most of the properties of the Ln^{III} ions. Upon the well-known lanthanide contraction, the Ln^{III} ionic radii decrease consistently in aqueous solution, from 125 pm for La^{III} through 99.5 pm for Lu^{III} as nicely revealed by a re-determination in 2011 [32]. In aqueous solution the coordination number (CN) decreases smoothly from 9 for the lighter Ln^{III} (larger radii) through 8 for the heavier Ln^{III} (smaller radii). Contrary to the crystal, for the exchange between water ions in the first and second hydration shell (especially in capping position) is fast, CN is between 9 and 8 for Ln^{III} in the middle of the series [32]. As the chemistry of elements is controlled largely by the nature of the outermost electrons, the valence electrons, and by atomic size, the chemical properties of REE are indeed very similar. With the exception of Ce^{IV} and Eu^{II}, lanthanide ions commonly occur in their trivalent oxidation state.

2.1.3 Coordination Compounds and Solution Chemistry

The Ln^{3+} are essentially spherical with a complexation behavior very similar to alkaline earth metal ions. Because of the large size of the cations, a coordination number greater than 6 (usually 8 to 9) in their compounds is common. Since the $4f$ -orbitals are not available for chemical bonding and are sufficiently shielded, the crystal field stabilization energy is of the order of 100 cm^{-1} which is small as compared to $\approx 30,000 \text{ cm}^{-1}$ in the case of d -transition elements. The lack of covalency in REE–ligand interaction implies that there are no orbital requirements for ligands around the metal center; the coordination polyhedra are determined by the steric requirement of the ligands and are therefore often ill defined. Consequently, the conversion of one geometry into another is very easy and common [33]. The ionic bonding character also causes the rapid ligand exchange. REE^{3+} cations display typical hard LEWIS acid properties that prefer coordination with O and F donor ligands, leading to regular occurrence of aqua and hydroxo ligands in the solid. The extremely facile ligand exchange at f -element centers makes the isolation of their coordination complexes difficult, particularly from aqueous solutions. A successful method of overcoming this is to increase the thermodynamic stability of the complexes by exploitation of the chelate and macrocyclic effects. Typical ligands used in such a strategy include β -diketonates, EDTA, and macrocyclic ligands such as crown ethers and cryptands.

2.1.4 Spectroscopic Properties

Lanthanide spectra are characterized by transitions involving f -orbitals. Three main types of transitions are observed in the absorption spectra of the lanthanide ions: (i) LAPORTE-forbidden $f \rightarrow f$ transitions, (ii) orbitally allowed $4f \rightarrow 5d$ transitions, and (iii) metal-to-ligand charge transfer (MLCT). As reflected by the solution chemistry (*cf.* previous section) ligand field effects hardly affect electronic energy levels, whereupon transitions observable in the visible range are often low in intensity and Ln^{III} compounds thus exhibit only pale coloring. In case of allowed $4f^n \rightarrow 4f^{n-1} 5d^1$ transitions, for instance in Ce^{III} and Tb^{III} with $n = 1$ and 8 causing energetically favorable empty and half-filled f sub-shell configuration, respectively, the corresponding absorptions found in the UV range are high in intensity. Additionally, some Ln^{III} , *e.g.*, Eu^{III} , Tb^{III} , Ce^{III} , and Ho^{III} , show nice luminescence properties (for which reason they find widespread application as phosphors in high-tech and daily-use optics and screens) applicable to chemical studies by means of luminescence spectroscopy such as time-resolved laser-induced fluorescence spectroscopy (TRLFS). Especially the latter is an often and extensively applied spectroscopic method for studying Ln^{III} electronic properties, investigating complexation with determination of, *e.g.*, coordination numbers and geometry as well as stability constants. Besides focusing on the metal ions by means of electronic spectra, several further spectroscopies can be applied to obtain complementary information on the interacting ligand.

2.2 ACTINIDES

The actinides (An) comprise that series of chemical elements of the periodic table with atomic numbers 89 (actinium) through 103 (lawrencium). Whereas for actinium and thorium the $6d$ sub-shell is in part filled, as of protactinium the $5f$ shell is successively filled with electrons. This particular type of valence electrons determines their chemical and spectroscopic behavior.

2.2.1 Natural Abundance and Distribution of the Actinides

All actinides are radioactive elements, of which thorium and uranium occur in nature as minerals such as (urano)thorite and pitchblende, with ^{232}Th , ^{235}U and ^{238}U being the initial elements of the natural radioactive decay series that comprise various decay products, and ending at (stable) isotopes of lead. Among the transuranium elements, ^{244}Pu as a primordial element as well as ^{239}Pu and ^{239}Np yielded by neutron capture of ^{238}U , can also be found in nature (by employment of ultratrace analyses). Of anthropogenic origin, such as radioactive waste from or contaminated sites after accidents in nuclear energy production, or fallout from surface nuclear weapon tests, are further isotopes of plutonium as well as neptunium, americium, curium, berkelium, californium, einsteinium, and fermium, the latter group being referred to as *minor actinides*.

The following section is adopted from S. HÜBENER, *Actinide Elements* [34], a chapter from the Encyclopedia of Physical Science and Technology.

2.2.2 Electronic Structure

The filling of the f -shell is a common feature of both lanthanides and actinides. However, considerable property differences exist for the $4f$ and $5f$ -electrons. Whereas both the $4f$ -orbitals of the lanthanides and the $5f$ -orbitals of the actinides possess the same angular part of the wave function, they differ in their respective radial parts. The energies of the $5f$, $6d$, $7s$, and $7p$ orbitals are comparable over a range of atomic numbers and since the orbitals overlap spatially, bonding can involve any or all of them. This is particularly important in the first half of the actinide series, with oxidation states up to +VII with a compound-to-compound variation in oxidation state, depending on the ligands, because the small energy differences between the valence orbitals can be compensated within the range of chemical bonding energies.

Since the $5f$ -orbitals are more extensive relative to the $7s$ and $7p$ -orbitals than the $4f$ -orbitals relative to the $6s$ and $6d$, they may show covalent contribution. The ligand-field model works so well [for the lanthanides] because of the atomic nature of the $4f$ shells in these compounds. In both the lanthanide and the actinide series, the cations are typical hard LEWIS acids. Their outermost electronic configuration resembles that of closed-shell systems, as the inner f -orbitals are largely or completely unavailable for bond formation. There is evidence for covalent bonding in actinide chemistry in the formation of the actinyl ions

AnO_2^+ and AnO_2^{2+} , in which both f - and d -orbitals participate in the An–O bonds, but the extent and even the existence of covalency in the bonding of simple An^{n+} species is a subject of controversy [and still ongoing interest]. The presence of a slight amount of covalency in lanthanide bonds has been attributed to involvement of $6s$ orbitals rather than of the $4f$ orbitals. Differences in interactions with soft donor atoms have been the basis of a proposal for greater degree of covalency in the bonding of An^{III} relative to that of Ln^{III} [17].

2.2.3 Oxidation States

Unlike the Ln, for which the dominant oxidation state is +III, the An elements exhibit a remarkable variety of oxidation states, ranging from +II to +VII. For the An up to U the higher oxidation states are the most stable, with a chemistry more transition-metal like [35]. Upon further increasing atomic number, the stability of the higher oxidation states decreases. From Am on – with the exception of No (+II) – the most stable oxidation state is +III, therefore a more lanthanide-like behavior is observed. For any oxidation state the ionic radii decrease regularly with increasing atomic number as a consequence of the decreased shielding by f -electrons of the outer valence electrons from the increasing effective nuclear charge. This actinide contraction is very similar to the lanthanide contraction.

An interesting feature with remarkable stability is the actinyl ion (AnO_2^{n+}), observed for the nominally high-charge ions of oxidation states +V and +VI (except for Pa^{V}), bearing two linearly coordinated oxygen atoms in quite short distances ($\approx 1.8 \text{ \AA}$). The strength of the metal–oxygen bond decreases with increasing atomic number from U through Am.

2.2.4 Solution Chemistry

In aqueous solution, the actinide ions interact with the surrounding water. In addition to coordination, metal ions can also act as LEWIS acids inducing hydrolysis of the bound water, releasing hydronium ions. The ion's acidity increases with the charge on the metal, with the M^{4+} ions being considerably more acidic than the actinyl ions, resulting in a much stronger tendency to undergo hydrolysis and the formation of polynuclear species and colloids. Complex formation involves a replacement of the coordinating water by suited ligands (representative speciation diagrams of U^{VI} are shown below). For a given ligand the stability of the complexes follows the order of effective charge on the metal ion as typical for hard acceptors (according to the HSAB principle by PEARSON [36], whereas the M^{4+} are stronger acceptors than the actinyl ions). Additionally, due to the axial yl -oxygen atoms, for the actinyl ions coordination is restricted to the equatorial plane, whereas for spherical M^{n+} ions coordination is unrestricted considering ligand field and metal valence orbital geometries. High stabilities of complexes formed by hard acceptors are not reflected in exothermic enthalpy changes, but rather in very positive entropy terms due to a large decrease of order as a result of complex formation.

Since the speciation of U^{VI} is crucial for understanding its (pH-dependent) complexation behavior towards ligands, its aquatic speciation is depicted for both nitrogen and ambient atmosphere (Fig. 1). In general, under acidic conditions U^{VI} occurs as the free uranyl aquo ion. Upon increasing pH, hydrolysis occurs, also referred to as olation and oxolation, and hydroxo species become more relevant, the latter of which forming both cationic and anionic complexes. As of slightly acidic to circumneutral conditions dissolution of, *e.g.*, atmospheric CO_2 results in carbonate formation and, subsequently, U^{VI} complexation up to alkaline media, yielding anionic binary (or ternary hydroxo) carbonate complexes. Furthermore, except for both strong acid and strong alkaline media, preferentially at higher total uranium concentrations, $[U^{VI}]$, polynuclear species predominate.

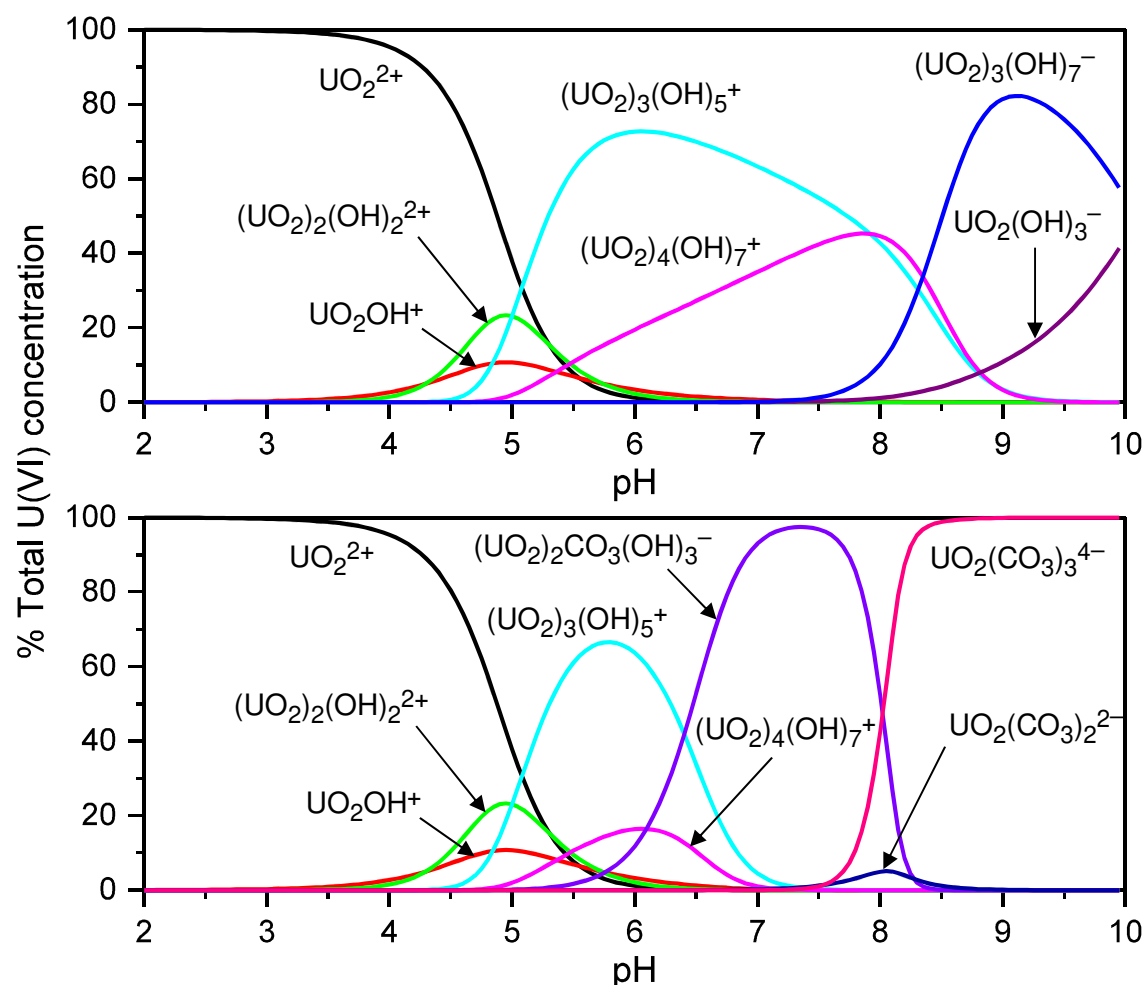


Figure 1. Aquatic speciation of 1×10^{-4} M U^{VI} in 0.1 M $NaClO_4$ medium at 25 °C under nitrogen atmosphere (top) and ambient atmosphere (bottom). Speciation calculation was performed with the EQ3/6 package [37] using the most updated thermodynamic data from NEA TDB [38]. Note that only species of at least 3% total U^{VI} concentration are displayed.

2.2.5 Spectroscopic Properties

Actinide spectra reflect the characteristic features of the f -orbitals. Analogous to lanthanide spectra, again three main types of transitions are observed in the absorption spectra of the actinide ions: (i) LAPORTE-forbidden $f-f$ transitions, (ii) orbitally allowed $5f-6d$ transitions, and (iii) ligand-to-metal charge transfer (LMCT). For the radial extension of $5f$ -orbitals is much larger than compared to corresponding lanthanides' $4f$ -orbitals, ligand-field contribution significantly affects electronic level energy differences and, thus, transitions. The latter fact combined with occurrence of higher oxidation states enabling easier ligand-to-metal charge transfer, the absorptivities and, thus, colors of actinide solutions are multifarious and often more intense as compared to those of lanthanides. Moreover, some actinides, particularly U, Am, and Cm, exhibit very favorable luminescence properties allowing acquisition of emission spectra for very low analyte concentrations (down to the nanomolar range). In contrast to spherical Ln^{3+} , high-valence state actinides occurring as actinyl ions, *viz.* uranyl, neptunyl, and plutonyl, provide further spectroscopic access by studying vibrational modes of the metal ions. Although NMR spectroscopy directly applied to the actinides is practically not feasible (*cf.* section 2.6), studies on the coordinating ligands as well as – in some rare but important cases – the actinyl oxygen atoms provide very valuable information. Consequently, actinide spectra are used in different ways. On the one hand, they can be used for the direct speciation of actinide ions as well as qualitative and quantitative verification. On the other hand, actinide spectra are used for the study of electronic and physicochemical properties, including information on symmetry, coordination number, or stability constants. Among the vast variety of spectroscopic methods, UV-Vis-NIR, TRLFS, EXAFS, as well as IR/Raman, and NMR spectroscopy are superior in gaining complementary information and allow for extensive investigations.

2.3 GLUTATHIONE

Glutathione (GSH) is a tripeptide consisting of L-glutamate (Glu), L-cysteine (Cys), and glycine (Gly), with an isopeptide bond between the former two (Fig. 2, top). It is the most ubiquitous and abundant low-molecular thiol present in concentrations up to 12 mM in mammalian cells [39]. As the most important intracellular reducing agent it is responsible for cellular redox state maintenance, therefore constituting an important antioxidant in humans, plants, animals, fungi, and some bacteria and archaea [40-42]. Upon oxidation, the thiol groups of two GSH molecules form a disulfide bridge, yielding glutathione disulfide (GSSG, Fig. 2, bottom) with concomitant release of two electrons (and two H^+).

Since GSH comprises the two chiral (naturally L-configured) amino acids glutamate and cysteine, and prochiral glycine, all methylene groups are diastereotopic, *i.e.*, possessing chemically (and hence also magnetically) inequivalent hydrogen atoms that, therefore, give rise to different ^1H NMR signals – a feature repeatedly emerging throughout this work. The two GS-moieties (I and II) are equivalent owing to a C_2 axis through the S–S bond, also in

the crystal as observed by KRETZSCHMAR ET AL. [43], whereupon the two moieties give rise to the same set of signals. However, each methylene group within one GS moiety bears distinct protons.

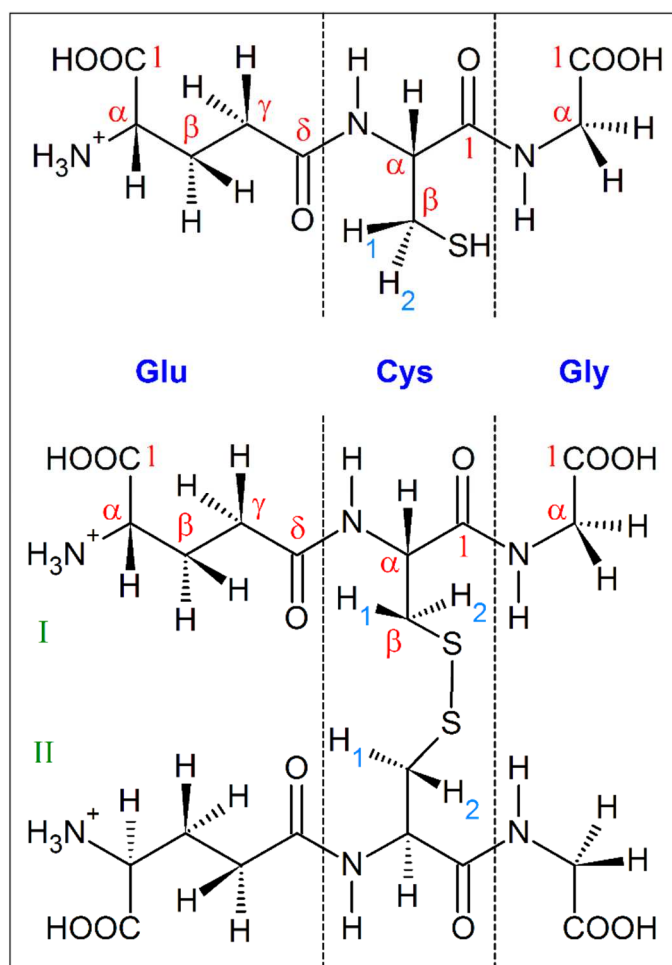


Figure 2. Generic structures of GSH (top) and GSSG (bottom), with labeling of the constituting α -amino acids L-glutamate (Glu), L-cysteine (Cys), and glycine (Gly) as well as the corresponding positions. Note the two GS-moieties (I and II) in GSSG, and the diastereotopic methylene groups, exemplarily indicated for Cys β .

Acting as a reductant together with its capability of heavy metal sequestration by its various functional groups, it plays a major role in various detoxification mechanisms of electrophiles such as radical oxygen species or heavy metals [44-47]. U^{VI} uptake into cells causes an alteration of the GSH pool, that is a decreasing GSH/GSSG ratio, as a response to oxidative stress [48-50], and is accompanied by reduction of U^{VI} to U^{IV} [51]. Consequently, under reducing conditions such as *in vivo*, GSH prevails in its reduced form. However, in the presence of air oxygen, other oxidants, or after cell death, GSSG is the predominating species. Note that, though having no free thiol group, GSSG is still capable of metal ion complexation due to its carboxylic and amino functionalities.

Table 1 comprises pK_a values for both GSH and GSSG, with both these terms used generically to note the ligand in general unless speciation is of importance. According to their respective protonation states (see also the speciation diagrams in Fig. A2, Appendix), GSH and GSSG are considered to form the following species: H_3GSH^+ , H_2GSH^0 , HGS^- , HGS^{2-} , and GS^{3-} , as well as H_6GSSG^{2+} , H_5GSSG^+ , H_4GSSG^0 , H_3GSSG^- , H_2GSSG^{2-} , $HGSSG^{3-}$, and $GSSG^{4-}$.

Table 1. pK_a values of GSH and GSSG protolysis sites.

protolysis site		GSSG, Ref. [52]	GSH, Ref. [53]	GSH, this work
Glu COOH	(I)	1.6 ± 0.1	2.3	not determined
	(II)	2.23 ± 0.03		
Gly COOH	(I)	3.15 ± 0.02	3.3	3.24 ± 0.03
	(II)	3.85 ± 0.01		
SH		–	9.0	9.01 ± 0.07
NH_3^+	(I)	8.83 ± 0.01	9.5	9.47 ± 0.03
	(II)	9.53 ± 0.02		

With its high natural abundance, different functional groups and reducing capability combined with its superior importance *in vivo*, GSH and GSSG provide outstanding characteristics and serve as convenient low molecular-size model peptides for the combination of actinide complexation research and NMR spectroscopy.

2.4 CITRATE

Citric acid, or in biochemical context often referred to as citrate, is a tricarboxylic acid, and eponymous for the citric acid cycle as the paramount metabolic pathway in aerobic organisms. It is hence not only a ubiquitous molecule but also an essential and highly concentrated constituent *in vivo*.

Citrate has four functional groups (see generic structure in Fig. 3), three carboxyl and one hydroxyl group, all of which are potential coordination sites. Corresponding pK_a values are given in Table 2. As a result, citrate is a strong complexing agent because it may easily form chelate complexes. The hydroxyl group in organic ligands is, in general, a very weak acid and only deprotonates at $pH > 12$ in the absence of metal ions. Furthermore, the configuration of these four functional groups imposes steric constraints on the coordination

and more than three groups cannot bind to the same metal ion. The non-bonded functional group(s) may be bridging to a second metal ion, and polynuclear complexes are therefore abundant in most metal–citrate systems [54].

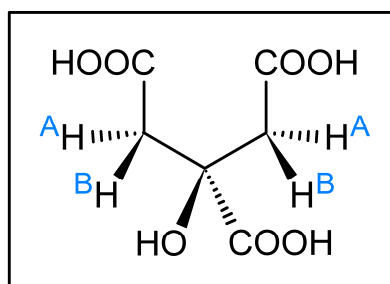


Figure 3. Generic structure of citric acid. Note the mirror plane perpendicular to the paper plane through the central carbon rendering the terminal carboxyl groups, the methylene groups, and hydrogen atoms in corresponding positions equivalent, but within a methylene group to be diastereotopic as indicated by A and B, respectively.

Table 2. pK_a values of citric acid protolysis sites, taken from Ref. [54].

protolysis site	$(C_q)COOH$	$(CH_2)COOH$ (I)	$(CH_2)COOH$ (II)	$(C_q)OH$
pK_a	3.1	4.8	6.4	> 12

For the actinide elements form HSAB-hard cations, the complexing agents *in vivo* are predominantly carboxylic acids from the citric acid cycle [18-20]. Accordingly, for all the actinides studied in man, the urinary excretion route appears to predominate. The limited studies which have been published indicate that plutonium and, perhaps, other *f*-elements are eliminated in the urine as citrate complexes [55]. Therefore, citrate is employed for studying actinide interaction owing to not only its biological importance and abundance, but also suitability for spectroscopic investigations as a model molecule for hydroxy- and polycarboxylic acids.

2.5 SELENIUM

Selenium is a naturally occurring trace element. Owing to its chemical similarity to homologous sulfur, it therefore occurs most commonly in sulfide ores of various metals. Upon both geological alteration and anthropogenic activity such as mining and smelting of sulfide ores, processing of copper, (particularly sulfur-rich) coal combustion, use of phosphate fertilizers, etc.) it is released into the environment [26, 56-57]. Moreover, and again for its close relationship to sulfur and its similar chemical behavior [58], Se analogues of S-containing amino acids, *viz.* selenomethionine and selenocysteine, are found in all three domains of life, being crucial constituents of enzymes such as glutathione peroxidase and glutathione-S-transferases [59].

The selenium isotope Se-79 is one of the long-lived (3.27×10^5 a) radionuclides considered to significantly contribute to the potential radiation dose from nuclear waste repositories. Owing to its potential migration capacity to the surface environment it is of interest in nuclear waste disposal problematic. As an essential nutrient and, thus, responsible for functionality of critical biomolecules, uptake of bioavailable radioactive selenium compounds is then very harmful owing to its effective radiotoxicity [27-30, 60].

Selenium exhibits various oxidation states in natural environments. Under (strong) reducing conditions selenium prevails as selenide or selenol (–II) or elemental selenium (± 0) or diselenide (–I), respectively, whereas for oxidizing conditions selenite (+IV) and selenate (+VI) are the predominating species, all of which – except elemental selenium – feature protolysis equilibria with pH-dependent speciation comprising conjugated acids and bases. According to the high acidity of selenic acid, $\text{Se}^{\text{VI}}\text{O}_2(\text{OH})_2$, only the fully deprotonated selenate ion is relevant ($\text{p}K_{\text{a}2} = 1.75$ [61]), whereas in the case of selenous acid, $\text{Se}^{\text{IV}}\text{O}(\text{OH})_2$, with $\text{p}K_{\text{a}}$ values of 2.64 and 8.36 [61], the hydrogen selenite HSeO_3^- and the selenite ion SeO_3^{2-} have to be considered regarding conditions found in the environment or nuclear waste disposals.

2.6 NUCLEAR MAGNETIC RESONANCE SPECTROSCOPY

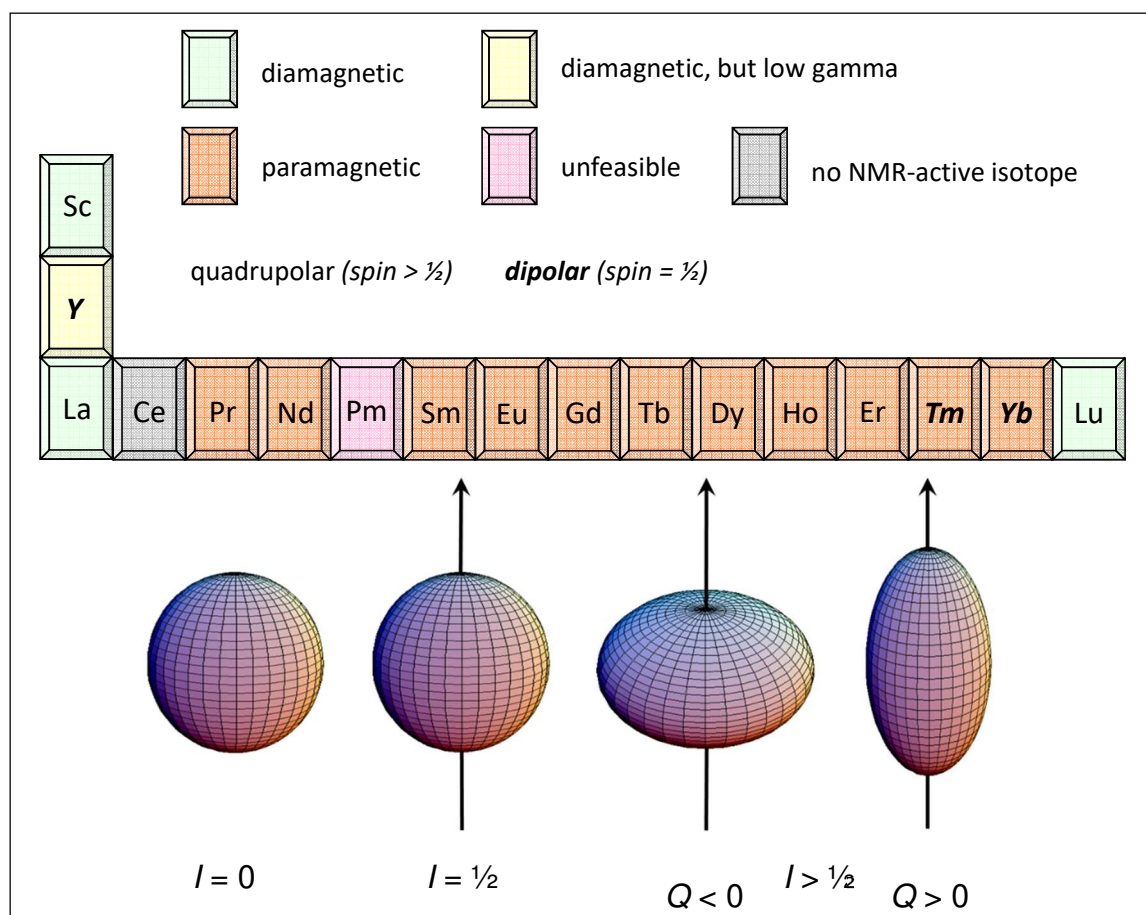
2.6.1 General Considerations

Basic knowledge on NMR spectroscopy in general is presupposed or can be found elsewhere, *e.g.*, J. KEELER *Understanding NMR spectroscopy* [62], or M. H. LEVITT *Spin Dynamics: Basics of Nuclear Magnetic Resonance* [63].

Briefly, NMR spectroscopy is a method which, in principle, can be applied to virtually any chemical element, but is practically restricted to elements with isotopes of particular properties, *i.e.*, at least a magnetic moment. Characteristics such as natural abundance, spin quantum number, and gyromagnetic ratio determine the sensitivity. By application of radio-frequency pulses to a sample exposed to an external magnetic field, transitions between nuclear spin levels are induced. Since the nuclei are sensitive to their electronic environment, changes in bonding, redox state, or ionic charges can be determined. Although NMR is predominantly used for structure elucidation of organic and biologic molecules or organometallic complexes, in certain cases investigations of (small) inorganic (ionic) compounds may be challenging, but likewise interesting and helpful.

As depicted in Scheme 1, nuclei with spin quantum number $I = 0$ (*gg* configuration)¹ possess no magnetic moment at all and are thus NMR silent (*e.g.*, ^{12}C , $^{16,18}\text{O}$, ^{32}S). Quite abundant and rather convenient are nuclei of $I = 1/2$, possessing a magnetic dipole (only) moment, hence being called *dipolar*, showing a spherical nuclear charge distribution, with

¹ *g* meaning *gerade* (German, even) and *u* meaning *ungerade* (odd), referring to the number of nucleons.



Scheme 1. NMR related properties of the rare earth elements (top) and illustration of nuclear charge distribution related to spin quantum number I and sign of electric quadrupole moment Q (bottom). Spheroids adapted from [64-65].

the number of one sort of nucleons being odd, the other even (gu or ug configuration; *e.g.*, ^1H , ^{13}C , ^{15}N , ^{31}P , ^{77}Se). The majority of nuclei, however, have $I > \frac{1}{2}$, that is, an additional electric quadrupole moment (Q), therefore referred to as *quadrupolar* nuclei (*e.g.*, ^{11}B , ^{17}O , ^{99}Tc) that can in principle be observed as long as $|Q|$ is sufficiently small. Because of their non-spherical nuclear charge distribution, either oblate or prolate, electric field gradients (EFG) owing to anisotropic electron density distribution around the nucleus as for, *e.g.*, asymmetric coordination geometry, give rise to very effective relaxation, which in the worst case precludes observability. Nuclei of ug or gu configuration always have half-integer, those of uu configuration integer spin quantum number, the latter of which being very rare among the periodic table (*e.g.*, $^2\text{H} \equiv \text{D}$, ^{14}N , ^{10}B , ^{138}La).

In addition to the atom's nucleus, as the complement one has also to take into account the atom's electronic configuration, which can in principle be diamagnetic or paramagnetic, *i.e.*, paired only or unpaired electrons being present, respectively. The latter of which one will come across among the series of transition metals, lanthanides, and actinides, bearing unpaired electrons in d - or f sub-shells, respectively. These unpaired electrons can be related to the nucleus under consideration *within the same atom*. In this case, owing to the

electron's much (by a factor of ≥ 658) larger magnetic moment compared to that of nuclei, strong interactions between nuclear spin and electron unpaired spin(s) occur, often rendering these particular nuclei not observable (see below). On the contrary, interaction of a (spin of a) nucleus under investigation with an electron unpaired spin *of a different atom* causes unique spectral effects as described in section 2.6.2 and later in this work.

Consequently, as depicted in Scheme 1, among the rare earth elements prevailing almost unexceptional as trivalent cations, the following situations can be found: (i) no NMR active isotope at all (Ce), (ii) such rare and short-living so that unfeasible (Pm), (iii) dipolar *but* disadvantageous paramagnetic (Tm, Yb), or (iv) diamagnetic *but* disadvantageous quadrupolar (Sc, La, Lu), as well as (v) *very* disadvantageous quadrupolar *and* paramagnetic (Pr through Er). Yttrium, allegedly of advantageous combination dipolar and diamagnetic, unfortunately is very insensitive showing very long relaxation times and affording for special equipment (low-gamma probe) since its gyromagnetic ratio γ (a measure for spectral sensitivity) is very low.

As the situation is at least just as bad for the actinides, illustration and discussion is superfluous, except for ^{239}Pu , in fact a spin- $1/2$ nucleus, for which YASUOKA ET AL. [66] from Los Alamos National Lab, USA, in 2012 labored to obtain some signals at 4 K.

Upon increasing atomic number, *i.e.*, number of nucleons, the shape of the nuclei progressively deviates from spherical shape, since its preservation is hardly feasible owing to the very short-range effect of the strong nuclear force disallowing regular (spherical) arrangement of both sorts of nucleons, *e.g.*, ^{235}U 's 92 protons and 143 neutrons.

2.6.2 NMR Spectroscopy of Paramagnetic Molecules

At this juncture the eponymous book of I. BERTINI ET AL. [67] is stressed and recommended for both introductory and further reading, the latter particularly for metallobiomolecules.

Nuclei of ligands in paramagnetic complexes are coupled to the electronic spin of the central atom by the electron–nuclear *hyperfine interaction*. As a result, large chemical (induced) shifts (relative to the diamagnetic system) in the NMR spectra of the ligands are observed. There are two independent mechanisms of *hyperfine interaction*: (i) the *contact* interaction, resulting from a finite probability of finding an unpaired electron spin on an atomic *s*-orbital, and (ii) the *pseudocontact* interaction, taking place through space, causing shift contributions only if the magnetic susceptibility of the central ion is anisotropic. ^1H shifts are predominantly due to pseudocontact contribution caused by dipolar interaction resulting from a supplementary magnetic field emanating from the anisotropic distribution of *f*-electrons at the paramagnetic metal center, increasing the effective magnetic field sensed by the nuclei and therefore causing shielding in principle for all nuclei. Often, ^{13}C shifts of adjacent atoms show alternating signs, attributed to spin polarization effects due to *contact contribution* [68] with unpaired electron spin density distributed along the molecular frame-

work. Not only that for one sort of probed nucleus, *e.g.* ^{13}C , the magnitude and the direction of the shifting depends on the characteristics of the metal ion itself but also the bonding and structure within the complex, the latter comprising coordination geometry and distances between metal ion and nuclei of interest.

Nuclear relaxation in paramagnetic complexes occurs due to the time-dependent terms in the nuclear spin Hamiltonian. The amount of relaxation effect depends on the intensity of electron–nuclear interaction and the rate at which this interaction is interrupted. Thus the relaxation rates of ligand nuclei are determined by two factors, *i.e.*, molecular structure and molecular dynamics in solution [33].

Lanthanide induced shifts (LIS) in NMR spectroscopy can be used as a helpful tool for signal separation, probing the potential binding sites and structure determination including geometries and distances, with application that has come to the chemists' attention as lanthanide shift reagents [69-70]. LIS comprise the *contact* term, depending on type and number of bonds between the (open shell) metal center and the atom of interest, and the angle and distance ($1/r^3$) dependent, through-space mediated *pseudocontact* term. Both of which can contribute to different extent, depending on, *e.g.*, the electronic configuration and the energy of the ground state or the ligand field splitting [67]. Due to its quite small paramagnetism, the signals of those molecules interacting with Eu^{III} are shifted (separated) sufficiently, however, with only low signal broadening [71].

Eu^{III} concentration-dependent LIS can be used not only for of the studying the complex structures but also determining their thermodynamic stability. In consideration of the overall research field of actinide chemistry with regard to both nuclear waste disposals and interaction with the biogeosphere, Eu^{III} is often used as an inactive analogue to trivalent (minor) actinides, particularly for isoelectronic Am^{III} , *e.g.*, SCHOTT, KRETZSCHMAR, ET AL. [72-73] or BARKLEIT, KRETZSCHMAR, ET AL. [74].

2.6.3 ^{77}Se NMR Spectroscopy

Among the stable selenium isotopes, the spin- $1/2$ nucleus of ^{77}Se is (the only) NMR-active, and suited to be directly observed by NMR spectroscopy. This method is in particular a valuable tool for the discrimination of oxidation and protonation states (*cf.* Fig. 4). In contrast to this structural sensitivity, the major drawback of NMR is the requirement of high concentrations (compared to other methods). Working with natural abundance of ^{77}Se (7.6%), for practical reasons the minimal concentration for routine NMR is 10^{-3} M. If, for any reason, lower concentrations are required, either ^{77}Se -enriched material or special NMR equipment is mandatory. Spin- $1/2$ nuclei with quite low γ , such as ^{77}Se , unfortunately possess long spin-lattice relaxation times (T_1), up to values of minutes (!). For quantitative measurements, the waiting time (interpulse delay, d1) between two acquisitions must not be shorter than $5 \times T_1$, resulting in time-consuming experiments. To overcome this, the chosen concentrations are mostly a compromise between experimental time and spectral S/N.

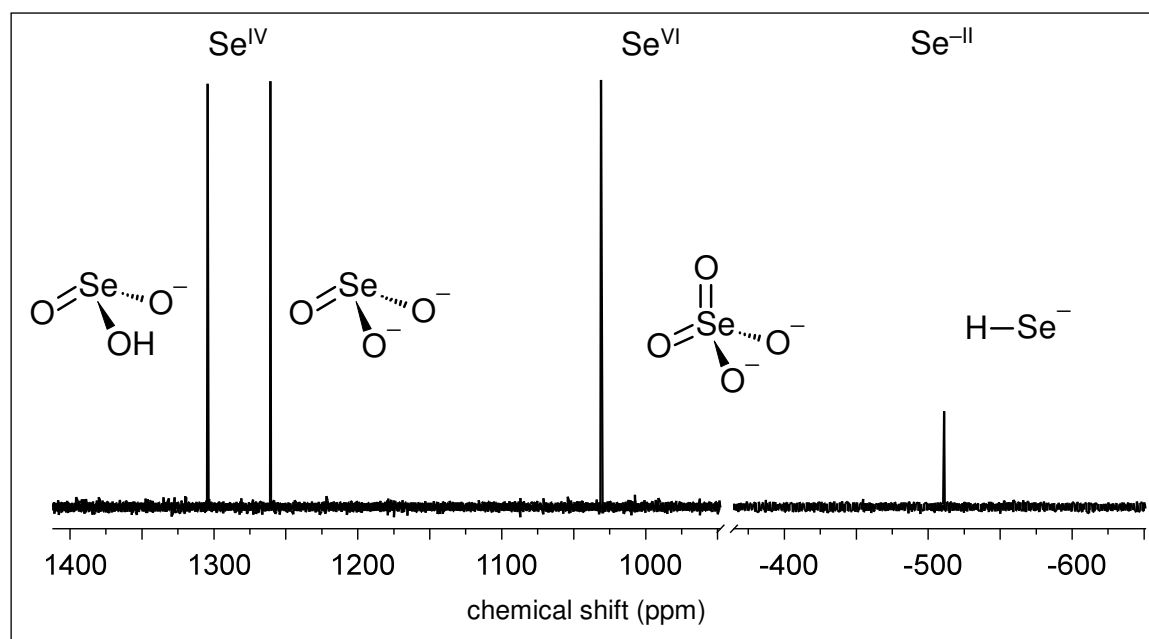


Figure 4. Superposition of ^{77}Se NMR spectra illustrating the sensitivity in discriminating different oxidation and protonation states in aqueous solution.

3 RESULTS AND DISCUSSION

3.1 GLUTATHIONE/GLUTATHIONE DISULFIDE TOPIC

General considerations

For GSH is one of the central molecules throughout this work, its NMR characteristics are extensively studied, particularly in dependence of pD (see Fig. 5), serving as reference data (blanks) allowing determination of the counterpart's contribution on interaction, that is, the metal ions' spectral impact upon complexation.

Briefly, the pD titration of the blanks reveals chemical shift changes and, to a lesser extent, line broadening, associated with protonation/deprotonation reactions of the functional groups. Therefore, these studies allow the determination of protonation constants, $\text{p}K_{\text{a}}$, which are critical figures for determining correct speciation.

Starting at low pD, upon addition of base primarily the Glu α ^1H signal starts to shift. Deprotonation of the functional groups results in a shielding of the adjacent ^1H nuclei. Since the α -position is closest to the functional groups, it is these particular hydrogen atoms' signals that reveal the strongest pD-induced spectral effects. Remarkably, even the signals of the Glu ^1H nuclei in β and γ position follow the spectral behavior of the α - ^1H , however, with attenuated magnitude. According to the acidities and thus onset of the individual deprotonation reactions, the corresponding signals start to shift with increasing pD. The titration spectra indeed represent well the de/protonation progress. Plotting the ^1H chemical

shift δ_{H} vs. pD (*cf.* Table A2, Appendix) a dose-response-fit results in sigmoidal curves of which the inflection points represent the $\text{p}K_{\text{a}}$ values. Hence, the Glu ^1H signals undergo two sigmoidal features, firstly sensing the abstraction of the carboxylic and secondly the ammonium proton. The Glu carboxyl $\text{p}K_{\text{a}}$ value could not be determined with sufficient reliability within the pD range investigated. A summary of the obtained $\text{p}K_{\text{a}}$ values together with literature data is given in Table 1 (p. 11).²

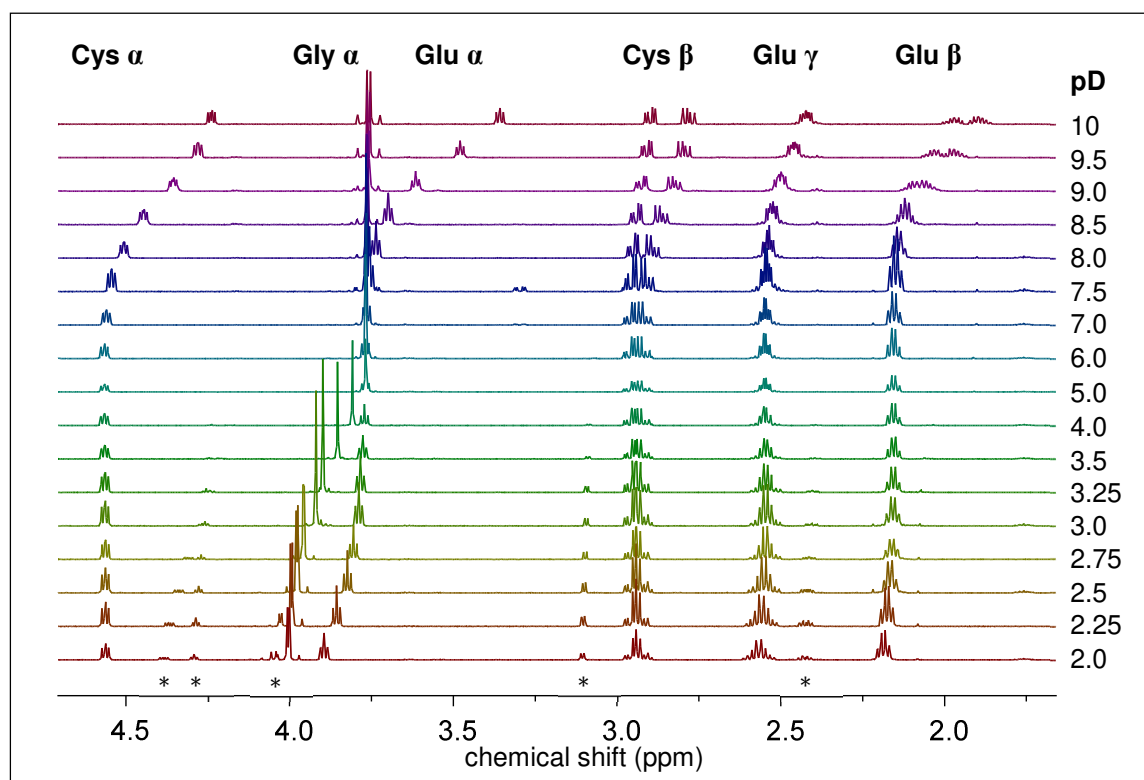


Figure 5. ^1H NMR pD titration series of 6.7 mM GSH. Note that only a part of the full spectrum is shown for clarity. Signals of glutamate and cysteinyl-glycine are indicated by *.

² Glycine is the only non-chiral proteinogenic α -amino acid, however, possesses enantiotopic hydrogen atoms, since the methylene group is prochiral. Although for the free glycine only one methylene ^1H signal is observed, upon binding in a peptide – by reducing both the symmetry and free rotational motion due to the partial double-bond character of amide bonds – the methylene group becomes diastereotopic and consequently two signals for both these hydrogen atoms are expected. Indeed, below pD 2.75 and above pD 7.5 two ^1H signals are observed, each actually split into a doublet, representing an AB spin system, with only small, but significant chemical shift differences. This non-equivalence is accompanied by a remarkable *geminal* coupling constant, *e.g.*, $|^2J| = 17.2$ Hz at pD 2. Above pD 2.75, the Gly carboxyl group starts to progressively deprotonate and the loss of this proton decreases the energy barrier for the rotation about the $\text{C}(\alpha)\text{--COO}$ bond and the chemical sites become equivalent upon fast rotational averaging of the individual magnetic environments. For higher pD values it appears that the double-bond character of the Cys–Gly amide bond is increased, resulting in both a lowered flexibility of this residue (rotation about the $(\text{Cys})\text{C}(=\text{O})\text{--NH}(\text{Gly})$ axis is slow on the NMR timescale) and an increased amide proton exchange rate – see also the notes together with the amide proton spectra given in the Appendix.

Apparently, as of pD 7 the thiol group starts to deprotonate as can be concluded from the chemical shift changes (increasing shielding) of the Cys α and β hydrogen atoms. This is accompanied by increasing diastereotopicity of the Cys β hydrogen atoms as determined by increasing chemical shift differences between the latter signals. Concomitantly, the *vicinal* coupling constants between the α and both the β ^1H nuclei change: increasing pD from 7.5 through 10, $^3J_{\beta_1,\alpha}$ decreases from 5.2 to 4.9 Hz, whereas $^3J_{\beta_2,\alpha}$ increases from 7.2 to 8.0 Hz. Therefore, one can assume conformational changes for the Cys side chain, since alterations in the *vicinal* coupling constants indicate changes in the dihedral angles. This is consistent with calculations by VILA-VIÇOSA ET AL. [75] who found the Cys side chain showing random conformation until above pH 8 the most probable conformation is the Cys amide nitrogen in *trans* position to the thiol group.

The hydrogen atoms of the peptide bonds also give rise to ^1H NMR signals. Because the NMR spectra are usually recorded in deuterated solvents, that is, throughout this work in D_2O solutions, hydrogen atoms bound to oxygen, nitrogen, or sulphur atoms undergo exchange reactions. Thus, protons of the peptide bond – $\text{C}(=\text{O})\text{NH}$ – are replaced by deuterons and hence are not detectable by ^1H NMR spectroscopy any longer. For pH-dependent spectra acquired in H_2O probing the amide protons refer to Fig. A1, Appendix. The amide groups are planar due to 40% double-bond character in the C–N bond, and the *trans* form is strongly favored [76]. For transition-metal ions it was found that they are able to substitute for a nitrogen-bound amide proton, but they suffer competition with hydrolysis and precipitation in neutral and basic solutions. Thus, simple amides in their neutral state can form adducts with metal ions at the oxygen, but substitution of an amide hydrogen does not occur in aqueous solutions [77].

Particularly at low pD, hydrolysis of the GSH's isopeptide bond yields glutamate and cysteinyl-glycine, with signals (δ_{H} in ppm for pD 2) at 4.38 and 2.43 as well as 4.29, 4.05, and 3.11 for Glu α and Glu γ , as well as Cys α , Gly α , and Cys β , respectively (Fig. 5, indicated by *). In the worst case the content of these cleavage products amounts to 18% (by signal integration).

3.1.1 Glutathione–Lanthanide System

Figure 6 shows luminescence spectra of 5.5×10^{-5} M Eu^{III} for sample series varying either pH or GSH/Eu ratio, with the spectra of each series normalized to the $^5\text{D}_0 \rightarrow ^7\text{F}_1$ magnetic dipole transition, respectively. Upon complexation, *i.e.*, alteration of local Eu^{III} symmetry, particularly the hypersensitive termed $^5\text{D}_0 \rightarrow ^7\text{F}_2$ electric dipole transition at 615 nm increases in intensity and the symmetry forbidden $^5\text{D}_0 \rightarrow ^7\text{F}_0$ transition at 578 nm appears. Remarkably, the pH-titration series (Fig. 6, left) with even 50-fold excess in GSH reveals significant but only weak spectral changes as of pH 3 although Glu COOH is already deprotonated to $> 80\%$ under these conditions (*cf.* Table 1). Therefore, the observed intensity changes are ascribed to the onset of Gly COOH deprotonation and, thus, acces-

sibility to Eu^{III} complexation. Accordingly, at constant pH 6 notable changes are detectable as of increasing GSH/Eu ratio above 15. The apparent complex formation constant was determined to be $\log K = 1.71 \pm 0.01$, with a reliable fit obtained for a 1:1 complex only. Therefore, the interaction is considered weak. Since the underlying spectra were collected for varying GSH/Eu ratios at constant pH 6 (Fig. 6, right), the concerning complex species is $[\text{Eu}(\text{HGSH})]^{2+}$.

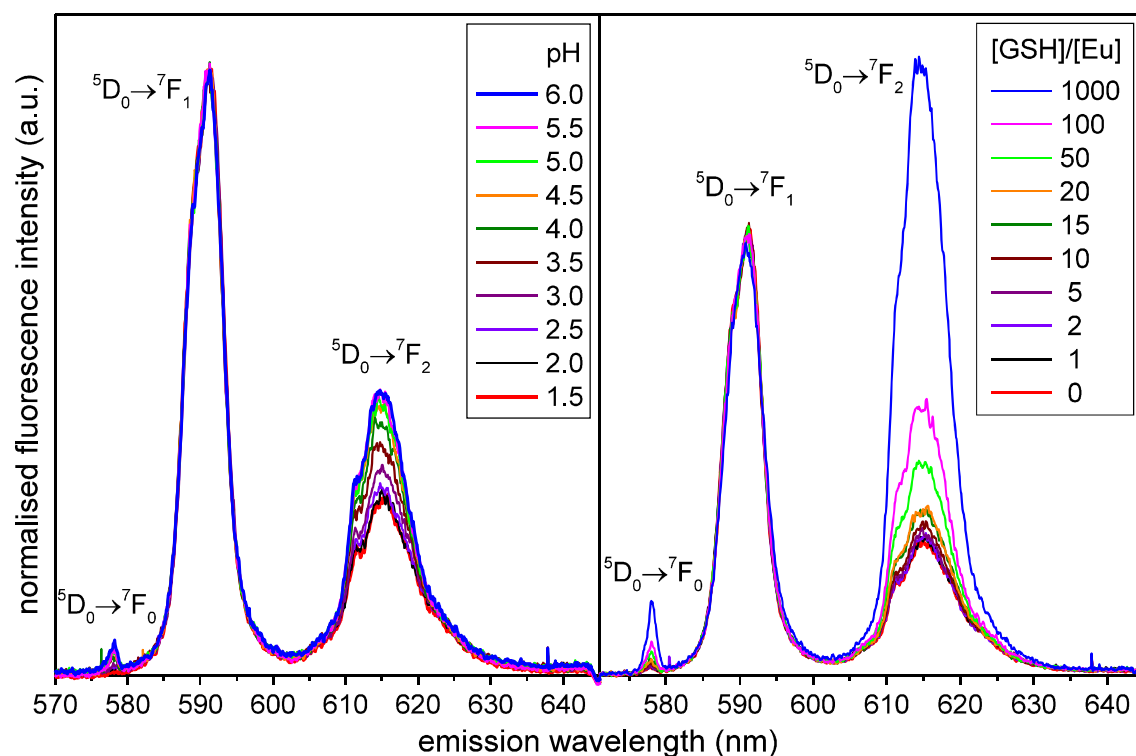


Figure 6. Luminescence spectra of 5.5×10^{-5} M Eu^{III} with 50-fold excess in GSH at varying pH (left), and at constant pH 6 for varying GSH/Eu ratios (right), with total ionic strength of 0.1 M. Note the characteristic luminescence transitions stated with the emission lines.

The obtained value agrees fairly well with La^{III} -GSH complex $\log K$ values of 2.35 [78] and 2.40 [79], and values of $2.4 \leq \log K \leq 3.1$ for Eu^{III} -complexes of various di- and tripeptides [80]. By contrast, the figures obtained by GARG ET AL. [81] ($6.5 \leq \log K \leq 7.8$) for GSH-complexes along the Ln^{III} series are rather doubtful.

GSH and GSSG solutions were also investigated by ^1H and ^{13}C NMR spectroscopy in the presence of varying La^{III} and Eu^{III} contents for pD 3 and pD 5, respectively. For comparison, further spectra in the presence of Lu^{III} , Ce^{III} , and Yb^{III} are shown in Figs. A3 and A4, Appendix. Since the complexes are labile in kinetic terms, the ligand exchange reaction is fast on all NMR timescales applied. Throughout this work, only molar fraction weighted averaged signals are observed according to Eqn. (1). For the only NMR active components are free and complexing ligand, the sum of molar fraction weighted chemical shift values can in general be reduced as

$$\delta_{\text{obs}} = \sum_i x_i \cdot \delta_i = x_f \cdot \delta_f + x_c \cdot \delta_c \quad (1)$$

with δ_{obs} observed chemical shift, commonly referred to as δ
 x_i molar fraction of component i
 δ_i chemical shift of component i
 x_f molar fraction of free ligand
 δ_f chemical shift of (a certain site in) free ligand
 x_c molar fraction of complexing ligand
 δ_c chemical shift of (a certain site in) complexing ligand

and the molar fractions complementing to unity: $x_c = 1 - x_f$. Consequently, upon successive addition of metal ion the fraction of free ligand (x_f) decreases while that of complexing ligand (x_c) increases, and the apparent signals correspondingly shift towards their respective complex attributed chemical shift values. Additionally, increasing contents of paramagnetic ion will influence the bulk susceptibility χ_{bulk} , that is, all molecules will inevitably be affected simply by its presence in the solution. Assuming that χ_{bulk} affects all components equally and isotropically, it can be estimated from signal shifts of molecules not specifically interacting with the paramagnetic ion such as the solvent.

$$\delta_{\text{obs}} = \sum_i x_i \cdot \delta_i + \Delta\chi_{\text{bulk}} \quad (2)$$

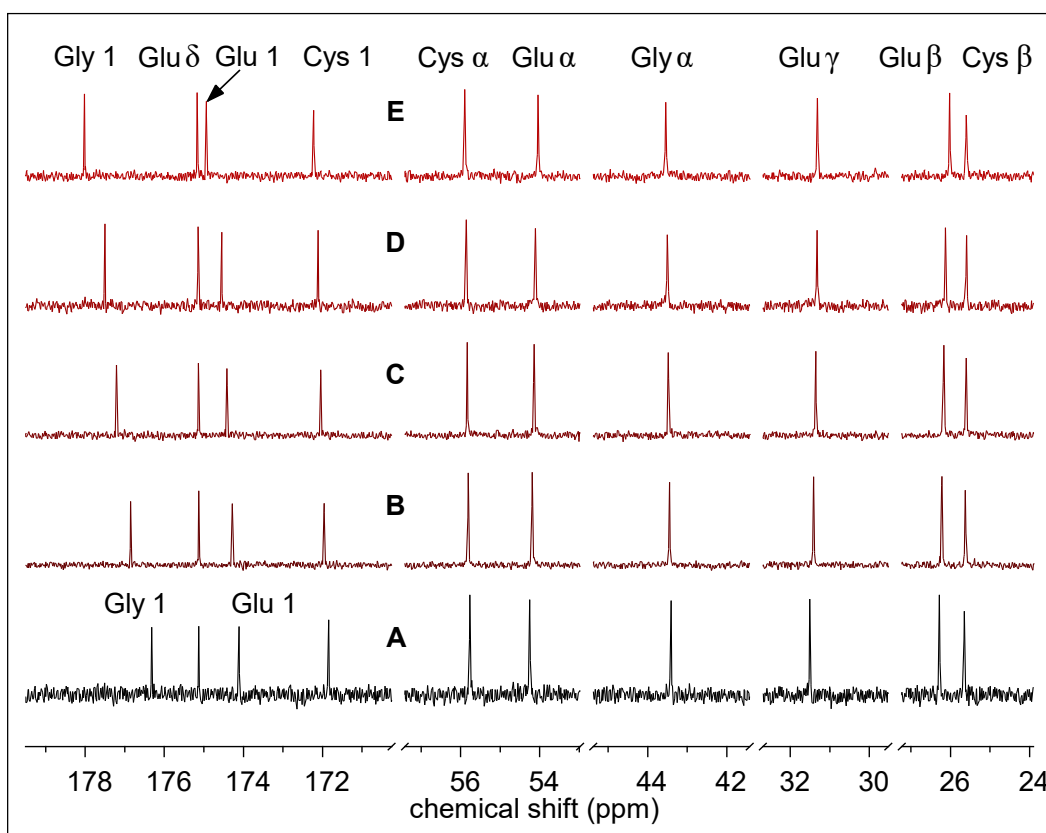


Figure 7. ^{13}C NMR spectra of 300 mM GSH at pD 5 without (A), and in the presence of (B) 30, (C) 60, (D) 100, and (E) 300 mM La^{III} .

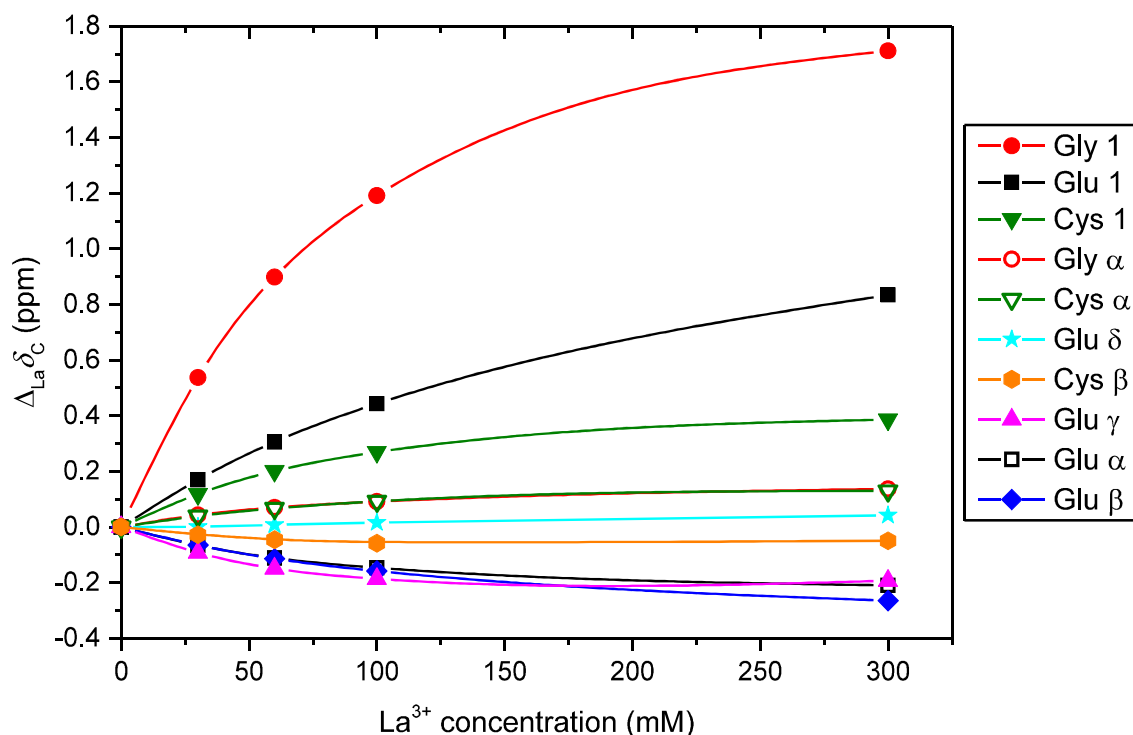


Figure 8. La^{III} -induced ^{13}C chemical shift changes ($\Delta_{\text{La}}\delta_{\text{C}}$) as a function of $[\text{La}^{3+}]$ obtained from spectra of 300 mM GSH at pD 5, with splines drawn for better visualization.

Owing to their electron configuration of $[\text{Xe}]4f^0$ and $[\text{Xe}]4f^{14}$, respectively, both La^{III} and Lu^{III} are closed-shell diamagnetic ions. On the contrary, Ce^{III} , Eu^{III} , and Yb^{III} respectively possess $4f^1$, $4f^6$, and $4f^{13}$ valence electron configuration, according to which these are open-shell paramagnetic ions being able to strongly influence the appearance of NMR spectra. Effects observed for one sort of probed nuclei does not necessarily correspond to another sort of nuclei. For instance, Ce^{III} causes both ^1H and ^{13}C GSH signals to unanimously shift downfield, whereas same amounts of Eu^{III} induce solely upfield shifts for ^1H signals, however, both upfield and downfield shifts for ^{13}C signals (*vide infra*). Both acquisition and interpretation is straightforward for the spectra obtained from diamagnetic solutions, hence serving as reference data since affected by pure complexation-induced chemical shift changes only. ^{13}C NMR spectra of La^{III} containing pD 5 samples are shown in Fig. 7, La^{III} -induced ^{13}C chemical shift changes, $\Delta_{\text{La}}\delta_{\text{C}}$, denoting the difference between δ_{obs} and δ_f , are depicted in Fig. 8. The positive charge of the trivalent metal ion causes a deshielding, *i.e.*, reduction of electron density at the nuclei at the binding sites, that is, the carboxyl groups (Gly 1 and Glu 1). The significantly smaller $\Delta_{\text{La}}\delta_{\text{C}}$ of the other carbon signals are ascribed to polarization effects (partial charges) and (minor) conformational changes. Corresponding ^1H spectra reveal $\Delta_{\text{La}}\delta_{\text{H}}$ of 0.07 ppm at most (for Gly α at 300 mM La^{III}) and are thus not presented.

Exemplary ^1H and ^{13}C NMR spectra obtained for the interaction of GSH and Eu^{III} at pD 5 are shown in Figs. 9 and 10, and the corresponding graphical evaluation of $\Delta_{\text{Eu}}\delta_{\text{C}}$ obtained from pD 3 and pD 5 spectra, including GSSG data, is given in Fig. 11 (see below). Spectra of GSH pD 3, and GSSG pD 3 and pD 5 solutions as well as the graphical evaluation of $\Delta_{\text{Eu}}\delta_{\text{H}}$ are given in the Appendix. Upon successive Eu^{III} addition, particularly those signals associated with the nuclei of the carboxyl groups and in α -position shift considerably, whereas signals related to molecular sites more distant to the binding sites remain less affected. At higher $[\text{Eu}^{\text{III}}]$, particularly the ^1H signals exhibit the impact of increasing bulk susceptibility. Thus, signals of, *e.g.*, the Cys residue also shift, although the thiol group does not interact with Eu^{III} . Moreover, altered ^1H signal splitting patterns for, *e.g.*, Gly α and Glu β/γ are due to LIS rendering the diastereotopic methylene protons' individual δ_{H} more distinct (increasing $\Delta\nu/J$ ratio) rather than conformation changes affecting scalar coupling constants ($J_{\text{H,H}}$).

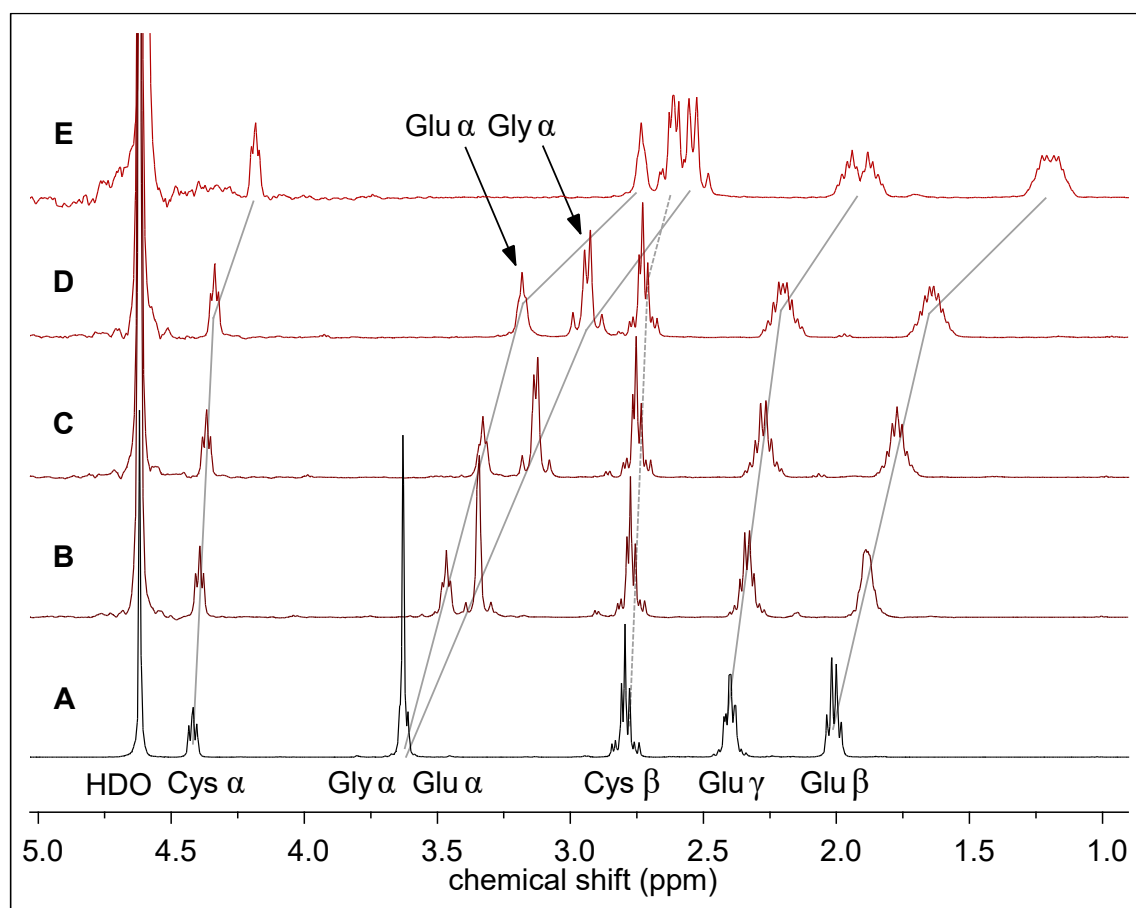


Figure 9. ^1H NMR spectra of 300 mM GSH without (A) and in the presence of (B) 30, (C) 60, (D) 100, and (E) 300 mM Eu^{III} at pD 5. Note the baseline perturbations due to water signal (denoted HDO) suppression by presaturation sequence.

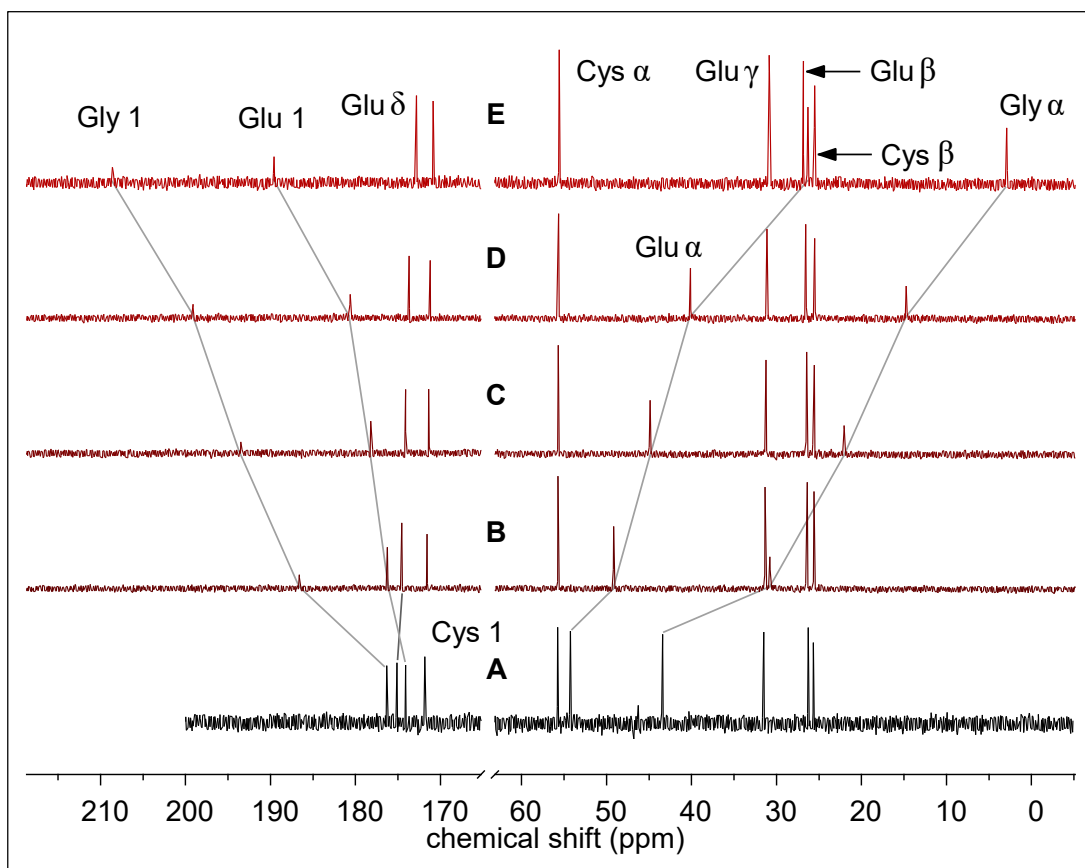


Figure 10. ^{13}C NMR spectra of 300 mM GSH without (A) and in the presence of (B) 30, (C) 60, (D) 100, and (E) 300 mM Eu^{III} at pD 5.

The approach comprises samples of 300 mM GSH and 150 mM GSSG, hence constituting the same effective concentrations in terms of qualitative similar binding sites, *i.e.*, Glu and Gly carboxyl groups. Because of their structural similarity, both ligands exhibit analogous spectral behavior. Particularly at pD 3 the determined $\Delta_{\text{Eu}}\delta_{\text{C}}$ are very similar for both ligands (Fig. 11, left). At pD 5 (Fig. 11, right), GSSG (Gly) $|\Delta_{\text{Eu}}\delta_{\text{C}}|$ are in principle smaller as compared to corresponding GSH values, however, approximate the latter for the highest $[\text{Eu}^{\text{III}}]$. This observation is, primarily, attributed to GSSG speciation. On the one hand, at pD 5 GSSG's second Gly carboxyl group is not yet fully deprotonated. On the other hand, in consideration of the quite high ligand concentrations applied, intermolecular interaction such as between Glu NH_3^+ and Gly COO^- is conceivable, *cf.* Fig. 14 (below). Therefore, accessibility to the binding site(s) is impeded – at least until exceeding a certain Eu^{III} concentration to overcome the competing processes.

For GSH, upon increasing pD, $|\Delta\delta_{\text{obs}}|$ increases accordingly owing to reduced competition between metal ions and protons for the binding sites. At pD 3, both Glu and Gly carboxyl groups possess considerably different degrees of deprotonation, *viz.* 83% and 37%, respectively. However, the determined $\Delta_{\text{Eu}}\delta_{\text{C}}$ values are almost identical for both sorts of carboxyl carbons. At pD 5, with both carboxyl groups now being fully ionized, the signals of the Gly moiety reveal (much) larger shifts as compared to the Glu moiety, regardless of the metal ion (*cf.* Figs. 8 and 11).

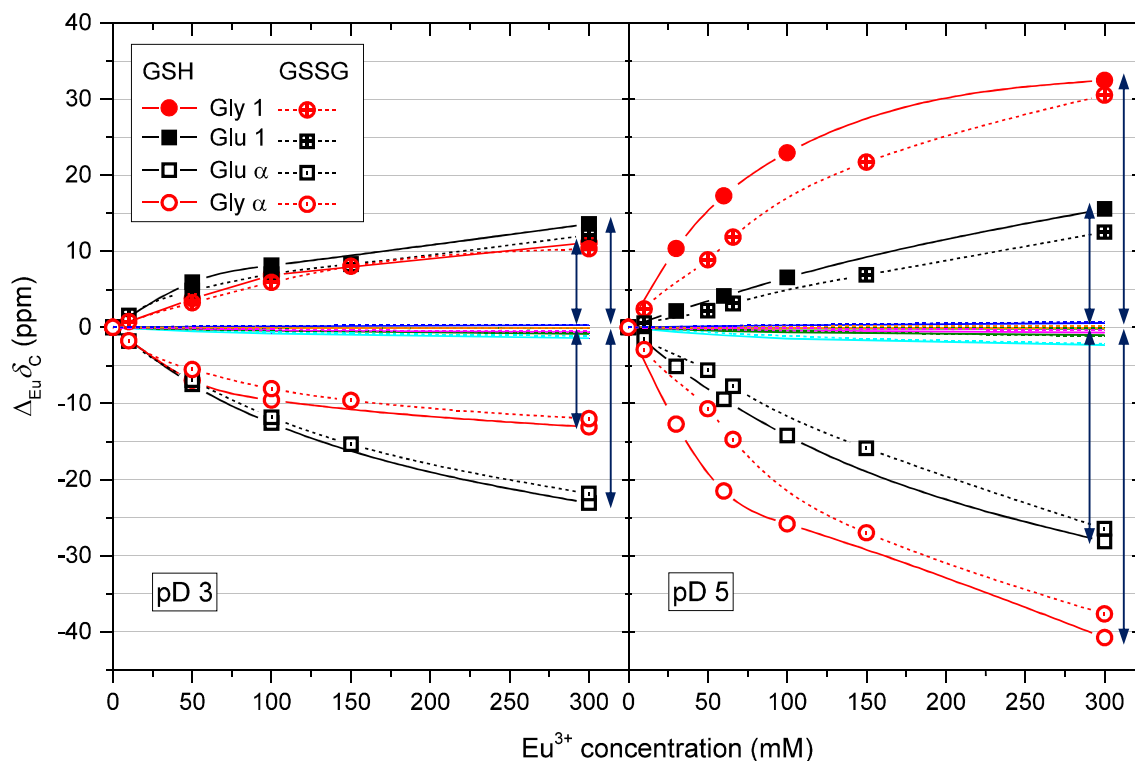


Figure 11. Eu^{III} -induced ^{13}C chemical shift changes ($\Delta_{\text{Eu}}\delta_{\text{C}}$) as a function of $[\text{Eu}^{3+}]$ obtained from spectra of 300 mM GSH and 150 mM GSSG at pD 3 (left) and pD 5 (right), respectively. Note the splines (solid for GSH, and dashed for GSSG) are drawn for better visualization. The remaining carbon sites are depicted by their respective data point connecting lines only.

Interesting are the effects caused by the unpaired electron–nuclear electronic and magnetic interactions. Regardless of both pD and moiety, both GSH and GSSG $\Delta_{\text{Eu}}\delta_{\text{C}}$ of adjacent atoms – at least for the carboxylic and α -carbons – show alternating signs, with $|\Delta_{\text{Eu}}\delta_{\text{C}}|$ of the α -carbons being larger than those of the carboxyl carbons (*cf.* lengths of facing arrows drawn in Fig. 11) although the latter are actually closer to the binding sites. According to SHERRY AND PASCUAL [82] who studied Ln^{III} –alanine structures, the ^{13}C LIS are dominated by polarization of unpaired spin away from the ligating carboxyl oxygen(s)³ and mediated by a direct delocalization of spin resulting in a larger unpaired spin density at the α -carbons than at the (closer) carboxyl carbon. Experiments with Gd^{III} , expected to be void of pseudocontact effects, reveal a larger negative spin density at C- α than the positive spin density at the carboxyl carbon. Since the spin delocalization *via* polarization falls off monotonically through a series of bonds away from the binding site, the positive spin density at the carboxyl carbon must be partially negated by a *direct* delocalization of negative spin density from the oxygen atom(s). Thus, the net effect of these two delocalization mechanisms results in both cancelling the spins at the carboxyl (and the β -carbon), and enhancing the spin at C- α . Although the ^1H LIS are primarily pseudocontact in origin, the α -hydrogen senses additional contact contribution, depending on the nature of the Ln^{III} . Of all lantha-

³ For the series from Pr^{III} through Tb^{III} the coordination mode is reported to be monodentate, whereas for Dy^{III} through Yb^{III} shown to be bidentate [82-84].

nides, Eu^{III} causes significant ^1H contact contribution as the LIS is larger for H- β than for H- α [82]. BLEANEY [85] and GOLDING AND HALTON [86] have shown by theoretical, GANSOW ET AL. [87] and BLEANEY ET AL. [88] by experimental evidence that Eu^{III} presents the largest ratio of contact/pseudocontact shifts across the lanthanide series.

To sum up, both TRLFS and NMR spectroscopy showed the rather weak and labile complexation of Eu^{III} by both GSH and GSSG. The Gly carboxyl group shows a higher affinity towards Ln^{III} than the Glu carboxyl group, owing to the electrostatic repulsion of the Ln^{3+} by the positively charged Glu $\alpha\text{-NH}_3^+$. Consequently, the time-averaged probability to find the Ln^{III} bound to the Gly COO is larger as for the Glu COO. The doubled number of functional groups in GSSG does not significantly increase complex formation.

On account of the rather small spectral effects of the diamagnetic metal ions, for judging on the carboxylate binding abilities the paramagnetic Eu^{III} enhanced spectral effects are very valuable. Additionally, the GSH spectra obtained for both diamagnetic and paramagnetic ions represent a good reference on the qualitative spectral effects to be expected upon interaction with other diamagnetic and paramagnetic ions, as subsequently investigated for the U–GSH system, expecting redox reactions with the metal occurring in its +VI and +IV valence states, respectively.

3.1.2 Glutathione–Uranium System under Oxidizing Conditions

The results shown in this section were achieved together with Alexander Strobel in the course of a supervised internship and a subsequent bachelor thesis [89].

Oxidizing conditions means the use of both oxidized glutathione (GSSG) and hexavalent uranium (U^{VI}), and the handling under atmospheric conditions. Upon increasing pD during sample preparation, in general above pD 3, precipitation of a solid phase occurred. After separation of the solid from the aqueous phase by centrifugation, both these fractions were treated individually. In the following both supernatant solutions and precipitates are discussed separately.

3.1.2.1 Solution studies

The obtained supernatants were, after pD adjustment if necessary, examined by TRLFS and NMR spectroscopy, and the remaining GSSG and U^{VI} contents determined by total organic carbon (TOC) analyses and ICP-MS, respectively.

Also the GSSG– U^{VI} system is characterized by molar fraction weighted averaged signals of both free and U^{VI} -bound GSSG, with the ligand exchange reaction being fast on the NMR timescale (in this section 9.4 T, 298 K), however, slowing down with increasing U^{VI} contents, whereupon the signals both broaden and shift towards the chemical shifts of the complex's signals.

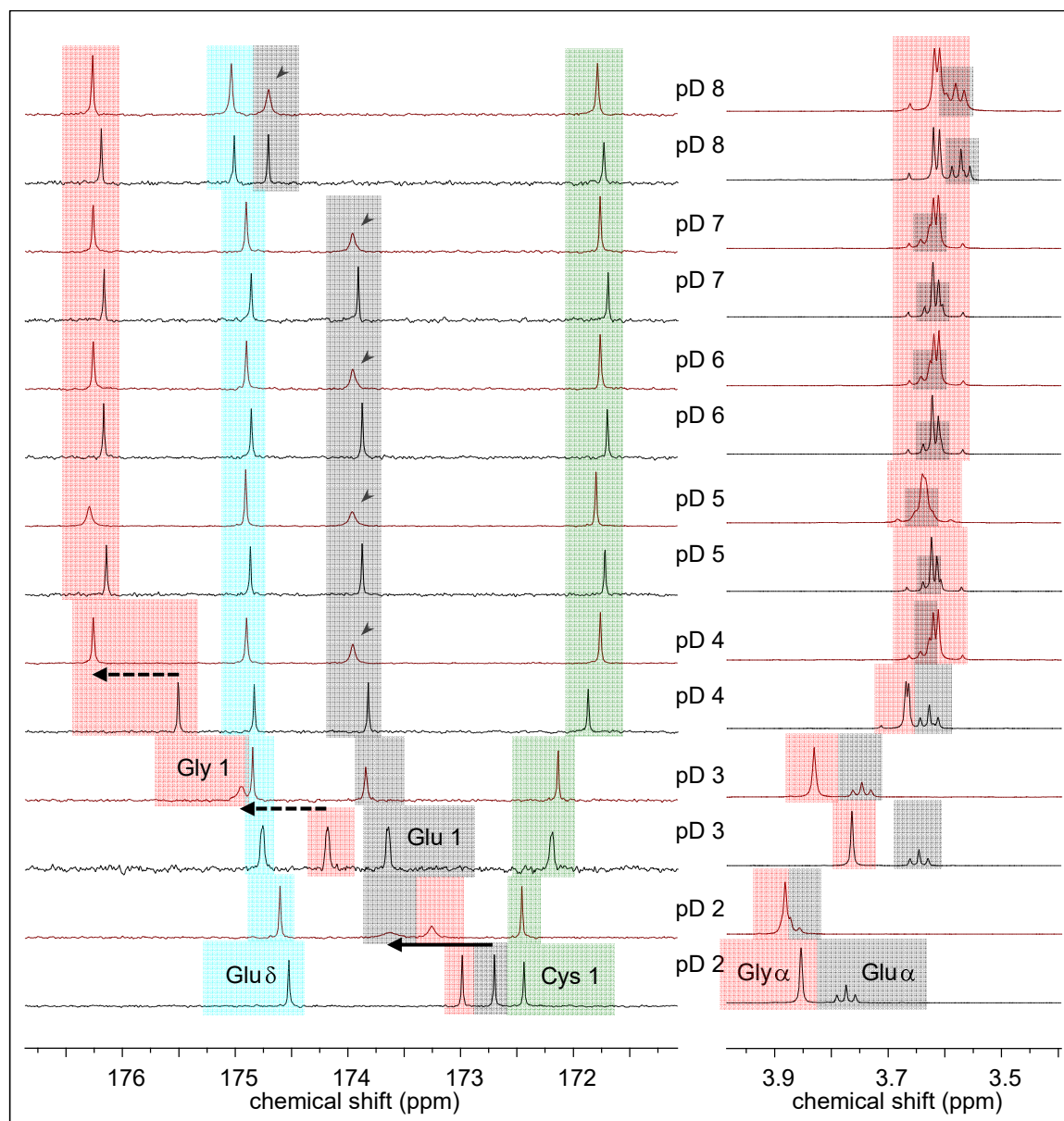


Figure 12. ^{13}C NMR carboxyl region (left) and ^1H NMR Gly α and Glu α region (right) of pD-dependent spectra of GSSG blanks (black) and U^{VI} containing solutions (red). Initial concentrations are 150 mM GSSG (for both blank and sample) and 75 mM U^{VI} , respectively. For clarity, signals of the individual sites are color-coded as stated with the spectra.

Figure 12 depicts both the ^{13}C carboxyl (left) and the Gly α /Glu α ^1H regions (right) of GSSG blanks (black) and U^{VI} containing sample solutions (red), with the individual signals colored for better visualization. Note that upon increasing pD even the blank signals themselves shift owing to changing GSSG speciation and, as a consequence of the occurring charges, changing conformation. Of importance is therefore to compare blank and sample spectrum for the same given pD value in order to figure out the U^{VI} -induced effects. Already at pD 2 the Glu carboxyl groups interact strongly with UO_2^{2+} as deduced from Glu 1 $\Delta\text{U}\delta_{\text{C}}$ of 0.93 ppm (solid arrow), whereas $\Delta\text{U}\delta_{\text{C}}$ of Gly 1 is about 0.27 ppm. The observed effects are larger for the Glu 1 than for the Gly 1 signal at pD 2 since the Glu

carboxyl groups are already ionized to about 50% while the Gly carboxyl groups are only by about 3%, *cf.* Table 1. Consequently, under these conditions the Glu carboxylate groups are much more accessible to U^{VI} complexation than the Gly carboxyl groups, despite the adjacent cationic protonated α -amino group. At pD 3, however, $\Delta_{U\delta C}$ of Glu 1 and Gly 1 now amount to 0.20 and 0.76 ppm, respectively, although the two Glu carboxyl groups are virtually completely deprotonated whereas the two Gly carboxyl groups are respectively deprotonated by about 41% and 12%. Therefore, complexation is determined by the Gly carboxylate groups as of pD values being close to its pK_a (dashed arrows). That is, U^{VI} -carboxylate binding is now better facilitated by Gly than Glu carboxylate groups.

Shiftings of the U^{VI} samples' signals attributed to Glu δ and Cys 1, *i.e.*, the amide carbons, are primarily ascribed to peptide backbone conformational changes upon U^{VI} complexation. Note that between pD 7 and pD 8 a shift of the blank ^{13}C and 1H Glu signals is due to onset of Glu NH_3^+ deprotonation. An analogous set of spectra recorded for sample concentrations of 150 mM GSSG and 7.5 mM U^{VI} , as well as for both series the corresponding spectra of the aliphatic carbons are shown in the Appendix.

TRLFS of 500 μM U^{VI} pH 3 samples at 25 °C showed decreasing fluorescence intensity with increasing [GSSG], lacking a shift of the emission lines accompanied with a mono-exponential decay in all samples. This behavior is characteristic for static fluorescence quenching upon formation of the non-fluorescing complex and concomitant decrease of free metal ion concentration. Calculated luminescence intensities were evaluated using the STERN-VOLMER Plot (see Appendix for details). After refinement by parallel factor analysis (PARAFAC), $\log K$ was determined as 4.81 ± 0.08 , according to a $\log \beta_{131} = 27.02 \pm 0.12$, associated with $[UO_2H_3GSSG]^+$.

U^{VI} luminescence spectra obtained from the supernatants of the 150/7.5 mM GSSG/ U^{VI} sample series acquired at 153 K are given in Fig. 13. The supernatants disclose the virtually identical spectral appearance for pD 3–5 to be determined by UO_2OH^+ according to the observed emission lines [90-91]. Time-resolved spectra show bi-exponential luminescence decays, with lifetimes calculated as $\tau_1 = 283 \pm 6$ and $\tau_2 = 70 \pm 3 \mu s$ (pD 3), $\tau_1 = 270 \pm 6$ and $\tau_2 = 75 \pm 2 \mu s$ (pD 4), and $\tau_1 = 242 \pm 6$ and $\tau_2 = 73 \pm 3 \mu s$ (pD 5). Taken together the species predominating under these conditions and the reported lifetimes at 153 K for UO_2^{2+} and $(UO_2)_2(OH)_2^{2+}$, *viz.* $286 \pm 29 \mu s$ [92] and $226 \pm 3 \mu s$ [93], respectively, the longer τ_1 values are attributed to UO_2^{2+} (pD 3–4) and $(UO_2)_2(OH)_2^{2+}$ (pD 5), the shorter τ_2 values are ascribed to UO_2OH^+ in accordance with the observed emission lines. Apparently, also under cryogenic conditions the U^{VI} -GSSG complexes are non-fluorescing. The predominance of UO_2OH^+ is somewhat surprising for the calculated speciation (Fig. 1) implies only a small fraction of this species to be present in solution, and for the applied $[U^{VI}]$ are quite high, polynuclear hydrolysis species are to be expected. It is, hence, concluded that GSSG preferentially forms complexes with UO_2^{2+} and $(UO_2)_2(OH)_2^{2+}$, shifting the equilibrium towards UO_2OH^+ .

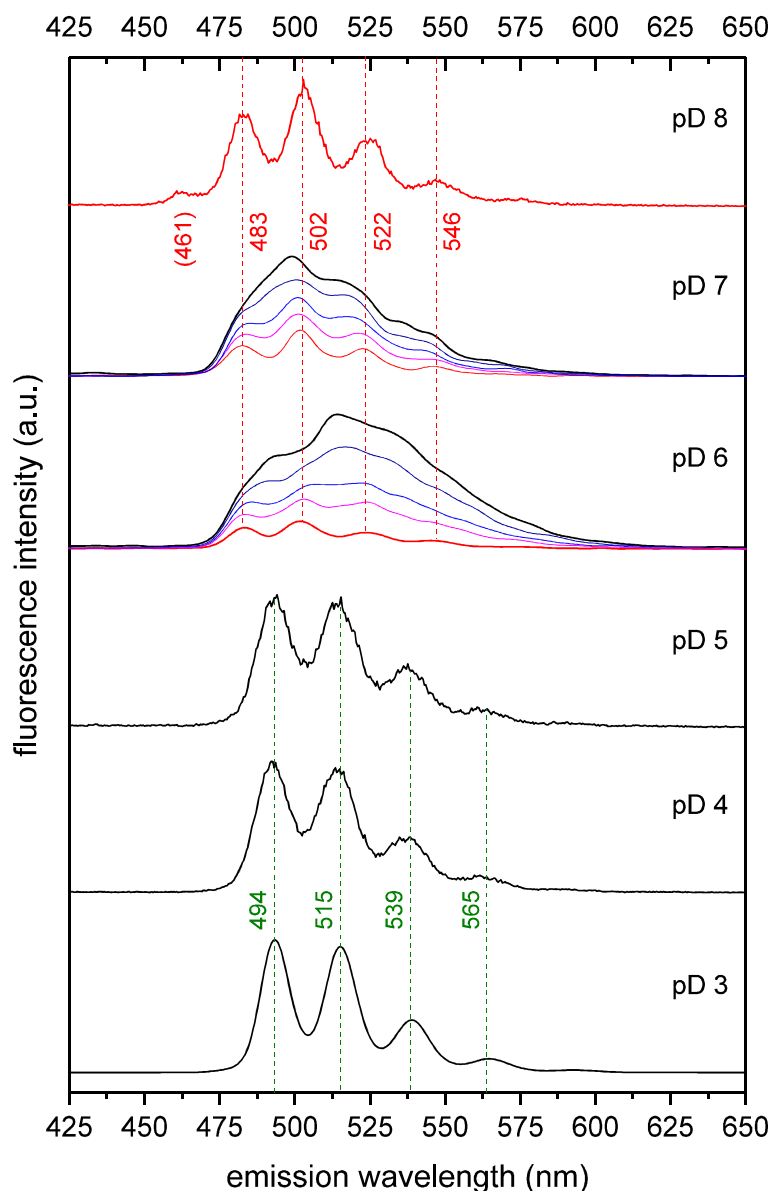


Figure 13. Luminescence spectra acquired at 153 K of supernatants obtained from 150 mM GSSG and 7.5 mM U^{VI} solutions at pD as indicated. For clarity, all spectra were normalized to the same maximum intensity and offset along the y-axis. Note the emission maxima (in nm) stated with the corresponding dashed lines, and the exemplary time-resolved spectra received after 50, 150, 250, and 1000 μ s.

In consideration of both U^{VI} and GSSG speciation (*cf.* species distribution respectively in Fig. 1 and Fig. A2, Appendix), for $pD \leq 4$ the GSSG– U^{VI} complex is binary, and formed by UO_2^{2+} bonding *via* a Glu carboxyl group for $pD < 3$, and a Gly (or Glu) carboxyl group as of pD 3. Therefore, the binary species can in general be denoted as



In the case of $n = 3$ the yielded net neutral species is prone to precipitation (*vide infra*). For the given concentrations, as of $pD > 3$ U^{VI} hydrolyzes [94], whereupon $(UO_2)_2(OH)_2^{2+}$,

UO_2OH^+ , and $(\text{UO}_2)_3(\text{OH})_5^+$ (also) occur in solution and are as well likely to be coordinated by GSSG. Interestingly, this change in U^{VI} speciation can be spotted also by NMR spectroscopy. In the pD range 2 through 4, for both sorts of carboxyl groups the observed $\Delta_{\text{U}\delta}$ are remarkably larger as compared to $\text{pD} \geq 5$ since UO_2^{2+} causes larger U^{VI} complexation-induced effects than the hydrolysis or carbonate species (*vide infra*). The reason is that for each single hydrolysis step or, in general, any additional LEWIS base coordination, the metal's LEWIS acidity decreases. Since the chemical shift is a measure for the electron density, the latter is much less withdrawn from the carboxyl groups – resulting in much less difference between blank and sample – upon (polynuclear) U^{VI} hydroxo/carbonate species complexation.

Owing to the ambient atmospheric conditions, as of $\text{pD} > 5$ speciation and, hence, TRF spectra show U^{VI} (hydroxo) carbonate species. Particularly the binary $\text{UO}_2(\text{CO}_3)_2^{2-}$ and $\text{UO}_2(\text{CO}_3)_3^{4-}$ species are distinguished by their remarkably long lifetimes reported respectively as 962 and 883 μs at cryogenic temperature [95]. Determined bi-exponential decay data, however, fit to lifetimes of $\tau_1 = 565 \pm 28$ and $\tau_2 = 112 \pm 10$ μs (pD 6), and $\tau_1 = 318 \pm 12$ and $\tau_2 = 65 \pm 7$ μs (pD 7). On account of these (τ_1) lifetimes being very uncommon for binary U^{VI} -carbonate complexes, the observed species are likely to contain GSSG. The most reasonable explanation for the peculiar lifetimes is that the (very long) carbonate-associated U^{VI} lifetimes are decreased by binding of quenching GSSG in these mixed-ligand complexes. In addition, a hypothetical binuclear quaternary U^{VI} hydroxo carbonate GSSG species may form by substituting GSSG for (two) water ligands in $[(\text{UO}_2)_2\text{CO}_3(\text{OH})_3(\text{H}_2\text{O})_3]^-$ upon which the lifetime of 144 μs (6 K) [95] declines and may be attributed to the observed pD 6 τ_2 of 112 μs . The pD 7 τ_2 of 65 μs can be the result of a further hydroxo or GSSG ligand (functional group) replacing remaining coordinating water. However, a definite decision cannot be made since the τ_2 values can also be due to hydrolysis species being present in the initial solution.

Both the quaternary U^{VI} hydroxo carbonate GSSG, and ternary U^{VI} carbonate GSSG species form polyanionic and, therefore, well soluble species for which reason carbonate containing U^{VI} -GSSG species do not precipitate (*vide infra*). Further considerations to and tentative formulae for these species are given in the Appendix. This attribution is corroborated by the NMR spectra, according to which the Glu 1 and Gly 1 signals still indicate complexation, bearing in mind the spectral implications regarding uranium's steadily decreasing LEWIS acidity. In comparison with the spectra of the analogous GSSG/ U^{VI} sample series with $L/M = 20$ (Fig. A15, Appendix), the 20-fold GSSG excess of course results in smaller $\Delta_{\text{U}\delta}$ values for the observed averaged signals exhibit more contribution of the free ligand. However, both the $L/M = 2$ and 20 series reveal similar line broadenings for Glu 1 and Gly 1, indicating the same molecular dynamics. Whereas the Gly 1 signal shows significant broadening only up to pD 5, the Glu 1 NMR signal of U^{VI} containing samples exhibit broadening up to pD 8 (see spearheads in Fig. 12). Increased line width implies a slower site exchange at the Glu carboxyl groups. Although less populated in terms of U^{VI} -

bound Glu carboxyl groups, the time interval the U^{VI} resides at this site is significantly longer as compared to the Gly carboxyl group. A conceivable explanation is the participation of the Glu α -amino groups functioning as hydrogen bond donors or, upon deprotonation (as of $pD > 7$), as both donor and acceptor group. Interaction with, *e.g.*, the U^{VI} -bound hydroxo or carbonato ligands or water in the second (first) coordination sphere as hydrogen bond acceptors (donors) provides additional stability. One may even think of a simultaneous interaction of both Glu residues (I and II) with the same U^{VI} hydrolysis or carbonate species, as can be deduced from GSSG's conformation found in the crystal structure (Fig. 14). A slowed down site exchange is in accordance with lacking observation of either or both free and U^{VI} -bound CO_3^{2-} (169.1 and 168.2 ppm, respectively [96]) in any ^{13}C NMR spectra owing to signals too broad to be observed.

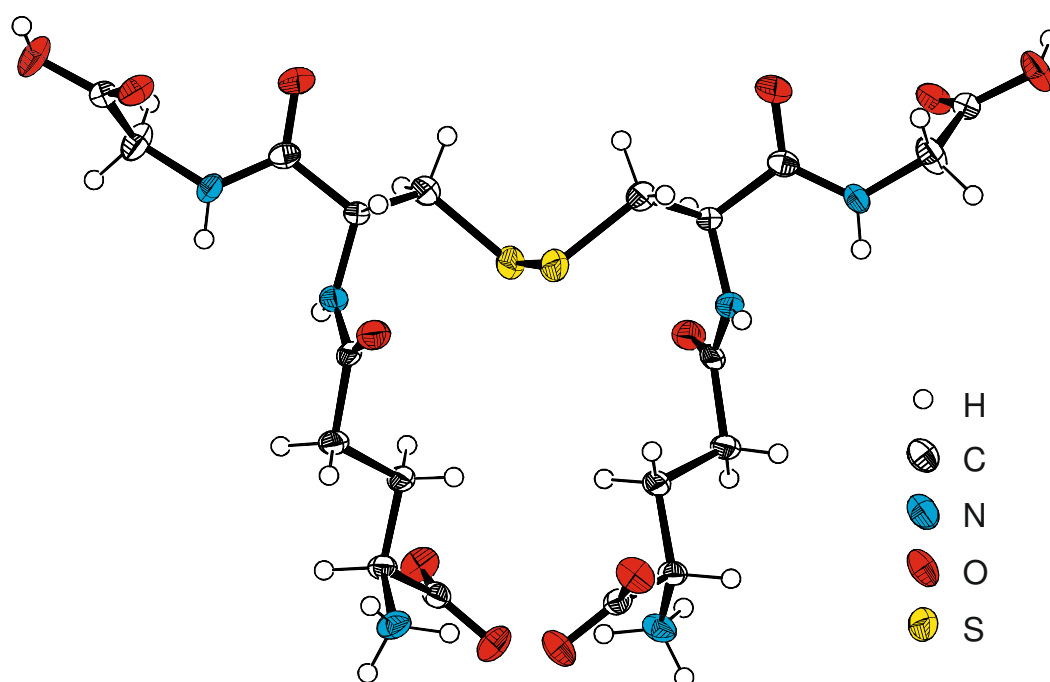


Figure 14. Crystal structure representation of GSSG at pH 3 (adapted from KRETZSCHMAR ET AL. [43], CCDC no. 981311).

1H NMR spectra of two series with 10 mM initial [GSSG] and both varying [U^{VI}] at pD 2 and (initial) 100 mM [U^{VI}] for varying pD values are shown in Figs. A12 and A13, Appendix. Whereas for pD 2 most of the initial GSSG and U^{VI} remain in solution (*cf.* re-determined concentrations stated with the spectra), already at pD 3 only fractions of dissolved U^{VI} and GSSG can yet be found. Although the pD 3 solution contains only 5-fold U^{VI} excess as compared to the 16-fold U^{VI} excess for pD 2 (owing to precipitate formation), the fraction of the GSSG- U^{VI} complex is larger in the former as concluded from the $\Delta_{U\delta}$ values. Interestingly, the 1H NMR spectra of the pD 4 and pD 5 samples show no GSSG related signals at all, indicating that the precipitate formed during sample preparation contains GSSG bound to U^{VI} (see below).

In summary, interaction between U^{VI} and GSSG was observed in solution for the entire pD range probed. A binary GSSG (1:1) complex is proven for $pD \leq 4$, whereas in the range $4 \leq pD < 6$ ternary GSSG hydroxo complexes are shown to (co-)exist, in both cases formed by carboxylate bonding. The complexes are supposed to be soluble as long as the complex species is not net neutral. As of pD 6 carbonate containing species arise. However, GSSG can (partially) compete with hydroxo and carbonate ligands upon formation of quaternary U^{VI} hydroxo carbonate GSSG, and ternary U^{VI} carbonate GSSG species.

3.1.2.2 Precipitate studies

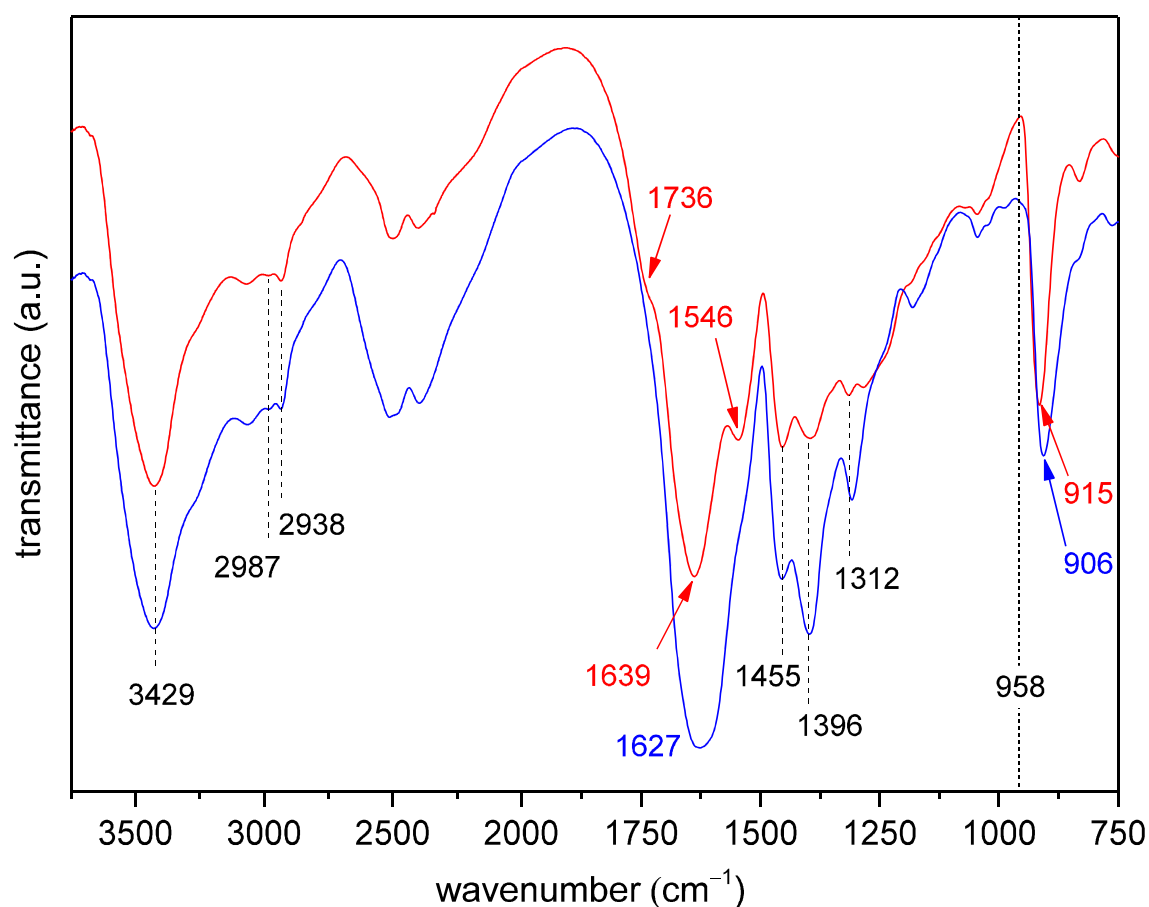


Figure 15. Exemplary IR spectra (KBr disc) of the washed and lyophilized precipitate pellets obtained from pD 2 (red) and pD 8 (blue) centrifuged suspensions of 150 mM GSSG and 7.5 mM U^{VI} .

IR spectra of the obtained bright yellow precipitates are depicted in Fig. 15 for the limiting pD values, *i.e.*, pD 2 and 8.⁴ Since the pD 4 and pD 6 spectra show only gradual alterations, they are given in the Appendix. Evaluation of the spectra unambiguously reveals features not only attributed to organics, but also indicating that GSSG is bound to

⁴ Although repeatedly washed with 1 M NaCl H_2O solution and subsequently lyophilized, the spectra refer to the pD (instead of pH) value the precipitates were obtained during NMR sample preparation. (*cf.* section 5.1.3.1)

U^{VI} . For the whole pD range sampled, the antisymmetric (ν_{as}) and symmetric (ν_s) COO stretchings are found at $1633 \pm 6 \text{ cm}^{-1}$ and $1396 \pm 1 \text{ cm}^{-1}$, respectively. For the lower two pD values a weak shoulder at 1736 cm^{-1} indicates that a fraction of the GSSG's carboxyl groups – most probably those of the Gly residues – are still protonated. Additionally, in the same spectral range the amide I and II bands with 1675 and 1546 cm^{-1} , respectively, can be found. Particularly the former smears with the COO bands, resulting in rather broad, hardly resolved⁵ bands, whereas the latter can be distinguished – at least at low pD. Moreover, though less indicative for complexation but for the sake of completeness, the broad $\nu(\text{OH})$ as well as $\nu_{as}(\text{CH}_2)$, $\nu_s(\text{CH}_2)$, and $\nu(\text{CH})$ appear at 3429 cm^{-1} , $2987 \pm 5 \text{ cm}^{-1}$, $2938 \pm 1 \text{ cm}^{-1}$, and $2864 \pm 8 \text{ cm}^{-1}$, respectively. The antisymmetric stretching of the uranyl unit, $\nu_3(\text{UO}_2)$, is found between 915 and 906 cm^{-1} for pD 2 through 8. Compared to the $\nu_3(\text{UO}_2)$ value of 961 cm^{-1} for the free UO_2^{2+} , upon increasing pH, *i.e.* ≈ 4 through 8.5, when hydroxo species start to predominate, the wavenumbers show bathochromic shifts: 943 , 923 , and 895 cm^{-1} attributed to $(\text{UO}_2)_2(\text{OH})_2^{2+}$, $(\text{UO}_2)_3(\text{OH})_5^+$, and $\text{UO}_2(\text{OH})_3^-$, respectively [97-98]. Since any ligand coordination of the uranyl ion causes a bathochromic shift,⁶ the successive binding of ligands results in progressive reduction of the $\nu_3(\text{UO}_2)$ frequency as shown for, *e.g.*, acetate and succinate U^{VI} complexes by LUCKS ET AL. [99].

As the pD 2 precipitate is unlikely to contain hydroxo species, and the IR spectrum reveals features unambiguously attributed to GSSG, the pD 2 precipitate is concluded to consist of a binary GSSG- U^{VI} complex. Concerning the low $\nu_3(\text{UO}_2)$ observed, the UO_2^{2+} is supposed to be coordinated by more than one carboxylate. Since under these pD conditions the Gly carboxyl groups are deprotonated to only a few percent (feature of COOH at 1736 cm^{-1} , see above), three structures of the precipitate species are conceivable to yield a net neutral compound taking into account the protonated cationic Glu α -amino groups. Either UO_2^{2+} is bound by two Glu COO of either the same (1:1) or two distinct GSSG molecules (1:2), or (1:2) by those Gly COO that are already deprotonated. In the first two cases charge balancing requires anionic counterions such as chloride from pD adjustment. These considerations are related to the species with $n = 3$ discussed for the aqueous complexes (*cf.* p. 29). That is, overall charged complexes remain dissolved in solution whereas net neutral complex species are likely to precipitate. Analogous to the supernatants, upon increasing pD concurrent change in both GSSG and U^{VI} speciation results in formation of ternary complexes. The gradual decrease of $\nu_3(\text{UO}_2)$ and the precipitates' TRLFS characteristics (Fig. 16) indicate decreasing contents of the (net neutral) solid binary GSSG- U^{VI} complex and increasing contents of (net neutral, polynuclear) solid ternary GSSG hydroxo U^{VI} complexes.

⁵ The major drawback is that the ratio between peptide-backbone and side-chain carboxyl groups is high (as compared to polypeptides or proteins with much more side-chain variability) and, additionally, the simultaneous occurrence of CONH, COOH, COO, and COOU.

⁶ As LEWIS base coordination causes an increase in electron density at the uranyl core, it therefore follows a decrease of the axially U-O bond force constant and, hence, a reduced vibrational frequency.

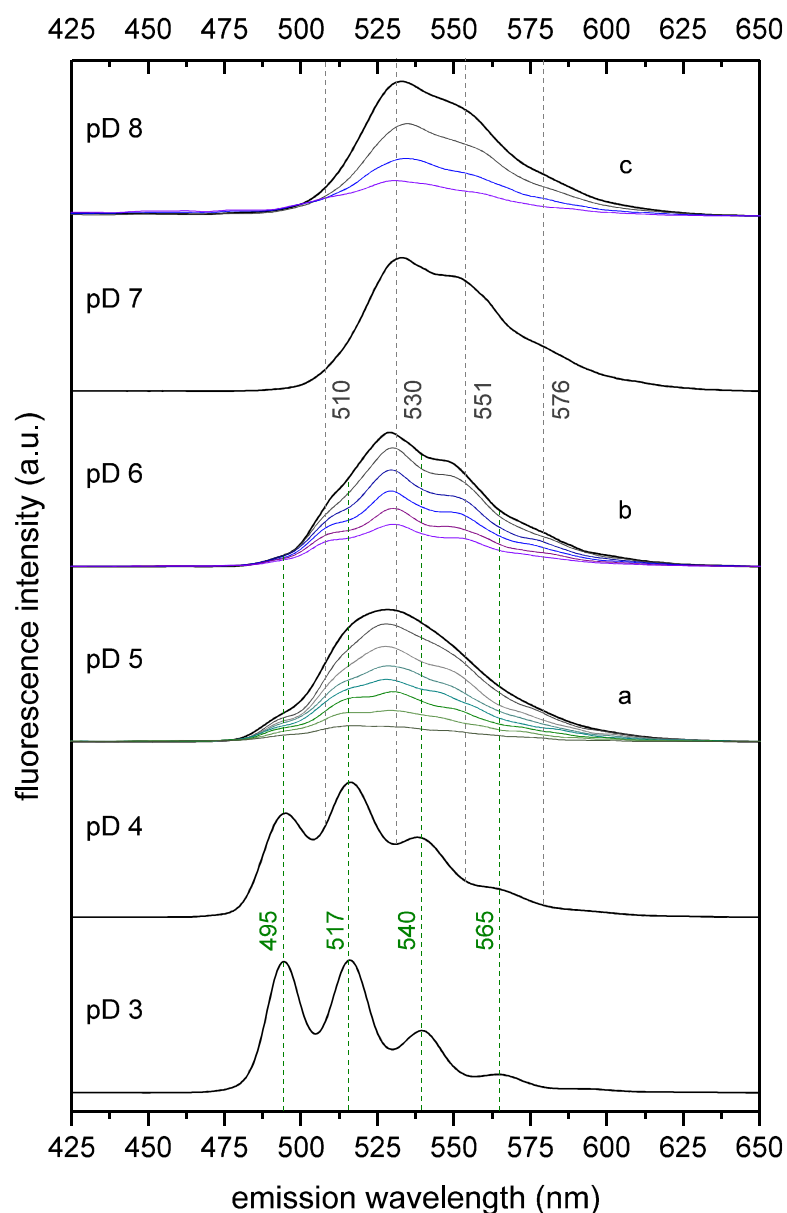


Figure 16. Luminescence spectra acquired at 153 K of precipitates obtained from 150 mM GSSG and 7.5 mM U^{VI} solutions at varying pD. For clarity, all spectra were normalized to the same maximum intensity and offset along the y-axis. Note the emission maxima (in nm) stated with the corresponding dashed lines, and the exemplary time-resolved spectra received after the following delays: (a) 50, 100, 150, 200, 250, 350, and 500 μ s; (b) 50, 100, 150, 200, and 250 μ s; (c) 50, 100, and 250 μ s.

For TRLFS studies, re-dispersion of the obtained solid phase as a suspension in part dissociates the underlying (non-fluorescing) GSSG-complexes. For both the complexes' formation constants and solubilities are finite, the participating U^{VI} species are thereby released. Subsequent shock-freezing by liquid nitrogen captures the species being present in solution and hints at the composition of the precipitated net neutral complex species.

The pD 3 spectrum reveals to be very similar to that of the corresponding supernatant. However, already the pD 4 precipitate spectrum evinces contribution from additional species with significantly different emission line maxima, whereupon the line-shapes and intensities change. The superposition is evident for the pD 5 spectrum in such a way that the components' individual spectra coincidentally complement to a featureless sum of signals. In the pD range 6–8 the other species determine the spectral appearance. All time-resolved spectra show bi-exponential luminescence decays with lifetimes steadily decreasing from $247 \pm 5 \mu\text{s}$ to $146 \pm 6 \mu\text{s}$ (τ_1) and from $78 \pm 3 \mu\text{s}$ to $30 \pm 1 \mu\text{s}$ (τ_2) for pD 3 through 8, respectively. In virtue of both the emission maxima and lifetime (τ_2) obtained, the low-pD spectra refer mainly to UO_2OH^+ , and to some extent to UO_2^{2+} (pD 3) and $(\text{UO}_2)_2(\text{OH})_2^{2+}$ (pD 4 and 5) as inferred from the τ_1 values, according to their respective lifetimes determined at 153 K (see above). $(\text{UO}_2)_3(\text{OH})_5^+$ occurs in the pD 5 and dominates the pD 6 spectrum, while $(\text{UO}_2)_3(\text{OH})_7^-$ does for the pD 7 and 8 spectra, respectively, as unambiguously evidenced by their corresponding emission lines and lifetimes (τ_1). Since the spectra for the latter two pD values reveal bands of $(\text{UO}_2)_3(\text{OH})_7^-$ especially at long delay times, the τ_1 between 166 and $146 \mu\text{s}$, *i.e.* $156 \pm 10 \mu\text{s}$, is ascribed to this hydrolysis species. The shorter high-pD τ_2 values cannot unambiguously be attributed to a certain species, but may be due to $(\text{UO}_2)_4(\text{OH})_7^+$.

The luminescence features reflect the changing speciation from UO_2^{2+} to (polynuclear) hydrolysis species and, by implication, from mononuclear binary $\text{U}^{\text{VI}}\text{-GSSG}$ to polynuclear ternary $\text{U}^{\text{VI}}\text{-GSSG}$ hydroxo species upon increasing pD. Notably, the precipitates do not contain (hydroxo) carbonates as evidenced by lacking characteristic features in both TRLFS (*vide supra*) and FT-IR spectra, the latter being sensitive to vibration modes typical for both uranyl and carbonate. Even though $(\text{UO}_2)_2\text{CO}_3(\text{OH})_3^-$ is highly abundant in the pD range 6 through 8, the IR spectra show no bands at 1530, 1380, and 923 cm^{-1} , corresponding to $\nu_{\text{as}}(\text{CO}_3)$, $\nu_{\text{s}}(\text{CO}_3)$, and $\nu_3(\text{UO}_2)$, respectively [100]. Although the applied $[\text{U}^{\text{VI}}]$ is in the millimolar range and U^{VI} solubility exceedance is to be expected, no metaschoepite ($\text{UO}_3 \cdot n \text{H}_2\text{O}$, $n < 2$) precipitated as proven by absence of its unique strong $\nu_3(\text{UO}_2)$ absorption found at 958 cm^{-1} [101], see corresponding dotted line in Fig. 15.

Analyses of the [U] remaining in solution for the sample series of initially either 10 or 150 mM GSSG and GSSG/U ratios of 2 and 20, respectively, are shown in Fig. 17. For both series of 20-fold GSSG excess (A and B) and irrespective of absolute [GSSG], the least U^{VI} contents remain in solution at $\text{pD} \approx 5$ when the predominating GSSG species bears a net charge of -2 . Upon further increasing pD less precipitate forms, corresponding to higher U^{VI} fraction remaining in solution according to the predominance of charged (anionic) and, thus, soluble U^{VI} GSSG (hydroxo) carbonate species. Sample series with only twofold excess in GSSG (C and D) reveal very little dissolved U^{VI} as of pD 3.

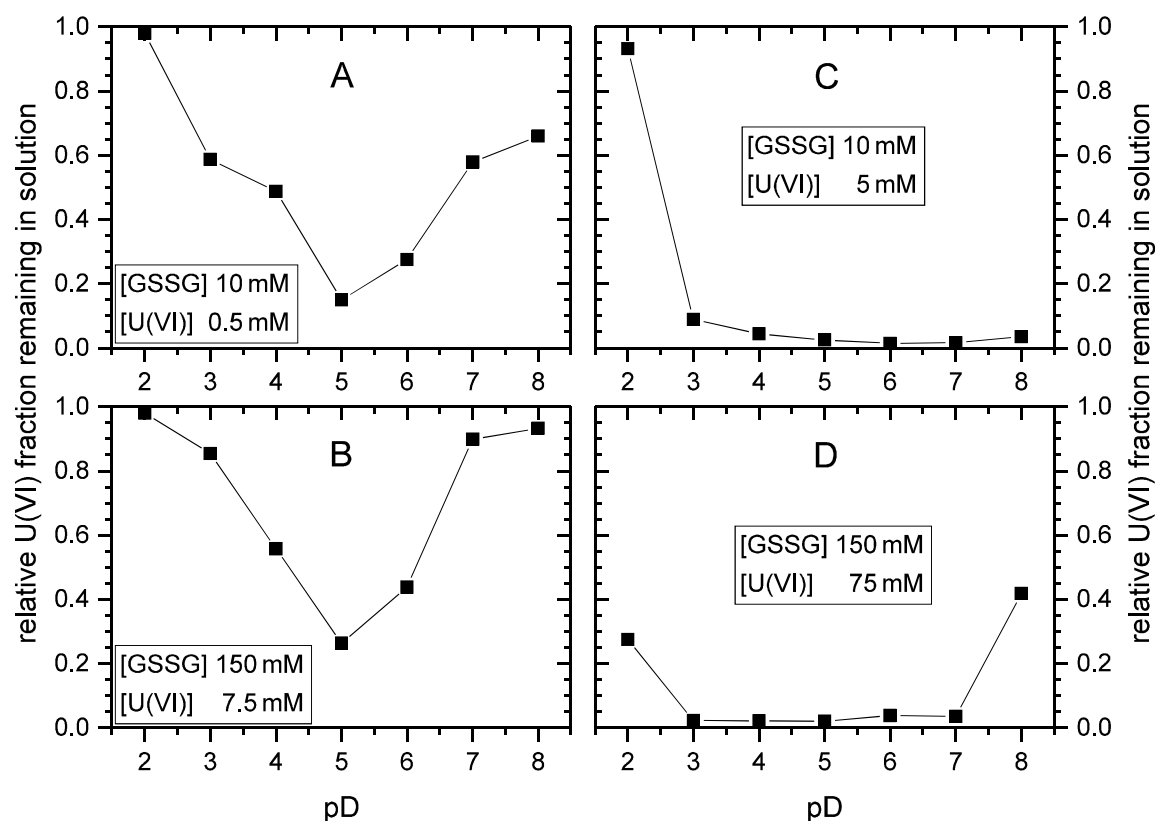


Figure 17. U^{VI} fraction remaining dissolved in solution for different sample series of varying both initial GSSG concentration (A and C 10 mM, B and D 150 mM, respectively) and GSSG/ U^{VI} ratio (20 for A and B, 2 for C and D, respectively).

Investigations on both the precipitate and the supernatant showed U^{VI} complexes of GSSG. Explicitly the cationic U^{VI} species are prone to form GSSG precipitates. The largest quantities of aqueous GSSG– U^{VI} complexes are observed for pD 3 – 4 as deduced from $\Delta_{U\delta}$ whereas net neutral, thus poorly soluble, binary U^{VI} GSSG and ternary U^{VI} hydroxo GSSG complexes form solid phases from pD 2 through 8, even in carbonatic media. Both the ternary U^{VI} carbonate GSSG and quaternary U^{VI} hydroxo carbonate GSSG complexes form (poly-)anionic species of high solubility. A final decision on the stoichiometries of the complexes formed must remain unanswered at this stage.

3.1.3 Glutathione–Uranium System under Reducing Conditions

The results shown in this section were achieved together with Toni Haubitz in the course of a supervised internship.

Reducing conditions means the use of reduced glutathione (GSH) and U^{VI} , and the handling under N_2 atmosphere. Analogous to the former section dealing with GSSG– U^{VI} investigations, because of precipitate formation supernatants and precipitates are again discussed separately.

3.1.3.1 Solution studies

Because of the structural and chemical similarity to GSSG, evaluation of the NMR spectra reveals analogous effects on GSH signals upon addition of U^{VI} . Therefore, where possible, the results are presented and discussed in condensed form.

Sample series of varying metal-to-ligand ratio (M/L)

1H NMR spectra of 5 mM GSH pD 2 solutions with U^{VI} contents between 6.7 and 67 mM are shown in Fig. 18. In comparison to the GSH blank solution the magnitude of the signals' shift increases with increasing U^{VI} concentration. Alike GSSG, GSH exhibits interaction with UO_2^{2+} already at pD 2, and the ligand exchange reaction is fast on the NMR timescale (for this section 14.1 T, 298 K), hence again only molar fraction weighted averaged signals can be observed. Analogously, the exchange rate decreases with increasing U^{VI} content and, therefore, the linewidth $\Delta\nu_{1/2}$ increases – most notably for the Glu α and Gly α signals. Consequently, with increasing U^{VI} content, the proportion of U^{VI} -bound GSH increases and the apparent signals progressively exhibit properties of the complex's signals. As can be seen, $\Delta_U\delta_H$ is larger for the Glu α than for the Gly α signal under these pD conditions. In fact, at pD 2 the Glu COOH is already ionized to about 33% whereas the Gly COOH is deprotonated only by about 5%, *cf.* pK_a values of GSH titration sites (Table 1, p. 11). In light of the small fraction of deprotonated Gly carboxylate, the observed Gly α $\Delta_U\delta_H$ values are remarkable in comparison to those of Glu α , *cf.* solid lines in Fig. 19. The diagram also discloses that the $\Delta_U\delta_H$ values can be fitted by asymptotic curves, especially for the signals of both the Glu and Gly moiety. This feature is to be expected, whereupon the asymptote represents the maximum U^{VI} -induced chemical shift, *i.e.*, upon even further increase of M/L the signals remain unaffected for the considered binding site is saturated in the whole ensemble of molecules probed. The impact of U^{VI} on the Cys moiety is very small since the thiol group as a typical soft LEWIS base shows no coordination to U^{VI} as a hard LEWIS acid according to the HSAB principle. The yet observed $\Delta_U\delta_H$ are ascribed to indirect effects following U^{VI} binding, such as changing solvation rather than changing conformation. Further discussion on that point is given below.

Two further series of varying M/L at pD 5 and 8 were investigated by 1H NMR (see Figs. A19 and A20, Appendix) with spectra portraying the samples' supernatants owing to precipitate formation. Briefly, the pD 5 spectra are very similar among each other with maximum $\Delta_U\delta_H$ of 10 ppb for Glu α since increasing M/L causes U^{VI} -GSH complex precipitation (*vide infra*) rather than increasing contents of aqueous U^{VI} -GSH species. The pD 8 spectra reveal virtually no $\Delta_U\delta_H$ in dependence of M/L. However, although again precipitates were formed, GSH removal from solution was much lower compared to pD 5.

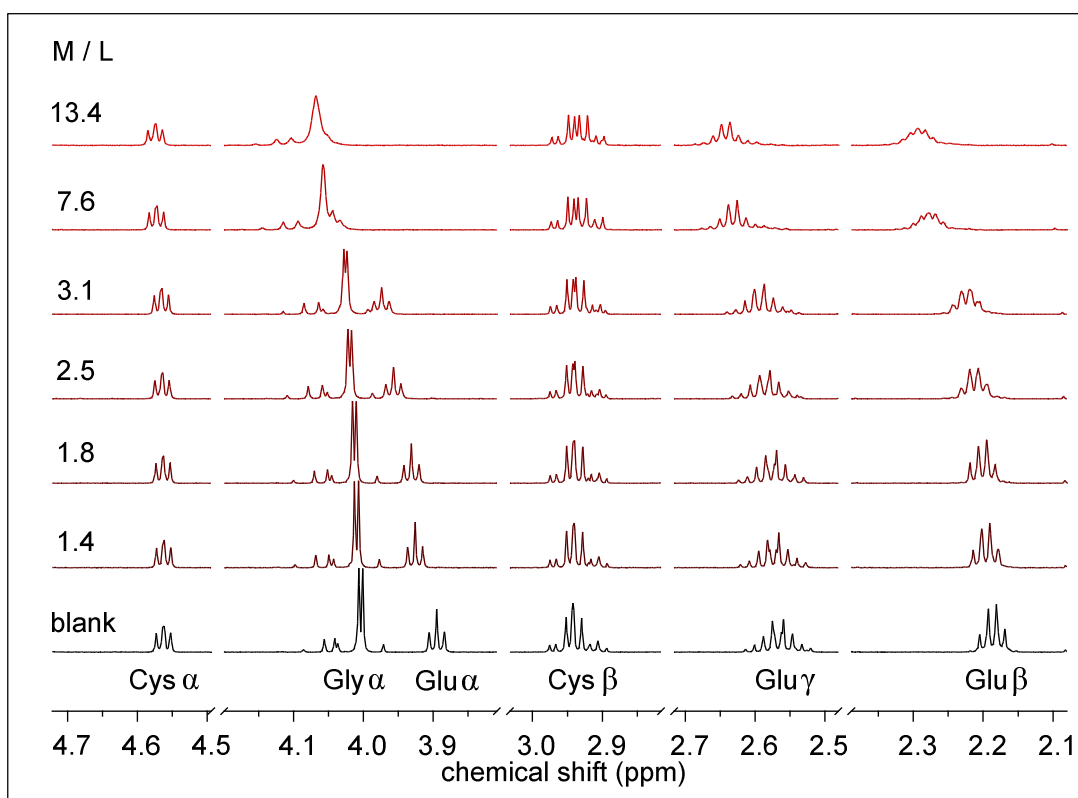


Figure 18. ^1H NMR spectra of 5 mM GSH and varying U^{VI} contents at pD 2. The re-determined M/L is stated with the spectra. For clarity, only parts of the spectra are shown.

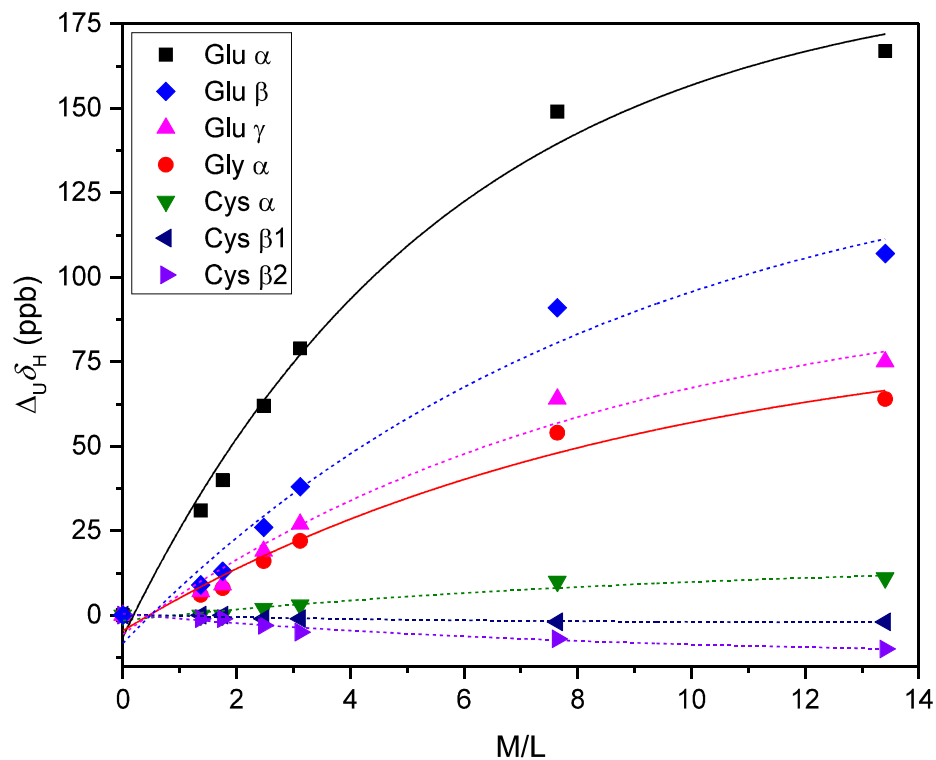


Figure 19. U^{VI} -induced ^1H chemical shift changes ($\Delta_{\text{U}}\delta_{\text{H}}$) as a function of M/L obtained from spectra of 5 mM GSH and varying U^{VI} content at pD 2 with concentrations re-determined by TOC and ICP-MS analyses. The lines represent asymptotic fits.

Sample series of varying pD values

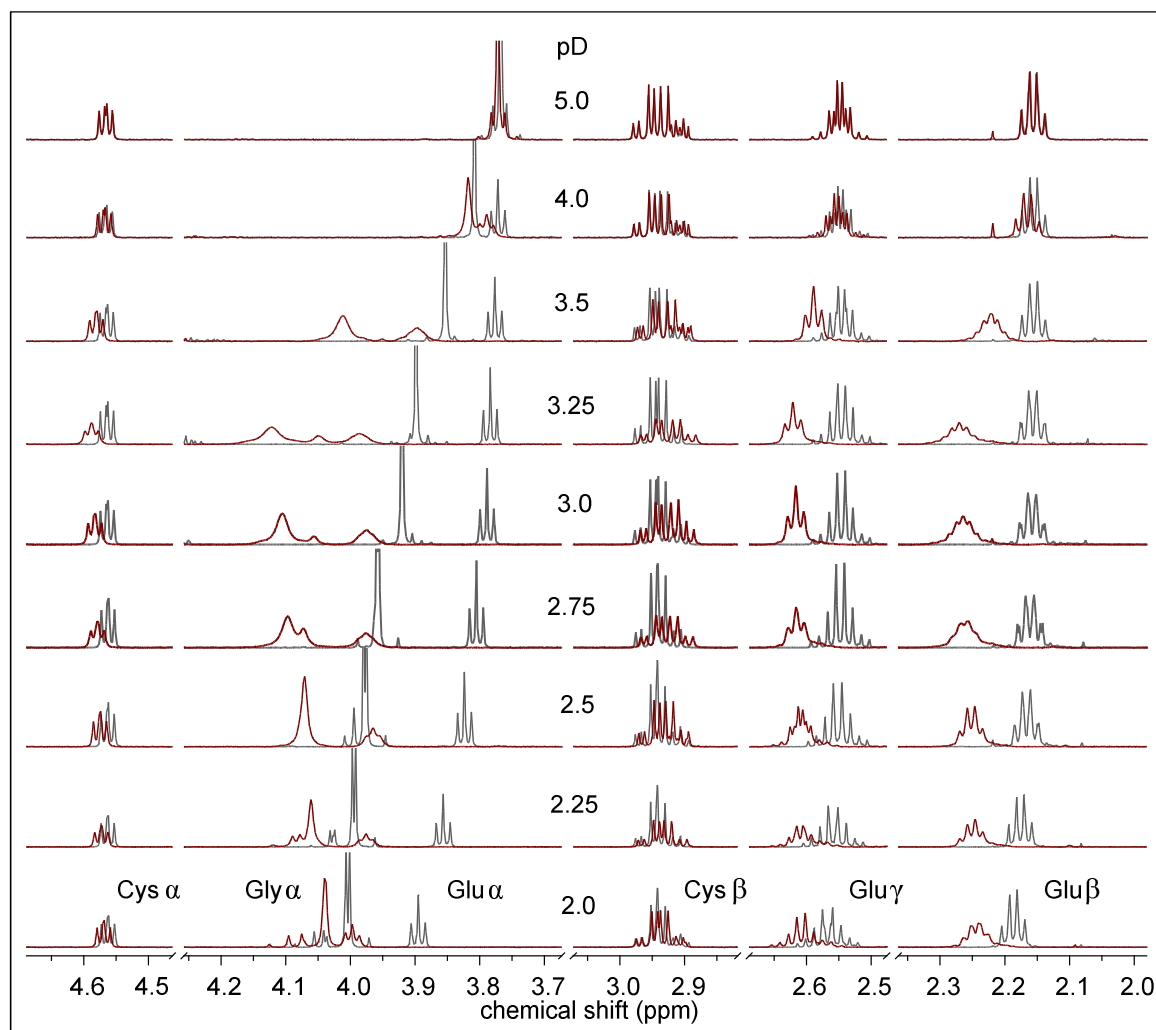


Figure 20. ^1H NMR spectra of 6.7 mM GSH blanks (grey) and samples with initial $M/L = 2$ (dark red) in the pD range 2–5. For clarity, only parts of the spectra are shown.

In addition to the $[\text{U}^{\text{VI}}]$ -dependent sample series, two sets of pD-dependent series were investigated with $[\text{GSH}]$ of 6.7 mM and given M/L of 0.5 and 2, respectively. Also in these cases the spectra are evaluated by comparison of the U^{VI} containing samples (red) – of either 3.3 or 13.3 mM – with the blanks (grey) at same pD. In principle, the spectra exhibit similar qualitative perturbations such as signal shift and broadening with the same correlation: the higher $[\text{U}^{\text{VI}}]$ the larger is the effect. For this reason the $M/L = 0.5$ spectra are given in Fig. A21, Appendix. The spectra of $M/L = 2$ are shown in Fig 20, and the graphical evaluations of both series juxtaposed in Fig 21.

The graphical evaluation of the pD-dependent $\Delta_{\text{U}}\delta_{\text{H}}$ in Fig. 21 reveals similar features for either M/L series, obviously with stronger magnitude for the samples of higher M/L . For the $M/L = 0.5$ series pD 2 sample accidentally a much higher $[\text{U}^{\text{VI}}]$ was applied during preparation (*cf.* re-determined U and GSH contents given in Fig. 22, see below), the pD 2 data points (open symbols) are considered as outliers. All other data points are reliable and

in accordance with those of the $M/L = 2$ data set, though. The graphs illustrate the pD-dependent *accessibility* to and *capability* of U^{VI} complexation by the two sorts of carboxyl groups. That is, because of its low pK_a the Glu COO can bind – is accessible for – U^{VI} already at much lower pD values. Accordingly, at low pD $\Delta_{U\delta_H}$ absolute values are largest for signals of Glu $\alpha/\beta/\gamma$, with the magnitude attenuating corresponding to the respective carbon's distance to the binding site, however, their 'curves' are of comparable slope. Complementary, the Gly COOH is less acidic (higher pK_a), that is, more basic, and hence less accessible owing to competition between U^{VI} and H^+ for the binding site, consequently showing smaller $|\Delta_{U\delta_H}|$ at low pD. However, as of pD values in the order of Gly pK_a , *i.e.*, commencing deprotonation, U^{VI} shows preferred binding to this site. The higher capability is reflected by larger $\Delta_{U\delta_H}$ resulting in the steeper 'curve'.

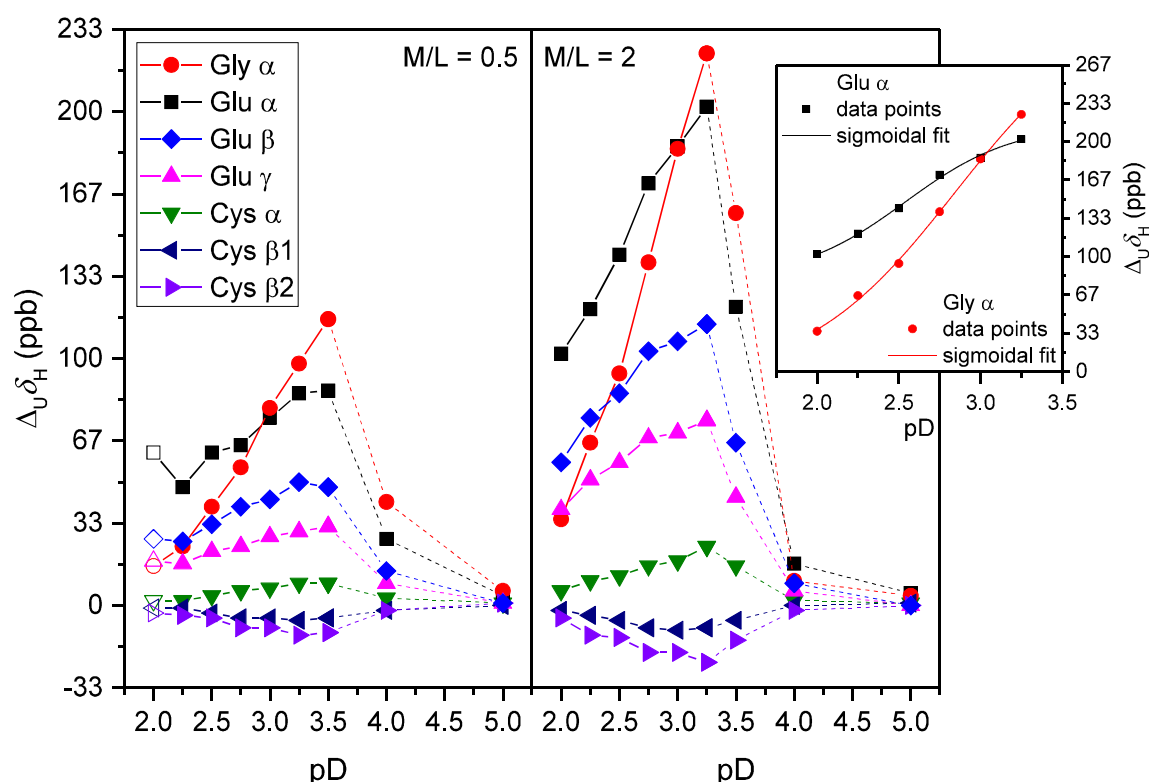


Figure 21. U^{VI} -induced 1H chemical shift changes ($\Delta_{U\delta_H}$) as a function of pD obtained from spectra of 6.7 mM GSH and initial M/L of 0.5 (left) and 2 (right), with lines drawn for better visualization. The inset shows dose-response-fits to the corresponding Glu α and Gly α $M/L = 2$ data points.

In fact, the solid lines (attributed to Glu and Gly residues) in Fig. 21 can be looked at as pD titration curves in presence of U^{VI} with the determined value being $\Delta_{U\delta_H}$ (instead of δ_{obs}). According to a pK_a determination, for instance of GSH, the plots show δ_{obs} as a function of pD, whereupon only the respective molar fraction x_i changes and, accordingly, determines the contribution of the chemical shifts of a signal in a certain site of a distinct species. For, *e.g.*, the Gly α the 1H signal of GSH with either protonated or deprotonated Gly carboxyl group is represented by equation (3).

$$\delta_{\text{obs}}^{\text{Gly } \alpha}(\text{blank}) = \delta_{\text{COOH}}^{\text{Gly } \alpha} \cdot x_{\text{COOH}} + \delta_{\text{COO}^-}^{\text{Gly } \alpha} \cdot x_{\text{COO}^-} \quad (3)$$

Assuming U^{VI} binding to the deprotonated carboxyl group only, and binding to either carboxylate group to occur independently, the observed signal now has one additional contribution: the chemical shift of the considered site for U^{VI} bound to the adjacent carboxyl group (COOU^{VI}), weighted by the respective fraction:

$$\delta_{\text{obs}}^{\text{Gly } \alpha}(\text{sample}) = \delta_{\text{COOH}}^{\text{Gly } \alpha} \cdot x_{\text{COOH}} + \delta_{\text{COO}^-}^{\text{Gly } \alpha} \cdot x_{\text{COO}^-} + \delta_{\text{COOU}^{\text{VI}}}^{\text{Gly } \alpha} \cdot x_{\text{COOU}^{\text{VI}}} \quad (4)$$

Insertion of Eqn. (3) into Eqn. (4) results in

$$\delta_{\text{obs}}^{\text{Gly } \alpha}(\text{sample}) - \delta_{\text{obs}}^{\text{Gly } \alpha}(\text{blank}) = \Delta_{\text{U}}\delta^{\text{Gly } \alpha} = \delta_{\text{COOU}^{\text{VI}}}^{\text{Gly } \alpha} \cdot x_{\text{COOU}^{\text{VI}}} \quad (5)$$

As can be seen, $\Delta_{\text{U}}\delta_{\text{H}}$ depends on the fraction of complex formed, and plotted against pD actually also represents sigmoidal curves. Accordingly, dose-response-fits were applied to the M/L = 2 Glu α and Gly α data points with the graphs shown as inset in Fig. 21. Of the fit parameters (given in Table A4, Appendix) the most interesting figures are the inflection points, *viz.* 2.55 ± 0.05 and 2.83 ± 0.12 in pD units for Glu α and Gly α , respectively, for these represent those pD values where the concentrations of free and U^{VI} -bound ligand are equal, reflecting the Gly carboxyl's higher capability in U^{VI} complexation. That is, one half of the Gly carboxyl is bound to U^{VI} at pD 2.83, a value remarkably below its corresponding pK_{a} , whereas half of the Glu carboxyl is bound to U^{VI} at pD 2.55, significantly above its pK_{a} . This qualitative difference in metal ion complexation is ascribed to COULOMB repulsion due to the positively charged Glu NH_3^+ in direct vicinity to the carboxyl group. Although, as a matter of fact, U^{VI} can only bind to the deprotonated carboxylate group, and by means of the degree of dissociation the fractions of COOH and COO^- can be determined in the absence of U^{VI} , the problem is to figure out the exact concentrations of COOH and COO^- in the presence of U^{VI} , particularly for that fraction U^{VI} replaced H^+ from COOH, since all these information are encoded in one single observed chemical shift value δ_{obs} .

The solid lines in Fig. 21 reflect the increasing fraction of aqueous GSH- U^{VI} complex formed. With regard to the discussion for GSSG and in view of both U^{VI} and GSH speciation (*cf.* Fig. 1 and Fig. A2, Appendix), the two binary complexes are $[\text{UO}_2(\text{H}_2\text{GSH})]^{2+}$, predominating for \approx pD < 2.3, and $[\text{UO}_2(\text{HGSH})]^+$, occurring for pD values above \approx 2.3 (onset of Gly COOH deprotonation).

There is, however, a break in the curves with a remarkable drop of the $\Delta_{\text{U}}\delta_{\text{H}}$ values (dashed lines), observed at pD 3.25 and pD 3.5 for M/L = 2 and 0.5, respectively. Around this pD coincidentally both U^{VI} and GSH exhibit significant speciation changes. On the one hand, hydrolysis causes lower U^{VI} LEWIS acidity and hence intrinsically smaller $\Delta_{\text{U}}\delta_{\text{H}}$ accompanied with these species. On the other hand, the predominating GSH species is now net monoanionic, rendering the concomitant observation of precipitate formation not sur-

prising. For GSH possesses only two carboxyl groups as compared to the four of GSSG, formation of net neutral and, therefore, poorly soluble complexes is much more prevailing. Based on the mono-, di-, and trinuclear U^{VI} and the GSH species occurring under these conditions, $[UO_2OH(HGSH)]^0$, $[(UO_2)_2(OH)_2(HGSH)_2]^0$, and $[(UO_2)_3(OH)_5(HGSH)]^0$ are reasonable net neutral complexes. However, taking into account both the GSH and the uranium fraction remaining in solution (Fig. 22), up to pD 5 metal and ligand are not removed from solution in a 1:1 ratio as implied by the stoichiometry of the first two ternary complexes stated, but rather excessive in uranium.

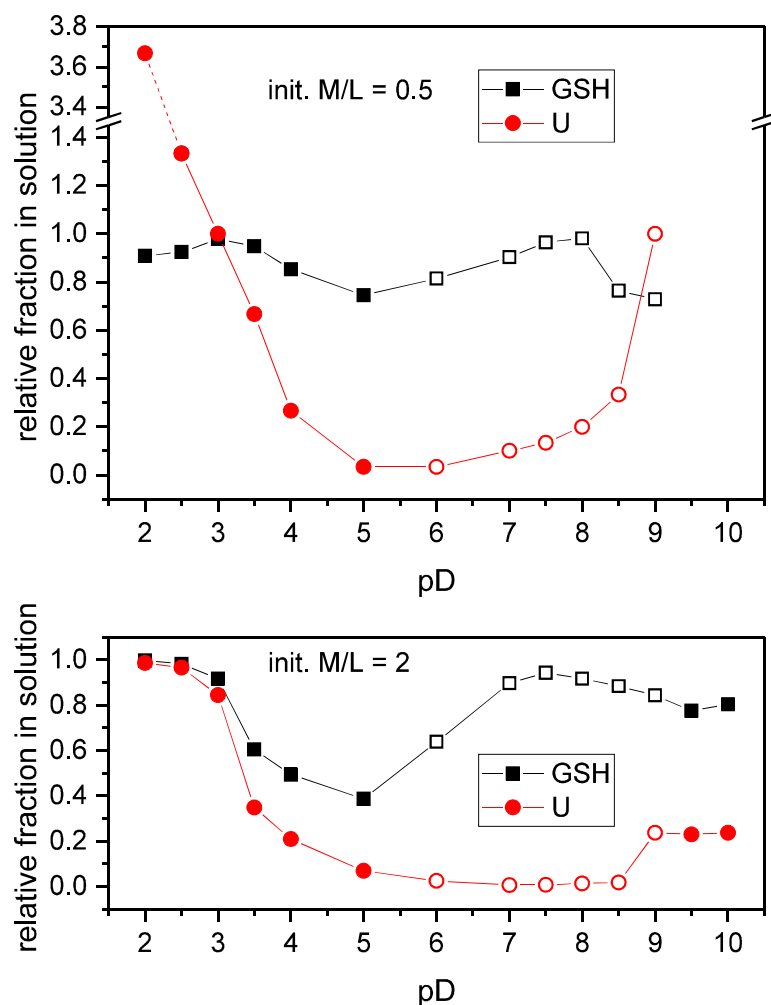


Figure 22. GSH and uranium contents remaining in solution as determined by TOC and ICP-MS analyses for sample series of initial 6.7 mM GSH and either 13.3 mM U^{VI} (bottom) or 3.3 mM U^{VI} (top). Note the relative scale on the y-axis with GSH and U^{VI} contents normalized by their initial concentrations, respectively. Lines are drawn for better visualization.

This hints at precipitation of polynuclear species bound to GSH upon which the contents of unbound GSH increase and thus the observed $\Delta_{U\delta_H}$ shrink further. However, the formed solid phase does not necessarily pertain to (stoichiometries of) solution species. Furthermore, spectra obtained for $pD \geq 6$ (Figs. A22 and A23, Appendix) show only minor U^{VI} -induced effects. Apparently, GSH cannot compete with hydroxo ligands for complexation.

However, as of pD 8.5 the Glu residue shows line broadening and some small $\Delta_{\text{U}}\delta_{\text{H}}$. The latter are significant for pD values associated with a neutral Glu α NH_2 group, suggesting its participation in coordination. Even a motif of U^{VI} chelation by Glu COO and the adjacent NH_2 is conceivable.

The data presented in Fig. 22 result from TOC and ICP-MS analyses and were normalized regarding initial $[\text{U}]$ and $[\text{GSH}]$, respectively. That is, both plots refer to the same initial $[\text{GSH}]$, however, with the $M/L = 0.5$ series containing only one quarter of the initial $[\text{U}^{\text{VI}}]$ as for $M/L = 2$. The former thus shows much less GSH removal. Open symbols refer to the pD range for which a redox reaction was observed (*cf. Redox studies*, section 3.1.3.3). TOC analyses are expressed as GSH equivalents, correspondingly including GSSG.

Spectral appearance – coupling constants and line widths

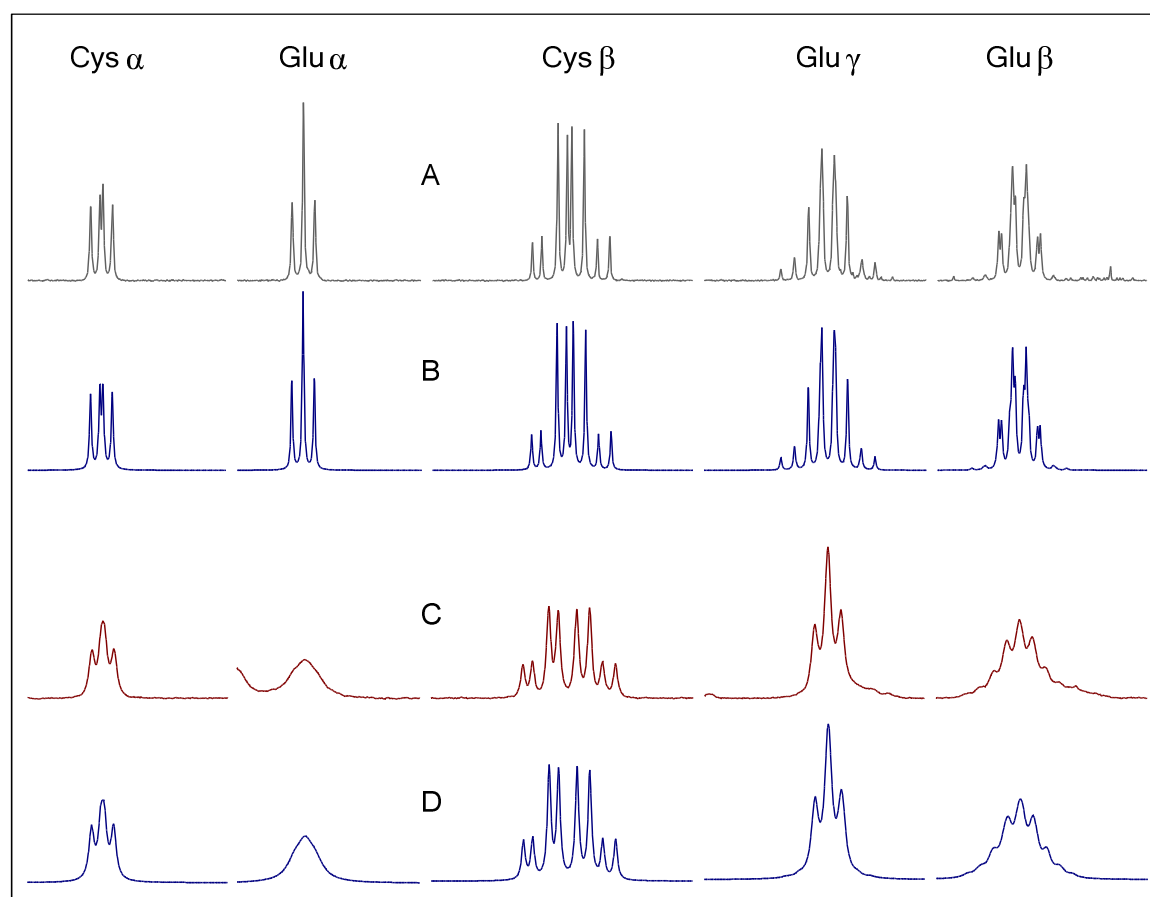


Figure 23. ^1H NMR spectra of the Cys and Glu signals of 6.7 mM GSH pD 3.25 blank (A) and the associated U^{VI} sample with $M/L = 2$ (C) as well as the corresponding spin simulations B and D, respectively. Note that for C and D the horizontal axis was shifted.

To further apprehend the signals' appearance and changes thereof, the couplings were examined in more detail. GSH is proven (by theory and experiment) to show no distinct predominating conformation in aqueous solution. As a matter of fact, even the blanks constitute averaged signals since segmental motion is such fast that data acquisition must nec-

essarily pertain to an average over many conformers [75, 102]. However, the conformation is by no means random, since not all conformers have equal probability of occurrence [79].

Since the spectra are of higher order⁷ and, thus, both Glu β and Glu γ coupling constant determination can be challenging, the spectra are simulated after input of δ , J , and $\Delta\nu_{1/2}$ values. The measured spectra – pD 3.25 GSH blank (A) and U^{VI} M/L = 2 sample (C) – are very good reproduced by the corresponding spin simulations B and D, respectively, depicted in Fig. 23. Numerical evaluation of the spin-simulated spectra is given in Table 3. An extensive analysis of the stable rotamers by correlating coupling constants with torsion angles by means of the KARPLUS relationship [103] surely is interesting and can be found elsewhere [79], but a simple comparison between the states prior to and after complexation just by dint of the coupling constants themselves is sufficient in this case.

Remembering that both Glu methylene groups possess diastereotopic hydrogen atoms,⁸ upon U^{VI} addition (A \rightarrow C, Fig. 23) the individual Glu γ signals shift towards each other, however, for Glu β shift away from each other, accompanied with small changes in the H-C(β)-C(γ)-H torsion angles, indicating that the molecular surroundings of the Glu β hydrogens becoming more distinct, while those of the Glu γ becoming more similar. This results in alterations in their signals' patterns as $\Delta\nu/J$ changes. In contrast, both the Cys α and β signals (included for validation) show significantly smaller $\Delta\delta$ as well as smaller $\Delta\nu_{1/2}$ and changes thereof, since as of being far from the binding sites, the Cys residue is least prone to direct U^{VI} complexation-induced changes of both conformation and electron density. Thus, spectral changes in the presence of U^{VI} are considered indirect, mainly attributed to changing solvation and hydrogen bonding of both Cys thiol and amide group.

Consequently, several structural isomers such as U^{VI} binding to either carboxylate group, their individual site exchange (temporary U^{VI} binding and dissociation), as well as interchanging conformer populations of both the free and the U^{VI} -bound GSH, *i.e.*, oscillation between averaged states of free and bound GSH, contribute to the apparent signals. However, taking into account ${}^3J_{H,H}$ to comprise values between ≈ 0 and ≈ 14 Hz, with the most probable values for staggered conformations (60° , 180° , 300°) being 3.5 and 14 Hz, respectively, the observed changes are in fact small. Thus, complexation appears to change the conformational status of the molecule very little, analogous to the findings for La^{3+} and Gd^{3+} [79], which could not be taken for granted since the latter are spherical ions, unlike UO_2^{2+} showing coordination in the equatorial plane only, perpendicular to the O=U axis.

⁷ Multiplication of the signal lines is caused by (i) diastereotopic methylene groups with each proton giving rise to its individual signal, hence *geminal* as well as – potentially different, dihedral torsion angle dependent – *vicinal* couplings and (ii) the frequency difference between two coupling signals ($\Delta\nu$) being in the order of their J value. Additionally, since $\Delta\nu \approx J$ the spectra show extreme ‘roof effects’ and the barycentre represents the actual signal position.

⁸ Associated with hindered Glu side chain mobility – as shown by means of ${}^{13}C$ T_1 measurements by YORK ET AL. [104] – in contrast to the high (pD dependent) mobility of the Gly residue; regarding the latter refer also to the footnote on page 18, and the notes with the amide proton spectra shown in the Appendix (p. 147).

Table 3. Numerical evaluation of the spin simulated spectra shown in Figure 23.

¹ H signal	δ_{H} in ppm		$\Delta\nu_{1/2}$ in Hz ^a		$ J $ in Hz		
	blank ^b	sample ^c	blank	sample		blank	sample
Cys α^{d}	4.564	4.588	0.8	2.9	$\alpha\beta 1$	5.0	5.0
					$\alpha\beta 2$	7.2	7.2
Cys $\beta 1$	2.957	2.949	0.6	1.8			
Cys $\beta 2$	2.925	2.904	0.6	1.8	$\beta 1\beta 2$	14.2	14.2
Glu α	3.784	3.986	0.60	10.0	$\alpha\beta$	6.3	5.7
Glu $\beta 1$	2.163	2.285	0.7	5.5	$\beta 1\beta 2$	14.8	14.0
Glu $\beta 2$	2.151	2.256	0.7	4.5	$\beta 1\gamma 1$	6.8	7.0
					$\beta 1\gamma 2$	8.3	8.0
Glu $\gamma 1$	2.559	2.625	0.65	3.9	$\gamma 1\gamma 2$	15.3	16.0
Glu $\gamma 2$	2.533	2.616	0.65	3.9	$\gamma 2\beta 2$	7.0	7.0
					$\gamma 1\beta 2$	8.7	8.0

^a $I_{\text{b}} = 0$; ^b 6.7 mM GSH pD 3.25; ^c 6.7 mM GSH pD 3.25 + U^{VI} with M/L = 2; ^d $^3J_{\text{NH},\alpha}$ unconsidered

In addition, line broadening is a prominent spectral feature, especially in those samples associated with notable U^{VI} interaction. Whereas the blanks' signals exhibit quite the same $\Delta\nu_{1/2}$ around 0.7 Hz, for the samples' spectra, in general, $\Delta\nu_{1/2}$ is increased. Alike $\Delta_{\text{U}\delta_{\text{H}}}$, $\Delta\nu_{1/2}$ values depend on the molecular site probed, *viz.* the closer the U^{VI} binding site the broader is the signal. Increasing either pD or [U^{VI}], both reducing the competition between H⁺ and U^{VI} for the binding site, results in broadening, reflecting a decrease in the exchange rate k_{ex} , *i.e.*, the rate constants determining how often U^{VI} is bound and released per unit time. Processes on the millisecond to microsecond time-scale, such as chemical exchange, strongly affect NMR line shapes since the inverse (in frequency units) covers the NMR spectral width. Owing to changing pD or M/L among the respective sample series, the exchange regime changes from *fast intermediate* to *slow intermediate*, *i.e.*, k_{ex} becomes smaller than half of the spectral distance between the two exchanging sites. Taking the maximal $\Delta_{\text{U}\delta_{\text{H}}}$ determined (≈ 140 Hz) as about one half of the frequency difference between the Gly α signals of both free and U^{VI}-bound carboxyl group, the exchange rate is roughly estimated to be in the order of 10^2 s⁻¹ for pD 3.25.

3.1.3.2 Precipitate studies

After evaluation of the GSH–U^{VI} solutions' supernatants, a brief analysis of the yielded *yellow precipitates* is given in the following. The pellets obtained after centrifugation were washed three times with 1 M NaCl solution and repeatedly centrifuged, thereby discarding the accruing supernatants. Some of the resulting solid phases were lyophilized (further referred to as *yellow powder*), of which parts were subjected to IR spectroscopy (KBr disc) as well as NMR and UV-Vis spectroscopy after re-dissolution. Addition of acid dissolves the complex and U^{VI} is released from GSH, however, both NMR (Fig. 29 B, below) and UV-Vis spectra (Fig. A24, Appendix), providing complementary information on ligand and metal respectively, disclose the precipitate to consist of GSH and U^{VI}. The FT-IR spectrum of the pD 5 sample yellow powder in Fig. 24 clearly shows features attributed to GSH and U^{VI} and is, in principle, very similar to those of the GSSG–U^{VI} system, however, reveals better resolution. That is, discrimination between both free and U^{VI}-bound carboxylate is possible, with $\nu_{\text{as}}(\text{COO})$ and $\nu_{\text{s}}(\text{COO})$ observed at 1630 and 1433 cm^{-1} as well as 1570 and 1400 cm^{-1} , respectively. The latter values are in very good agreement with the values (1580 and 1400 cm^{-1}) reported for acetate U^{VI} complexes [99]. Accordingly, the difference in $\nu_{\text{as}}(\text{COO})$ and $\nu_{\text{s}}(\text{COO})$ frequencies being larger than 150 cm^{-1} is due to monodentate carboxyl binding to U^{VI} [105-106]. Consequently, the U^{VI}-bound carboxylate is attributed to Gly COO, whereas the free carboxylate is assigned to the Glu moiety, forming a zwitterion with the adjacent Glu α -ammonium group (as in crystalline GSSG, *cf.* Fig. 14). Finally, $\nu_3(\text{UO}_2)$ is found at 906 cm^{-1} , indicating ternary GSH hydroxo U^{VI} complexes. The U/GSH ratio in the solid is uncertain, however, considering polynuclear species, estimated to ≈ 3 .

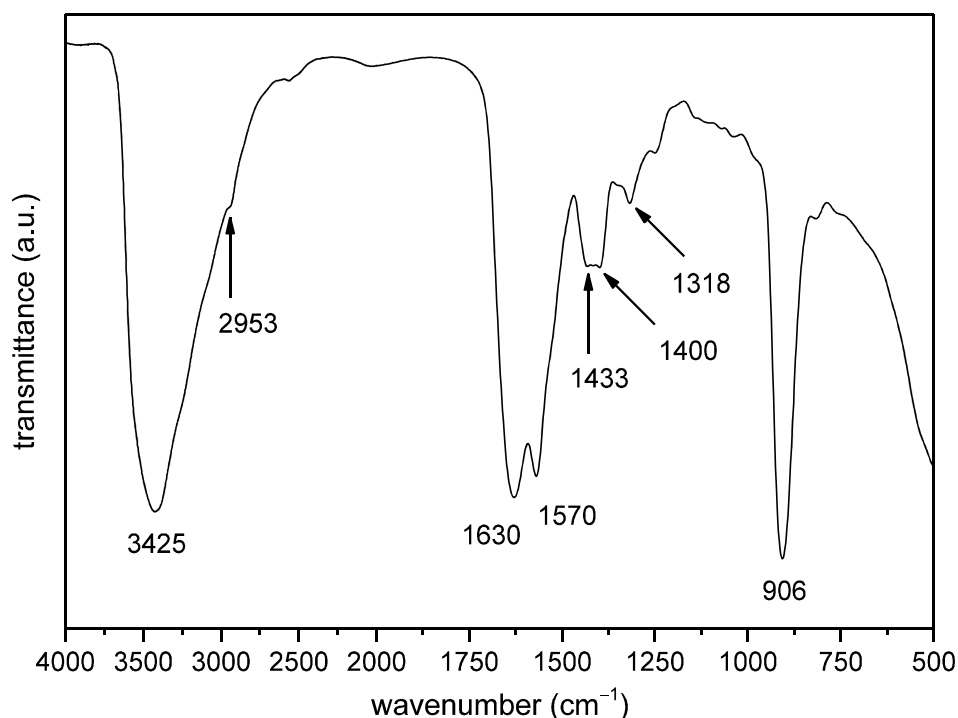


Figure 24. FT-IR spectrum (KBr disc) of the washed and lyophilized precipitate (yellow powder) obtained from 6.7 mM GSH pD 5 solution of initial M/L = 5.

In order to examine the yellow precipitate's morphology, under N_2 atmosphere a sample of initial 6.7 mM GSH and 3.3 mM U^{VI} at pH 7 was freshly prepared, but not centrifuged. One droplet of the obtained yellow suspension was used for transmission electron microscopy (TEM). In addition to bulky amorphous particles attributed to the GSH- U^{VI} yellow precipitate depicted in Fig. 25 A, the TEM micrographs additionally showed nanocrystalline material (B) stuck to its surface, selected area electron diffraction (SAED) revealed to be a uranium(IV)-oxide phase.

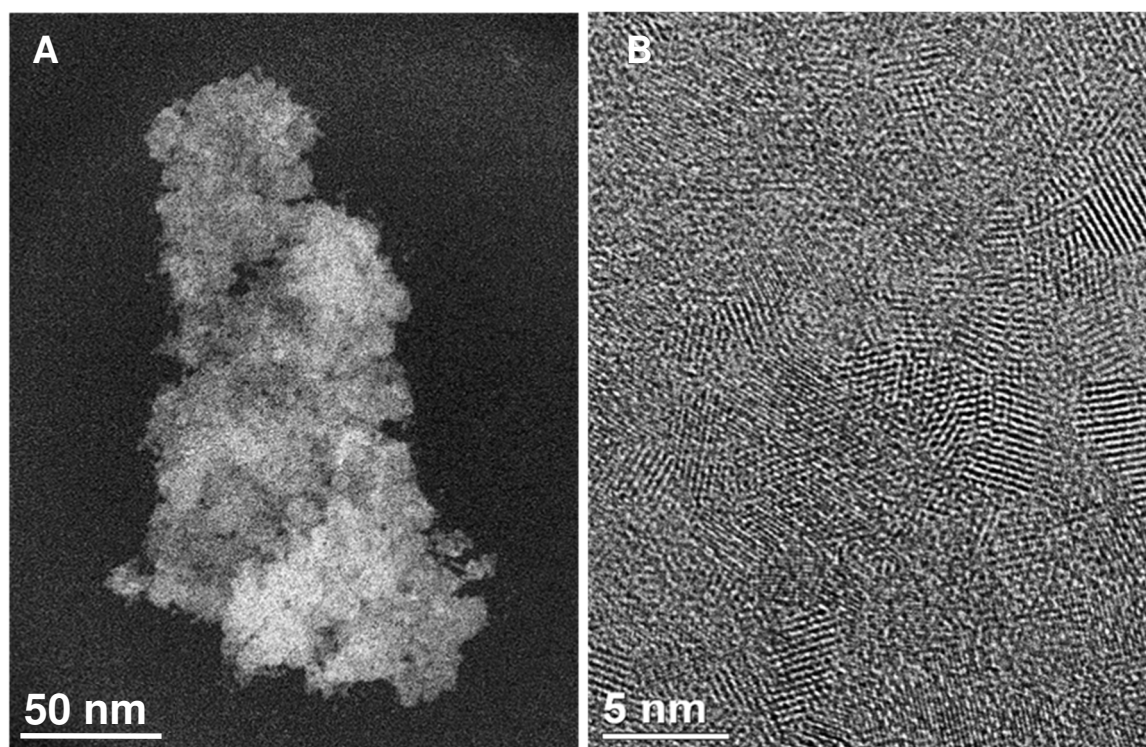


Figure 25. TEM micrographs obtained from a dried aliquot of a freshly prepared sample suspension of initial 6.7 mM GSH and M/L = 0.5 at pH 7, with (B) representing a magnification of the fringe of the particle shown in (A).

Energy-dispersive X-ray (EDX) spectroscopy confirmed the bulk material to consist of uranium and GSH, with signals of nitrogen and sulfur unambiguously attributed to the latter, whereas sodium and chlorine are residuals from pH adjustment (HCl, NaOH), with the analyses depicted in the Appendix.

Apparently, under neutral conditions both the GSH-induced reduction of U^{VI} and the subsequent formation of nanocrystalline U^{IV} -oxide are fast *in situ*. Both formation process and examination of the chemical nature of the uraninite-like UO_{2+x} phase are discussed in the following section.

3.1.3.3 Redox studies

The microscopic and spectroscopic results presented in this chapter and the mechanistic considerations discussed thereafter are subject of a recent publication by KRETZSCHMAR, HAUBITZ, ET AL. [107].

Both the remaining clear pale yellow supernatant discussed in the *Solution studies* (section 3.1.3.1) and the yellow precipitate covered in the *Precipitate studies* (section 3.1.3.2) remaining as a wet paste pellet leftover after decanting the former fraction, were stored, *i.e. aged*, under N_2 atmosphere in the glovebox. As before, both fractions are discussed separately and will hereafter referred to as *aged wet paste pellet* and *aged supernatant*.

Aged GSH- U^{VI} precipitate

Upon ageing, the wet paste pellet changed its color from bright yellow *via* green (after four weeks) and olive to dark-brownish to black, *cf.* Fig. 26. Evidently, the aged wet paste pellet was subject of a proceeding reaction.

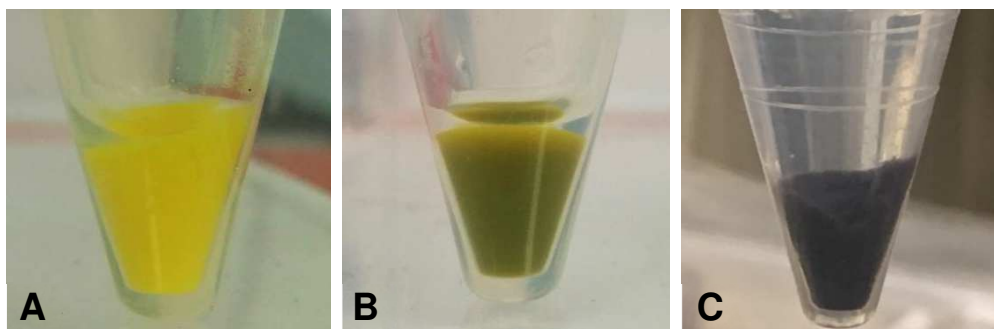


Figure 26. Photographs of the GSH- U^{VI} precipitates: pellet immediately after iteratively repeated centrifugation and washing with 1 M NaCl solution (A) and after ageing for 1 (B) and 5 months (C).

Figure 27 depicts UV-Vis spectra obtained from wet paste pellets aged for both one month (red spectrum) and five months (black spectrum) after dissolution in 1 M $HClO_4$. In accordance with the observed color changes for the wet paste pellet, the content of U^{VI} decreases while that of U^{IV} increases as concluded from accordingly changing intensities of the corresponding absorptions. Since the material aged for one month only, substantial amounts of U^{VI} -GSH precursor are present in the sample. Treatment of this one month aged sample with 1 M K_2CO_3 (dashed blue spectrum) reveals U^{VI} (hydroxo and carbonato species) attributed signals only, indicating that the carbonatic media extracts only the fraction of hexavalent uranium from the GSH precursor. Treatment with acid, however, dissolves the material revealing the same U^{VI} fraction and, additionally, U^{IV} -oxide phases soluble under acidic conditions. Thus, the apparent green color is likely a mixture of both unreacted yellow ternary GSH hydroxo U^{VI} precipitate and dark brownish U^{IV} -oxides, the latter not dissolving in alkaline carbonate solution.

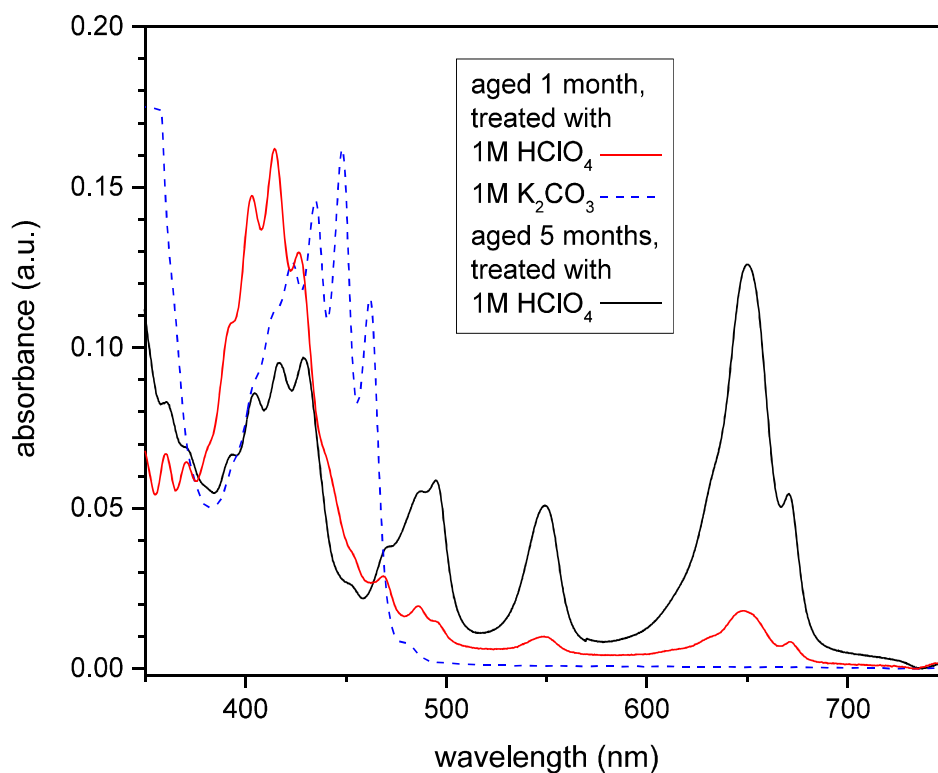


Figure 27. UV-Vis spectra (quartz cuvette, $d = 1$ cm) of the wet paste pellet obtained from 10 mM GSH and 5 mM U^{VI} at pH 8 aged for one month, treated with either 1 M HClO₄ (red) or 1 M K₂CO₃ (dashed blue), and aged for five months and treated with 1 M HClO₄ (black).

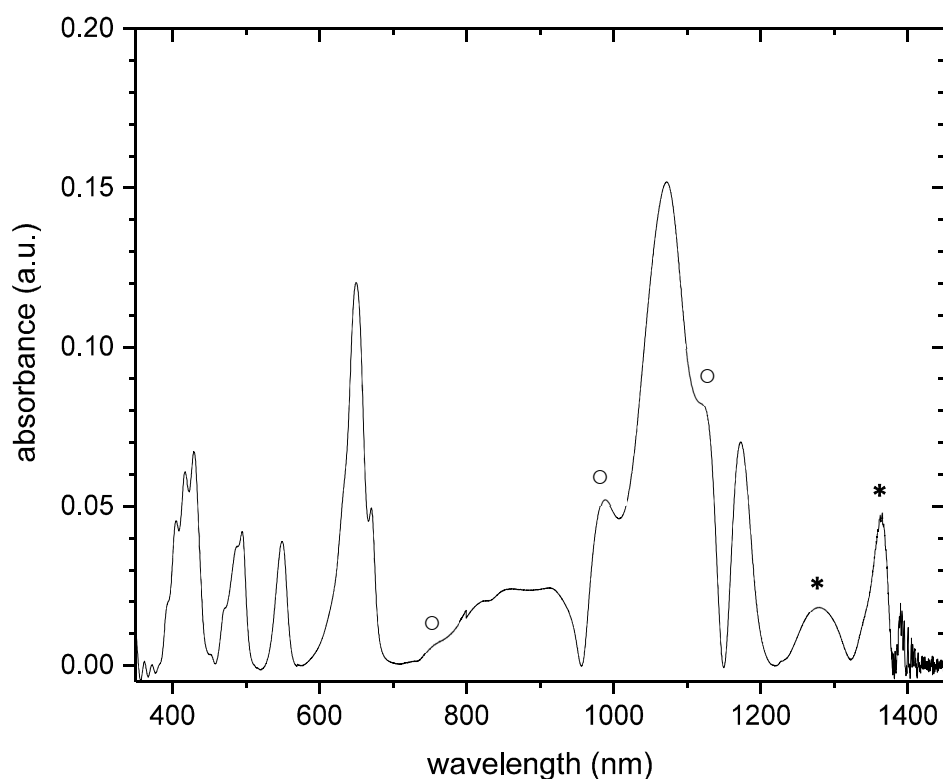


Figure 28. UV-Vis-NIR spectrum (quartz cuvette, $d = 1$ cm) of the aged (dark brown) wet paste pellet obtained from 10 mM GSH and 5 mM U^{VI} at pH 8, after dissolution in 11 M HClO₄ and filtration through a 0.2 μ m syringe filter, with band positions given in Table A6 (Appendix).

The absorption spectrum acquired down to the near-infrared (NIR) range (Fig. 28) discloses absorptions ascribed to U^V – features marked by \circ are underpinned by literature values, for those indicated by * assignment is tentative – indicating the reduction of U^{VI} by GSH to occur *via* a one-electron transfer. Corresponding observed and literature absorption maxima are given in the Appendix (Table A6, p. 169). Because U^V is scarcely observed in general, and for aqueous solutions in particular, comparison of found and published absorption bands is difficult.

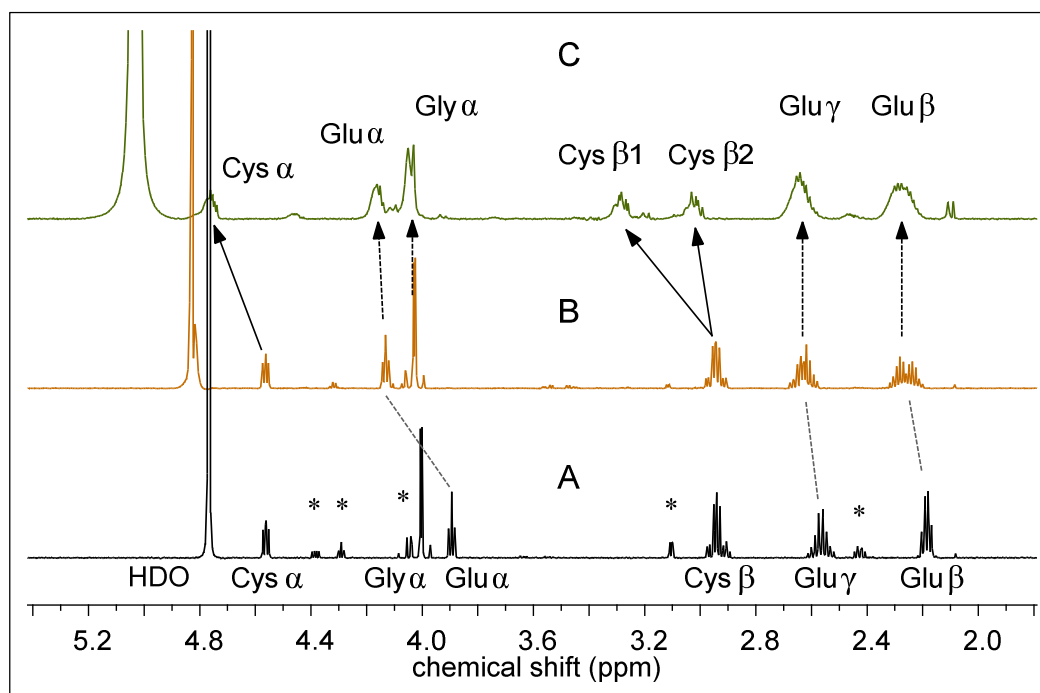


Figure 29. ^1H NMR spectra of GSH pD 2 blank (A); repeatedly washed GSH- U^{VI} sample suspension precipitate promptly lyophilized (B) or after ageing as wet paste for two months (C), re-dissolved in 0.5 M DCl, respectively. Signals of cysteine and glutamate indicated by *.

Complementary to UV-Vis-NIR spectroscopy probing the oxidation state of the metal, NMR spectroscopy aims at examining the ligand's alteration upon the evident redox reaction. Fig. 29 comprises spectra of yellow powder gained after lyophilizing the washed precipitate of a freshly prepared suspension (B) and two months aged, wet paste precipitate obtained from an analogous suspension (C) re-dissolved in 0.5 M DCl, respectively. Comparison between blank (A) and solution B reveals differences primarily due to varying pD, *viz.* blank in A pD 2, samples in B and C pD 1, hence virtually only affecting the Glu moiety (dashed lines) owing to Glu carboxyl group protonation in 0.5 M DCl. As indicated by arrows, the signals assigned to the Cys β CH_2 group appear remarkably distinguished and the correlating Cys α signal (corresponding H,H-correlation spectrum (COSY) depicted in Fig. A25, Appendix) significantly shifts downfield while both Gly and Glu moiety attributed signals show only little to no shiftings, both features characteristic for GSSG. Consequently, the very nature of the analytes differs: the sample attributed to B still exhibits GSH in its reduced form, whereas upon ageing GSH was oxidized to GSSG, with the SH

groups of two GSH molecules forming the S–S bond in GSSG. Thus, particularly the Cys signals are affected, whereas the Glu and Gly signals for both GSH and GSSG scarcely differ from one another. Additionally, the spectral appearance is attributed to paramagnetic uranium ions (of valence states lower than +VI) present in the solution, affecting both the relaxation time and the solution's bulk susceptibility upon which all signals, including that of HDO, show considerable broadening. For the solution is highly acidic, U^{4+} does not interact with GSH, hence paramagnetic signal shifts occur primarily for water.

Apparently, the aged wet paste pellet was right in the reaction to proceed, *i.e.*, reduction of U^{VI} to U^V with the latter existing transiently prior to disproportionation to U^{VI} and U^{IV} . Upon dissolution in $HClO_4$ the reaction quenched and, consequently, all these three oxidation states are simultaneously present in solution. These findings suggest the redox reaction between GSH and U^{VI} to occur *via* a one-electron transfer with the reduction of U^{VI} to U^V , and a subsequent disproportionation of U^V to U^{IV} and U^{VI} , the latter in accordance with theoretical and experimental studies described elsewhere [108-110].

As long as the ageing pellet contains both sufficient amounts of water as the reaction medium (*i.e.*, remains wet) and free GSH as reductant, the redox reaction proceeds further. For the complexation by GSH is labile, *i.e.*, shows facile ligand exchange, *solution* inevitably contains free GSH. Notably, the reaction was occasionally observed to proceed zonally, *i.e.*, from the interface between aqueous solution remainder after decantation and precipitate towards the bulk material and sample tube bottom (*cf.* photograph with 'continued ageing', Scheme 10, p. 122). This is ascribed to better accessibility of the (ternary GSH) U^{VI} hydroxo complexes to remaining free GSH acting as reductant.

Aged GSH- U^{VI} solutions

Morphology studies

Also the pD- and M/L-dependent sample solutions' supernatants, as used for the solution NMR studies – still containing uranium and GSH – were allowed to age for several weeks under N_2 atmosphere whereupon the solutions changed their color from pale yellowish *via* colorless to pale brownish. Apparently, the initial uranium's +VI valence state has changed. No further yellow precipitate was formed, though. Aliquots of these aged pale brownish solutions were investigated by both light microscopy and TEM, see Fig. 30.

Already the light microscope image (Fig. 30 A) reveals the native solution to contain a spongy material based on bulky agglomerates. The TEM micrographs disclose a remarkable network-like structure (Fig. 30 B) likely by reason of specific assembly rather than an artifact due to TEM sample preparation whereby the solvent (water) evaporates in N_2 atmosphere after application to the sample grid. Interestingly, the network consists of chains made up of 2 – 5 nm sized particles (Fig. 30 B – D). Therefore, the diameter of these chains is in fact the same as that of the nanoparticles as can be seen in Fig. 30 D1 – D4. In the first place, the latter are considered to be uraninite, and will later be characterized in detail.

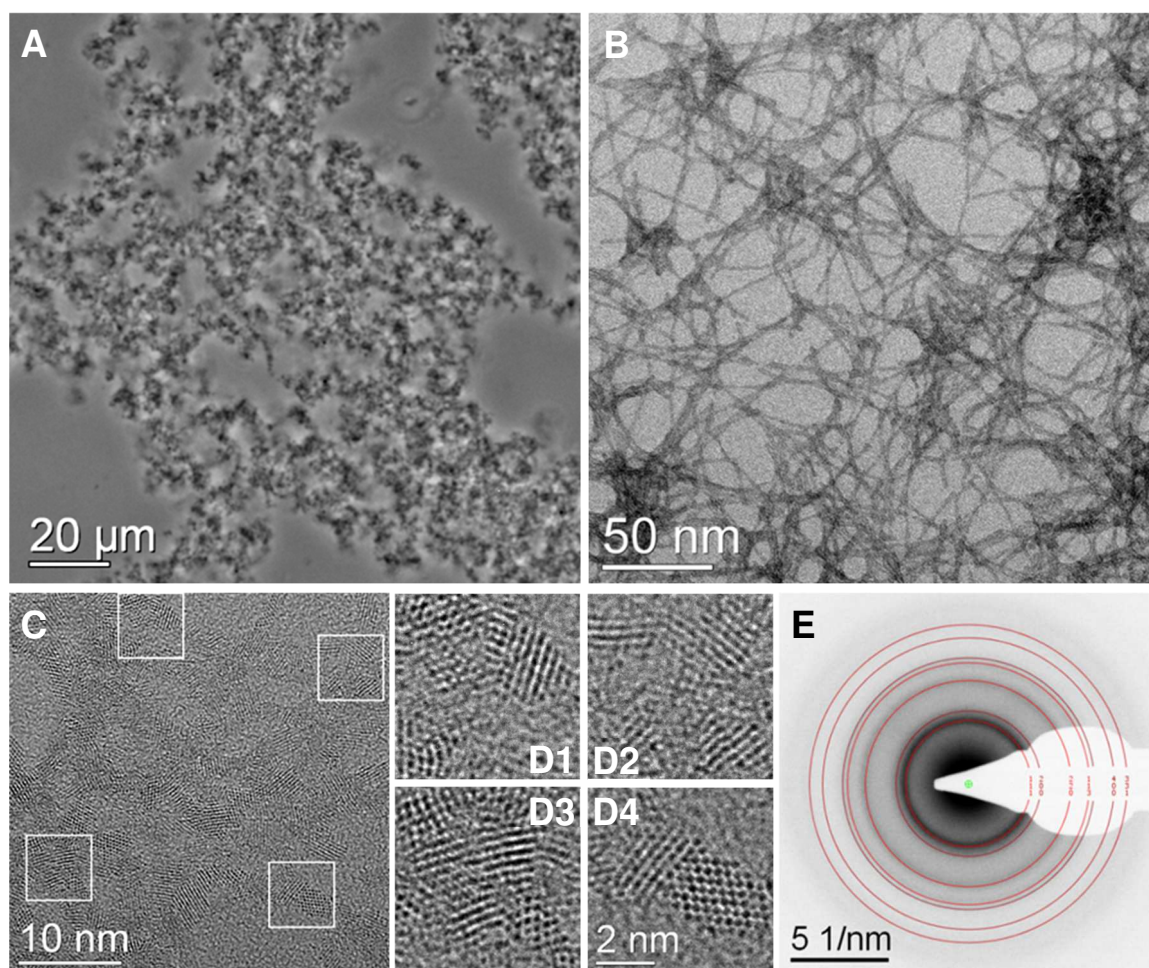


Figure 30. Light microscope image (A) and TEM micrographs at different magnifications (B–D) obtained from the aged pale brownish supernatant of the sample of initial 6.7 mM GSH M/L = 0.5 at pD 7, and (E) SAED pattern with red rings showing the simulated diffraction pattern based on the fluorite-type UO_2 structure (ICSD card 24224).

These UO_2 nanocrystals constitute initial building blocks that form $\approx 20 - 40$ nm sized short-chain units (see Fig. 31 C). Considering the latter as higher building blocks, they further associate either “end-on”, appearing as extended chains, or “side-on”, causing branching. The nanocrystallites do not show a preferred orientation within these chains, and neither do the chains in the network, however, both formation of the chain-like building blocks itself and their arrangement as network are by no means random, but likely provoked by GSH or, more likely, GSSG. The nanocrystals themselves being colorless, upon assembly the agglomerates exhibit a brownish appearance, hereafter referred to as *brownish precipitate*. For discussion on the color *vide infra*. As a result of agglomeration, the particle size increases remarkably (*cf.* Figs. 30 A, and 31 A and B), allowing easy precipitation by centrifugation, according to which the brownish color is shown to better advantage (Fig. 31 D).

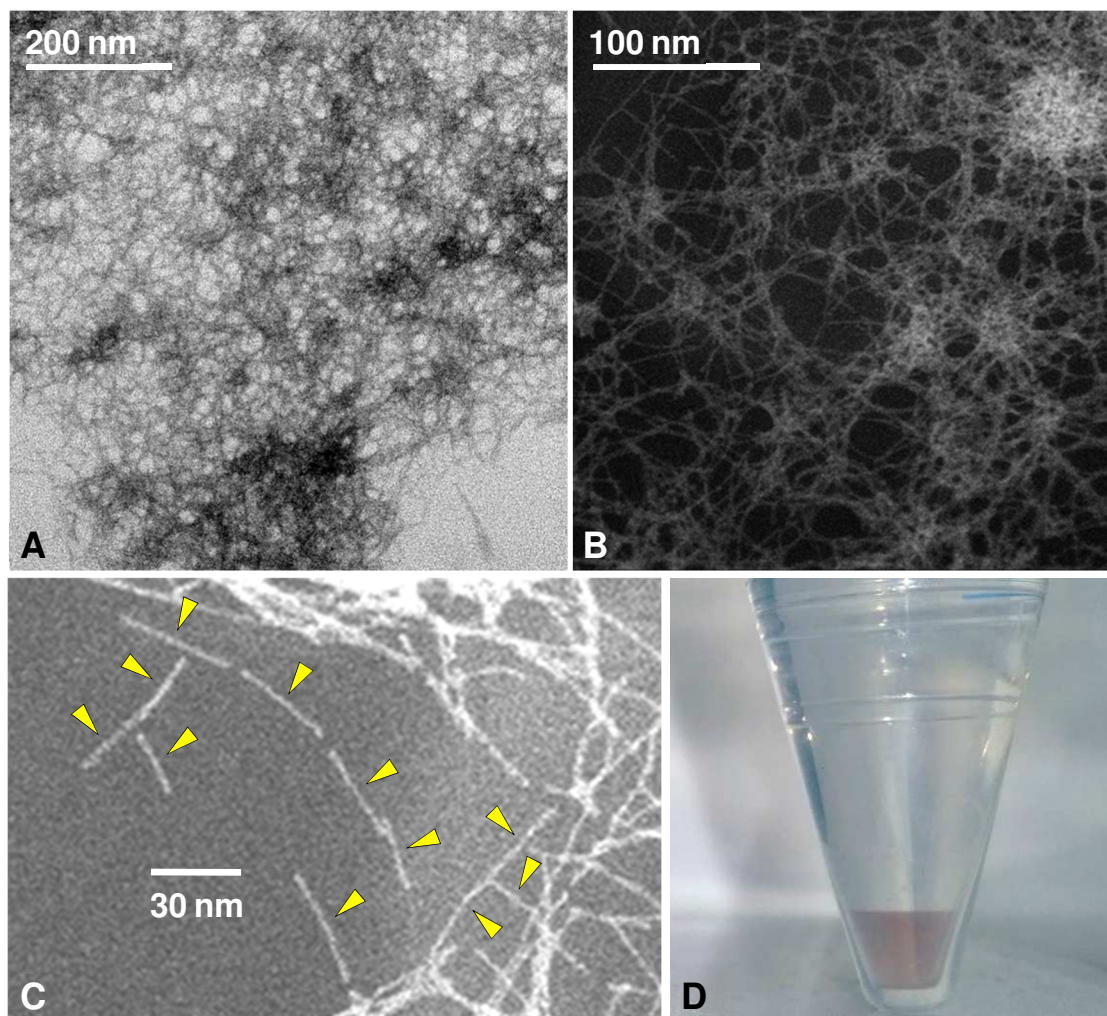


Figure 31. Aged pale brownish supernatant of the initial 6.7 mM GSH M/L = 0.5 pD 7 sample: (A) bright-field TEM image, (B and C) TEM micrographs (scanning mode) with yellow spear-heads indicating chain-like building blocks, and (D) photograph of the centrifuged material.

The particle size distribution was estimated by means of dynamic light scattering (DLS) applied to an analogous, non-centrifuged, aged pale brownish supernatant obtained from a pD 8 sample. Analyses reveal two fractions with 100 and 1000 nm averaged hydrodynamic diameter (*cf.* Fig. A29, Appendix). The individual quantities cannot unambiguously be stated since bigger particles are able to mask smaller ones. However, an explanation of the two fractions is straightforward according to which the bigger particles are the assembled network-like structures and the smaller particles some fragments and/or precursors.

Chemical nature

Besides the fascinating morphology, as part of the TEM analysis, the chemical nature of the particles was also investigated by both energy-dispersive X-ray (EDX) spectroscopy and selected-area electron diffraction (SAED). The composition of the brownish precipitate is verified by EDX spectroscopy with the only significant material-based signals associated with uranium and oxygen (*cf.* Appendix). As compared to the EDX spectrum of the freshly

prepared U^{VI}-GSH suspension (see Appendix), the count number was much less because the material was not as compact owing to both the remarkable spacing in the network-like morphology and the lower overall loading on the TEM grid, since prepared from an aged supernatant instead of a freshly prepared suspension.

On closer inspection it turned out that the SAED pattern obtained matches various uranium oxide structures, among them a vast variety of UO₂-based structures with stoichiometries deviating from UO_{2.0}. To get an impression, Fig. A30 (p. 175, Appendix) shows several simulated (*i.e.*, ICSD reference data related) diffraction patterns superimposed as red rings, all of which being both very similar to one another and matching quite well the experimental data, such as UO_{2.0}, UO_{2.12}, U₄O₉, and UO_{2.34}, with oxygen to uranium ratios (O/U) between 2.0 and 2.34, respectively. As a counter example, the mismatching pattern of U₃O₈ (O/U = 2.67) is enclosed. These findings are in good agreement with a recent paper [111] and references cited therein, stating that the ideal fluorite structure is modified by oxidation of UO₂: “For $2 \leq O/U \leq 2.33$, the anion sublattice is strongly affected, while the cations keep their fluorite arrangement. [...] At higher O/U values ($2.33 < O/U \leq 3$), the fluorite arrangement of the cations can no longer accommodate the excess anions, and compounds with a layered structure (U₃O₈ and UO₃) are formed. Evaluation of the uranium valence mixing in the binary oxides is not straightforward, as charge compensation can be achieved by different oxidation mechanisms, *e.g.*, in U₃O₇ one may consider: U^{IV} + 2 U^V or 2 U^{IV} + U^{VI}.” Consequently, the obtained UO₂ fluorite-type matching SAED pattern specifies the network-like material to an UO_{2+x} phase with $0 < x \leq 0.34$.

Finally, the centrifuged network-like brownish material (Fig. 31 D) was dissolved in 5 M HClO₄ and subjected to UV-Vis spectroscopy. Expecting a low final concentration owing to the wide spaced and thus dispersed material, a 250 cm liquid waveguide capillary cell (LWCC) instead of a conventional 1 cm cuvette was used. Figure 32 depicts the corresponding UV-Vis spectrum together with band positions (numerically given in Table A7, Appendix) of both U^{IV} and U^{VI}. Considering the molar absorptivities at the absorption maxima $\epsilon(\lambda)$ of 9.7 M⁻¹ cm⁻¹ at 413.8 nm [94] and 56.1 M⁻¹ cm⁻¹ at 648.5 nm [112] for U^{VI} and U^{IV}, respectively, the concentration is $\approx 2.5 \times 10^{-5}$ M each. As U^{IV} is fairly stable in acidic media [112], oxidation of U^{IV} to U^{VI} upon dissolution and during acquisition of the UV-Vis spectrum is excluded. Unfortunately, the LWCC is applicable to the UV-Vis range only, thus not allowing NIR studies. On account of the one-electron transfer taking place as figured out from the aged wet paste pellets, U^{IV} must be due to precedent U^V disproportionation. Accordingly, upon dissolution of the brownish network-like material in 5 M HClO₄, U^V – likely being the other oxidation state causing deviation from UO_{2.0} stoichiometry – was accidentally dismutated to (further) U^{IV} and U^{VI}. Since the brownish pellet obtained by centrifugation has not been washed prior to dissolution, the U^{VI} content may be somewhat overestimated.

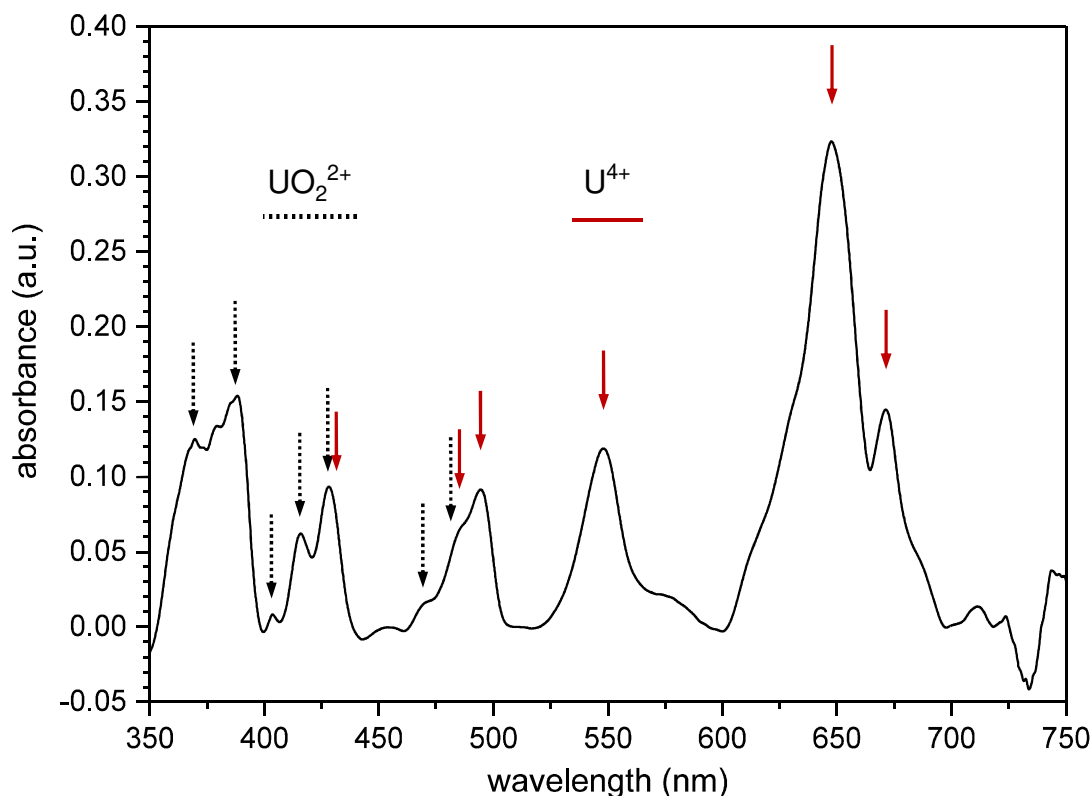


Figure 32. UV-Vis spectrum of the pale brownish material obtained from centrifugation of the aged supernatant of the initial 6.7 mM GSH M/L = 0.5 pD 7 sample (shown in Fig. 31 D) re-dissolved in 5 M HClO₄ and acquired with a LWCC ($d = 250$ cm). Note the band positions for U^{VI} and U^{IV} indicated by dotted-line and red-line arrows, respectively.

As long as the nanoparticles are solubilized, the solution of interest is colorless. Upon agglomeration, *i.e.*, formation of higher building blocks, chains, and the final network-like phase, the solution exhibits a reddish-to-brownish appearance. The observed coloring of the nanoparticle phase is not yet fully understood. It may be due to either its morphology, *viz.* a dispersed, “very diluted” solid phase with big spacing between the network’s chains, hence also “diluting” the expected dark-tone color, or its chemical nature of mixed valence states, *viz.* U^{IV} and U^V oxides, with a corresponding mixing of their individual colors.

In a simple proof-of-principle study with samples containing 6.7 mM GSH and 3.3 mM U^{VI} at both pD 2.25 and 8.5, respectively, the reaction of U^{VI} and GSH was stimulated by mercury lamp light-irradiation. ¹H NMR spectra for both U^{VI} free and U^{VI} containing solutions of either pD irradiated are shown in the Appendix. Briefly, light-irradiation was successful only for the U^{VI} containing sample and only at low pD. However, neither at high pD nor any of the GSH blanks showed substantial molecular changes except further GSH isopeptide bond cleavage yielding cysteinyl-glycine and glutamate, the fragments amounting to 33%.

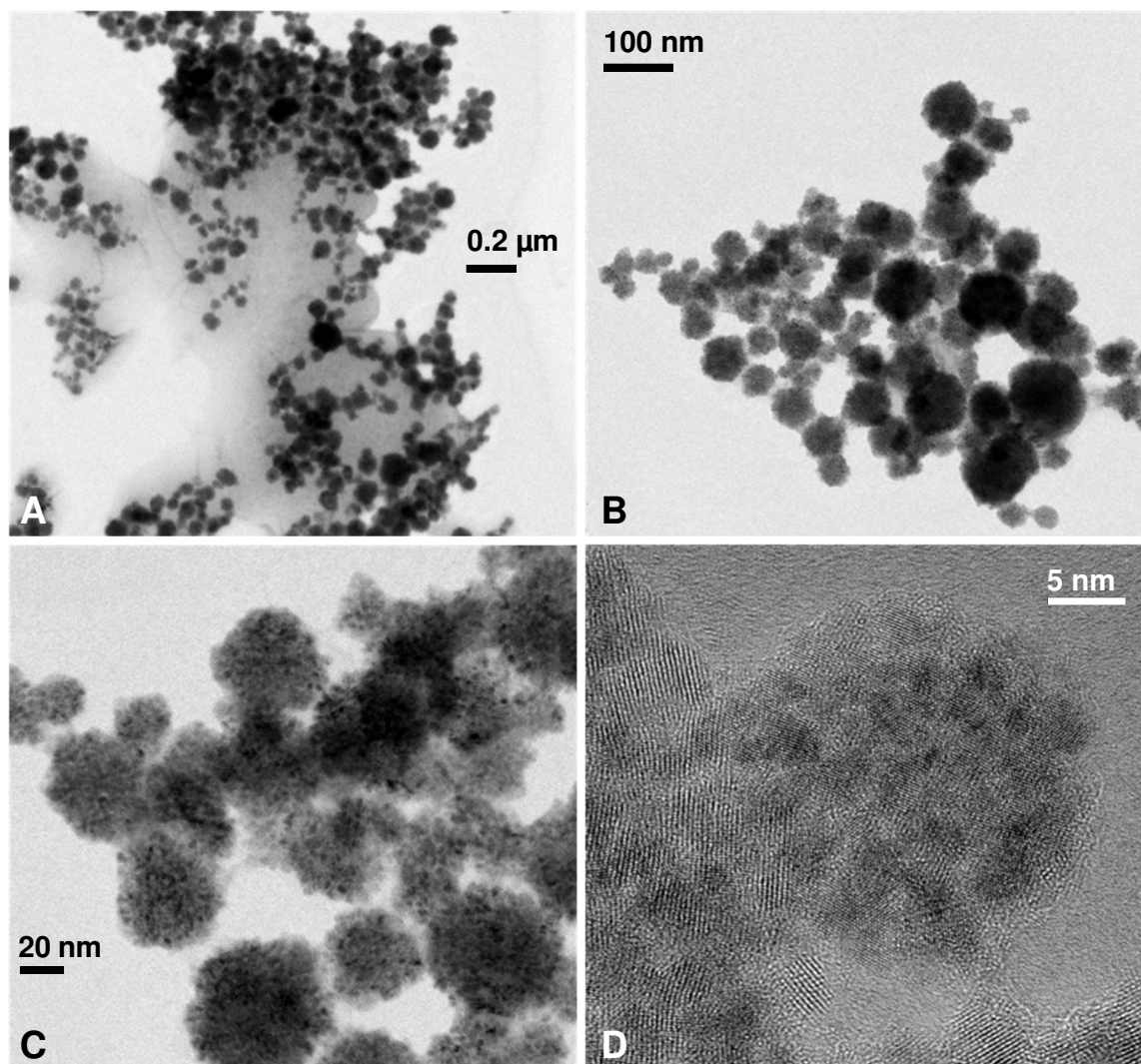


Figure 33. Bright-field TEM micrographs of dark grey precipitate obtained *after light-irradiation* of a 6.7 mM GSH and 3.3 mM U^{VI} pD 2.25 sample at different magnifications. Note the NaCl matrix appearing light grey in the upper left image is due to specimen preparation by solvent evaporation.

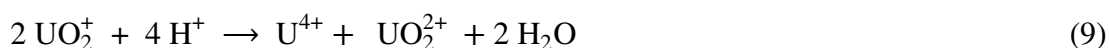
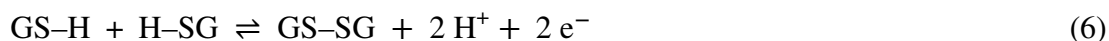
By means of this light-irradiation a photoreaction is induced, reducing U^{VI} to U^{IV} and, again, UO_2 nanoparticles are formed, as determined by TEM in combination with SAED. However, the in this way obtained nanoparticles (i) are formed within minutes instead of weeks as for the network-like phase, (ii) agglomerate in the “conventional” spherical fashion (see Fig. 33; note the NaCl matrix in (A) due to specimen preparation by solvent evaporation), and, (iii) exhibit the “conventional” dark-grey to black color. Hence, it is concluded that the mild conditions, *i.e.*, chemical reduction by GSH in combination with the slow proceeding association for several weeks, facilitates the unique network-like arrangement.

Combining the findings of TEM and UV-Vis spectroscopy, it is plausible that the nanocrystalline brownish network-like material contains mixed uranium valence states and is, hence, best described by hyperstoichiometric UO_{2+x} with $0 < x \leq 0.34$. Whatever its synthetic route – organic-phase synthesis by thermal decomposition of uranyl acetylacetonate

in an oleic acid-oleylamine-octadecene mixture [113], virus-catalysed reduction of U^{VI} by face-centered cubic iron nanoparticles [114], abiotic reduction by redox-active minerals [115-117], biogenic formation by means of microorganisms [14-15, 118-120], or even upon light-irradiation-induced reduction – the yielded UO₂ nanoparticles agglomerate as spheric aggregates. Therefore, the network-like morphology is definitely new and unique and phenomenologically observed by high-resolution TEM methods. The outstanding morphology is somehow provoked by the presence of GSH or, more likely, its oxidation product GSSG, since this feature is exclusively observed for the GSH induced formation of UO₂ nanocrystals, however, not yet understood.

Mechanistic considerations

Notably, for pD 2 – 5 as well as pD ≥ 10 neither GSSG formation nor reduced uranium was observed. Hence, the redox reaction and the concomitant nanocrystal formation could only be evidenced for samples with pD 6 through 9. The overall reaction is quite complex, for the individual reaction steps have to be looked at against the backdrop of chemical reaction kinetics, thermodynamics, as well as acid-base and redox reaction processes, comprising speciation changes of both GSH and U^{VI}. Of special interest is the question whether the U^V is a substantial intermediate in the redox reaction process or whether the reduction occurs directly from U^{VI} to U^{IV}.⁹ The strongest indication are the UV-Vis-NIR signals ascribed to U^V, as observed for the HClO₄ dissolution of the aged wet paste pellet of an initial pD 8 sample solution. Taking into account the standard redox potentials E° of the half-cell reactions given in Eqns. (6) through (8), *i.e.* +180 mV [121], +263 ± 4 mV [38], and +87.8 ± 1.3 mV [122], respectively, corrected by the concentrations and pH conditions used, by means of the NERNST equation the electromotive force ΔE and, hence, the corresponding changes in GIBBS free energy $\Delta_R G$ can be estimated.¹⁰ Please refer to the Appendix for the respective calculations as well as an E vs. pH plot acquired during sample preparation (Fig. A34) together with comments related thereto.



⁹ The very same question will again arise in the light-irradiated uranyl–citrate system.

¹⁰ Consider this as an approach to get a starting point to explain observations, being aware that some issues were not/could not be taken into account: (i) the formation of polynuclear species and their electrochemical behavior, whereas E° values are only tabulated for the reduction of monomeric free uranyl ion to the respective lower valence states; (ii) impact of ionic strength on both speciation and redox potentials; (iii) reaction progress not considered, *i.e.*, constant ‘initial’ concentrations only.

Already the (formal) half-cell reaction equations disclose that the pH dependencies of electron release from GSH, Eqn. (6), and acceptance by UO_2^{2+} to form U^{4+} , Eqn. (7), work in opposite directions, whereupon ΔG becomes progressively less negative with increasing pH and, therefore, the reaction unlikely to take place (*cf.* Fig. 34). As of $\text{pH} \approx 6$, $\Delta_R G$ is positive and no redox reaction is to be expected for the $\text{U}^{\text{VI}}/\text{U}^{\text{IV}}$ case. Eqn. (6) nicely reveals that GSH becomes more reductive with increasing pH, while the formation of U^{V} is independent from pH. Thus, $\Delta_R G$ not only is more negative as compared to the $\text{U}^{\text{VI}}/\text{U}^{\text{IV}}$ case in the entire pH range, but becomes even more negative with increasing pH (owing to the impact of the GSH term). The subsequent disproportionation of U^{V} to U^{IV} and U^{VI} , Eqn. (9), is irreversible and strongly pH-dependent, *i.e.*, favored with increasing acidity, explaining the better observability of U^{V} at higher pH values. To conclude so far from a thermodynamic perspective, in principle, both reduction reactions are possible at least up to circumneutral conditions, however, the $\text{U}^{\text{VI}}/\text{U}^{\text{V}}$ reaction (Eqn. (8)) seems both to be favored over the $\text{U}^{\text{VI}}/\text{U}^{\text{IV}}$ reaction (Eqn. (7)), and as of circumneutral pH the only way to facilitate U^{VI} reduction by GSH.

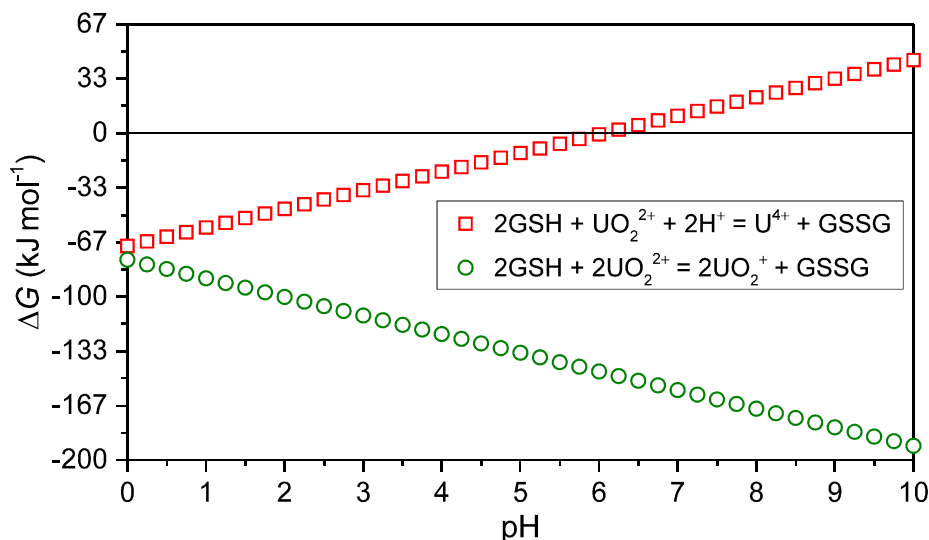
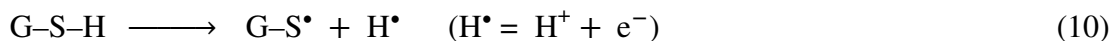


Figure 34. Calculated changes in GIBBS energy in dependence of pH for the redox reactions of GSH with U^{VI} for both redox couples $\text{U}^{\text{VI}}/\text{U}^{\text{IV}}$ (□) and $\text{U}^{\text{VI}}/\text{U}^{\text{V}}$ (○).

At first glance this contradicts the experimental findings that except for pD 6 through 9 no redox reaction could be observed. However, that does not mean that beyond that pD range GSH is not able to act as a reductant at all. KRETZSCHMAR ET AL. [43] have shown in other studies that GSH acts as a reductant at pD 3, for instance, reducing arsenic(V) to arsenic(III) compounds.

Although for alkaline media the pH conditions are well suited for the redox reaction to yield uranium in its +V state, there must be some other reasons preventing the reaction for both low and high pH values. Therefore, once more the speciation is considered. As of pD 3.3, 9.0, and 9.5 (according to $\text{p}K_a$ values) H_4GSH respectively predominates as HGSH^- , HGS^{2-} , and GS^{3-} , that is, primarily net negatively charged species. Concurrently, U^{VI}

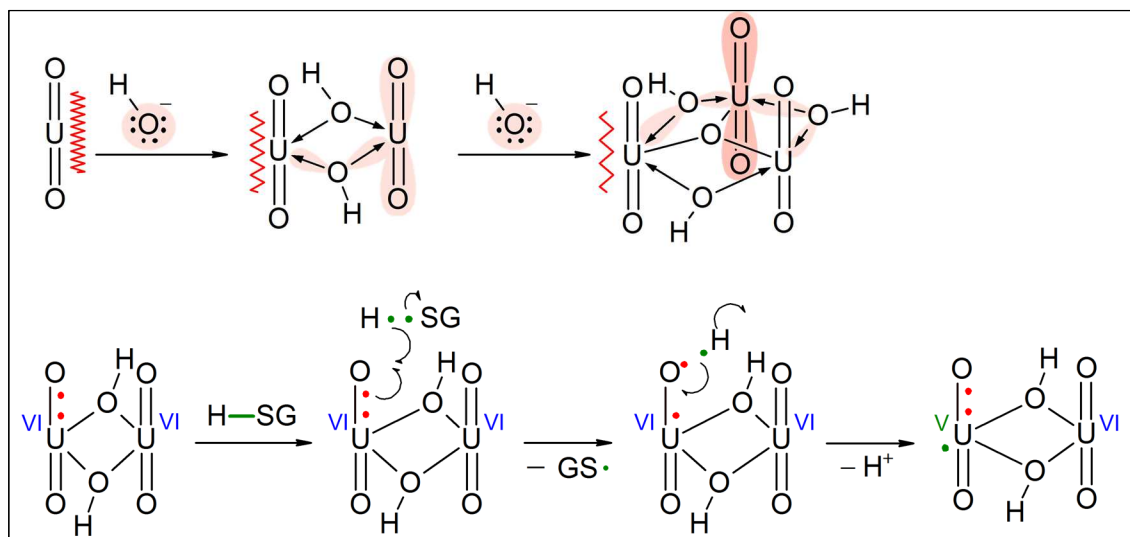
changes its speciation from free UO_2^{2+} to (polynuclear) hydrolysis species, at first all of which being cationic, and above pH 7 also existing as anionic species, *cf.* speciation diagram (p. 8). Hence, COULOMB repulsion may become of significant influence with increasing number of deprotonated GSH functional groups.



With regard to the latter statement, the question arises if the thiol group is required to be protonated for the redox reaction to happen, implying that it is not the charge repulsion itself that prevents the reactions, but rather the sulfhydryl hydrogen (ion) as crucial mechanistic participant. Particularly the reaction shown in Eqn. (10) is in very agreement with the finding that as of pD 10 the redox reaction does not happen any longer owing to (heterolytic) deprotonation of the thiol group ($\text{p}K_a$ 9.0). Obviously, in order to yield a hydrogen atom as the effective reduction equivalent, the S–H bond requires homolytic cleavage, which is likely to facilitate since the bond is only slightly polarized, in accordance with molecular dynamics [102] that the S–H group behaves as a hydrophobic group and is not immediately solvated. In contrast, a concerted two-electron transfer requires a transition state including the uranyl and two GSH simultaneously acting together for both disulfide formation and release of electrons in pairs facilitating direct $\text{U}^{\text{VI}}/\text{U}^{\text{IV}}$ reaction. Such a mechanism is considered to be very unlikely. Instead, it is more probable that one GSH releases the electron to yield U^{V} and both a hydrogen atom and a thiyl radical as given in Eqn. (10), and the observed U^{IV} is formed upon disproportionation. According to a very recent paper dealing with the proton-coupled electron transfer of glutathione oxidation [123], the electron/proton transfer (stepwise or concerted) is the rate determining step, whereas the thereby formed thiyl radical dimerizes at a diffusion limited rate upon relaxation by self-terminating (electron pairing) second-order reaction yielding GSSG. Thus, the thiyl radical constitutes an intermediate too short-lived to be detected by NMR.

Finally, a hypothetical mechanism how the reduction of U^{VI} to U^{V} *via yl-oxygen* by the GSH thiol group hydrogen atom (Eqn. (10)) proceeds is sketched in Scheme 2. According to SZABO ET AL. can “the *yl*-oxygen in the uranyl ion be labilized in two ways, either by coordination of a strong LEWIS base or by photochemical activation” [124]. Upon binding of ligands, *i.e.* LEWIS bases (B), the $\text{O}=\text{U}=\text{O}$ entity withdraws electron density and, hence, exhibits decreasing LEWIS acidity in agreement with red-shift of $f \rightarrow f$ transition in UV-Vis absorption spectra (decrease of the HOMO–LUMO gap) and reduction of the $\text{U}-\text{O}_{\text{yl}}$ bond force constant and the concomitant decrease in $\text{O}=\text{U}=\text{O}$ vibration frequencies as observed in vibrational spectroscopies. This is well established and nicely seen for, *e.g.*, carboxylate, carbonato or hydroxo ligands [94, 97-99, 125-127]. The same holds true for U^{V} , finding an electron explicitly at the uranyl ($\bullet\text{UO}_2^+$), whereupon U^{V} shows a significantly reduced LEWIS acidity owing to the decreased cation charge since the “additional $5f$ -electron in UO_2^+ occupies a nonbonding $5f_\delta$ orbital and induces a weakening of both axial and equato-

rial bonds as reflected by the increase of 0.10 and 0.09 Å in the U–O_{yl} and U–water bond distances, as compared to those in UO₂²⁺ [128]. Since donation of electron density towards the uranyl(VI) (B| + UO₂²⁺ : B → UO₂²⁺) elongates and, therefore, weakens the U^{VI}–O_{yl} bond, species with U^{VI} lowered in LEWIS acidity are supposed to be better suited to be reduced this way than the mononuclear uranyl aquo ion.



Scheme 2. Illustration of increase in electron density (pale red background) of U–O_{ax} bond and its changing bond properties (symbolized by the spring) upon hydroxo ligand coordination (top); hypothetic mechanism of hydrogen-atom-transfer based reduction of U^{VI} to U^V by GSH via axially U-bound oxygen (bottom); for clarity, coordinating water is not shown.

Although the already increased U^V bond lengths foreshadow the way towards U^{IV}, particularly in polynuclear species, disproportionation is considered less effective since it requires two successive protonation reactions, according to which the dismutation is much more effective at low pH. Therefore, the pD 6 – 9 samples – both (aged) supernatant and, particularly, wet paste pellet – are likely to contain U^V in sufficient amounts.

After formation and disproportionation of U^V, the thereby obtained U^{IV} hydrolyses, and together with U^V forms mixed-valence uranium oxide particles. The occurrence of at least two different valence states in the nanoparticles is ascribed to the reduction of polynuclear species. Under the conditions applied, *viz.* millimolar [U] at near-neutral pH, uranium in all its valence states forms polynuclear and hydrolyzed species. Upon condensation of these particular species, mixed valence state – U^V by reduction, and U^{IV} by U^V dismutation – containing nanoparticles form. For the redox reaction proceeds (i) in a pD range GSH cannot compete with hydrolysis for U^{VI} binding by its carboxyl groups, and (ii) zonally rather than uniformly in the wet paste pellet, it is concluded that unbound GSH acts as the reductant, *i.e.*, *intermolecularly*.¹¹

¹¹ Also an issue recurring for the uranyl–citrate system.

3.1.4 Comparison of Lanthanide– and Uranium–Glutathione System

The facile ligand exchange at *f*-element centers particularly in aqueous solutions [16] is confirmed by observation of only averaged GSH/GSSG attributed NMR signals for both the Ln^{III} and the U^{VI} system. However, for sufficiently high [U^{VI}] the exchange regime tends to change from fast intermediate to slow intermediate on the ¹H NMR timescale.

Both Ln^{III} and U^{VI} are bound by GSH's carboxylate groups, with the Glu carboxyl group showing better accessibility, and the Gly carboxyl group higher capability. That is, as of pD values in the order of magnitude of its p*K*_a value (pD ≈ 2.5), the Gly carboxyl group is the better binding site for the considered metal ions. Nonetheless, the other, *i.e.*, Glu carboxyl group is also capable of metal ion interaction. Ln^{III} containing solutions did not exhibit precipitation for the applied conditions, that is, up to pD 5 in high millimolar range. The high solubility of the Ln^{III} complexes observed is due to their charge. Possible 1:1 and 1:2 Ln^{III}–GSH complexes formed by either H₂GSH⁰ or HGSH[−], which are the predominating species in the pD range sampled, are overall cationic. Only the [Ln(HGSH)₃]⁰ 1:3 complex would be net neutral and thus potentially precipitating. However, as concluded from Eu^{III} TRLFS data, in solution solely the 1:1 [Eu(HGSH)]²⁺ forms with a rather small log *K* of 1.71 ± 0.01.

GSH/GSSG interaction is in principle stronger with U^{VI}. Complementary to the Eu^{III} results, whenever net neutral binary GSH/GSSG or ternary hydroxo GSH/GSSG U^{VI} complexes form in solution, both these U^{VI} systems revealed extensive precipitation owing to the low solubility of these complexes. Binary U^{VI} GSSG and ternary U^{VI} hydroxo GSSG complexes form solid phases from pD 2 through 8, even in carbonatic media. The largest quantities of aqueous GSSG–U^{VI} complexes are observed for pD 3 – 4, with the association constant for pH 3 determined as log *K* = 4.81 ± 0.08 for a 1:1 complex.

Owing to its remarkably high concentrations *in vivo*, GSH is a potential, at least transient, ligand, and even if not binding as a ligand itself, it can act as a reductant since complex formation seems not essential for the redox reaction to occur. GSH's redox activity is less applicable to lanthanides, however, all the more valuable for actinides, since the latter themselves are distinguished by their various redox states. GSH has proven to readily reduce uranium from +VI to +IV state at circumneutral conditions with concomitant formation of nanocrystalline UO_{2(+x)}. One can assume that not only uranyl in particular, but actinyl ions in general can be reduced by GSH for appropriate conditions. Since assembly to the observed UO_{2(+x)} network-like structures proceeds only slowly, the 2 – 5 nm sized nanocrystals are in the first place colloidal and, thus, considered mobile, but then prone to agglomerate and/or adsorb at suited surfaces.

3.2 CITRATE TOPIC

General considerations

In the following, citric acid is considered four-basic, *i.e.*, H_4Cit . Accordingly, ionized forms are denoted H_3Cit^- , H_2Cit^{2-} , $HCit^{3-}$, and Cit^{4-} . Although the alcoholic hydroxyl group is a very weak acid in aqueous solution, upon complexation, particularly to strong LEWIS acids such as aqueous uranium ions, the proton abstracts even for pH conditions far below the corresponding pK_a . Therefore, the commonly used notation $HCit^{3-}$ may represent (coordinating ligand) species with either protonated alcoholic hydroxyl or protonated carboxyl group. Note that, for convenience, unless of importance or in semi-structural formula notation, the terms ‘citrate’ and ‘Cit’ are used generically.

To comprehend the spectral changes upon varying sample conditions, pD for instance, blank spectra of reference samples containing only citric acid were acquired. By reason of deprotonation, the methylene 1H nuclei become more shielded (signals shift upfield) whereas all the ^{13}C nuclei exhibit a deshielding whereupon the signals unanimously shift downfield (*cf.* Fig. 35). The magnitude of these shifts is larger between pD 2 and pD 5 than for pD 5 and pD 8, according to the pK_a values of the carboxyl groups (*cf.* Table 2, p. 12). The pD 5 spectrum shows signal broadening and thus lower S/N owing to protonation/deprotonation reactions due to pD close to pK_{a2} . Once more, for co-existing species only averaged signals are observed.

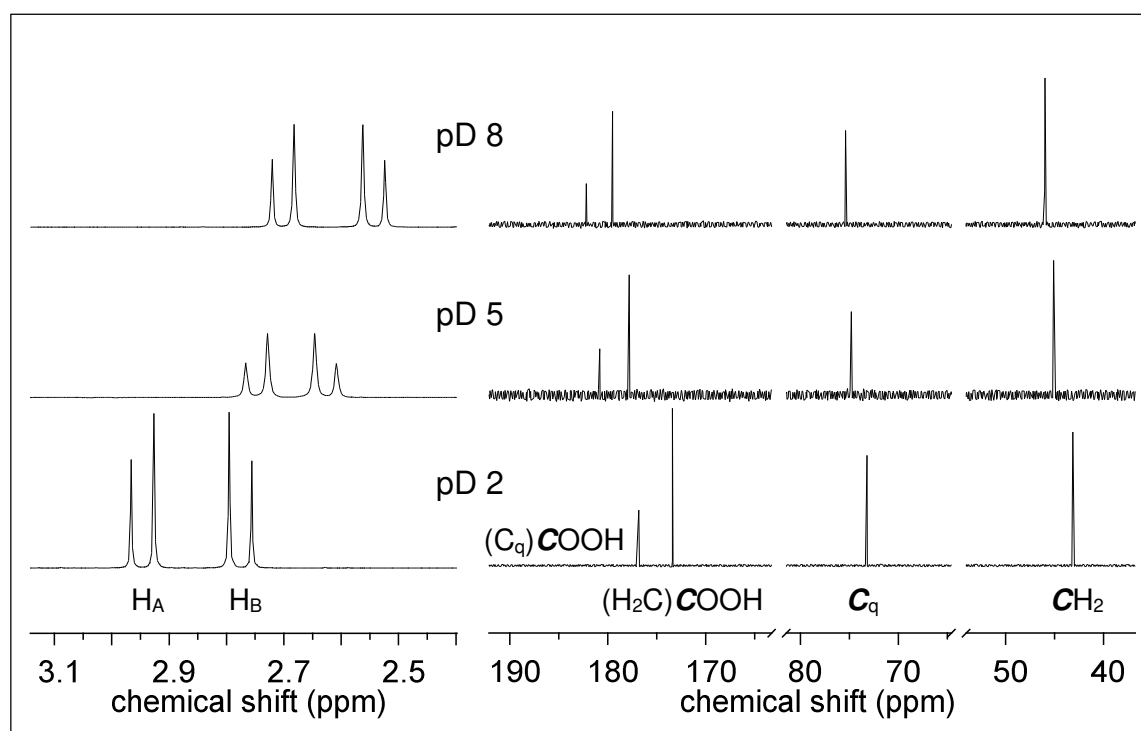


Figure 35. 1H (left) and ^{13}C (right) NMR spectra of citric acid in D_2O at pD as indicated together with signal assignment.

3.2.1 Uranium–Citrate Complex Structures

With hexavalent uranium (UO_2^{2+}), all ionized species of citric acid may form complexes. However, UO_2^{2+} has a linear dioxo-structure and the ligand should coordinate in the equatorial plane perpendicular to the O–U–O axis. Since this sets some constraints on the stoichiometry of the complexes due to the steric hindrance, only two carboxylate groups may simultaneously coordinate to the central uranium, resulting in the strong interaction of the alcoholic hydroxyl group and the uranium [54]. In order to comprehend the chemical changes on both U^{VI} and citrate upon light-irradiation, a sound understanding of the starting point is mandatory and therefore the state of knowledge for is given beforehand. The aqueous chemistry of the U^{VI} –Cit system is complex, as evidenced by more than 70 years of investigation [129] and still controversial discussions on speciation as well as complexes' stoichiometries and geometries. As early as 1954, FELDMAN ET AL. draw the conclusion that citric acid chelates U^{VI} in a tridentate fashion involving two carboxylates and the hydroxyl group [130]. In equimolar systems, and also in excess citric acid, in the pH range 2 to 4 U^{VI} –Cit forms the 2:2 tridentate complex. At about pH 4 the dimer is reacted to form trimeric species, still tridentate, being a mixture of 3:3 and 3:2 chelates [131]. In a paper by BERTO ET AL. [132] and Refs. cited therein, a good overview on literature together with formation constants obtained up to $I = 1$ M, including specific ion interaction theory (SIT) approach for the activity coefficient, is presented. Well established are the 1:1 and 2:2 species $[(\text{UO}_2)(\text{HCit})]^-$ and $[(\text{UO}_2)_2(\text{HCit})_2]^{2-}$, respectively, the latter of which being by far the most important and most stable ($\log \beta^\circ = 21.3 \pm 0.5$) [54]. KAKIHANA ET AL. [106] (unfortunately, stating neither concentrations nor pH values) tried to bring their ^{13}C NMR spectra in accordance with a linear 3:2 complex structure. At the same time, however more systematically and accurately in terms of sample conditions, NUNES AND GIL [133] published ^1H and ^{13}C NMR results on the U^{VI} –Cit system. Besides signal assignment, they confirmed the 2:2 structure proposed earlier [134] and suggested a 3:2 complex structure. PASILIS AND PEMBERTON [135] conducted Raman and attenuated total reflection FOURIER-transform infrared (ATR FT-IR) spectroscopy as well as electro-spray ionization mass spectrometry (ESI-MS) experiments on the U^{VI} –Cit system, corroborating the existence of 3:3 and 3:2 species. Also LUCKS [136] found strong evidence for 3:3 species containing $\mu_3\text{-O}$ by means of EXAFS in aqueous solution. Finally, in a contribution by T. Z. FORBES' group [137] the long proposed trimeric 3:3 species, which in fact is $[(\text{UO}_2)_3(\mu_3\text{-O})(\text{Cit})_3]^{8-}$, was proven by single-crystal X-ray diffraction, and the repeatedly taken up 3:2 species coexisting and predominating at $\text{pH} > 5.5$ and being dominant as of circumneutral pH, was shown to be a stoichiometric sub-unit forming the macrocyclic 9:6 complex $[(\text{UO}_2)_9(\mu_2\text{-OH})_3(\mu_3\text{-O})_3(\text{Cit})_6]^{15-}$ (*cf.* Fig. A35, Appendix). Figure 36 depicts a compilation of representative structures of the dimeric and trimeric species described in both aqueous solution (EXAFS, [136]) and in the solid state (single-crystal X-ray diffraction, [137-138]), which will be referred to again later.

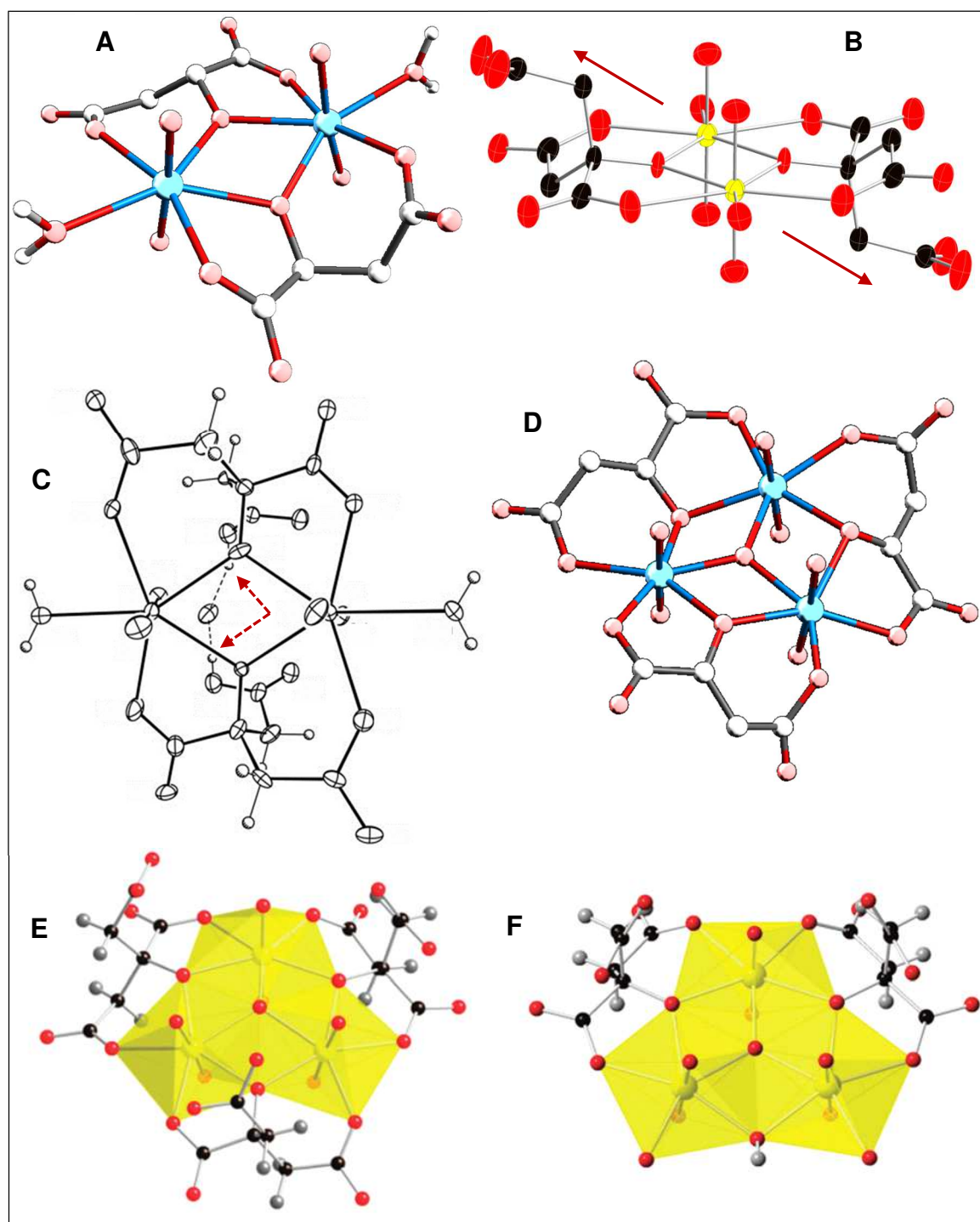


Figure 36. Molecular structures of U^{VI} -Cit dimeric (A–C) and trimeric (D–F) complexes as determined from aqueous solution (A and D, according to [136]) and from single crystals (C, taken from [138]; B, E, and F, taken from [137]). Note that structures A and D show no unbound $CH_2COO(H)$ moieties since not covered by EXAFS data acquisition.

3.2.1.1 Uranyl–Citrate Dimer

Complex geometry

Although the 2:2 complex's structure is established to contain two five- and two six-membered chelate rings in alternating fashion, also other geometries are conceivable but not discussed elsewhere. Thus, in the first place, a closer look is taken at the different reasonable complex geometries. Figure 37 depicts five geometries, further referred to as A-, B-, C-, D-, and E-type. The first two types contain both two five- and six-membered chelate rings each, whereas the C-type possesses six-rings only, and D-type one five- and three six-rings. Within one Cit ligand, the hydroxy group is bridging the uranyl units (μ_2 -O), the five-ring forms by the central carboxylate and the six-ring by one of the terminal carboxylates whereas the other remains unbound. In contrast, the E-type type is made of a structure without bridging μ_2 -O site but all four Cit functional groups coordinating, thereby forming two six- and two seven-rings.

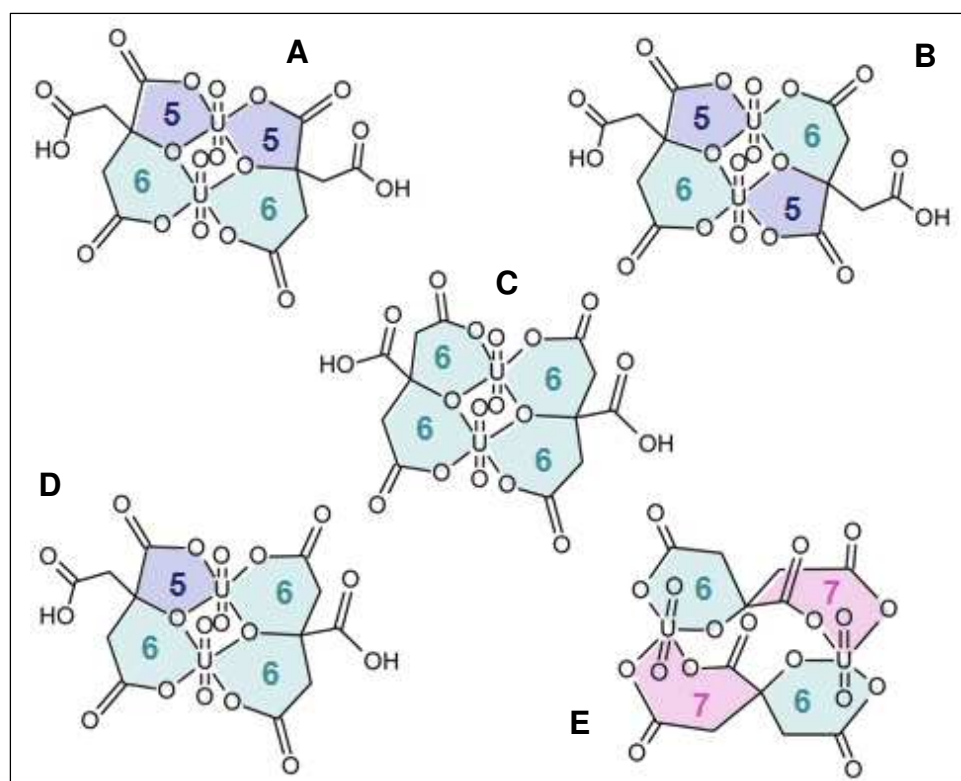


Figure 37. Conceivable 2:2 U^{VI} -Cit complex structures for different geometries, illustrating chelate ring sizes and arrangement. Note that coordinating water is omitted for clarity.

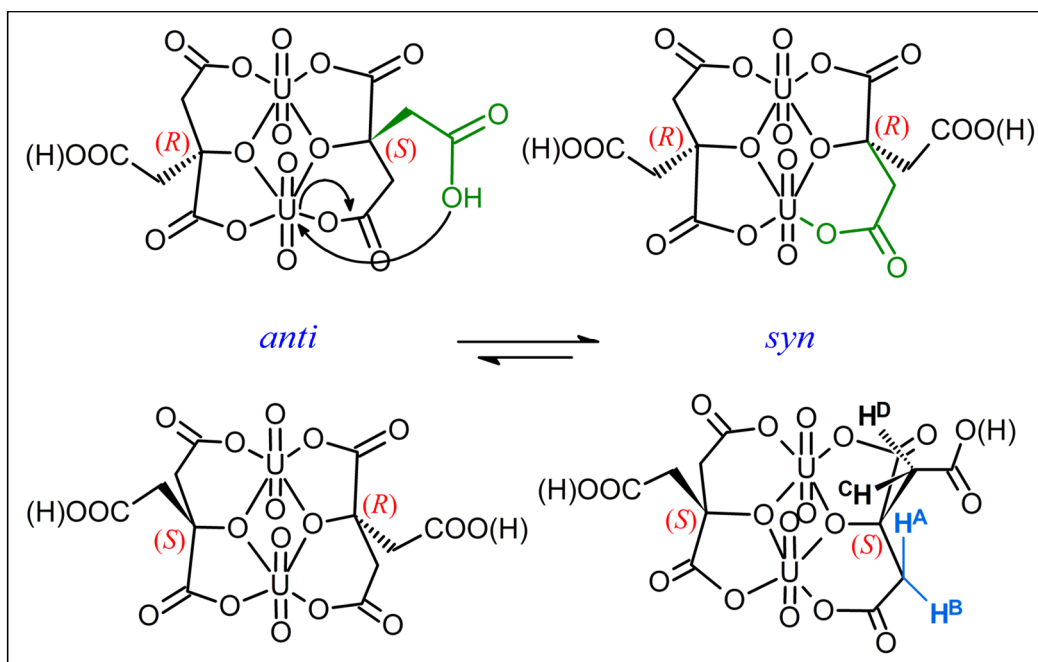
DFT calculations reveal the geometry types to increase in energy for the series A – E, respectively. Whereas the C-type geometry is already larger by +45 kJ mol^{-1} , D- and E-type geometries are +85 and +100 kJ mol^{-1} above A-type energy, which is in agreement with the observation of a complex structure lacking the more stable five-membered chelate ring to be unlikely. Therefore, the following closer inspection focuses on A- and B-type geometries, among which the latter exhibits five- and six-membered rings alternating, so

that each uranium atom shows the same arrangement of nearest neighbors (besides the two *yl*-, one central carboxyl-, one terminal carboxyl-, and two μ_2 -bridging oxygen atoms). The A-type geometry, however, possesses differing uranium atoms' nearest neighbors, *i.e.*, while either uranyl bears two μ_2 -O, one is coordinated by two terminal carboxylates whereas the other is by two central carboxylates, rendering the uranium atoms distinct. Among the methods applied to the U^{VI} -Cit system in general, and investigating the 2:2 complex in particular, *i.e.*, UV-Vis [134, 139], EXAFS [136, 140], as well as Raman, IR, and ESI-MS [135], it is questionable if any is able to discriminate between A- and B-type in aqueous solution, since the two UO_2 units in both geometries possess the same pentagonal bipyramidal coordination geometry as well as same number and type of nearest neighbor atoms. This is corroborated by comparison between DFT-calculated (for details *cf.* section 5.2.9) $U-O_{yl}$ bond lengths of 1.784(3) and 1.785(3) Å and U-U distances of 3.91(4) and 3.91(5) Å for both A- and B-type geometry, and the values obtained from EXAFS [136], *viz.* 1.784(1) and 3.903(6) Å, respectively. Correspondingly, Raman-active ν_1 and IR-active ν_3 for UO_2 are calculated to 841 and 905 cm^{-1} , and 842 and 907 cm^{-1} for A- and B-type geometry, respectively. Experiment determines the values as $\nu_1 = 826 cm^{-1}$ [135, 137] and $\nu_3 = 919 cm^{-1}$ [135, 141]. Deviation by 16 cm^{-1} at most is a very good agreement, all the more interesting are the virtually identical values calculated for both geometry-types. So far, all spectroscopic results obtained from solution studies do not contradict the A-type geometry.

Complex configuration

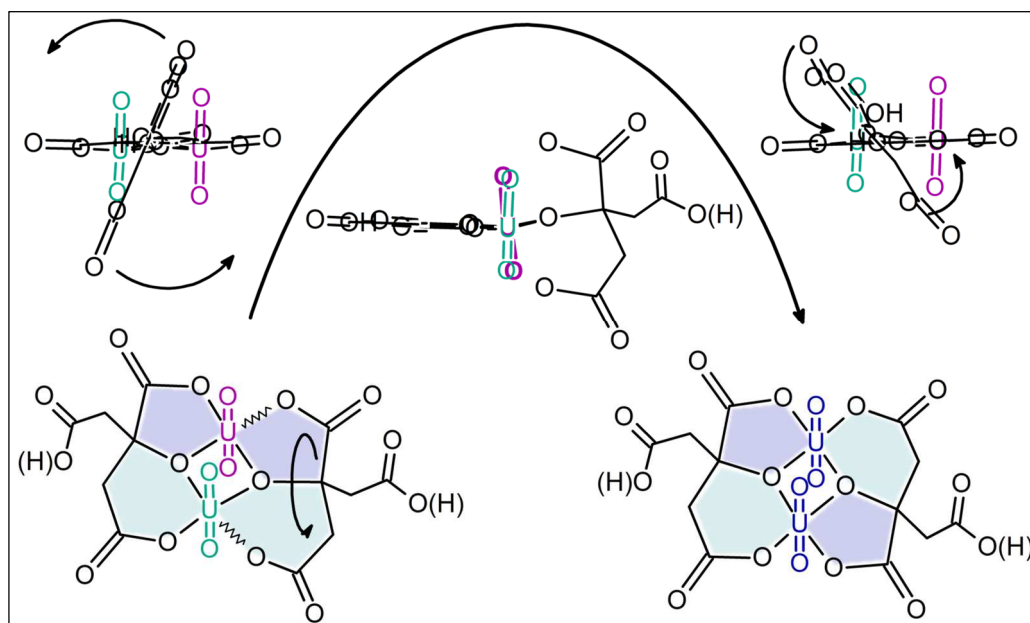
Remarkably, neither publication dealing with the U^{VI} -Cit system considers that, since Cit itself is prochiral, upon complexation a chiral center in C_q is induced, with the resulting complexes possessing asymmetric carbons of different configuration and eventually forming spectroscopically *distinct isomers*. Moreover, although being aware of site exchange for the terminal carboxyl groups, changing configuration upon that process is not regarded.

As exemplarily depicted in Scheme 3, the given initial orientation of the complex' two unbound $CH_2COO(H)$ is *anti*, *i.e.*, on opposite sides of the molecular plane, with the chiral centers of (*R*) and (*S*) configuration, respectively. Upon intramolecular site exchange between free (green) and U^{VI} -bound (black) terminal carboxyl, the configuration of one central carbon (C_q) changes. Finally, the $CH_2COO(H)$ are *syn*, *i.e.*, on the same side of the molecular plane, with the molecule being of (*R,R*) configuration. The corresponding enantiomers, (*S,R*) and (*S,S*) respectively, are depicted below, resulting in two diastereomeric pairs of enantiomers. Enantiomers can, in general, not be distinguished spectroscopically, however, for diastereomers exhibit different physical properties they can be discriminated and, thus, give rise to distinct spectra. Upon *syn-anti* interconversion the complex geometry remains unchanged, that is, the depicted example still is B-type. Analogously, complexes of A-type geometry also reveal in total two diastereomeric pairs of enantiomers, one pair each forming the *syn* and *anti* isomers. Since the C_q in type C are not asymmetric, there is only one pair of diastereomers, however. Regardless of geometry-type, for steric constraints the *anti* isomer is in principle considered favorable. In consideration of both geome-



Scheme 3. Generic structures of U^{VI} -Cit 2:2 complex B-type geometry, configurations of the chiral carbon atoms and an exemplary configuration change upon intramolecular site exchange (green carboxyl). Note that the resulting two diastereomeric pairs of enantiomers are denoted *syn* and *anti*, and the uranyls' fifth coordination site occupied by water is left out for clarity.

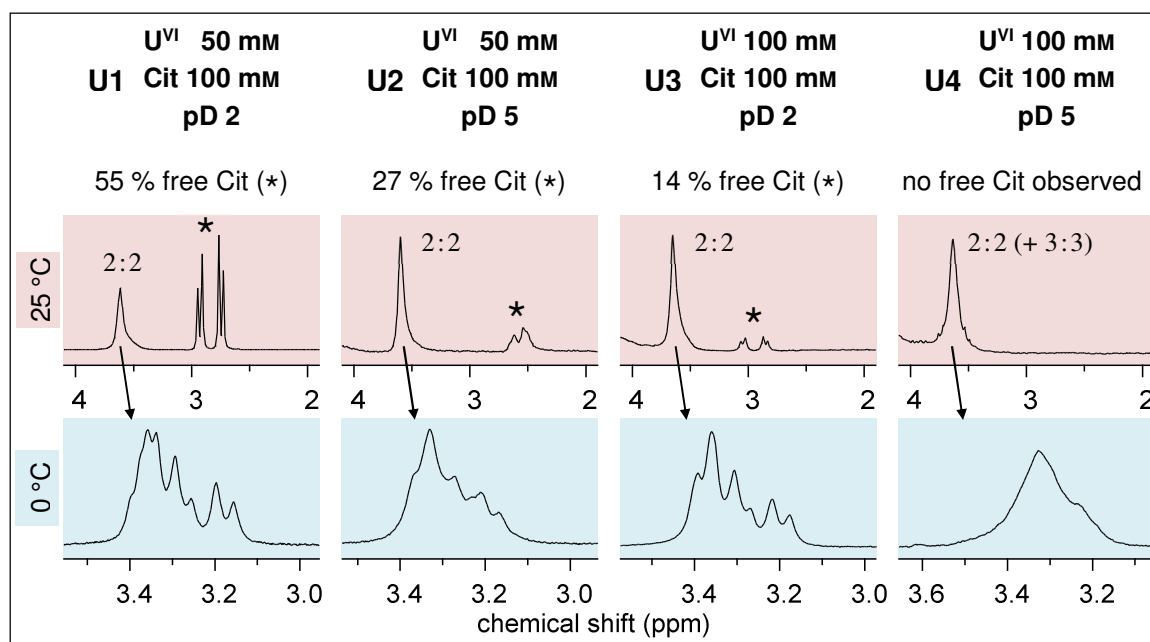
try and configuration, the DFT-calculated energies (in kJ mol^{-1}) relative to A *anti* (± 0) are as follows: A *syn* (+4), B *anti* (+11), and B *syn* (+53). Simply by these energy values, one may think that (i) A-type geometry is most likely, and (ii) both A-type configurations coexist (in equilibrium) slightly favoring the *anti* configuration. Especially when assuming an accuracy for calculated energies of $\pm 10 \text{ kJ mol}^{-1}$, the *energy difference* between both A-type isomers and at least the B-type *anti* isomer may be low, therefore allowing for interconversion. However, as sketched in Scheme 4, geometry change requires the (more or less simultaneous) cleavage (\ddagger) of both the U^{VI} -bound central and terminal carboxyl group of the same Cit molecule, a rotation about the $\mu_2\text{-O}-C_q$ bond (\odot), and formation of a five- and six-membered ring at the opposite uranium, respectively. Therefore, the *activation barrier* is considered to be very high for the interconversion between geometry-types. This implies that for sufficiently high energy supply the activation barrier may be overcome. Being aware that solution structures are not necessarily the same as in (crystalline) solids, regardless of the preparation conditions for single-crystals, *i.e.*, room-temperature ([137] and Refs. cited therein) or hydrothermal synthesis (*e.g.*, [138, 142-144]), dimeric U^{VI} -Cit complexes are without exception of B-type geometry. Notably, for hydrothermal conditions (180 °C) there are also crystal structures that reveal the 'high-energy' (B-type) *syn* configuration. A corresponding example is depicted in Fig. 36 C, for which the arrangement is facilitated by a hydrogen bonding water molecule bridging the *syn* CH_2COOH (see arrows). Otherwise, the unbound $\text{CH}_2\text{COO}(\text{H})$ residues are *anti*, for instance Fig. 36 B. Further spectroscopic evidence for both B-type isomers to be present in solution and, once more, excluding any A-type isomer, is discussed below.



Scheme 4. Changing complex geometry, exemplarily shown from A-type to B-type, upon dissociation of the U^{VI}-bound carboxyl groups, rotation of the Cit ligand about the μ₂-O-C_q bond, and re-binding of the carboxyl groups at the opposite uranyl.

The four samples U1 through U4 considered for light-irradiation (*cf.* section 3.2.2), *viz.* 100 mM Cit and either 50 or 100 mM U^{VI} for both pD 2 and pD 5, were in advance measured by ¹H and ¹³C NMR as ‘dark’ reference blanks, with Scheme 5 showing a concise summary of the ¹H spectra. Moreover, further ¹H, ¹³C, and ¹⁷O NMR reference spectra were acquired. In contrast to the GSH/GSSG samples exhibiting only averaged signals, the U^{VI}-Cit system is characterized by distinct signals for both free and U^{VI}-bound Cit. Regardless of pD or [U^{VI}], signals of free and U^{VI}-bound Cit are always well separated, allowing easy signal integration for quantification. Owing to the high stability constants, especially for the 2:2 complex, even for pD values as low as pD 2 the sample of equimolar [U^{VI}] and [Cit], U3, reveals 14% free ligand only, and for the corresponding pD 5 sample, U4, no free ligand is detected by ¹H NMR spectroscopy (*cf.* Scheme 5). In addition to the signal caused by the 2:2 complex observed in all samples, the U4 sample exhibits some small but well resolved signals attributed to the emerging 3:3 complex (*vide infra*). Unfortunately, at 25 °C the 2:2 complex’ ¹H signals overlap in an unresolved broad feature. However, upon decreasing temperature the resolution improves obviously owing to reduced dynamics. Note that the dependence of exchange rate on sample conditions is nicely revealed by signal separation at 0 °C. That is, increasing either [U^{VI}] or, particularly, pD results in a loss of signal resolution since the exchange is facilitated by the reduced competition between U^{VI} and H⁺/D⁺ for CH₂COO⁻. Additionally, the protonated free CH₂COOH residues are able to form intramolecular hydrogen bonds, hence reducing intramolecular dynamics at low pD.

Figure 38 shows a double-quantum filtered (DQF) COSY acquired at 0 °C that reveals the correlations for the two types of diastereotopic methylene groups as indicated in blue and black. Likewise shown is a deconvolution for the horizontal ¹H NMR spectrum unveil-



Scheme 5. Composition of the U^{VI} -Cit U1 – U4 samples prior to light-irradiation, the respective mole fraction of free Cit (*) at 25 °C, and the corresponding region of the ^1H NMR spectra (obtained at 9.4 T) showing the signals of free and U^{VI} -bound Cit at 25 °C (red panel) with an expansion of the U^{VI} -Cit signals upon cooling down to 0 °C (blue panel).

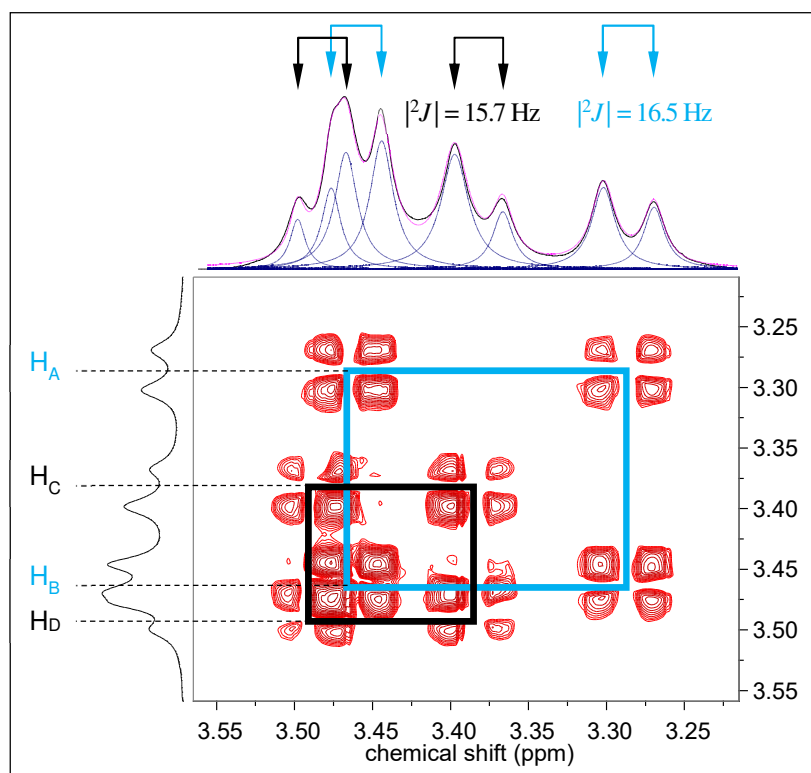


Figure 38. H,H-DQF-COSY spectrum (acquired at 11.7 T and 0 °C) of 100 mM Cit and 50 mM U^{VI} pD 2 D_2O solution, with the correlating signals indicated according to Scheme 3. The horizontal 1D- ^1H spectrum shows a signal deconvolution as well as *geminal* couplings and their corresponding values. Note: signals of citric acid (δ_{H} 2.75 and 2.55 ppm) are not shown.

ing the individual 2:2 U^{VI}-Cit complex signals. In principle, the complex signals are considerably shifted¹² downfield as compared to the unbound ligand. Regarding the complex, the signals of one methylene group show only little $\Delta\delta$ (*i.e.*, difference between respective δ_{H} values) and a smaller $|^2J|$ of 15.7 Hz, while the other shows considerable $\Delta\delta$ and a larger $|^2J|$ of 16.5 Hz. That methylene group adjacent to the free carboxyl group, CH₂COOH, potentially being able to rotate (at least for intramolecular dynamics) about the C_q-CH₂ bond, is assigned CH_CH_D, while the other, adjacent to the U^{VI}-bound carboxyl group, CH₂COOU^{VI}, is fixed within the complex chelate structure. These ¹H occupy equatorial and axial positions, the latter of which hence being more shielded, and assigned H_B and H_A, respectively (*cf.* Fig. 38 and Scheme 3).

The signals in both ¹H and ¹³C NMR top spectra shown in Fig. 39 are solely attributed to U^{VI}-bound Cit. For the given conditions, *viz.* 250 mM in both U^{VI} and Cit at pD 2.5, the 2:2 is the only complex species. Presence of mononuclear (1:1 or 1:2) species potentially being present under these pH conditions can be ruled out since in the corresponding range, 70 – 90 ppm, only one C_q-attributed signal is observed.¹³ $\Delta_{\text{U}}\delta_{\text{C}}$ of the alkoxy-bound carbon is notable 11.5 ppm, that of the central carboxylate is 8.8 ppm. Upon U^{VI} complexation the ¹³C signals of both the terminal carboxylate and the methylene groups are doubled as indicated by red arrows, however, with one corresponding set being shifted by 6.2 and 3.7 ppm, the other by 0.5 and 0.4 ppm, respectively. Accordingly, the significantly shifted signals attribute to the CH₂-COOU^{VI} residues, while the CH₂COOH residues' signals are shifted only little since the chemical environment is similar to free Cit (including intramolecular hydrogen bonds). Interestingly, the C_q-attributed signal seems rather narrow compared to the other signals, in particular those of the CH₂COO carbons. On closer inspection of the expansions in Fig. 39, a second set of minor signals can be found (see blue arrows) close to the major signals, with the former in part resolved (C_qCOO) and in part overlapping, also causing skewed and broadened signal bases. These minor signals are attributed to the less favored isomer. Already NUNES AND GIL concluded from their NMR studies¹⁴ that “the five-ring fragment formed by the terminal carboxyl group remains while the other carboxyl groups are rapidly alternating in the binding to the uranyl ion” [133]. It

¹² The ¹H chemical shift values observed for the methylene protons in Cit complexes of hexavalent uranium are larger than expected for complexation of a (diamagnetic) divalent cation and, therefore, electrostatic effects only. The additional deshielding effects are ascribed to contributions from the magnetic anisotropy of the uranium-oxygen multiple bond [145].

¹³ The signal of C_q is considered the best probe for the discrimination between monomeric, dimeric and trimeric species. Trimeric species show somewhat smaller $\Delta_{\text{U}}\delta_{\text{C}}$ than the dimeric species owing to decreased U^{VI} Lewis acidity. Especially the mononuclear species can be easily distinguished from the polynuclear species for the latter reveal the alkoxy μ_2 -O bridging between two U^{VI}, hence causing remarkable downfield shifts for C_q, while the former, if any, show much weaker interaction with the C_q-OH group.

¹⁴ On account of both equipment and conditions (1.9 T, 29 °C), and the corresponding NMR timescale and spectral resolution, observation of the *anti* isomer was simply not feasible. The conclusions regarding the dynamics drawn from their observations are still applicable, however, they did not notice or at least comment on the concomitant yield of a different isomer.

is precisely for this reason why the *syn* isomer's ^{13}C signal of the terminal carboxyl carbon (189.3 ppm, *cf.* Fig. 39) is well resolved while the other minor isomer's related signals are hardly observable upon averaging with those of the major isomer. Combining both the inert five-ring forming $\text{C}_q\text{COO}-\text{U}^{\text{VI}}$ bond and the rather labile binding in the six-ring forming $\text{CH}_2\text{COO}-\text{U}^{\text{VI}}$ bond might be a further hint to the validity of the B-type geometry. The two uranyl units in the A-type geometry constitute one inert (two five-rings) and one labile center (two six-rings), whereas for the B-type either uranyl participates in such an inert binding motif.

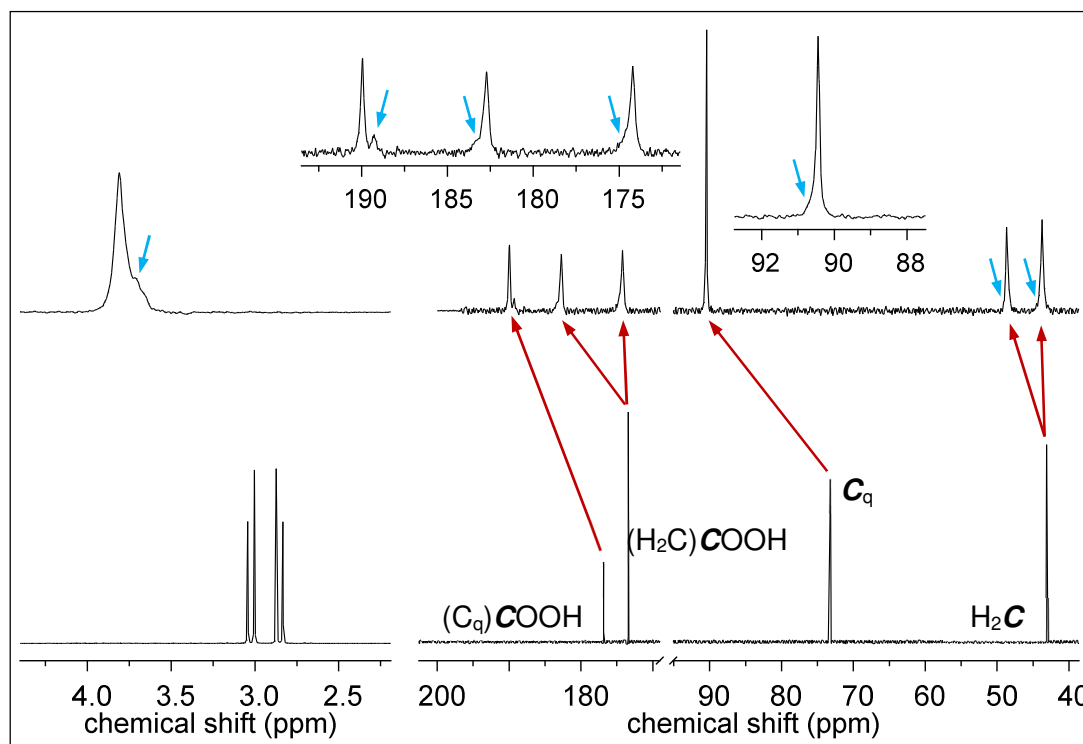


Figure 39. ^1H (left) and ^{13}C (right) NMR spectra of 250 mM citric acid pD 2.5 solutions without (bottom) and in the presence of 250 mM U^{VI} (top). The red arrows indicate signal shifts upon addition of equimolar U^{VI} , the blue arrows pointing to minor signals for better visualization.

By means of the ^1H and ^{13}C spectral appearance and the corresponding NMR time-scales, the *anti-syn* interconversion rate, k_{ex} , can be roughly estimated. Taking up the ^1H spectra in Scheme 5 and the signals' T -dependent distances, the exchange regime changes from intermediate slow (broadened but resolved signals) to intermediate fast (broad and unresolved) with increasing temperature. Hence, at 25 °C k_{ex} is assumed to be in the order of $\sim 10^2 \text{ s}^{-1}$, whereas upon cooling to 0 °C the rate slows down to $\sim 10^1 \text{ s}^{-1}$, whereby the dimension $[k_{\text{ex}}]\text{s}^{-1}$ denotes the number of displacements per second. Considering these k_{ex} as a function of T ($\Delta T = 25 \text{ K}$), the activation energy for the intramolecular site exchange (*cf.* Scheme 3) can be estimated to be approximately 60 kJ mol^{-1} for acidic conditions and in *syn* \rightarrow *anti* direction (*vide infra*). This value is reasonable taking into account, for instance, the breaking of both the $\text{CH}_2\text{COO}-\text{U}$ and the intramolecular hydrogen bonds.

In order to assign the two sets of signals to the isomers, ^{17}O NMR spectroscopy¹⁵ was exerted. First, the ^{17}O NMR of $\text{UO}_2(\text{NO}_3)_2$ blank in D_2O with natural ^{17}O abundance shown in Fig. 40 exhibits three signals, attributed to water (HDO, commonly used as reference, $\delta_{\text{O}} = 0.0$ ppm), nitrate, and the free uranyl ion. For the uranyl constitutes two formal triple bonds, $\oplus|\text{O}\equiv\text{U}\equiv\text{O}|\oplus$, the corresponding ^{17}O signal appears in the high frequency range of the spectrum. Whereas the signal of NO_3^- is rather broad ($\Delta\nu_{1/2} = 178$ Hz), the signal of UO_2^{2+} is remarkably narrow ($\Delta\nu_{1/2} = 12$ Hz), see inset in Fig. 40. These findings can be explained, on the one hand, by effective quadrupolar relaxation due to both EFG around the ^{17}O ($I = 5/2$, $Q = -2.5$ fm²) themselves and quadrupolar coupling to the neighboring nitrogen (^{14}N : $I = 1$, $Q = 2.0$ fm²) as well as some (minor) protonation-deprotonation dynamics of the nitrate ion. ^{238}U , on the other hand, has no magnetic moment at all, and the overall symmetry of the uranyl ion is higher ($D_{\infty h}$) as compared to nitrate (D_{3h}). It is noteworthy that (the only NMR-active oxygen isotope) O-17 has a natural abundance of 0.038% only. ^{17}O (solution) chemical shifts of uranyl complexes found in the literature are therefore quite rare. Those reported, however, disclose no simple correlation upon complexation by organic and inorganic ligands (*cf.* Table 4) in contrast to the systematic weakening of the $\text{U}-\text{O}_Y$ bonds (force constants) as evidenced by the UO_2 ν_1 and ν_3 bathochromic shifts in vibrational spectroscopies [125, 127, 147].

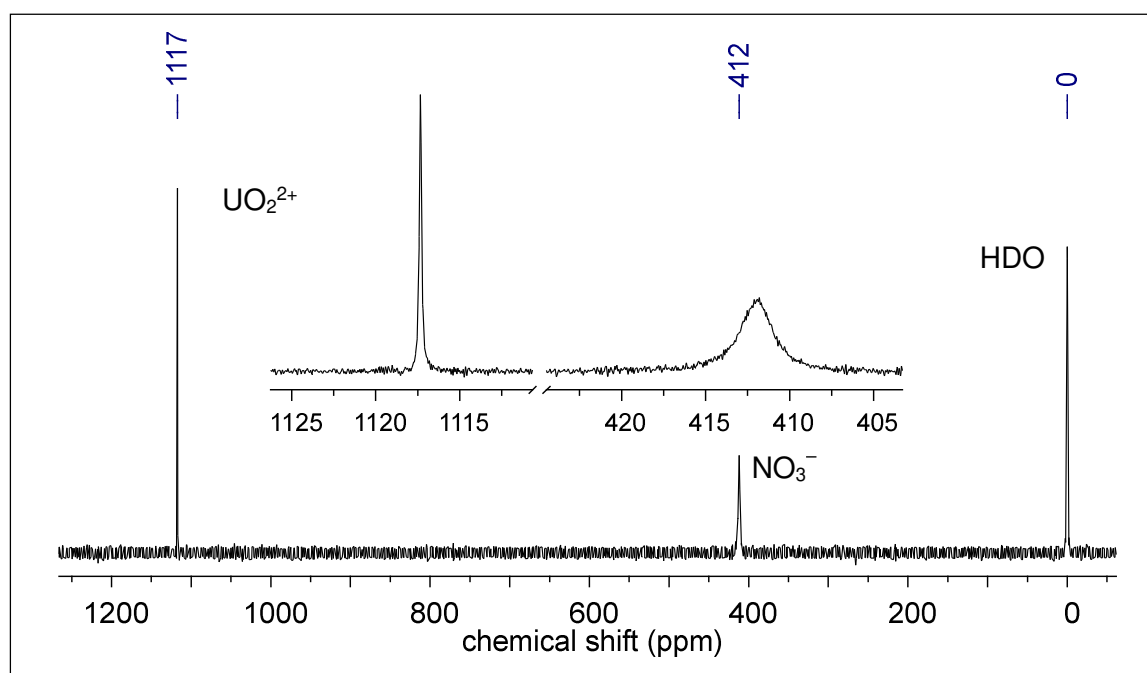


Figure 40. ^{17}O NMR of 0.5 M natural ^{17}O abundance $\text{UO}_2(\text{NO}_3)_2 \cdot 6 \text{H}_2\text{O}$ in D_2O at pD 1.

¹⁵ A quite recent review on ^{17}O NMR spectroscopy is given by CASTIGLIONE ET AL. [146].

Table 4. ^{17}O chemical shift values for various uranyl complexes.

U^{VI} complex	δ_{O} (ppm)	conditions	ref.
$\text{UO}_2(\text{D}_2\text{O})_5^{2+}$	1114 ^a	pD 2.5	this
	1117 ^a	pD 1	work
$\text{UO}_2(\text{H}_2\text{O})_5^{2+}$	1116	pH 1.5, $T = -5\text{ }^\circ\text{C}$	[148]
	1118	$-\log[\text{H}^+] = 3.15$, $I = 0.5\text{ M}$	[149]
	1121	1 M HClO_4	[150]
$(\text{UO}_2)_2(\text{OH})_2^{2+}$	1120	$-\log[\text{H}^+] = 3.71$, $I = 0.5\text{ M}$	[149]
$(\text{UO}_2)_3(\text{OH})_5^+$	1125	$-\log[\text{H}^+] = 3.71$, $I = 0.5\text{ M}$	[149]
$\text{UO}_2\text{SO}_4(\text{aq})$	1119.5	$T = -5\text{ }^\circ\text{C}$	[151]
$\text{UO}_2(\text{SO}_4)_2^{2-}$	1120.1	$T = -5\text{ }^\circ\text{C}$	[151]
$(\text{UO}_2)_p(\text{OH})_q(\text{SO}_4)_r$	1126.2	$-\log[\text{H}^+] = 5$	[151]
UO_2F^+	1121.6	pH 1.5, $T = -5\text{ }^\circ\text{C}$	[148]
$\text{UO}_2\text{F}_4^{2-}/\text{UO}_2\text{F}_5^{3-}$	1123	pH 8.8, $T = -5\text{ }^\circ\text{C}$	[152]
$\text{UO}_2(\text{CO}_3)_3^{4-}$	1098	3.5 M (TMA)OH	[147]
	1098	pH 7.9	[150]
	1099	pH 9.7–11.8	[153]
$(\text{UO}_2)_3(\text{CO}_3)_6^{6-}$	1105	pH 6	[150]
$\text{UO}_2(\text{O}_2)(\text{CO}_3)_2^{4-}$	1094	pH 9.7–11.8	[153]
$(\text{UO}_2)_2(\text{O}_2)(\text{CO}_3)_3^{6-}$	1103	pH 9.7–11.8	[153]
$(\text{UO}_A\text{O}_B)(\text{pmg})\text{F}_2^{3-}$ ^{b,c}	A 1121.3, B 1127.4	pH 8.8, $T = -5\text{ }^\circ\text{C}$	[152]
$(\text{UO}_A\text{O}_B)(\text{pmg})_2\text{HF}^{4-}$	A 1120.8, B 1126.8	pH 8.8, $T = -5\text{ }^\circ\text{C}$	[152]
$(\text{UO}_A\text{O}_B)_3(\text{AMP})_3^{8-}$ ^d	A 1112 ^e , B 1126 ^e	pH 10.58	[124]
<i>syn</i> - $(\text{UO}_A\text{O}_B)_2(\text{DCit})_2^{2-}$	A 1120, B 1136	pD 2.5	this
<i>anti</i> - $(\text{UO}_{A1}\text{O}_{B1})(\text{UO}_{A2}\text{O}_{B2})(\text{DCit})_2^{2-}$	A1 1122, B1 1124 A2 1127, B2 1143	pD 2.5	work

^a Uranyl aquo ion observed chemical shift differences are ascribed to both signal referencing relative to residual HDO in deuterated water instead of pure (or 90%) $^1\text{H}_2\text{O}$ and the high overall uranyl concentrations since acquisition performed at natural ^{17}O abundance; ^b non-equivalence of the oxygen atoms within the same uranyl unit hence denoted A and B; ^c *N*-(phosphonomethyl)glycine, glyphosate, $\text{HOOCCH}_2\text{NHCH}_2\text{PO}_3\text{H}_2$; ^d adenosine-monophosphate, “Complex-II”; ^e read-out from literature spectrum

The ^{17}O NMR spectrum of 250 mM in each U^{VI} and Cit at pD 2.5 is depicted in Fig. 41. Since both ^1H and ^{13}C NMR reveal no free Cit (*cf.* Fig. 39), and all the U^{VI} -bound Cit is considered to constitute complexes of $\text{U}^{\text{VI}}/\text{Cit} = 1$, only little free UO_2^{2+} is present in the sample ($\delta_{\text{O}} = 1114$ ppm). There is again a set of two major and a set of four minor signals (see also Table 5). With the aid of DFT-calculated structures and δ_{O} values the set of major signals can unambiguously attributed to the *syn* isomer, and those of the minor signals to the *anti* isomer. Basically, the B-type geometry renders the *anti* and *syn* isomers to be of C_i and C_2 symmetry, respectively. Thus, with the unbound CH_2COO residues being on opposite sides and the center of inversion in the middle of the molecular plane all corresponding atoms are equivalent, the *anti* isomer should give rise to one ^{17}O signal only. Accordingly, the *syn* isomer with a C_2 rotational axis and the unbound CH_2COO residues being on one side of the molecular plane, the respective uranyl oxygen atoms on each side (either *trans* or *cis* to that residue) generate a separate ^{17}O signal, hence two signals overall and therefore best described by and denoted as $\text{O}_A=\text{U}=\text{O}_B$, consequently attributed to the two major 1:1 signals, *cf.* Fig. 41 and Table 4.

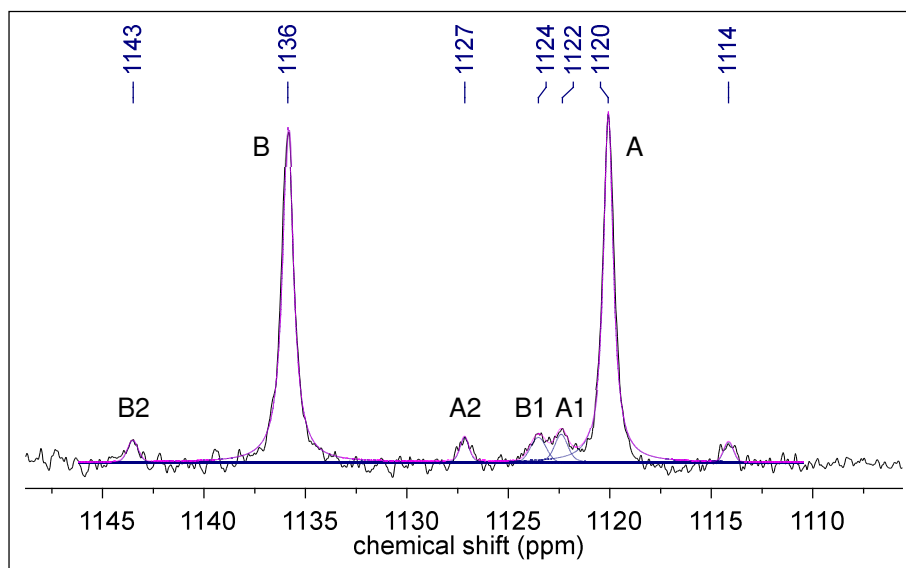


Figure 41. ^{17}O NMR uranyl region of natural ^{17}O abundance uranyl nitrate and citric acid, both 250 mM, in D_2O at pD 2.5, together with spectral deconvolution.

The DFT-computed 2:2 *anti* isomer solution structure reveals the molecule to be distorted in such a way, that the overall symmetry is reduced to C_1 (*cf.* Fig. 42). Consequently, the four uranyl oxygen atoms become nonequivalent and therefore generate distinct resonances, corresponding to the four minor signals observed. Although DFT calculation overestimates the δ_{O} values by 15–32 ppm, they are in very good agreement in terms of relative chemical shift differences found by experiment (Table 5). Regarding the DFT-calculated structure, that uranyl unit being part of the twisted six-membered ring fragment, U2 in Fig. 42 C1/2, shows reduced linearity (171.1°) and considerable deviation of coplanar equatorial ligand coordination. The corresponding uranyl oxygen atoms exhibit the two largest chemical shift values calculated, whereas the oxygen atoms of the other uranyl unit showing equatorial coplanarity reveal both the smallest and the most similar δ_{O} values.

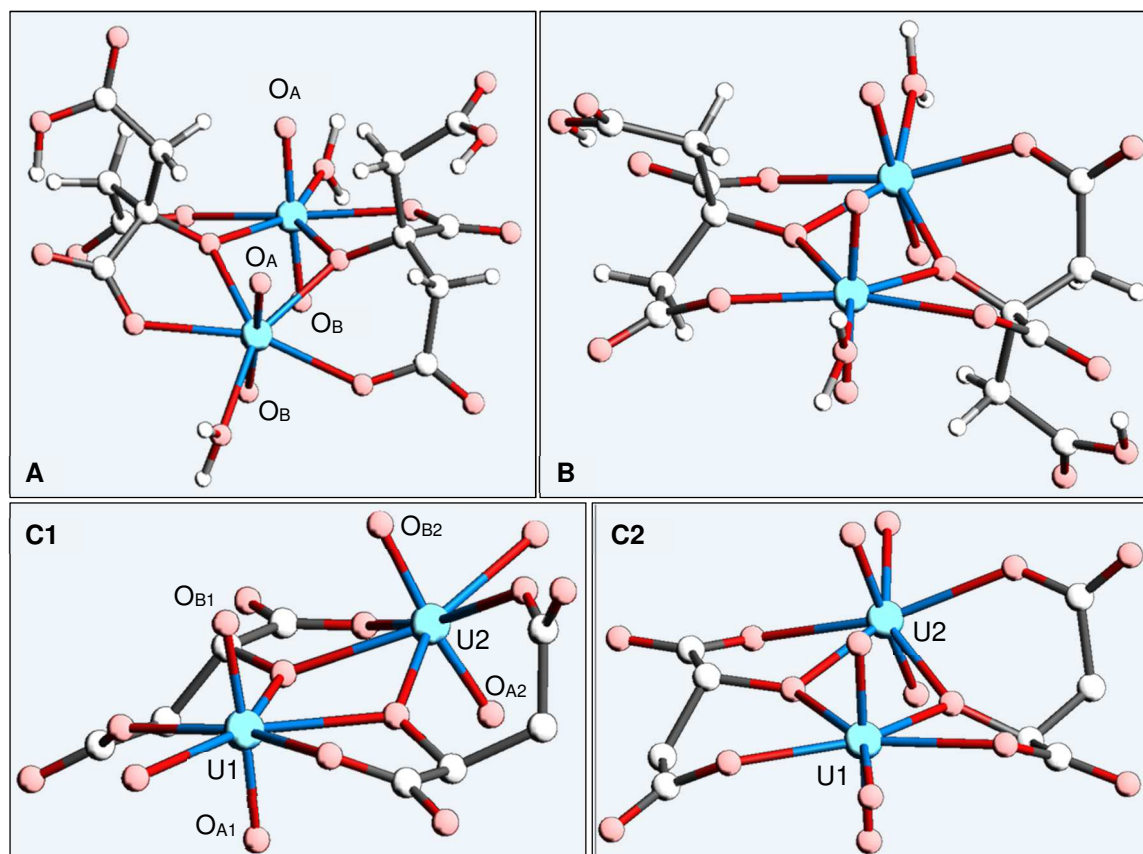


Figure 42. DFT-calculated structures of U^{VI} -Cit 2:2 complex *syn* isomer (A) and *anti* isomer (B). C1/2 depict the *anti* complex basic structure with hydrogen atoms and unbound CH_2COOH moieties omitted for clarity, highlighting structural peculiarities. Note the uranyl oxygen atom labeling corresponds to ^{17}O NMR signal assignment in Fig. 41 and Table 4.

Table 5. ^{17}O chemical shift values (in ppm) obtained from DFT calculation and experiment.

site	<i>syn</i>		<i>anti</i>			
	A	B	A1	B1	A2	B2
observed	1120	1136	1122	1124	1127	1143
calculated	1135	1157	1142	1143	1159	1168

The number of ^{17}O resonances is, first and foremost, determined by molecular symmetry, *i.e.*, of the molecule as a whole and, apparently, of the local uranyl environment as well. Observed chemical shift values are in fact impacted not only by bond-mediated effects but also additional through-space contributions from the ligands, in solution also including hydration shell related interaction ($U=O \cdots H_2O$).

SZABO ET AL. [124] investigated uranyl complexation by nucleotides and observed ^{17}O NMR resonances occurring in pairs. The authors attributed the ^{17}O chemical shift differences between uranyl oxygen atoms ($\Delta\delta_O$), at least 14 ppm in case of adenosine-monophosphate (AMP), to distances of 3.96(5) and 4.97(5) Å, respectively, to the non-bonding oxygen atoms in the nucleotide's monophosphate group, as determined from crystallo-

graphic data [124]. Furthermore, in a preceding study on U^{VI}-glyphosate complexes SZABO already observed 6 ppm $\Delta\delta_{\text{O}}$ with one of the glyphosate's phosphonate oxygens suspected to cause an analogous effect [152]. In the first place the observation of two resonances per uranyl unit ($\text{O}_A=\text{U}=\text{O}_B$) can be explained simply by symmetry, each set of uranyl oxygens being either *cis* or *trans* to the nucleotides, hence sensing different chemical environments and thus becoming nonequivalent. Although the principal arguments of SZABO and coworkers are comprehensible, the spatial distance of 3.96 Å for the respective (phosphate) oxygen atoms seems quite large to cause the observed effect. Furthermore, the U^{VI}-Cit dimeric *syn* isomer shows analogous spectral effects, *viz.* $\Delta\delta(\text{O}_A,\text{O}_B) = 16$ ppm, but the structures (regardless of geometry-type and isomer) are lacking comparable (carboxyl) oxygen atoms in distance < 4.5 Å. Instead, as an alternative explanatory approach, we suggest the methylene group hydrogens of the *cis* CH₂COO(H/D) moieties to be responsible for the observed chemical shift differences between O_A and O_B. Particularly since these unbound moieties are quite fixed within the molecular structure because of the intramolecular hydrogen bonds, the U=O···HC distances are considered to fluctuate only little (hindered rotation about the C_q-CH₂ bond) in accordance with the comparatively small ¹⁷O NMR linewidths ($\Delta\nu_{1/2}$) < 50 Hz. U=O···HC(*cis*) distances are calculated as 2.49–2.97 Å for the B-type *syn* isomer, and to be about 2.41–2.67 Å for the *anti* isomer. Apparently, the *cis* *yl*-oxygen atoms are shielded by a through-space interaction, with the magnitude of the effect potentially depending on both number of and distance between the respective *cis* *yl*-oxygen and methylene hydrogen atoms. Consequently, the additional through-space effects increase the distinction between observed δ_{O} , however, the latter are not determined by these interactions only, the more they are a sum of contributions from the overall chemical environment. For example, the *anti* isomer's disparity in O_{A1}=U=O_{B1} resonances (*cf.* Fig. 42) are primarily due to the distorted coordination geometry around the uranyl entity and, to some extent, enhanced by additional contribution from methylene hydrogens. At this state of knowledge one can only speculate on the nature of the through-space interaction. Dipolar (¹⁷O-¹H) interaction would preferably impact the relaxation rate instead of chemical shift. Consequently the effect is supposed to be caused diamagnetic shielding from the nearby hydrogen atoms' electron density. Perhaps, the remaining uranyl oxygen lone pair interacts with the spatially close hydrogen atoms' anti-bonding σ^* -orbital, hence being affected by number and geometry, *i.e.*, distance and orientation, thus being most effective when pointing mutually to one another in short distance.

Against the backdrop of the U=O···HC distances, the U^{VI}-AMP complex of SZABO ET AL. [124] was considered to test the hypothesis. The nucleoside's 4' and one of the 5' hydrogen atoms exhibit a short spatial distance to one (sort of) uranyl oxygen(s), *i.e.*, O_A. For the AMP 3:3 "Complex-II" the corresponding distances were obtained from the crystal structure (CCDC deposition no. 291668). In fact, each uranyl oxygen atom in the respective *cis* position (O_A) shows one short 2.51(5) Å and one larger 2.86(5) Å distance to one H-5' and one H-4', respectively, as illustrated in Fig. 43, while the oxygen atoms on the opposite side (O_B) are lacking such 'contacts', according to δ_{O} of 1112 and 1126 ppm, respectively (see also Table 4) [124].

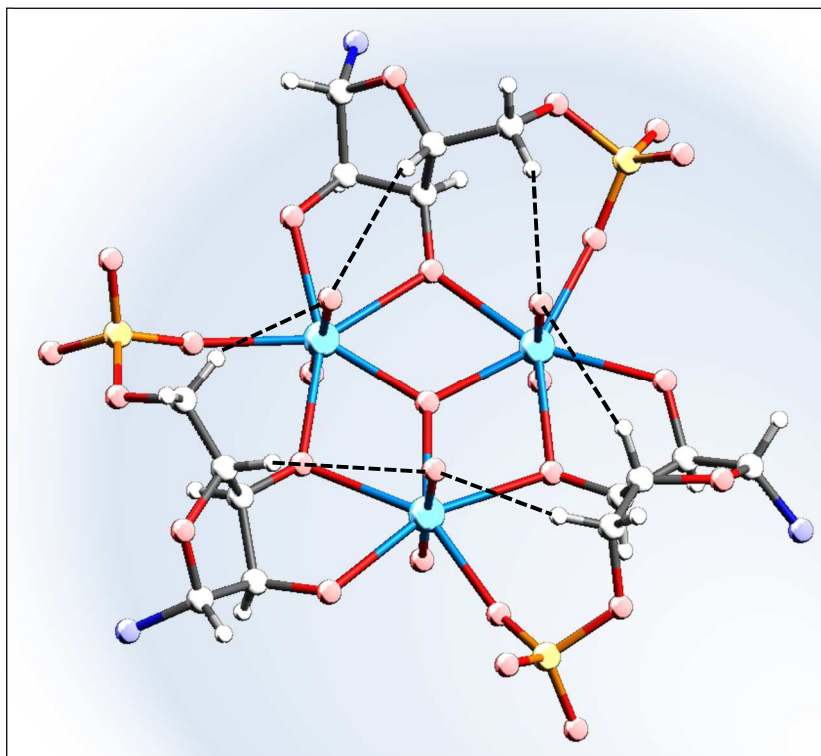


Figure 43. Visualization of close spatial proximity between one of the oxygen atoms in each of the uranyl entities and specific hydrogen atoms shown for uranyl-adenosine-monophosphate complex (according to [124], taken from CCDC deposition no. 291668; note that the adenine parts are left out for clarity).

3.2.1.2 Uranyl–Citrate Trimers

On account of the U^{VI} –Cit 3:3 complex structures obtained from aqueous solution by means of EXAFS [136] and single-crystal X-ray diffraction [137] (see Fig. 36 D and E, respectively), interpretation of the NMR spectra is rather straightforward. Nonetheless, NMR spectroscopy allows important insights into both complex structures from the ligand's perspective and, especially, solution dynamics.

For the applied conditions, *viz.* pD 7.5 and equimolar U^{VI} and Cit concentrations, trinuclear species predominate in solution [130]: the 3:3 complex and a 9:6 macrocycle [137] together with its 3:2 sub-unit (*cf.* Fig. 44). In this regard, it is conceivable that there is also a 6:4 sub-unit involved as the 9:6 species is unlikely to form trimolecularly. Since as of circumneutral pH conditions complexes of not only 1:1 but also 1.5:1 U:Cit stoichiometry are formed, the sample solutions show free Cit present in solution (indicated by * in the following spectra), with mole fractions of 11.7%, 29.8%, and 58.5% of $[Cit]_{tot}$ for free Cit, 3:3, and 3:2 (including 6:4 and 9:6) complexes, respectively, obtained from signal integration.

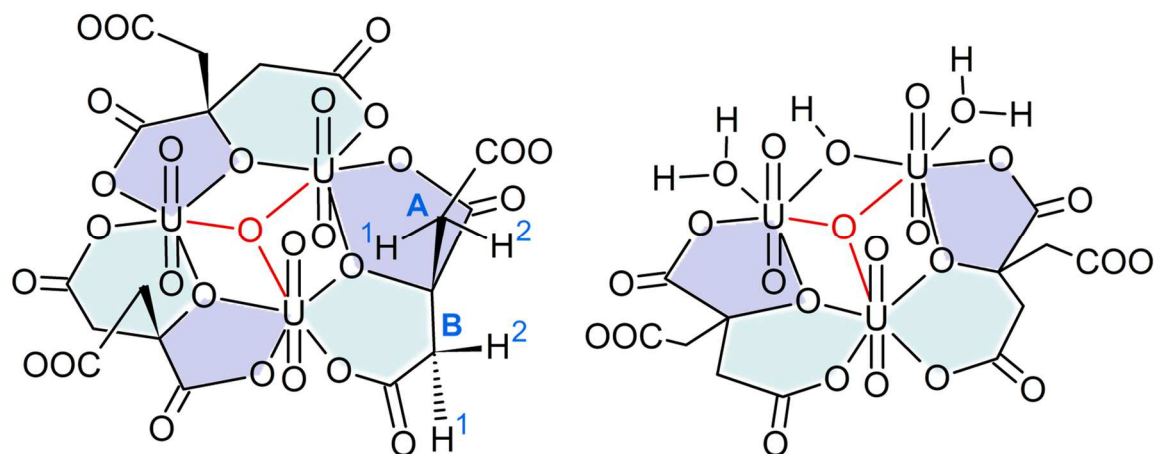


Figure 44. Generic structures of U^{VI} -Cit 3:3 complex (left) and 3:2 sub-unit of 9:6 complex (right) according to [137], highlighting sites of interest.

Accordingly, the broad signals observed in both 1H and ^{13}C spectra (indicated ∇ , see 1D spectra in Figs. 45 and 46, below) pertain to the 3:2 complexes and are due to both inter- and intramolecular dynamics. The former covers the build-up and break-down reaction equilibrium between the macrocyclic complex and its sub-units while the latter refers to the site exchange of the CH_2COO^- as described already. Being completely ionized at pD 7.5 ($pK_{a3} = 6.4$ [54]) and, thus, showing no competition between U^{VI} and H^+/D^+ for COO binding, intramolecular site exchange is easily facilitated and again yields different isomers. Therefore, particularly the signals of the terminal carboxylate carbons are very broad (*cf.* Fig. 45, green ^{13}C expansion with $lb = 15$ Hz applied). Considering the spectral appearance and the frequency differences of the terminal carboxylate carbons (using the well-resolved signals as indicators) the apparent exchange rate is notably larger as for the (pD 2.5) 2:2 complex, estimated to be in the order of $\sim 10^3$ s^{-1} . Consequently, discrimination between corresponding isomers is not feasible.

The symmetric 3:3 complex (Fig. 44, left) is characterized by a bridging μ_3-O and three bridging μ_2-O-C_q , and attributes to the, in contrast, well-resolved signals. Interestingly, unlike the 2:2 and the 3:2 U^{VI} -Cit complexes, the 3:3 complex possesses no coordinating water molecules¹⁶ for the coordination of the uranyl entities is saturated by the Cit ligands.

The H,C-heteronuclear multiple-bond correlation (HMBC) spectrum in Fig. 45 exhibits $^1J_{C,H}$ correlations breaking through (indicated by double-headed arrows; ≈ 125 Hz), which is regarded advantageous in this case, providing information on C-H connectivity. Therefore, the methylene 1H signals (A1, A2) and (B1, B2) can be correlated to the two (sharp) CH_2 signals, correspondingly denoted A and B, with $\Delta_{U\delta_C}$ of 1.2 and 3.3 ppm, respectively. In comparison to the $\Delta_{U\delta_C}$ values observed for the (pD 2.5) 2:2 complex, 0.4 and 3.7 ppm respectively, the methylene carbons in the U^{VI} -bound moieties are quite simi-

¹⁶ This fact will be of importance in section 3.2.2 since U^{VI} -coordinating water appears to be a prerequisite for the photo-induced reaction in the U^{VI} -Cit system.

lar, whereas the 3:3 complex' free moieties' signal is somewhat stronger shifted. The central carbon C_q shows correlations to both pairs of methylene 1H , whereas that to B2 is very weak and $\Delta U\delta_C$ amounts to 8.9 ppm, which is significantly smaller compared to the 2:2 value of 11.5 ppm.

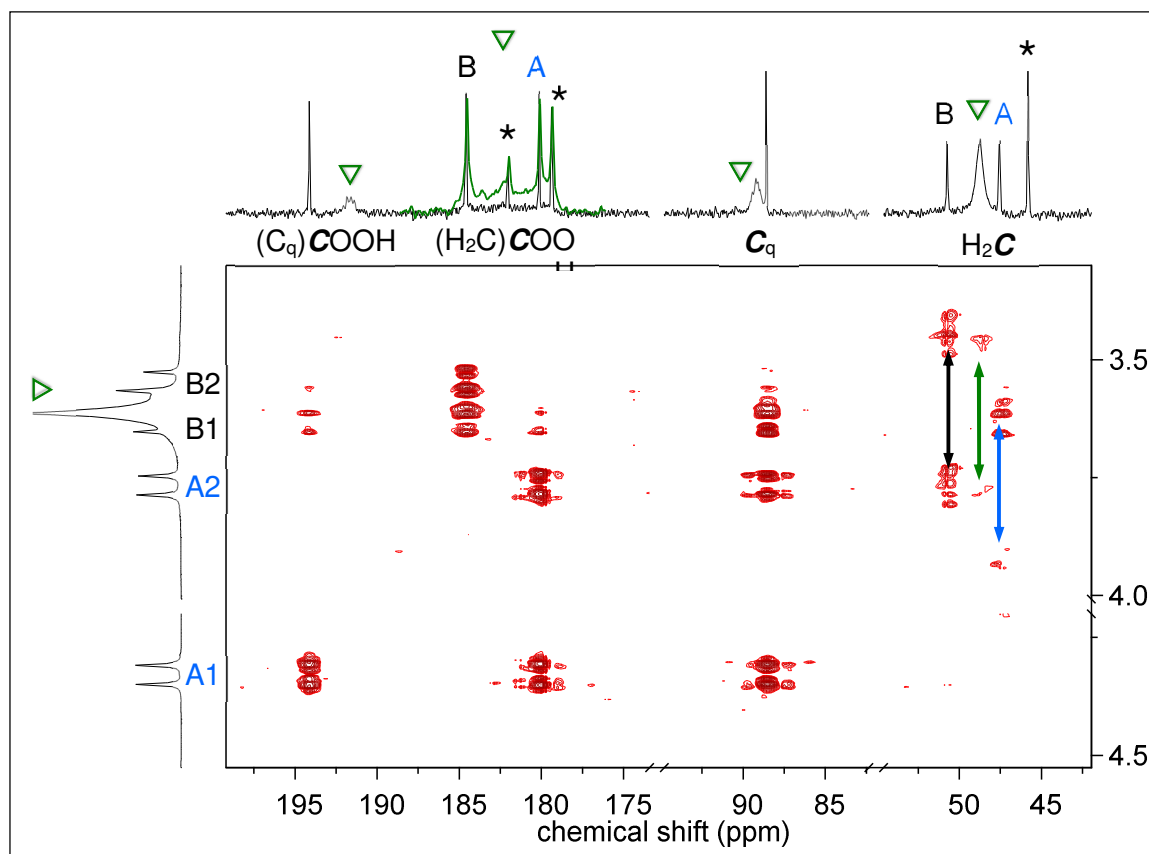


Figure 45. H,C-HMBC (transposed; 6 Hz opted for $^nJ_{C,H}$) of 250 mM U^{VI} and 250 mM Cit at pD 7.5. 1H and ^{13}C 1D-spectra used as projections, with an expansion with $lb = 15$ Hz (green). Note the double-headed arrows indicate $^1J_{C,H}$ correlations breaking through, free Cit is indicated by $*$.

As already stated earlier and in association with the bathochromic shift of $UO_2 v_1$ and v_3 upon changing speciation from dimeric to trimeric U^{VI} -Cit complexes [135, 137, 141] the decreasing U^{VI} LEWIS acidity results in smaller $\Delta U\delta_C$. Owing to the μ_3-O , the 3:3 complex is tightened in its radial dimension, whereupon in the single-crystal structures the $\mu_2-O \cdots \mu_2-O$ and $U \cdots U$ distances shorten from 2.711 to 2.591 Å and 3.890 to 3.758 Å, respectively, when going from 2:2 to 3:3 complex, and the latter showing a $\mu_3-O \cdots U$ distance of 2.24 Å [137]. EXAFS fits of the aqueous solution structures revealed the $U \cdots U$ distances to shorten from 3.90 to 3.80 Å, and the $\mu_3-O \cdots U$ distance to be 2.20 Å [136]. Thus, upon this compression, increasing orbital interactions may also contribute to shielding effects.

$\Delta U\delta_C$ amounts to 8.1 ppm for the central carboxyl ^{13}C , similar to 8.8 ppm in the 2:2 complex, and $^3J_{C,H}$ correlations could be detected to A1 and A2, but B1 only. Based on the $^2J_{C,H}$ correlations between A1/A2 and that terminal carboxylate showing the smaller $\Delta U\delta_C$,

viz. 0.5 ppm, the corresponding ^{13}C signal is denoted A, while the B1/B2 ^1H signals show $^2J_{\text{C,H}}$ correlations to the other carboxylate ^{13}C signal, B, which reveals a larger $\Delta_U\delta_{\text{C}}$ of 3.5 ppm.¹⁷ This value is rather small compared to the 6.2 ppm observed for the corresponding 2:2 complex signal. Compared to the three other methylene ^1H signals, δ_{H} of A1 is much different and remarkably larger although the adjacent carboxylate unambiguously indicates this moiety to be unbound.

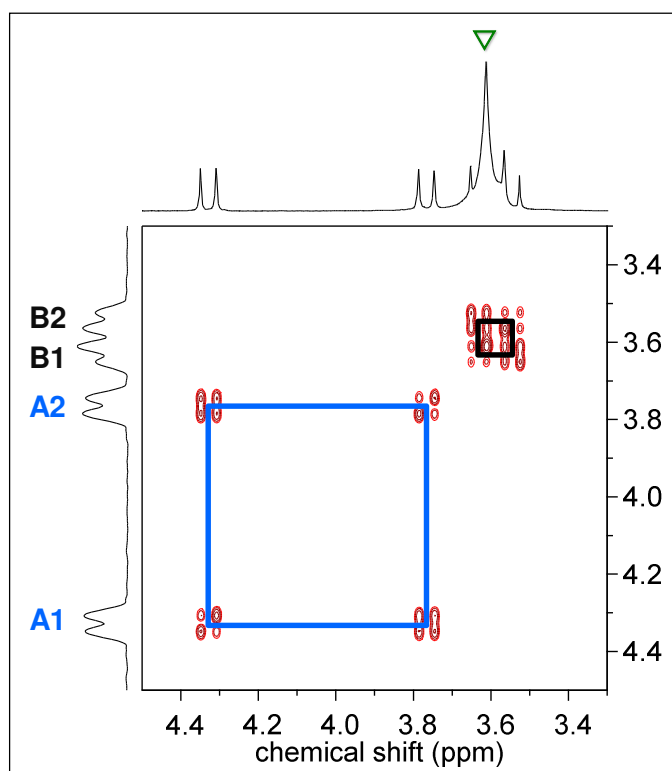


Figure 46. H,H-COSY of 250 mM in each U^{VI} and Cit at pD 7.5, with the internal projection applied vertically, the 1D- ^1H spectrum used horizontally, and signals of free Cit not shown.

At room temperature the ^1H NMR signals of the 3:3 complex are well-resolved in contrast to the unresolved, exchange-averaged 2:2 complex attributed signals for pD 2 and 5 (Scheme 5) and pD 2.5 (Fig. 39 top left). There are again two pairs of methylene ^1H correlations (Fig. 46). One of them, denoted A1/A2 ($|^2J| = 16.1$ Hz, blue), exhibits a ‘large diastereotopicity’ $\Delta\delta_{\text{H}}$ of 0.56 ppm, indicative of notable differences in chemical environment. The other methylene proton pair, B1/B2 ($|^2J|$ of 15.8 Hz, black), shows a much smaller $\Delta\delta_{\text{H}}$ value of 0.09 ppm.

Apparently, the three unbound CH_2COO moieties do not undergo site exchange since all ^{13}C $\Delta\nu_{1/2}$ are notably small, *viz.* 0.8, 0.4, and 0.5 Hz, for both terminal and central COO,

¹⁷ The missing observation of some $J_{\text{C,H}}$ couplings is due to mismatch between the magnitude of the coupling constant and the value of 6 Hz as opted for $1/(2J)$ coupling evolution time. Owing to the arrangement of the moieties, the couplings attributed to sites with torsion angles close to 90° are very small. Therefore, the *transoid* $^3J_{\text{C,H}}$ are larger and, thus, closer to 6 Hz, whereas the *cisoid* ones are significantly smaller. In addition, $^3J_{\text{C,H}}$ are in principle larger than $^2J_{\text{C,H}}$.

CH₂, and C_q, respectively. Therefore, the ligands themselves are considered inert in terms of intramolecular site exchange, although the CH₂COO^{VI} binding fashion is similar to the 2:2 complex and the higher pD enables easier (*i.e.*, faster) exchange as for pD 2.5. For the unbound CH₂COO⁻ moieties are ionized at pD 7.5, instead of intramolecular hydrogen bonding as for low pD, on the one hand electrostatic repulsion between carboxylate and (*cis*) uranyl oxygens may be the reason for hindered rotation about the C_q-CH₂ bond. On the other hand, with reference to the single-crystal structure that the “trimeric species interacts with a Na⁺ cation [...] to form a sandwich complex with a U:Cit ratio of 6:6” [137] (*cf.* Fig. A36, Appendix), and since this species is highly charged, an analogous solution structure is conceivable. Given this particular arrangement, the intramolecular CH₂COO⁻ site exchange is precluded, concomitantly preventing the interconversion between different stereoisomers, with the only isomer being the all-*syn* configuration (*cf.* Fig. 44, left). Further clue to this structure is the remarkable downfield shift of H(A1), already NUNES AND GIL [133] took notice of.¹⁸ Not only that no isomerization takes place, but also this unbound residue must somehow been kept in a well-defined, say rigid, conformation. That is, little to no rotation about the C_q-(A)CH₂ bond takes place, whereupon H(A1) is steadily sensing a remarkably different chemical environment. The latter fact is not surprising against the backdrop of being a diastereotopic methylene hydrogen adjacent to the chiral center in a rigid conformation complex molecule. Remarkably, upon increasing the temperature up to 65 °C (despite some *T*-induced chemical shift changes, *viz.* 10 ppb/K) the 3:3 complex attributed signals show no alteration, not even broadening or averaging (*cf.* Fig. A37, Appendix), further corroborating the fixed conformation within the all-*syn* configuration.

Observation of only one isomer, *viz.* all-*syn*, does not exclude the (theoretical) existence of other configurations. Thus, any pair of ordered triples of enantiomeric forms is conceivable: (*R,R,R*)/(*S,S,S*) as well as (*R,R,S*)/(*S,S,R*), (*R,S,R*)/(*S,R,S*), and (*S,R,R*)/(*R,S,S*), among which the latter six configurations constitute the (only) other diastereomeric form of the 3:3 complex, however, being not observed in solution (this work) and neither in the crystal [137]. Still, the all-*syn* configuration appears as two (spectroscopically indistinguishable) enantiomeric forms, say all-*R* and all-*S*, which behave like mirror images. The concomitant opposite overall arrangement of alternating five- and six-membered rings (as for 2:2 complex B-type geometry) can be seen upon comparison between the crystal structure in Fig. 36 E and the generic structure in Fig. 44 (left), when starting for a given uranyl unit and going clockwise, for instance. Unfortunately, the authors did not comment on whether the obtained single-crystals are enantiopure.

¹⁸ However, since their proposed structure was erroneous – 3:2 stoichiometry, μ_3 -O, and one uranyl perpendicular to the other two – they misinterpreted the origin of the observed spectral effects. Consequently they concluded that the particular proton must occupy a “special position with respect to the magnetic anisotropy and electric field effects of the uranyl groups” [133].

3.2.2 Photoinduced Reactions in the Uranium–Citrate System

3.2.2.1 State of knowledge

As early as 1953 HEIDT AND MOON [22] reported on the reaction between photo-activated U^{VI} and sucrose and closely related substances, evidencing U^V as an intermediate in aqueous solution. General reviews on the photochemistry of the uranyl ion are provided by, *e.g.*, BURROWS AND KEMP [23] as well as YUSOV AND SHILOV [24], and, more recently, NATRAJAN [154]. The U^{VI} sensitized photo-decomposition of malonic, succinic, and glutaric acids investigated by HECKLER ET AL. [155] between pH 0.5 and 3.0 yields CO_2 and the corresponding remainder after decarboxylation, *i.e.*, acetic acid, 2,3-dihydroxybutanoic acid, and butanoic acid, respectively, as decomposition products, thereby stating that the reaction rate increased with increasing pH. ADAMS AND SMITH [156] showed the complete (partial) U^{VI} reduction to U^{IV} in absence (presence) of oxygen in solution whereas the reverse reaction, that is U^{IV} –Cit oxidation, is observed to be faster upon light-irradiation than by molecular oxygen.

In 1974 OHYOSHI AND UENO [157] conducted an extensive study on the photochemical reduction of U^{VI} in citric acid solution. Oxidation of citrate is found to yield CO_2 , acetone and an unidentified ketocarboxylic acid intermediate, and the rate to be highest at pH \approx 3.0 – 4.0, assigned to an effective intramolecular energy transfer at this pH, and decreasing above pH 4.5, attributed to an energy transfer hindrance due to hydrolyzed species or polynuclear U^{VI} –Cit complexes. Moreover, an absorption peak observed at about 1460 nm is ascribed to intermediate U^V . The reaction is assumed to proceed by oxidation of U^{VI} –bound citrate within the complex, *i.e.*, *intramolecularly*, with its rate also depending on concentrations of both U^{VI} and Cit. However, the latter fact does not conclusively prove the nature of the mechanism to be *intra-* or *intermolecular*. In fact, as found by STEUDTNER [158], for excessive U^{VI} no photoreaction takes place at all since all Cit is complexing, therefore concluding that free Cit is required to facilitate *intermolecular* photoreaction.

In a 1994 paper, DODGE AND FRANCIS [159] report on photo-degradation of the U^{VI} –Cit complex as well, extended by pH-dependent studies under both aerobic and anaerobic conditions, and identification of the degradation products by HPLC–UV-Vis and, after derivatization to the corresponding methyl esters, by GC–MS. Among them, acetic, acetoacetic, β -ketoglutaric, and malonic acids as well as acetone were identified. It is stated that at pH 6.0 the U^{VI} –Cit 2:2 complex is degraded to the 1:1 complex, yielding U^V *via intramolecular* one-electron transfer from U-bound Cit to U^{VI} , β -ketoglutaric acid, and carbon dioxide. Then U^V disproportionates, and β -ketoglutarate is further oxidized to acetate upon U^{VI} photo-irradiation. At pH 3.5 the protonated 2:2 complex is degraded to the 1:1 complex, acetoacetic acid, and carbon dioxide, with direct reduction of U^{VI} to U^{IV} by a two-electron transfer mechanism. The acetoacetic acid undergoes further degradation to acetic acid, carbon dioxide, minor amounts of acetone (due to an intramolecular rearrangement of acetoacetic acid), malonic acid, and other unidentified products. Although providing some

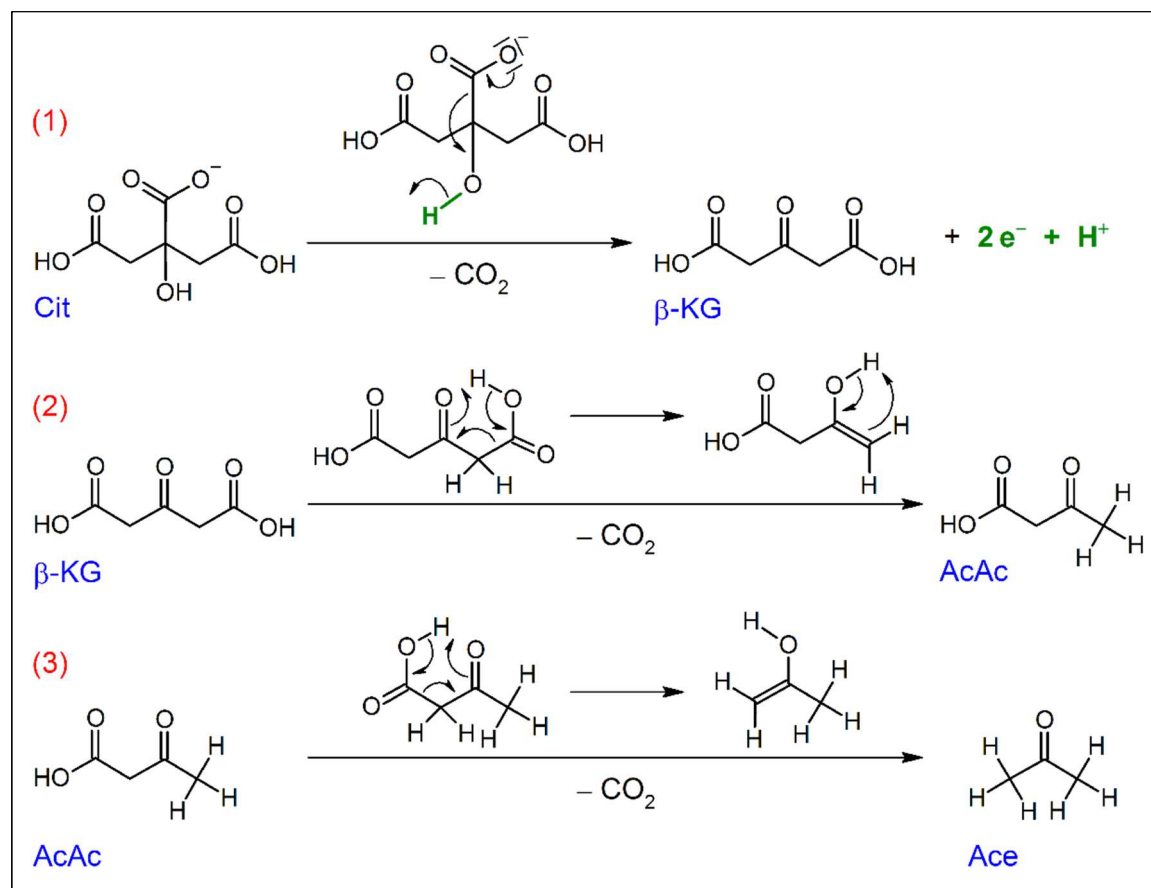
chemical reactions based on their observations, the authors owe an explanation on how, *i.e.* mechanistically, acetic and malonic acid have been formed. Moreover, initially obtained U^{IV} is, because of the presence of oxygen, re-oxidized to U^{VI} and precipitated as $UO_3 \cdot 2H_2O$. On the contrary, under anaerobic conditions the U^{VI} -Cit complex is only partially degraded and U present as U^{IV} . In principle, excessive Cit retards U precipitation.

R. STEUDTNER investigated in his doctoral thesis [158] the interaction of U^{VI} with citric acid by means of TRLFS and UV-Vis spectrophotometry, among which also the photochemical reduction of U^{VI} by citric acid was intensively studied. Based on these findings in general, and the already achieved quite sound understanding from uranium's perspective in particular, the present work covers continued studies on the photo-induced reactions in the U^{VI} -Cit system. The focus is on gaining complementary information, *i.e.*, investigating spectroscopically the system from the ligand's perspective.

So far, most investigations performed are black-box experiments presenting final products and therefrom proposed reaction pathways. However, in order to observe and comprehend the molecular alterations, *i.e.*, Cit degradation *in situ*, particularly one- and two-dimensional NMR spectroscopy was applied to answer remaining crucial questions and clarify discrepancies, supported by quantum chemical calculation, EXAFS and UV-Vis spectroscopy. Following (partial) deuteration of the intermediates *in statu nascendi*, the latter are unambiguously identified by their corresponding NMR signals characteristic for distinct (H/D) isotopomers, providing mechanistic traceability of U^{VI} -Cit complex degradation. Prior to discussing the spectroscopic results, a proposed reaction mechanism and its evaluation by means of DFT calculation is presented.

3.2.2.2 Proposed and DFT-calculated reaction mechanism

On the basis of both indications from literature and chemical reasoning a conceivable reaction mechanism is proposed as illustrated in Scheme 6. An important mechanistic reaction step is decarboxylation of the *terminal* carboxylate groups *via* a six-membered transition state, as is a typical reaction found for β -keto acids. The initial step (1) is a decarboxylation which, however, does not occur *via* a six-membered transition state since involving the *central* carboxylate, whereupon carbon dioxide, (formally) a hydrogen ion and two electrons are released, thereby yielding β -ketoglutarate (β -KG). Further decarboxylation steps then produce acetylacetonate (AcAc) and acetone (Ace). Notably, the only U^{VI} -reduction facilitating reaction step is (1), while the subsequent degradation steps are carbon-related redox reactions. That is, the carboxyl carbons are oxidized to carbon dioxide and the methylene carbons are reduced to methyl carbons, with respectively changing oxidation states $+III \rightarrow +IV$ and $-II \rightarrow -III$.



Scheme 6. Proposed reaction mechanism for the decomposition of citric acid (Cit) upon light-irradiation. The (intermediate) molecules are abbreviated as follows: β -ketoglutarate (β -KG), acetoacetate (AcAc), and acetone (Ace).

Results shown in the following were achieved in co-operation with Prof. Dr. Satoru Tsushima, Institute of Resource Ecology, Helmholtz-Zentrum Dresden-Rossendorf.

Quantum chemical calculations on DFT level were performed using the Gaussian 09 program [160] employing the DFT method with BECKE's three-parameter hybrid functional [161] and LEE-YANG-PARR's gradient corrected correlation functional (B3LYP) [162] through the use of the conductor-like polarizable continuum model (CPCM) [163-164]. The energy-consistent small-core effective core potential (ECP) and the corresponding basis set suggested by DOLG ET AL. [165] were used for uranium. The most diffuse basis functions on uranium with the exponent 0.005 (all s -, p -, d -, and f -type functions) were omitted as in previous studies [125, 166]. The calculations were conducted to get deeper insights into the mechanistic principles rendering uranium reduction and Cit conversion. It was therefore initially determined which of the different U^{VI} -Cit complexes present in the sample solutions is susceptible to photo-induced reactions at all. Upon photo-excitation of the 2:2 complex the lowest-lying triplet state reveals bond elongation ($\text{U}-\text{O}_{\text{yl}}$), however, no bond dissociation, with α/β spin density of the complex localized exclusively on the UO_2 entity, cf. Fig. 47, concluding that $[(\text{U}^{\text{VI}}\text{O}_2)_2(\text{Cit})_2]^{2-}$ itself is *photochemically inactive*.

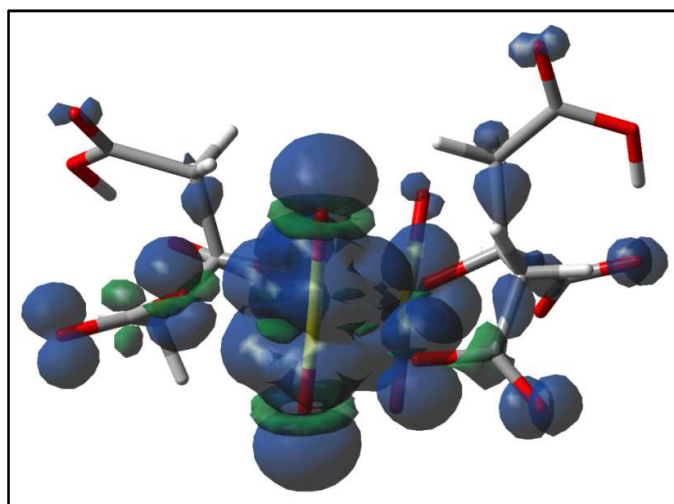


Figure 47. Visualization of the DFT-calculated spin density of the lowest-lying triplet state of U^{VI} -Cit 1:2 complex.

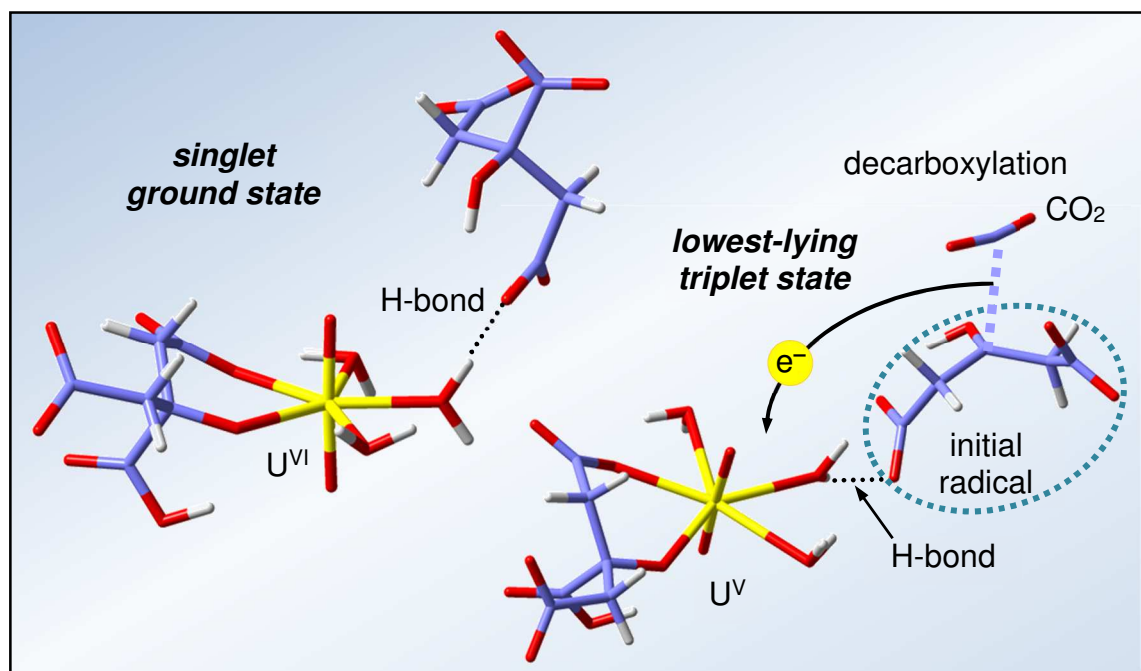
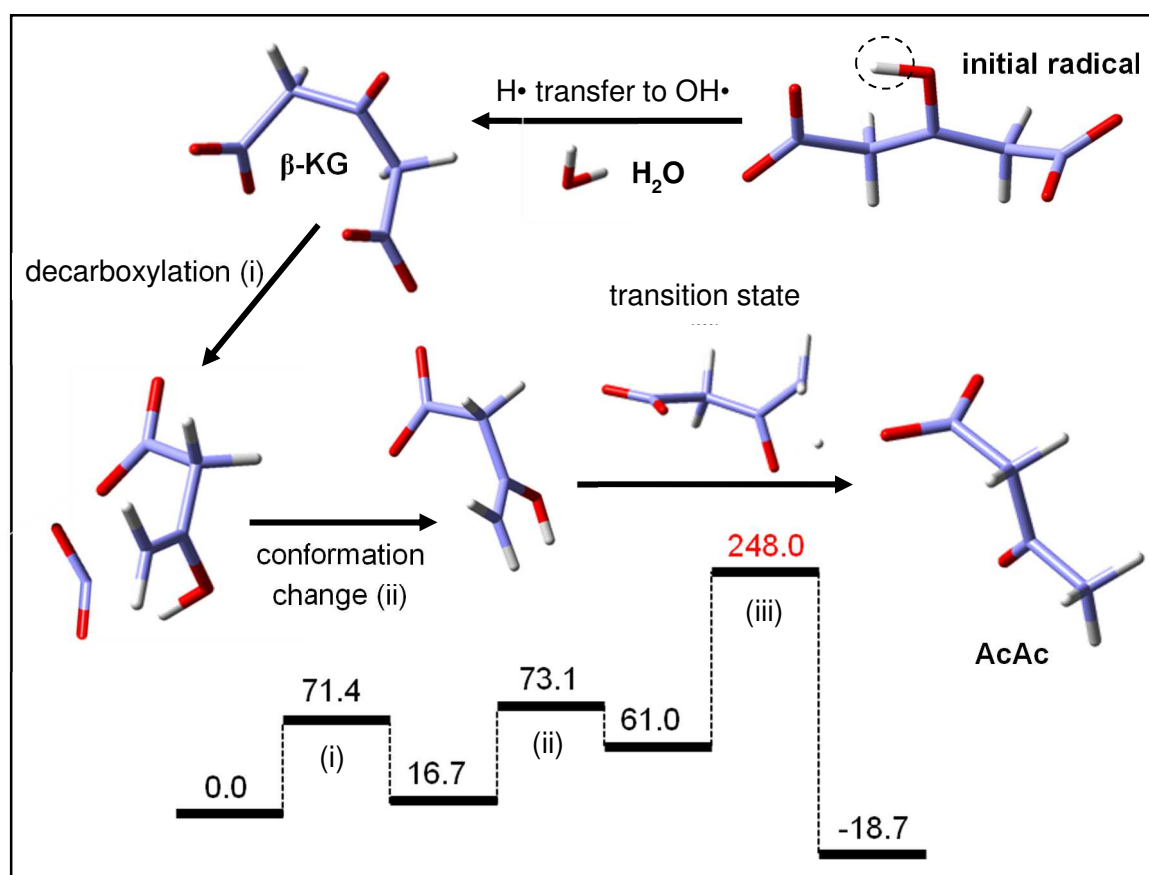


Figure 48. Depiction of DFT-calculated U^{VI} -Cit (1:1) complex and hydrogen bonded Cit association structure as singlet ground state (left), and the corresponding lowest-lying triplet state after photo-excitation of the hydrogen bonded Cit, the subsequent single electron transfer to reduce U^{VI} to U^V and the remaining initial radicalic species after decarboxylation. Note: U (yellow), O (red), C (blue), and H (white).

Instead, and in very accordance with findings of STEUDTNER [158], who figured out that for excessive U^{VI} no photoreaction takes place at all, and the experimental results presented in this work (*vide infra*), that photo-degradation and U^{IV} formation is remarkably high for samples excessive in Cit, therefore regarding free Cit being crucial for the whole mechanism to take place at all. This is due to the fact that the initial abstraction of the *central* carboxylate group, as proposed in step (1) in Scheme 6 and verified by DFT cal-

culations as depicted in Scheme 7 can only happen in *free* Cit, since this particular functional group is the most potential binding site at all for U^{VI} complexation (remember inert five-ring fragment) and, therefore, not suited for decarboxylation. In fact, the remaining fifth U^{VI} coordination sites in the 2:2 complexes are occupied by water molecules, acting as hydrogen bond donors, assuring free Cit to be held close (enough) to U^{VI} but leaving the Cit functional groups unbound and, therefore, susceptible for photoexcitation, as schematically shown (for a 1:1 complex) in Fig. 48. The corresponding lowest-lying triplet state now shows cleavage of the central carboxyl group, oxidizing the carboxyl carbon to CO_2 . One of the two C_q-COO bonding electrons is transferred to the uranyl unit reducing U^{VI} to U^V , and the other is retained by C_q , thus constituting a radicalic species. It thereby forms a sp^2 hybridized carbon, according to the trigonal planar arrangement of the substituents (*i.e.*, two CH_2COO and OH) and the radicalic electron potentially found in the p_z orbital not involved in hybridization. The radical is stabilized by the electron withdrawing ($-I$) effect of the OH group and, probably, by showing some delocalization over the neighboring CH_2COO groups. There might be even an indication for this species in the 1H NMR spectra by the broadened methylene signals of free Cit, both immediately and up to several days after irradiation, *cf.* red asterisks in Figs. 49 (p. 89) and 57 (p. 98), whereas the respective spectrum recorded 16 days after irradiation then again shows Cit signals much less broadened.



Scheme 7. DFT-calculated degradation progress of the radical obtained after initial Cit decarboxylation as well as GIBBS energies of reactions and activation barriers in kJ mol^{-1} . Note: C (blue), O (red), H (white).

The mechanism proposed in Scheme 6 conveniently stated the formally correct release of two electrons and one hydrogen ion, the former of course somehow facilitating U^{VI} reduction, and the subsequent degradation to proceed *via* two decarboxylation reactions of β -KG. However, as illustrated in Scheme 7, DFT reveals the radicalic species to relax by (C_q) -O-H hydrogen atom transfer, most likely to a hydroxyl radical (OH^\bullet) present in solution, by that means forming water and β -KG, with the subsequent decarboxylation forming AcAc. After CO_2 abstraction both the CH_2 -COO bonding electrons are retained, now at the CH_2 moiety, thereby forming a short-lived biradical. After pairing of the two radicalic electrons to form a $=CH_2$ moiety, a rotation of the hydroxyl residue is required in order to obtain a conformation suited for the final hydrogen transfer from O-H to $=CH_2$, upon which both the keto and methyl group in AcAc are formed. The latter step is calculated to constitute a remarkably high activation barrier as stated with Scheme 7. Note that this particular step is already depicted as the *enol-keto* re-arrangement in Scheme 6, for instance after the six-membered transition states in steps (2) and (3). Figure A41 (Appendix) illustrates how the high activation barrier is overcome by BORN-OPPENHEIMER molecular dynamics with the modes of the O-H and $(sp^2/sp^3)C$ -H stretching vibrations quite close in frequency (*i.e.*, energy), 3470 and $\approx 3100/3000\text{ cm}^{-1}$ respectively, on the one hand, and the involved sites being sufficiently close in space on the other hand, allowing an effective transfer. Although the corresponding O-D and $(sp^2/sp^3)C$ -D vibrations are even closer in frequency, *viz.* 2520 and 2300/2200 cm^{-1} , respectively, the deuterium bond dissociation energies are slightly higher according to lower zero-point energies.

3.2.2.3 NMR-spectroscopic proof of the reaction mechanism

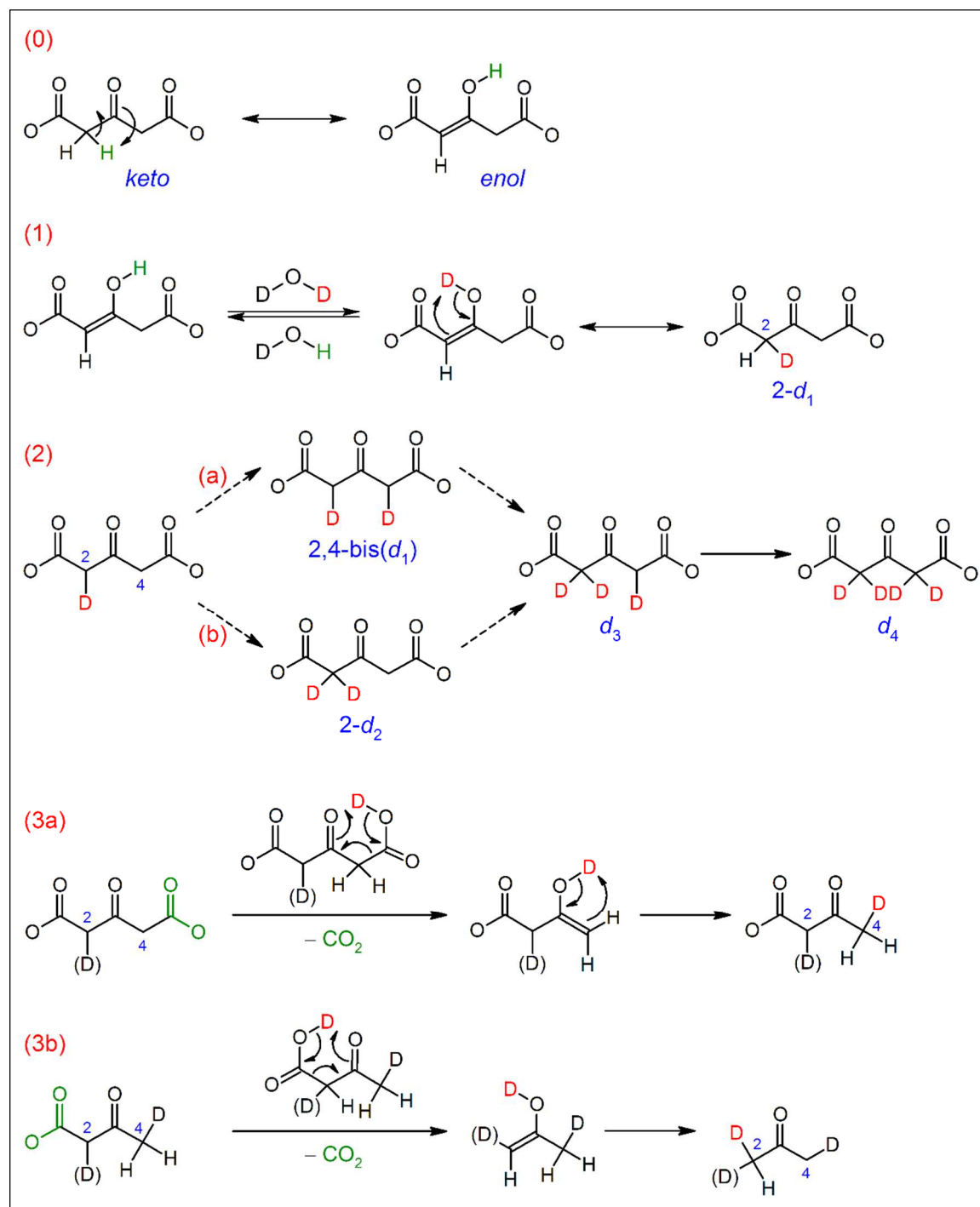
In the following a kind of combinatorial approach is presented upon which each degradation product undergoes *in situ* deuteration in D_2O and, hence, exhibits all possible forms of deuterated isotopomers, unambiguously distinguishable by NMR spectroscopy.

Deuteration reactions of the intermediates are visualized in Scheme 8. Aliphatic residues do actually not bear exchangeable protons. However, the first intermediate in the Cit degradation reaction sequence, β -KG, like all β -keto acids, shows *keto-enol* tautomerism, considered as prerequisite¹⁹ for the subsequent deuteration reactions. Since the samples are prepared in D_2O , the *enol* with its alcohol group now has in fact a labile proton being able to be exchanged for a deuteron, step (1).²⁰ The thus formed singly deuterated $2-d_1$ β -KG is still susceptible to further deuteration in either methylene group (step 2a and 2b), thereby yielding both the symmetrically and asymmetrically bi-deuterated 2,4-bis(d_1) and 2- d_2 β -KG, respectively. Subsequently the tri-deuterated (d_3) and fully deuterated d_4 β -KG are produced as well. Depending on both the respective methylene group isotopomer step 3a is starting with, and which site is decarboxylated, that methylene group becoming the methyl

¹⁹ For this reason methylene protons of citric acid itself are not susceptible to substitution.

²⁰ Apparently, the H/D exchange reaction at acidic sites such as hydroxyl groups is much faster than the *keto-enol* interconversion because of its high-energy transition state, *cf.* Schemes 6, 7, and 8.

group is gaining an additional deuteron, whereas the other methylene group remains unaffected in this step. The different acetone methyl group isotopomers (see also Fig. 50, below) are formed analogously (step 3b). Decarboxylation explains why also methyl groups, though being in terminal molecular position, show deuteration as well, for the process abstracts a terminal carboxyl group and, after re-arrangement of the *enol* to the *keto* form, the deuterioxy (OD) deuteron is used for formation, say deuteration, of the methyl group.



Scheme 8. Visualization of exemplary reactions causing partial and complete deuteration of the intermediates β -ketoglutarate, acetoacetate, and acetone.

Light-irradiation – in the following symbolized by $h\nu$ – of the samples U1 through U4 already characterized as dark reference blanks (Scheme 5, p. 69) directly inside the borosilicate glass NMR tube caused changes in the sample composition as reflected by the corresponding spectra. For convenience, in the following the samples are denoted by their initial composition [in mM] ($[U^{VI}]/[Cit]/pD$).

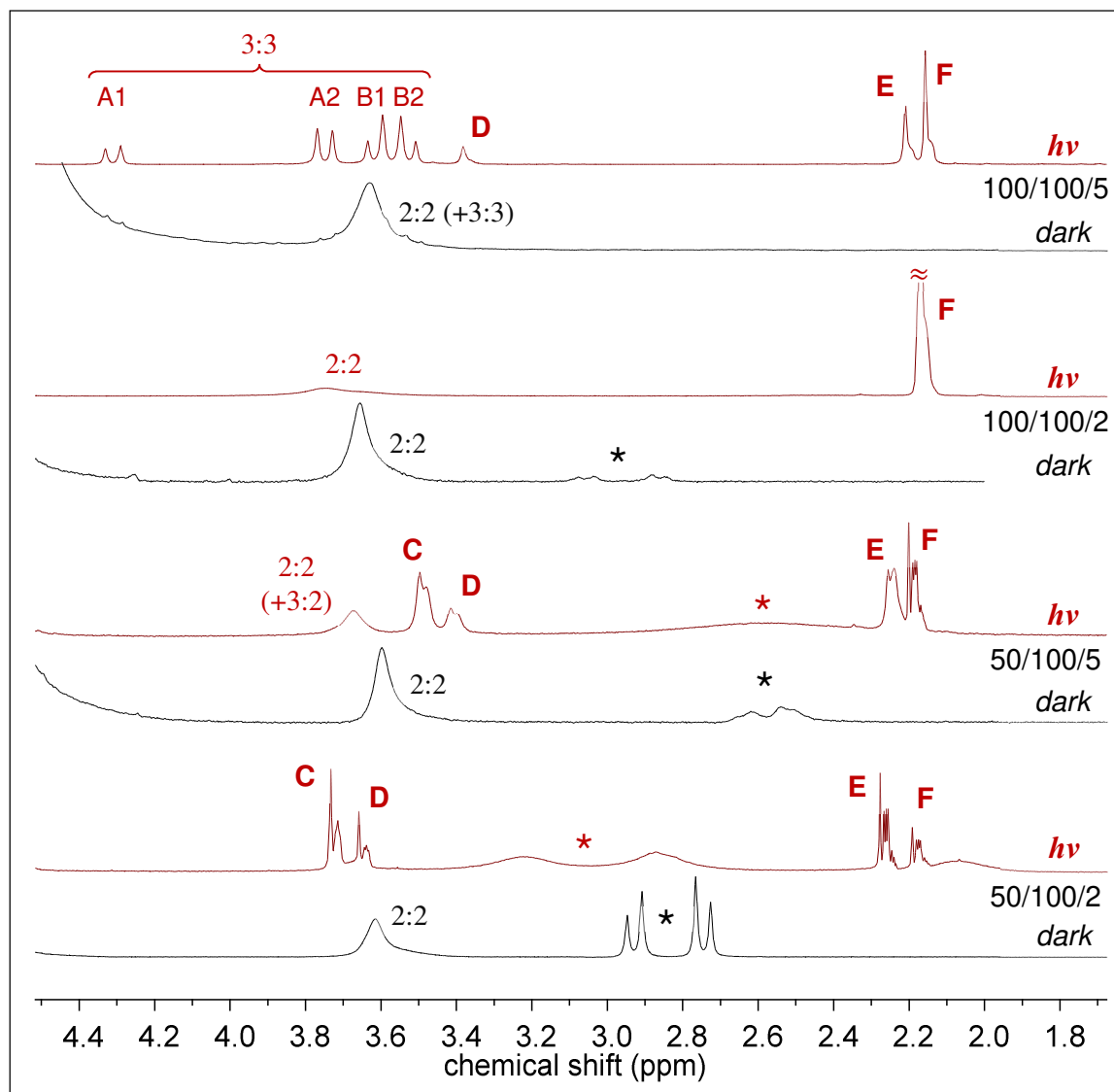


Figure 49. 1H NMR spectra of sample solutions as indicated [in mM]: ($[U^{VI}]/[Cit]/pD$), prior to (*dark*) and after light-irradiation ($h\nu$). The signals are denoted as follows: free Cit (*); degradation products: β -ketoglutarate (C), acetoacetate (D, E), and acetone (F); U^{VI} -Cit complexes according to their respective stoichiometry with the signals of both 2:2 (and 3:2) complex unresolved, and those of the 3:3 complex (A1/2, B1/2) well-resolved.

Figure 49 depicts 1H NMR spectra of samples prior to and after light-irradiation designated '*dark*' and ' $h\nu$ ', as black and red spectra, respectively. The spectra are distinguished by two prominent features: appearance of new signals marked C through F, assigned to the degradation products of Cit, and decreasing signals of both free Cit and U^{VI} -Cit 2:2 complex in consequence of irradiation. Notably, for the (100/100/5) $h\nu$ -sample the signals

of the 2:2 complex completely disappeared, instead the 3:3 complex attributed signals (*cf.* Fig. 46) increased remarkably in intensity. Already at this stage it can be concluded that the speciation has changed.

Figure 50 shows the ^1H NMR spectrum of sample (50/100/2) immediately after light-irradiation and expansions of the signals of interest denoted C through F, assigned to the methylene groups in β -KG (C), the methylene and methyl group in AcAc (D and E, respectively), and the methyl groups in Ace (F). Depicted are also a deconvolution and the corresponding sum of signal groups D and E. Both comprise a singlet and a 1:1:1 triplet, and E an additional 1:2:3:2:1 quintuplet, the latter two showing multiplicities characteristic for ^1H coupling to one and two (equivalent) spin-1 nuclei, respectively, and signal splitting by 2.2 Hz, typical for $^2J_{\text{H,D}}$. Consequently, the signals are due to partially deuterated methyl and methylene groups as indicated. Analogously, both β -KG's (equivalent) methylene groups' and acetone's methyl groups' isotopomers give rise to the same overall signal pattern. Note that heavier isotopes cause upfield shift, thus separating the individual isotopomers' signals. Completely deuterated methylene (CD_2) and methyl (CD_3) groups are not detectable by ^1H NMR spectroscopy.

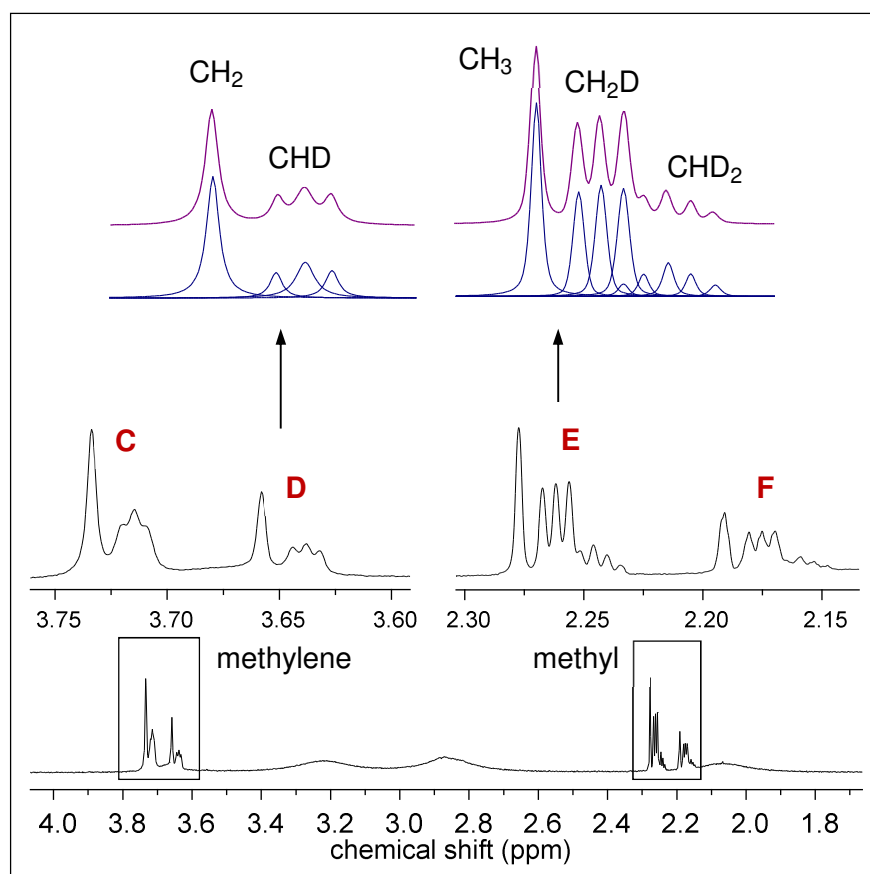


Figure 50. ^1H NMR spectrum of sample U1 (50/100/2) immediately after light-irradiation together with expansions of the regions indicated, and signal assignment to the positions in β -ketoglutarate (C), acetoacetate (D, E), and acetone (F), as well as deconvolution (blue) and the corresponding sum (magenta) of both the D and E signal group and their attribution to the respective isotopomers.

For the spectrum of the U3 (100/100/2) *hν*-sample in Fig. 49 is quite clear, ^{13}C , attached proton test (APT), and H,C-heteronuclear single-quantum coherence (HSQC) spectra were acquired to back up the assignment to acetone (Fig. 51). The ^{13}C spectrum reveals one signal in the carbonyl region and two signals in the aliphatic region, the latter of which being a singlet and a 1:1:1 triplet showing a splitting by 19.6 Hz. The APT discloses the aliphatic singlet carbon to be a methyl group (negative), the triplet to be a methylene group (positive). Finally, the HSQC shows the correlation between the aliphatic carbon(s) and the ^1H signal(s) denoted F. By means of the characteristic 1:1:1 triplet appearing in a ^1H decoupled ^{13}C spectrum the triplet is attributed to an acetone methyl group bearing one deuterium (CH_2D), being responsible for the $^1J_{\text{C,D}}$ of 19.6 Hz, whereas the singlet is due to an acetone CH_3 .

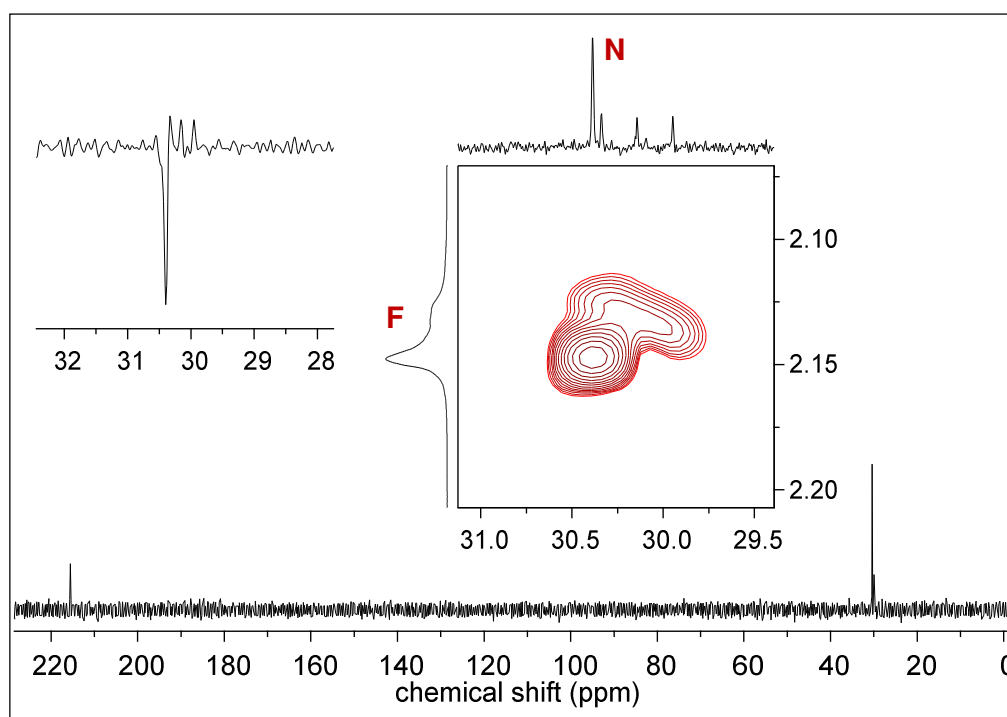


Figure 51. Spectra acquired for the justification of ^1H signal group F ascribed to acetone isotomers in light-irradiated U3 (100 mM U^{VI} , 100 mM Cit, pD 2) sample: ^{13}C NMR (bottom), APT (top left), and transposed H,C-HSQC of the aliphatic signal with the correlating ^{13}C signal denoted N.

Additionally, the HMBC spectrum of the (100/100/5) *hν*-sample given in Fig. 52 (bottom) confirms the assignment of the F signal to acetone by dint of the correlation between the methyl group ^1H and the carbonyl ^{13}C signal M (indicated by arrow), proving connectivity. Signals D and E also show the characteristic features of partially deuterated methylene and methyl carbons K and L in their respective correlation signals as depicted by the HSQC insets in Fig. 52 (top). Assignment of signals denoted A(1/2) and B(1/2) as well as C_qCOOU to the U^{VI} -Cit 3:3 complex is unequivocal according to both the corresponding correlation signals and the reference spectra given in Figs. 45 and 46 above. By means of both δ_{C} and the negative phase in the APT projection, E corresponds to a methyl

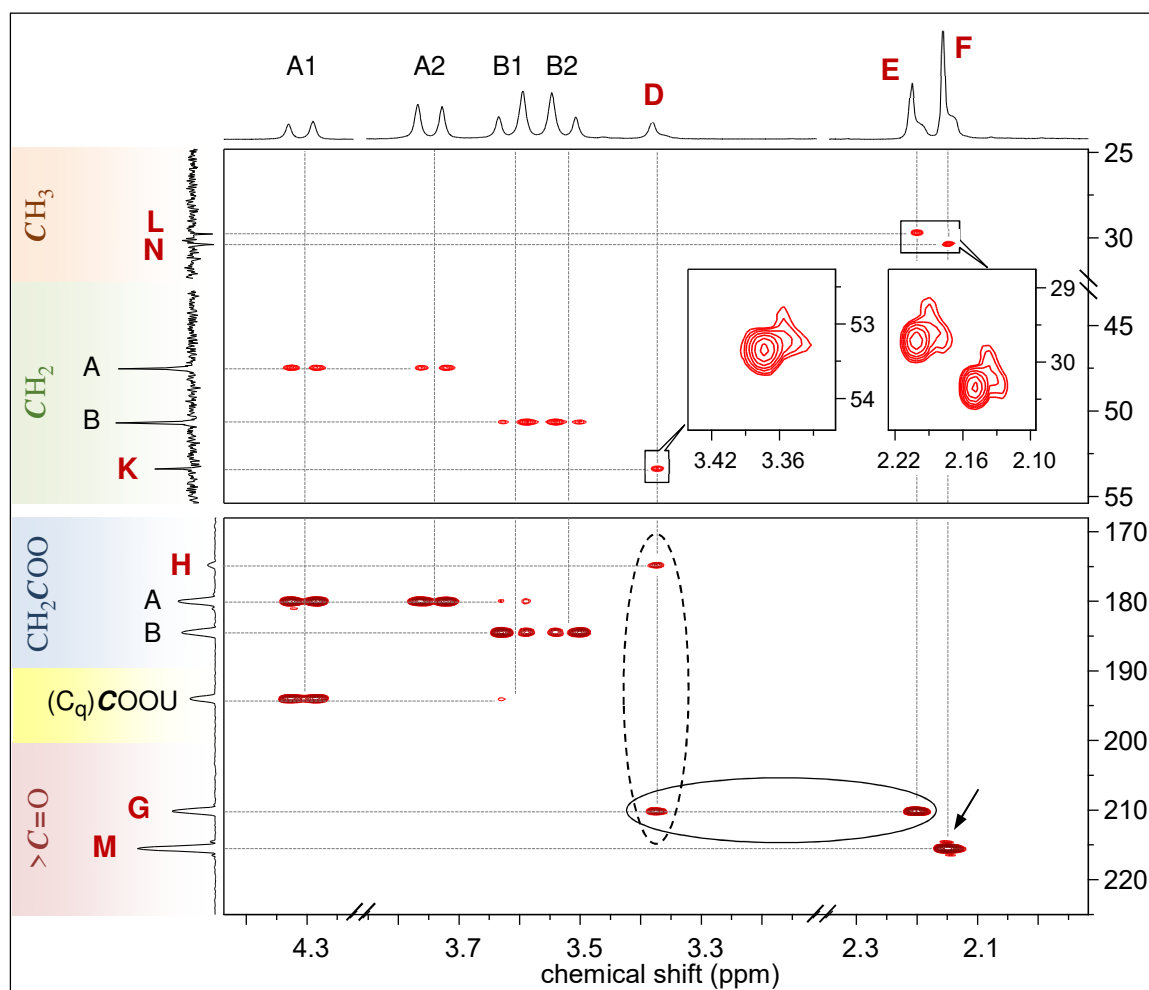


Figure 52. H,C-HSQC (top, 130 Hz opted as $^1J_{C,H}$, APT spectrum applied vertically) and H,C-HMBC (bottom, 6 Hz opted as $^nJ_{C,H}$, internal projection used vertically) spectra of the light-irradiated U4 (100/100/5) sample. Note the characteristic chemical shift regions for common features as indicated.

carbon (L), whereas D exhibits positive phase and δ_C characteristic for a (somewhat deshielded) methylene carbon (K). Note that both 1H and ^{13}C signals of the 3:3 complex' methylene group B(1/2) show similar δ , confirming this structural feature. Interestingly, the HMBC unveils not only the 1H signal D to show correlations to both a carbonyl (G) and a carboxyl (H) carbon (dashed ellipse), but also that both the 1H signals D and E show correlations to the same carbonyl carbon (solid ellipse). Therefore, signals D/K and E/L as well as G and H belong to the same molecule comprising CH_2 , CH_3 , $>C=O$, and COO , ergo acetoacetate.

Starting from citric acid, one of the photo-oxidation products is AcAc, still bearing one of the initial Cit's carboxyl groups, and possessing a carbonyl group, the latter resulting from either oxidation of the alkoxyl-bound carbon ($C_q-OH \rightarrow C=O$) or decarboxylation of another carboxyl group. Taking up the latter process, a further decarboxylation of AcAc yields acetone. It can therefore be deduced that there must be at least one further intermediate oxidation product on the reaction pathway from Cit to AcAc. Taking into ac-

count that upon reaction from AcAc to Ace a CH_2COOH is reacted to a CH_3 , the precursor molecule yielding AcAc must contain another CH_2COOH in place of AcAc's CH_3 . The thus deduced molecule is β -KG. For this molecule is highly symmetric, only one CH_2 ^1H signal is expected, which is, according to the electron withdrawing environment, quite downfield. Obviously, this intermediate attributes to ^1H signal group C, *cf.* Fig. 50. It is noteworthy that β -KG could be detected only immediately after light-irradiation by quickly obtained ^1H NMR (see also time-dependent spectra in Fig. 57, below). Moreover, reference samples of both AcAc (lithium salt) and β -KG were prepared in D_2O for both pD 2 and 5 and subjected to NMR spectroscopy (*cf.* Figs. A38 and A39, Appendix). The Li-AcAc pD 5 sample discloses signals of (partially) deuterated AcAc and minor contents of acetone as well. However, the Li-AcAc pD 2 sample and both the pD 2 and 5 β -KG samples predominantly contain acetone but only small amounts of β -KG and AcAc, respectively. Obviously, even without light-irradiation decarboxylation facilitates very easily for β -KG in principle, and for AcAc in high acidic media. Consequently, the *in situ* formed degradation product β -KG constitutes a short-living intermediate.

3.2.2.4 Multispectroscopic examination of uranium reduction

Complementary to the hitherto considered oxidation of citrate upon light-irradiation, in the following the uranium's fate, *i.e.* reduction, is scrutinized. For this purpose, EXAFS and UV-Vis-NIR spectroscopy were employed. Finally, NMR spectra are discussed revealing the paramagnetic reduced uranium to remarkably shift the signals of corresponding complex species.

Table 6. EXAFS sample designation and composition as well as U^{IV} contents after light-irradiation as determined from X-ray absorption spectra factor analyses.

sample designation	composition [in mM] ($[\text{U}^{\text{VI}}]/[\text{Cit}]/\text{pH}$)	U^{IV} contents (%)
U14-48	(50/100/5)	70
U14-49	(50/100/2)	94
U14-50	(50/50/5)	38
U14-51	(50/50/2)	36

Samples for EXAFS investigations (series U14-X, X = 48 through 51, *cf.* Table 6)²¹ were prepared analogous to those for NMR, however, using H_2O and $[\text{U}^{\text{VI}}] = 50$ mM in all samples, accordingly applying 50 and 100 mM [Cit], with aliquots of required quantity shock-frozen with liquid N_2 after the solutions turned dark. Upon light-irradiation through quartz cuvettes the color changed from straw yellow, characteristic for U^{VI} , *via* darker tones of yellow and orange to olive-brownish as is typical for U^{IV} (see also the photographs with

²¹ In case of future reference, this designation is maintained here.

Figs. 55 and 56, below). Aliquots of remaining solutions were instantly subjected to UV-Vis-NIR spectroscopy after dilution (see Fig. 53). The yield of U^{IV} in the light-irradiated samples was determined by means of X-ray absorption spectra (XAS, Fig. A40, Appendix). In agreement with U^{VI} and U^{IV} reference-based XAS factor analyses (Table 6) the UV-Vis-NIR absorption spectra of irradiated sample solutions excessive in Cit disclose intense features at 487, 556, 659, and 841 (± 1) nm, unambiguously attributed to U^{IV} (*cf.* [112]). Bands at 433 ± 1 nm are caused by the U^{VI} -Cit precursor complex. Additionally, two further absorption bands can be observed at 931 nm (50/100/2 U14-49 *hv*-sample) and ≈ 751 nm (pH 5 U14-48 and -50 *hv*-samples). Although weak, it is remarkable that the latter was also observed in the U^{VI} -GSH aged precipitate redox reaction samples. Together with the former, both features are supposed to be due to U^V , with literature reporting on U^V absorptions at 738 and 940 nm [167], and 760 nm [168].

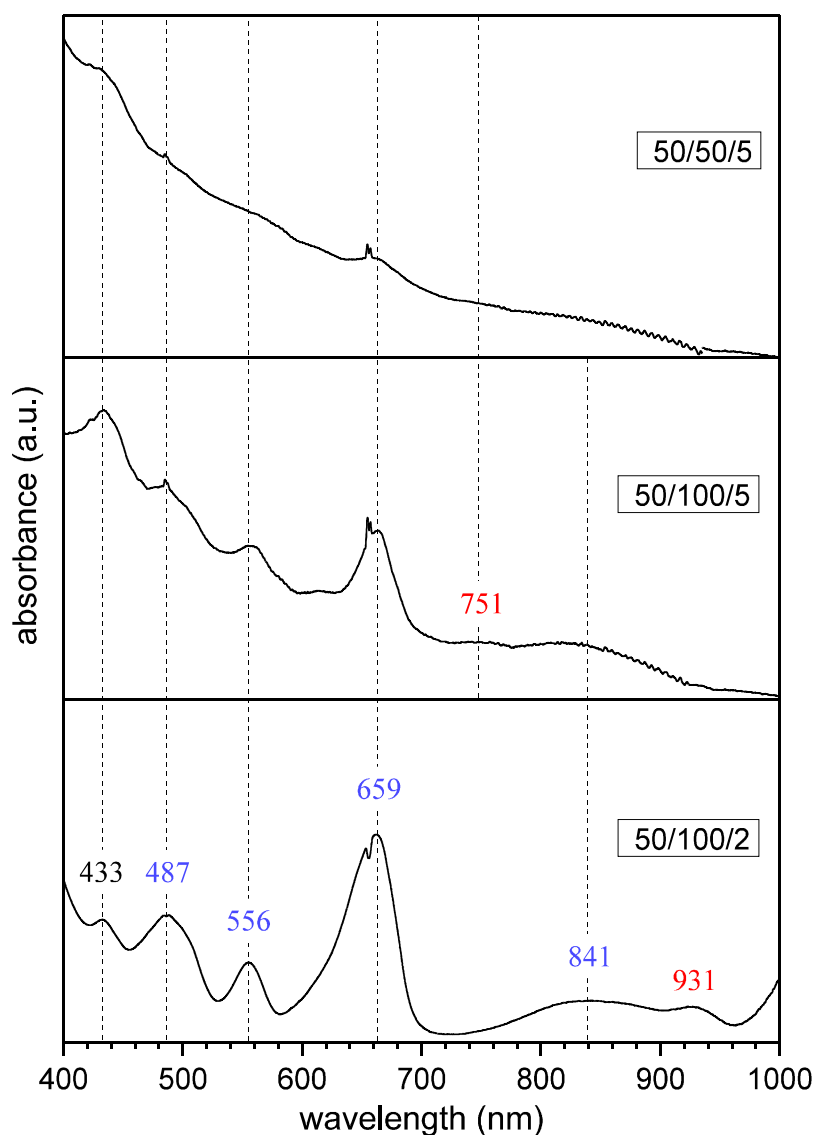


Figure 53. UV-Vis-NIR absorption spectra ($d = 1$ cm) after dilution of aliquots taken from light-irradiated solutions as prepared for EXAFS measurements with sample composition according to ($[U^{VI}]/[Cit]/pH$) [in mM] and absorption maxima indicated.

Figure 54 shows both the raw k^3 -weighted and the R -space plots of the FOURIER-transformed EXAFS data for the U14-X series. The latter represent a pseudoradial distribution function of the U near-neighbor environment, and the peaks appear at lower R values relative to the true near-neighbor distances as a result of the EXAFS phase shifts which are different for each neighboring atom (0.2 – 0.5 Å) [140]. The spectra disclose features of U–O_{yl} at short distance, particularly for the two [U^{VI}]/[Cit] = 1 samples, since containing higher contents of U^{VI} precursor as well as U^{VI}–O_{eq} and U^{IV}–O at somewhat larger distances, arising from complexes of the starting and the reduced material, respectively. Features of μ -O–U and U–U indicate bi- and trinuclear U^{VI}–Cit (*cf.* p. 79) and polynuclear U^{IV} species, respectively. Particularly the dark brown (50/50/5) sample shows a strong U–U EXAFS peak and a remarkably increasing baseline towards lower wavelengths in the UV-Vis-NIR spectrum (Fig. 53, top). The latter findings agree with the 15 – 25 nm colloids determined by photocorrelation spectroscopy. Since the U⁴⁺ are considerably more LEWIS acidic than the uranyl (V and VI) ions, they show a much stronger tendency to undergo hydrolysis and formation of polynuclear species and colloids.

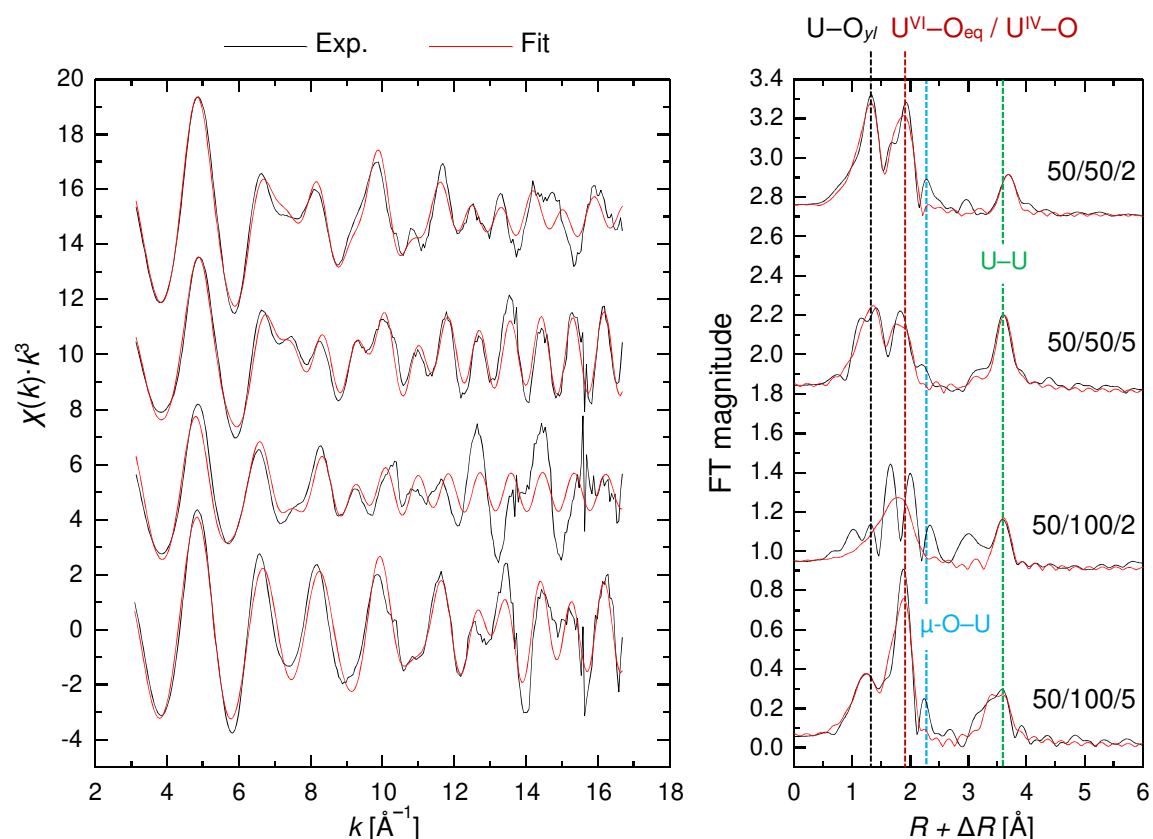


Figure 54. U L_{III}-edge k^3 -weighted EXAFS data (left) and corresponding FOURIER transforms (right) for samples with ([U^{VI}]/[Cit]/pH) [in mM] composition as stated with the spectra.

Spectra in Figs. 55 and 56 depict the ¹H NMR low-field regions of the *hν*-samples (red) for which the corresponding high-field region is shown in Fig. 49 (*vide supra*). Depending on pD, the spectra disclose signals remarkably downfield shifted, *viz.* 24 and 53 ppm for initial pD 2 and pD 5, respectively, unambiguously demonstrating paramagnetic uranium complexes.

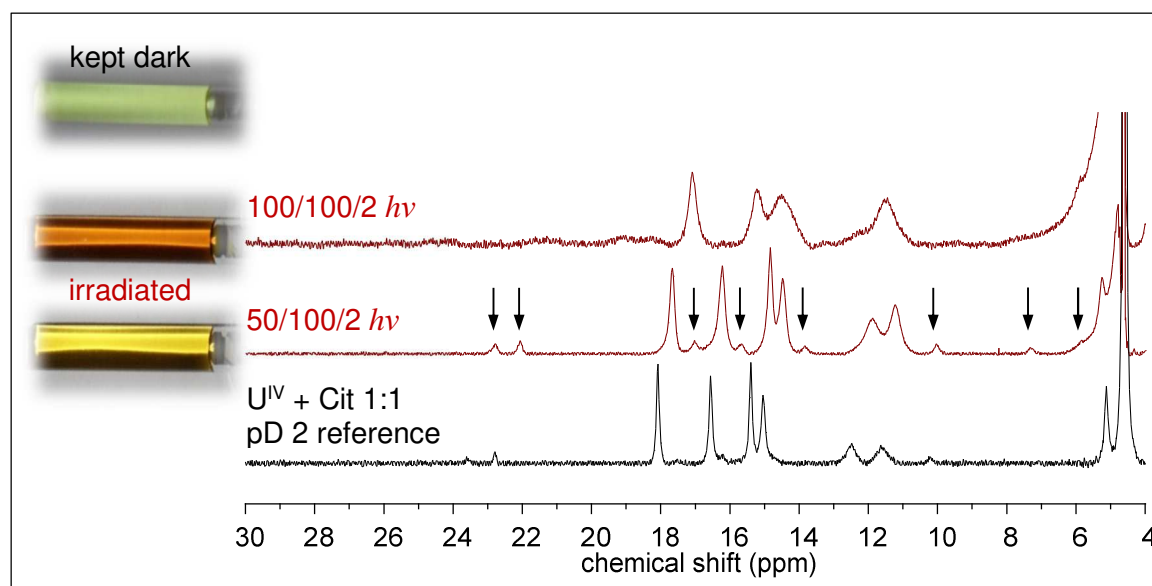


Figure 55. ^1H NMR low-field region of light-irradiated pD 2 samples (red) and U^{IV} -Cit reference sample (black, 50 mM in both U^{IV} and Cit, in D_2O , pD 2), together with photographs showing the solutions' altered color as compared to a corresponding U^{VI} -Cit solution kept dark. Note the arrows indicating a second set of minor signals.

In order to figure out whether the observed low-field signals attribute to Cit-complexes of tetravalent uranium, U^{IV} -Cit reference spectra (black) were acquired for both pD 2 and pD 5, of samples being equimolar in both Cit and electrolytically synthesized U^{IV} . Interestingly, apart from a small (pD-dependent²²) shift, the (50/100/2) $h\nu$ -sample and the corresponding pD 2 U^{IV} -Cit reference are virtually identical, and the analogous (100/100/2) sample showing broadened, apparently averaged, signals, proving both these samples to contain citric acid complexes of tetravalent uranium.

Spectra obtained for the light-irradiated pD 5 samples (Fig. 56) exhibit signals of remarkable ^1H chemical shift values in general, and far from the signals of the corresponding U^{IV} -Cit pD 5 reference in particular. Furthermore, for U^{V} also constitutes an yl -structure, in addition to the paramagnetism due to the unpaired f -electron, also the uranyl multiple bond magnetic anisotropy contributes to overall spectral effects. Taking into account that U^{V} shows somewhat increased stability against disproportionation for both increasing pD and presence of chelating ligands, it is thus concluded that the observed signals are due to Cit complexes of pentavalent uranium. The (broad) signals at $\delta_{\text{H}} = 13$ and 8.5 ppm in the (50/100/5) $h\nu$ -spectrum are assumed to be caused by U^{IV} complexes. In the pD 2 solutions the absence of any signals attributable to U^{V} is due to either a two-electron transfer taking place under these conditions as proposed by DODGE AND FRANCIS [159], thereby reducing U^{VI} directly to U^{IV} , or fast disproportionation of U^{V} to U^{VI} and U^{IV} very likely occurring at acidic conditions.

²² The pD values stated refer to the initial (dark reference) sample conditions. After (repeated) light-irradiation the sample NMR tubes were kept closed, that is, pD was not adjusted.

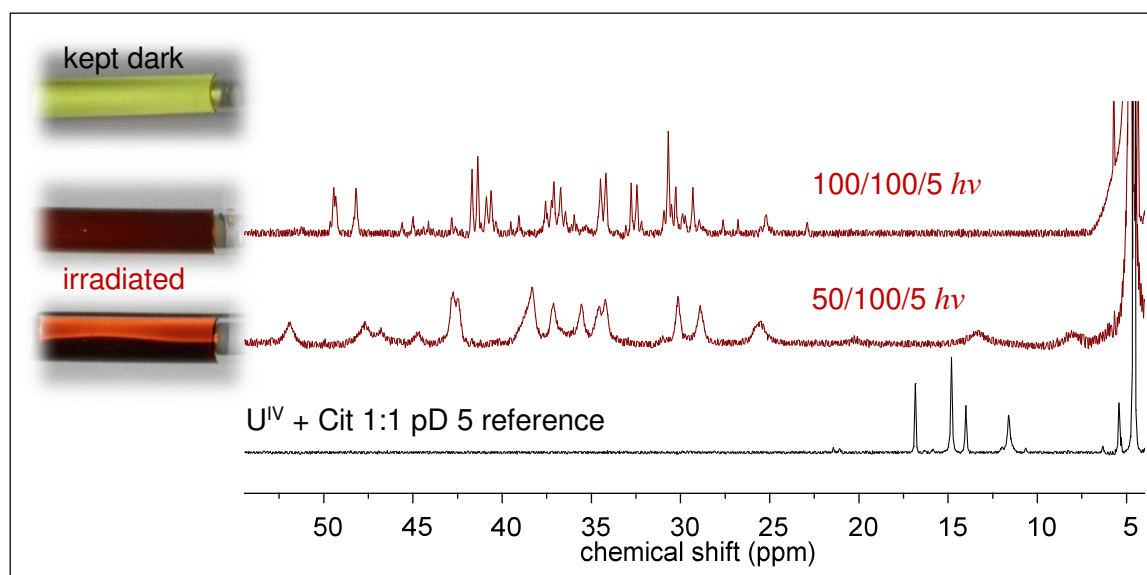


Figure 56. ^1H NMR low-field region of light-irradiated pD 5 samples (red) and U^{IV} -Cit reference sample (black, 50 mM in both U^{IV} and Cit, at pD 5), together with photographs showing the solutions' altered color as compared to a corresponding U^{VI} -Cit solution kept dark.

Although the *in situ* formed β -KG and AcAc both are chelating keto acids, they cannot compete with the superior complex formation capabilities of Cit with its four functional groups. Therefore, the photo-reduced uranium complexes are considered to be primarily Cit complexes. The multitude of signals can be explained by the principal predomination of polynuclear species under the given pD conditions and especially by the occurrence of species containing two uranium atoms of different oxidation states, such as $(\text{U}^{\text{V}})(\text{U}^{\text{VI}})(\text{Cit})_2$, hence reducing the molecules' symmetry (of potentially occurring *syn* and *anti* isomers) and causing (paramagnetic) anisotropy effects.

Upon light-irradiation and the various intermediate decarboxylation reactions, the Cit contents decrease and pD increases, the latter due not only to CO_2 formation but also H^+ expenditure on U^{4+} formation (either way), resulting in changing sample conditions and, hence, uranium speciation. As can be seen in Fig. 49 (above), the ^1H high-field spectra of the U4 (100/100/5) sample reveal the 2:2 U^{VI} -Cit complex to be predominating in the dark reference, however, after light-irradiation the only U^{VI} -Cit related signals attribute to the 3:3 complex. Additionally, after (repeated) light-irradiation, it was this particular sample that first showed turbidity, as can be seen in the NMR tube photograph in Fig. 56 (middle), implying colloid formation. Less turbidity was observed in the U2 (50/100/5) *hv*-sample since prepared with Cit in excess, thereby preventing colloid formation by complexation. For the latter sample, time-dependent ^1H NMR spectra are depicted in Fig. 57, demonstrating that (i) again sample conditions changed as described for the U4 (100/100/5) sample, whereupon the 3:3 U^{VI} -Cit complex emerges (indicated by arrows), and (ii) the largely paramagnetic shifted signals are observable for (at least two) weeks after light-irradiation, implying U^{V} -attributed chelates to be stable against disproportionation. For reasons discussed above regarding the 2:2 complex, the 3:3 complex lacking coordinating water serving as hydrogen bond donor is supposed to be *photochemically inactive*.

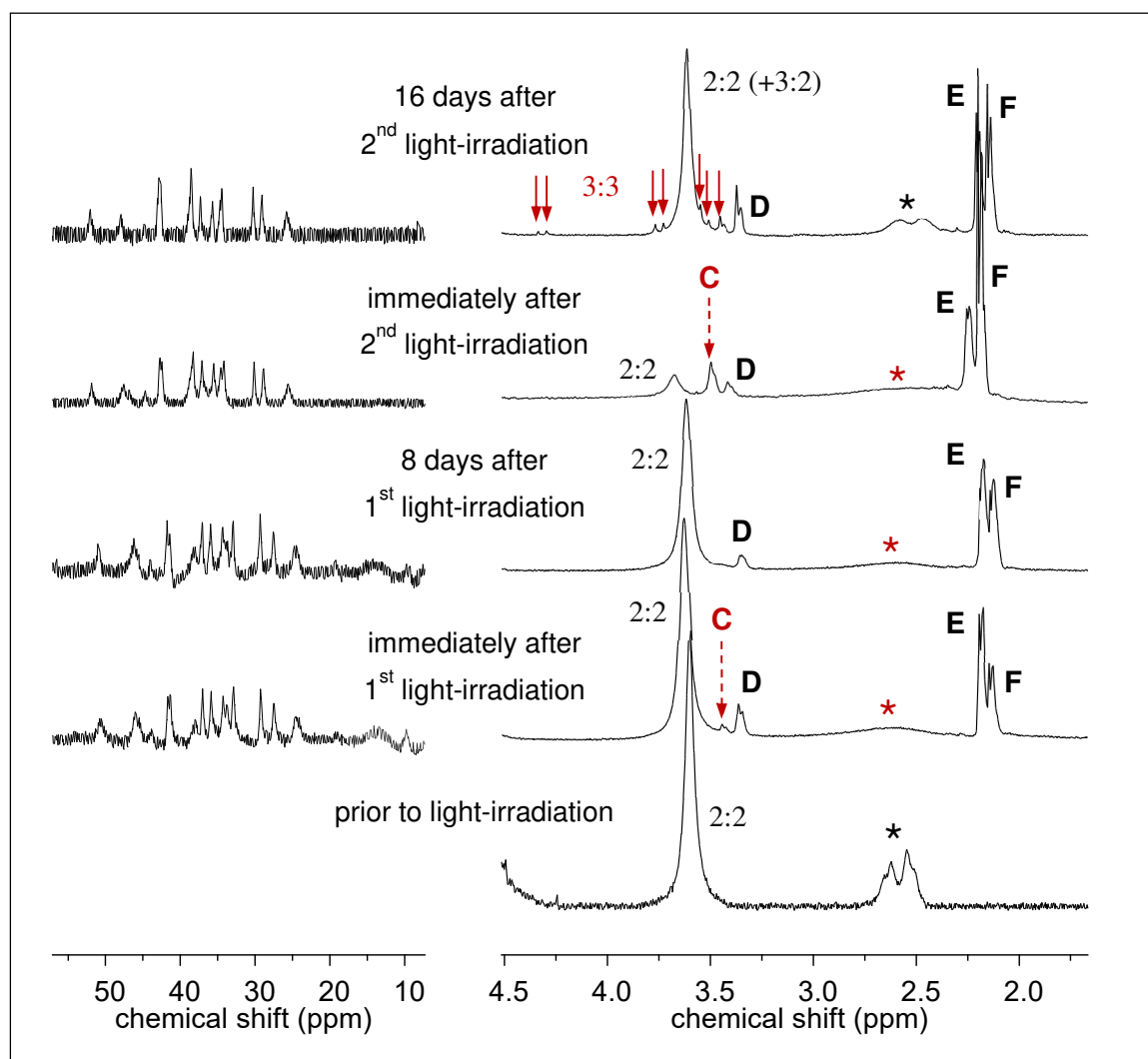


Figure 57. Time-dependent ^1H NMR spectra of the (repeatedly) light-irradiated U2 (50/100/5) sample. Note: red solid arrows indicate the emerging $\text{U}^{\text{VI}}\text{-Cit}$ 3:3 complex, free Cit is denoted (*). The 2nd light-irradiation was performed immediately after acquisition of the preceding spectrum (middle).

For the 3:3 complex possesses only hydrogen bond acceptor sites (in the Cit ligands' periphery), and the free Cit in solution is only able to act as hydrogen bond donor *via* the alcoholic OH group since all carboxyl groups are deprotonated, the geometric preconditions may be unsuited. Correspondingly, in case of sample conditions (particularly pD) suited for the existence of the 3:2 $\text{U}^{\text{VI}}\text{-Cit}$ complex (sub-unit of 9:6 macrocycle) and free Cit to be present in the solution, light-irradiation may allow U^{V} formation within the 3:2 complex, for the latter (sub-unit) contains coordinating water. As the latter is considered quite stable, dismutation of the obtained U^{V} is unlikely and may be an interesting route aiming at the synthesis of long-time stable $(\text{U}^{\text{V}})(\text{U}^{\text{VI}})_2(\text{Cit})_2$ complexes for comprehensive studies on usually short-living U^{V} . Note that there are also signals with δ_{H} of about 20 and 13 ppm ascribed to U^{IV} , however too broad to be visible in the depiction.

Additionally, apart from the light-induced reactions, in both U^{IV} -Cit reference and (50/100/2) $h\nu$ -sample, two principal signal sets are visible, a major and a minor one with intensity ratio of $\approx 12:1$, respectively (see Fig. 55, above). The latter, indicated by arrows, comprises eight signals of equal intensity, whereas the major signals are likely to count also eight, two of which, however, are in part or completely obscured by the water signal or (coincidentally) suppressed upon water suppression sequence. The particular number of eight signals implies just as much spectroscopically different methylene protons, indicating that two Cit are complexing, each ligand with different binding fashion, rendering each diastereotopic methylene group different. Note that again different stereoisomers can be formed. On the one hand, 1:1 and 1:2 U^{IV} -Cit complexes with $\log \beta_{101} = 13.5 \pm 0.2$ and $\log \beta_{102} = 25.1 \pm 0.2$, respectively, have been shown to exist [169], implying that the major signals attribute to the more stable one. On the other hand, the presence of a 1:1 complex to be present in the samples is peculiar, for a 1:1 complex with one ligand only, *i.e.*, four Cit methylene protons, cannot give rise to eight signals, unless there are two distinct isomers of the 1:1 complex, given the fact that they are of equal quantity. This can only be the case for two diastereomers (or diastereomeric pairs of enantiomers) formed by oppositely configured Cit ligands and only if the U^{4+} itself constitutes a chiral center, *e.g.*, with three different functional groups of citrate and at least one water as ligand, thereby forming (*R,R*) and (*S,S*) as well as (*R,S*) and (*S,R*) configurations. Since U^{4+} is spherical, thus showing no steric requirements, all isomers are equally populated and concomitantly showing signals of same intensity. Taking further into account the magnetic anisotropy of the paramagnetic U^{4+} , the different signals are expected to be well separated. It is likely that the set of major signals attributes to a 1:2 complex, with the spectroscopic findings implying that one ligand bears an unbound CH_2COO residue, for the seventh and eighth signal are close to (or obscured by) the water signal, showing much less hyperfine shift owing to larger distance to the paramagnetic center. The signals at $\delta_H \approx 12$ ppm show considerable broadening compared to those found between 14 and 18 ppm, indicating some intramolecular dynamics. For the binding of a second (trianionic) ligand both the LEWIS acidity of U^{4+} decreases and steric constraints increase owing to both metal-ligand orbital geometry requirements and ligand-ligand interaction, it is plausible that the ligand nuclei are more shielded and, thus, the major signals are observed less downfield as compared to the minor (1:1) signals.

3.2.2.5 Recapitulation

To sum up, by means of NMR experiments themselves, but even more in combination with complementary spectroscopies, such as UV-Vis-NIR and EXAFS applied in this work and TRLFS as exerted by STEUDTNER [158], as well as quantum chemical calculations deep insights into uranium-Cit photo-degradation mechanisms could be gained. In consequence of light-irradiation, aqueous solutions of U^{VI} and Cit were shown to yield reduced uranium and degradation products of Cit, *viz.* β -ketoglutarate, acetylacetonate, and acetone. The same but no other organic degradation products are observed regardless of sample conditions applied, *i.e.*, excessive and equimolar Cit for both pD 2 and pD 5. As already observed by OHYOSHI AND UENO [157] and DODGE AND FRANCIS [159] for pH 3.5 and 6.0,

respectively, uranium reduced at pD 2 is U^{IV} as directly formed by a two-electron transfer, whereas at pD 5 in the first place U^V is obtained by a one-electron transfer. Missing U^V evidence at low pH/pD does not necessarily mean no formation at all, for its disproportionation is very fast under acidic conditions. It can still be possible that the transient concentration of U^V is beyond detection limit, however, increases with increasing pH/pD since disproportionation is slowing down. Therefore, the NMR signals observed for the pD 5 samples at 1H chemical shift values between 25 and 53 ppm, in combination with (weak) UV-Vis-NIR absorptions at about 751 and 931 nm, are assigned to U^V complexes of Cit. For the U^{VI} in fact is bound in the 2:2 complex, and reduced by a distinct free Cit, the thus reduced U^V is considered to be still bound within the complex, most likely now being $[(UO_2^+)(UO_2^{2+})(Cit)_2]^{5-}$. Although both the *yl*- and equatorial O– U^V bonds increase in length upon the additional electron [128], the complex is supposed to be sufficiently stable. With regard to a paper [110] and Refs. cited therein dealing with the mechanism of actinyl V disproportionation, two An^V species form a cation–cation complex, one of which being the acceptor and the other being the donor. The initial step is a bridging of the two An^V species by an *yl*-oxygen. Considering this, the two uranyl V entities *within* a binuclear species cannot dismutate *intramolecularly* since both the probability of finding the necessary second U^V within the same 2:2 complex is quite low and citrate complexation is rather rigid and neither rotation about bonds within the complex allows for such bridging geometry. For the *yl*-oxo-bridging configuration between entities of *different* binuclear complex ions is impeded because of both electrostatic repulsion owing to highly charged anions and steric hindrance, also *intermolecular* dismutation is unlikely. Since, additionally, disproportionation involves two successive protonation reactions (thus, much more effective at low pH), the solutions of initially pD 5 (and further increasing with reaction progress) certainly contain long-living (*cf.* Fig. 57) U^V –Cit complexes as determined by NMR. The remarkable further downfield shift as compared to the signals ascribed to (also paramagnetic) U^{IV} complexes is attributed to both complex geometry, since coordination is restricted to the equatorial plane, imposing steric (and orbital) constraints with strong interaction with the electron unpaired spin, and additional deshielding owing to the uranyl-related magnetic anisotropy.

Moreover, not only that both reaction rate and yield are highest at $pH \approx 4$ [157-159] and decrease again upon further increasing pH, but also no reduced uranium is observed under aerobic conditions above pH 7 [158]. Combining these observations and the mechanistic considerations in this work, it is likely that H^+/D^+ are mechanistically crucial constituents. Specifically the formation of U^{4+} (on either way) requires H^+/D^+ to break the U^{VI} and U^V *yl*-oxygen bonds. Additionally, decarboxylation *via* six-membered transition state and subsequent *enol-keto* re-arrangement also require H^+/D^+ . In regard to decarboxylation, CO_2 formation can be seen as an additional entropic driving force. By dint of reaction progress, degradation of free Cit, expenditure of H^+ (*i.e.*, increasing pH) and formation of CO_2 , the latter to some extent dissolving in solution as carbonate and thereby also forming U^{VI} complexes [158] – all these effects reduce the ability to or finally prevent further U^{VI} –Cit photo-oxidation.

3.3 SELENIUM TOPIC

Results shown in this section were in part achieved in co-operation with Dr. Erica Brendler, Institute of Analytical Chemistry, TU Bergakademie Freiberg, operating a 9.4 T NMR spectrometer. In the course of this work, a 14.1 T device was purchased by the Institute of Resource Ecology, HZDR, and experiments were in part repeated.

For risk assessment the understanding of the mobility properties of selenium, including redox and sorption processes, is essential. Before running experiments investigating the sorption behavior, knowledge about the aqueous speciation – in dependence of the environmental conditions – is mandatory.

Retardation of water-soluble selenium oxyanions, selenate (SeO_4^{2-}) and selenite (SeO_3^{2-}), is governed by the respective thermodynamics of both the aqueous phase and the interactions with mineral surfaces. The still most comprehensive overview about selenium chemistry is presented by the respective volume of the Organization for Economic Cooperation and Development (OECD) / Nuclear Energy Agency Thermochemical Database (NEA TDB) by OLIN ET AL. [61]. However, although many papers have been published since 2005, some gaps still need to be closed. One of the open questions is a detailed acquisition of the dimerization of aqueous HSeO_3^- ions, which starts at concentrations around 1 mM [170]. The NEA TDB reported a broad variety of conductometric and cryometric [171-174], potentiometric [175-177], calorimetric [178], and kinetic [179-182] studies supporting this phenomenon. OLIN ET AL. [61], despite considering the existence of Se^{IV} binuclear species, could not recommend stability constants for these species. TORRES ET AL. [25, 170] presented a set of thermodynamic constants for this system recently, but their list of species is not backed-up by independent spectroscopic evidence. Another weak point concerning Se chemistry is the nearly complete lack of spectroscopic investigations at elevated temperatures, the latter of importance owing to after-decay heat, at least in short-period terms after spent nuclear fuel discharge. In addition, the effect of competing cations being present in considerable amount in natural waters (such as alkaline earth metals) is not well understood. By closing these gaps, a thermodynamic description of the Se mobility in natural systems could be assessed with much more confidence and lower uncertainties.

3.3.1 ^{77}Se NMR Spectroscopy

The most important parameter for quantitative NMR measurements is T_1 . Only if the relaxation is complete one can avoid a saturation of the transitions and acquire the full intensity of the signal. Spin-lattice relaxation times were determined by the *saturation recovery* setup. By means of this method, the time for the spins to recover from a saturated state is measured. From the time-dependent build-up curves, the respective T_1 can be extracted by exponential analysis according to Eqn. (12):

$$I(t) = I_0 (1 - \exp\{-t/T_1\}) \quad (12)$$

with $I(t)$ signal intensity at respective time t
 I_0 signal intensity at $t = 0$
 t time
 T_1 longitudinal relaxation time

Accordingly, $T_1(^{77}\text{Se})$ determined at 9.4 T amount to 1.7 s and 14.4 s for HSeO_3^- and SeO_3^{2-} in 0.9 M aqueous solutions containing 10 vol-% D_2O with pH adjusted to 5 and 13, respectively. In a former study [183] T_1 of SeO_4^{2-} was determined to be 11.7 s for 1 M, and to depend only little on concentration with the end-point of a dilution series ending with 10.6 s for 10 mM. Because of these findings, the waiting time ($d1 \geq 5 \times T_1$) between two acquisitions is quite long, *i.e.*, 72 s for 1 M SeO_3^{2-} . At least for the HSeO_3^- anion this value is less than 10 s. To overcome these long $d1$ values, the excitation pulse (based on determined $\pi/2$ pulses) was reduced to $\pi/6$, allowing reduction of $d1$ and, therefore, faster accumulation of still quantitative spectra.

Each NMR active nucleus exhibits – more or less – concentration and pH-dependent chemical shifts due to changes in the magnitude of intra- and intermolecular interactions, with, *e.g.*, solvent molecules or as a consequence of changes in (aqueous) speciation. In the case of aqueous selenium chemistry, both the concentration and the pH impact the position of the dissociation equilibrium and, thus, the predominating species. If interconversion of coexisting selenium species is fast on the NMR timescale, the apparent ^{77}Se NMR signal is again a weighted average. The resulting peak position states the position of the equilibrium and, therefore, contains information on the composition of the sample.

The experimental setup consists of the respective sample solution and, where applicable, an external reference, the latter preferentially generating an easy distinguishable and not overlapping signal. This signal allows for both spectral referencing in order to monitor peak position changes relative to this particular signal and field homogeneity assessment by means of its line shape.

3.3.2 Se^{IV} Dimerization in Aqueous Solution

The following section is part of investigations comprising DFT (MØLLER-PLESSET perturbation theory, MP2) prediction of vibrational frequencies as well as IR, Raman, and ⁷⁷Se NMR spectroscopic measurements by KRETZSCHMAR ET AL. [184]. The latter, being the contribution of the author to the cited article, will be described in detail here.

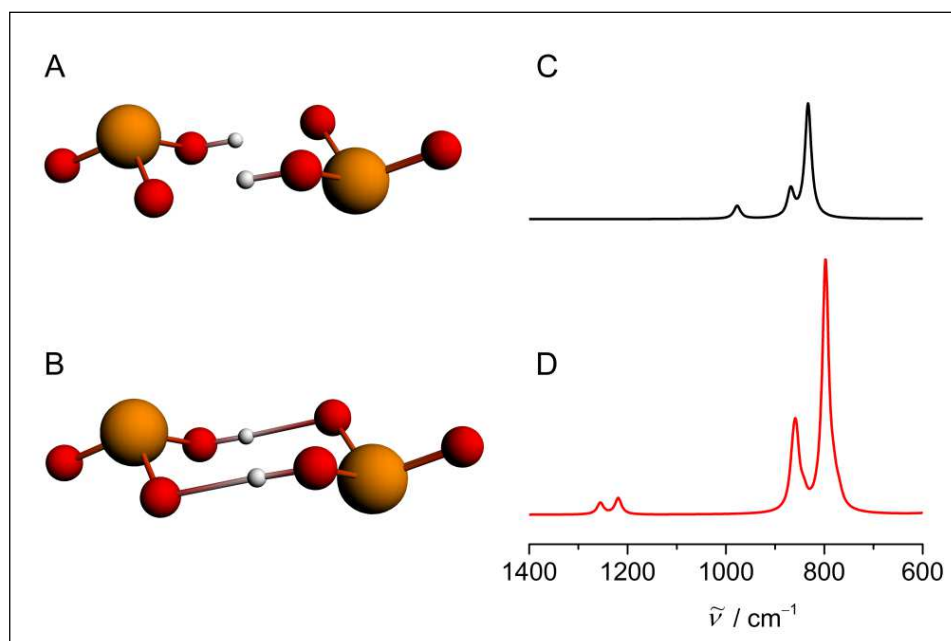


Figure 58. Model structures of hydrogen selenite monomers (A) and hydrogen selenite dimer (B) with corresponding MP2 predicted IR spectra (C) and (D).

Considering the protonation state at moderate pH values with HSeO₃⁻ predominating (*cf.* speciation diagram in Fig. A43, Appendix), the formation of a homo-dimer (HSeO₃⁻)₂ *via* hydrogen bonding (see Fig. 58) was hypothesized. MP2 predicted IR spectra of different aqueous Se^{IV} species revealed dimer characteristic features. Subsequent IR experiments, supported by ⁷⁷Se NMR spectra, confirmed the existence of this dimeric species.

As the electronic environment of selenium changes only slightly upon dimerization, the monomer and the dimer are expected to possess, if any, only minor differences in selenium chemical shifts δ_{Se} . Since this hydrogen bonding between two monomers may cause a reduced proton exchange rate the NMR line width would, therefore, possibly serve as a more sensitive probe for these molecular processes than δ_{Se} itself. Figure 59 shows NMR spectra obtained for pH_c 5 and pH 13 solutions at different Se^{IV} concentrations as well as their graphical evaluation. Note, in the following, owing to the high ionic strengths applied, a correspondingly corrected pH value, *viz.* pH_c, is used for the moderate pH values. For definition and details please refer to the Experimental section 5.1.5.

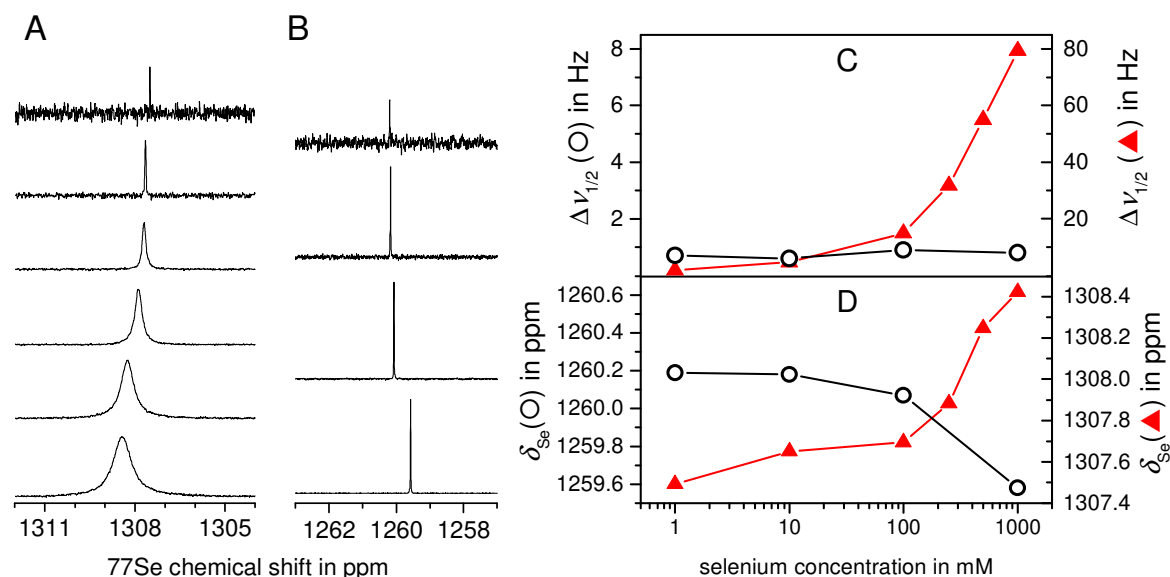


Figure 59. ^{77}Se NMR ($B_0 = 14.1$ T) of Se^{IV} at pH_c 5 (A) and pH 13 (B) with concentrations ranging from 1 mM through 1 M, and constant total ionic strength (3 M); dependence of line width (C) and chemical shift (D) at pH_c 5 (▲) and pH 13 (○) on selenium concentration.

Spectra of the alkaline solutions reveal the signal at $\delta_{\text{Se}} \approx 1260$ ppm, unambiguously attributed to SeO_3^{2-} . With increasing total selenium concentration, hereafter denoted as $[\text{Se}^{\text{IV}}]$, the latter signal marginally shifts upfield, whereas that of the pH_c 5 solutions, found at $\delta_{\text{Se}} \approx 1307$ ppm, shows a slight downfield shift. Taking into account the overall chemical shift range for aqueous Se^{IV} species of about 50 ppm, the observed δ_{Se} changes of approximately 0.5 and 1 ppm for pH 13 and pH_c 5, respectively, are in fact small. For SeO_3^{2-} it is a simple intermolecular effect due to the high sample concentration, whereas for the pH_c 5 solution the signal is a molar fraction weighted average signal due to selenium site exchange between the monomer and the dimer, *i.e.*, dimer association and dissociation,²³ confirming the expected δ_{Se} for both hydrogen selenite monomer and dimer to be very similar. Upon increasing $[\text{Se}^{\text{IV}}]$ the apparent signal's barycenter therefore shifts towards δ_{Se} of the dimer, indicating an increasing content of the latter.

The dimerization is based on the fact that HSeO_3^- itself can act as both hydrogen bond donor and acceptor. At low $[\text{Se}^{\text{IV}}]$, *i.e.* dilute aqueous solutions, hydrogen bonds form primarily with water just because of its excess. However, upon increasing $[\text{Se}^{\text{IV}}]$ the sheer number of HSeO_3^- increases, with the preferential HSeO_3^- hydrogen bonding properties taking effect. According to its $\text{p}K_{\text{a}}$ values [61], *viz.* 2.64 and 8.36, the donor site ($\text{Se}-\text{OH}$) is more basic than water (hence longer available for hydrogen bonding) and the acceptor site ($\text{Se}-\text{O}^-$) is negatively charged since much more acidic (thus earlier charged) than water. Therefore, HSeO_3^- speciation by its $\text{p}K_{\text{a}}$ values on the one hand determines the range of existence for the homo-dimer, with optimum pH around 5.5, and, on the other hand, intensifies by COULOMB attraction.

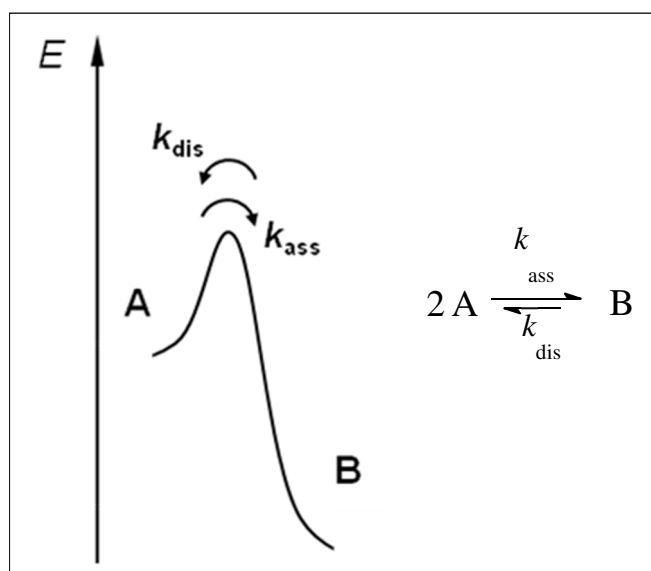
²³ Not to be confused with dissociation in terms of deprotonation.

The apparent linewidth, $\Delta\nu_{1/2}$, results as the sum of different individual linewidth contributions from various effects, *e.g.*, natural line width (resulting from energy uncertainty), magnetic field inhomogeneity (the line width of the reference sample is used as an indicator), and dynamics (exchange reactions). The former two effects are assumed to be the same in all cases. Since all measurements were carried out using a coaxial insert containing sodium selenate solution as a secondary reference, the latter can be used as an indicator for magnetic field inhomogeneities. In order to exclude line broadening contribution from chemical shift anisotropy (CSA) relaxation enhancement – as this can become a very effective relaxation mechanism in particular for heavy nuclei and with decreasing symmetry of the electron density distribution of the nucleus under consideration – measurements were carried out at different magnetic field strengths (14.1 and 9.4 T), resulting in similar spectral behavior,²⁴ for spectra of the latter device see Appendix. Analysis of $\Delta\nu_{1/2}$ clearly shows that the pH_c 5 solution exhibits a strong line width dependence on concentration ranging over two orders of magnitude, whereas $\Delta\nu_{1/2}$ of the pH 13 solution is virtually constant. As other concentration-dependent effects such as changes in susceptibility or viscosity would affect the spectra at both pH_c and have been excluded by keeping the ionic strength constant, these cannot be reasons for the broadening of the signal at pH_c 5. Therefore, line broadening is attributed to exchange processes between different species in the solution – the hydrogen selenite monomer, HSeO_3^- , and its dimer, $(\text{HSeO}_3^-)_2$. These results are in agreement with the line broadening observed in 2 M Se^{IV} solutions in the pH range 4–7 by KOLSHORN AND MEIER [185]. They suggested that additional species, *e.g.* $(\text{HSeO}_3^-)_2$, are involved in the equilibrium.

This system can be regarded as a chemical exchange²⁵ between two species, A and B, with the reaction $\text{A} \rightarrow \text{B}$ running faster than its reverse $\text{B} \rightarrow \text{A}$ owing to an asymmetric energy barrier, according to Scheme 9. This two-site exchange is characterized by two parameters: (i) thermodynamically by the *equilibrium constant* K , determining the fractions of monomer A and dimer B found in solution for given selenium concentration – equivalent to the molar fraction weighted averaged selenium chemical shift δ_{Se} (heavily biased towards the major state chemical shift depending on height of the asymmetric energy barrier), bearing in mind that $K = k_{\text{ass}}/k_{\text{dis}}$ and (ii) kinetically by the timescale of the observed *exchange rate* k_{ex} as the difference of individual concentration changes per unit time with the *rate constants* k_{ass} and k_{dis} by which two monomers associate and one dimer dissociates, respectively, according to Eqn. (13).

²⁴ Re-determination of $T_1(^{77}\text{Se})$ for 1 M Se^{IV} pH 5 solution at 14.1 T revealed 4.5 ± 0.1 s (*inversion recovery*) and 5.2 ± 0.4 s (*saturation recovery*, as was applied for the measurement at 9.4 T revealing 1.7 s). CSA contribution can thus be excluded, since $T_{1,(\text{CSA})} \propto 1/B_0^2$. The simple explanation is dissolved oxygen enhancing relaxation, for the early samples investigated at the 9.4 T device were shipped and the coaxial tube was inserted immediately prior to NMR measurement, hence exposed to air. This is by no means an issue, because any oxidation of Se^{IV} to Se^{VI} would have been ascertained by the characteristic signal of the latter and, notwithstanding, the observed effects for both δ_{Se} and $\Delta\nu_{1/2}$ concur with the later on-site measurements at the 14.1 T device.

²⁵ This is the major reason for the considerably smaller relaxation time observed for Se^{IV} at pH 5 (see p. 102).



Scheme 9. Depiction of the asymmetric energy barrier and the corresponding chemical equilibrium between sites A and B.

$$k_{\text{ex}} = k_{\text{ass}}[A]^2 - k_{\text{dis}}[B] \quad (13)$$

Taking into account that $k_{\text{ass}} > k_{\text{dis}}$ (to be precise $k_{\text{ass}} = K \times k_{\text{dis}}$), at low $[\text{Se}^{\text{IV}}]$ with the monomer (A) being predominant, the observed exchange rate is determined by $k_{\text{ass}}[A]^2$, whereas for increasing $[\text{Se}^{\text{IV}}]$ the second term gains influence, and, therefore, with the dimer (B) being predominant, the observed exchange rate is mainly reflected by the dissociation of the dimer $k_{\text{dis}}[B]$. Hence, the observed spectral effects depend on total $[\text{Se}^{\text{IV}}]$ only, as can be expected from self-association. Consequently, line broadening effects are due to k_{ex} changing the regime from fast intermediate to slow intermediate upon increasing $[\text{Se}^{\text{IV}}]$. That is, k_{ex} becomes smaller than one half of the spectral distance between the two exchanging sites, which can be roughly estimated to be in the order of 10^3 s^{-1} for 1 M Se^{IV} solutions – assuming 10 ppm ($\cong 1140 \text{ Hz}$) $\Delta\delta_{\text{Se}}$ between monomer and dimer.

To provide further evidence for the presence of Se^{IV} dimers, EXAFS spectroscopy of a 1 M Se^{IV} solution in H_2O , $\text{pH}_c = 5$, $I = 3 \text{ M}$ was performed. EXAFS did not reveal the expected Se–Se interaction. This does not necessarily contradict the existence of the dimers, but is rather due to vibrational or static disorder causing destructive interference of the Se–Se paths (data not shown).

Speciation calculations performed at $I = 0.3 \text{ M}$ predicted the HSeO_3^- dimer to increase rapidly in concentration in the range of 1–100 mM and to be predominant as of 100 mM at $\text{pH}_c 5$ (*cf.* Fig. A43 and corresponding Table A8, Appendix). Significant NMR spectral changes (both chemical shift and line width) appeared at $[\text{Se}^{\text{IV}}] \geq 100 \text{ mM}$. This threshold does not exactly match the one predicted by speciation calculations based on complexation constants derived from potentiometric titrations. Indeed, NMR experiments were performed at $I = 3 \text{ M}$, for which the speciation (and hence the dimer/monomer ratio) might be different compared to lower I used for calculations. To perform speciation calculations

at high ionic strength using the SIT or PITZER model, one would need a consistent set of ion-ion interaction coefficients, which are not available so far. In fact, it appears that the dimer is favored with increasing ionic strength. The latter fact is reasonable for the additional electrolyte requires water for solvation, hence reducing water activity and, concomitantly, number of water molecules available for hydrogen bonding, thus favoring hydrogen bonding between two HSeO_3^- . Although dimerization at first sight implies a decrease in entropy, consequently disfavoring the process, one has to take into account the already existing hydrogen bonds between the monomers and water. Upon dimerization these particular structuring water molecules are released, therefore actually increasing the overall number of microstates, *i.e.*, entropy.

Based on predicted characteristic vibrational modes and their unequivocal experimental verification by means of IR spectroscopy (see Fig. A44, Appendix) together with further ^{77}Se NMR spectroscopic support, the existence of the hydrogen selenite dimer was unambiguously proven for the first time [184].

3.3.3 Temperature Impact on Se^{IV} and Se^{VI} Speciation

Chemical shifts are in principle temperature-dependent. On the one hand, temperature changes affect the chemical shift, actually (in liquids $\frac{1}{3}$ the trace of) the shielding tensor σ , particularly by changing the population of rovibrational modes [186], causing electron density redistribution upon changing bond lengths and angles. On the other hand, changes in the solvent's physical properties such as solvation ability or density and, concomitantly, bulk susceptibility may also lead to chemical shift changes for the observed nucleus. According to DUDDECK [187], temperature-induced signal shifts are more or less linear and positive, *i.e.*, higher temperatures correspond to larger chemical shifts, and depend strongly on the structure of the compounds. In addition to the pure temperature-induced chemical shift changes $\Delta_T\delta$ (δ meaning δ_{Se}), also referred to as the temperature coefficient, alterations in the speciation may impact the chemical shift value, particularly when observing averaged signals due to fast site exchange. This behavior was used as a probe to monitor temperature induced changes in aqueous selenium speciation. For this purpose, 100 mM aqueous solutions were prepared at ambient temperature. Se^{IV} solutions were adjusted to pH 4, 10, and 13, that of Se^{VI} to pH 4 and 7.5. Since the speciation of both the Se^{IV} pH 13 and Se^{VI} pH 7 solutions are straightforward, *i.e.*, SeO_3^- and SeO_4^{2-} , respectively, and will not change upon heating, they were used as reference systems. Immediately before NMR measurement, 10 vol-% of D_2O were added (for spectrometer lock), thus concentrations being finally 90 mM. Afterwards Se concentration and pH were re-determined. Temperature-dependent measurements were carried out at 23, 35, 45, and 60 °C with an accuracy of ± 0.1 °C. The results obtained for Se^{IV} are shown in Fig. 60 and Table 7. Additionally, to confirm the findings regarding temperature impact on selenium speciation, the samples were also investigated by IR spectroscopy at different temperatures (see Fig. 61, below).

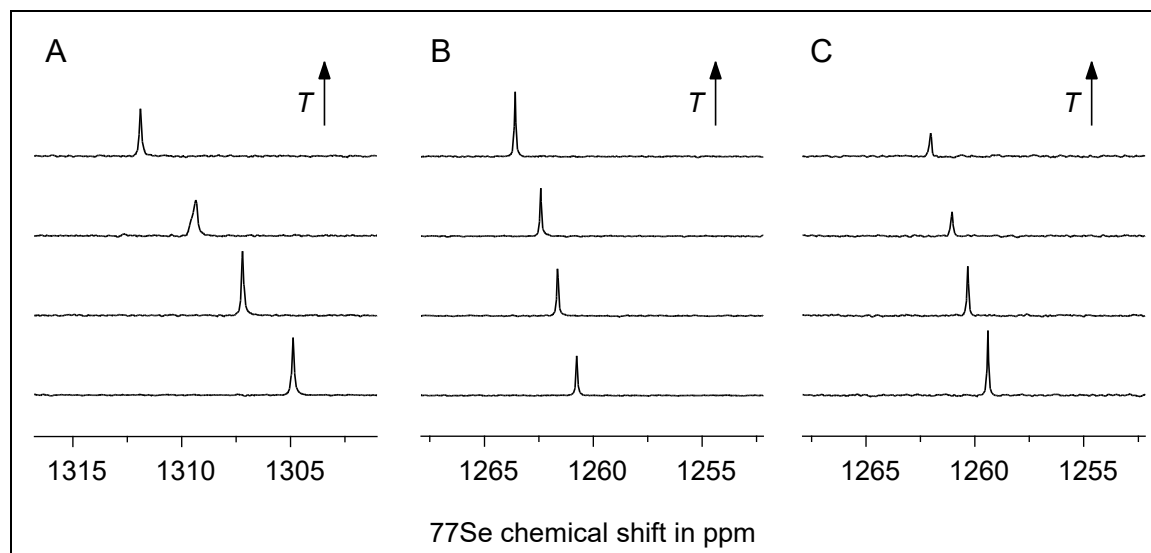


Figure 60. ^{77}Se NMR spectra of 90 mM Se^{IV} pH 4 (A), pH 10 (B) and pH 13 (C) solutions at variable temperatures: 23, 35, 45, and 60 °C (from bottom to top). Note the occasional subpar shimming.

Table 7. Temperature-induced selenium chemical shift changes in dependence of pH for 90 mM Se^{IV} solutions obtained from linear fitting.

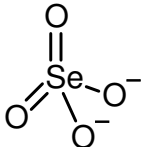
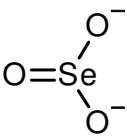
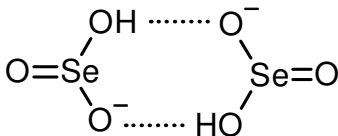
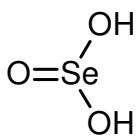
pH	$\Delta_T\delta_{\text{Se}}$ in ppb/K	R^2
4	191 ± 6	0.9967
10	77 ± 1	0.9996
13	71 ± 2	0.9973

Se^{VI} reveals $\Delta_T\delta$ of 68 ± 1 and 78 ± 2 ppb/K for pH 4 and 7.5, respectively. For Se^{IV} , at pH 13 SeO_3^{2-} being the only species present, $\Delta_T\delta$ amounts to 71 ± 2 ppb/K. At pH 4 the predominating species is HSeO_3^- , actually its dimer, with a remarkable $\Delta_T\delta$ value of about 191 ± 6 ppb/K. For the pH 10 solution a different value is observed. According to $\text{p}K_{\text{a}2}$, at this pH also a small fraction ($\approx 3\%$) of protonated species is present. Since the observed signal again is a molar fraction weighted average, $\Delta_T\delta$ also constitutes an average, with the value close to that of SeO_3^{2-} as the predominating species, the other species contributing, however, obviously possesses a significant higher $\Delta_T\delta$. Taking 1304.9 and 1259.4 ppm from the bottom row spectra given in Figure 60 A and C as the limiting δ values for HSeO_3^- and SeO_3^{2-} , respectively, the observed δ in the corresponding spectrum in B, 1260.7 ppm, yields a fraction of 0.03, which is pretty accurate the amount of protonated species expected for pH 10. Consequently, the B series reveal the molar fraction weighted average of the species giving rise to the signals in both the A and C series, respectively. Accordingly, $\Delta_T\delta = 77 \approx 0.03 \times (191) + 0.97 \times (71)$ [ppb/K]. Compared to the value of saturated H_2SeO_3 in H_2O being 94 ppb/K [188], the herein determined values are reasonable.

The considerably different $\Delta_T\delta$ of the pH 4 Se^{IV} signal is worth to be discussed. At first, since the chemical shift range increases with atomic number within a particular group, and also increases with atomic number along a period, so does the sensitivity of the chemical shift towards temperature. Fundamentally, the ^{77}Se nuclei are progressively less shielded with increasing temperature, but somehow the hydrogen selenite (dimer) is much more.

In order to better comprehend the temperature-induced changes on the molecular level, Table 8 summarises some spectroscopically obtained figures. Although selenate^{VI} is the most oxidized species considered, δ_{Se} does not reveal the highest value since δ_{Se} is not only correlated with the oxidation state, but rather with coordination number and, to some extent, with the mean bond length. In accordance with natural abundance ^{17}O chemical shift (δ_{O}) measurements (spectra shown in Fig. A45, Appendix), both selenium and oxygen nuclei are more shielded as compared to the selenite^{IV} ion.

Table 8. Comparison of selected spectroscopic observables for Se^{VI} and Se^{IV} oxo species.

formula	$\text{Se}^{\text{VI}}\text{O}_4^{2-}$	$\text{Se}^{\text{IV}}\text{O}_3^{2-}$	$(\text{HSe}^{\text{IV}}\text{O}_3^-)_2$	$\text{H}_2\text{Se}^{\text{IV}}\text{O}_3$
generic structure				
$d(\text{Se}-\text{O})$ in Å ^a	1.643	1.701	1.704 ^b	1.714
$\nu_{\text{as}}(\text{SeO})$ in cm^{-1}	870	734	820	894 ^c
$\delta(\text{Se}-\text{OH})$ in cm^{-1}	–	–	1205	1236 ^c
$\delta(^{17}\text{O})$ in ppm ^d	196	212	not determined	n.d.
$\delta(^{77}\text{Se})$ in ppm ^e	1032	1260	$\approx 1315^{\text{f}}$ (1305 monomer)	1289 ^g
$\Delta_T\delta$ in ppm/K	78 ± 2	71 ± 2	191 ± 6	94 ^h

^a mean values obtained from EXAFS, Ref. [189]; ^b dimeric species not considered, 0.5 M HSeO_3^- solution;

^c Ref. [190]; ^d relative to $\delta(\text{bulk H}_2\text{O}) = 0$ ppm; ^e relative to $\delta(\text{Me}_2\text{Se}) = 0$ ppm; ^f estimation; ^g Ref. [191];

^h saturated H_2SeO_3 in H_2O , Ref. [188], also reporting on δ_{Se} values of SeO_3^{2-} , HSeO_3^- , and H_2SeO_3 , that seem peculiar and hence not be stated here.

All the Se^{IV} species have very similar mean bond lengths in solution, slightly increasing upon protonation, however, as already stated above, differ notably in δ_{Se} – at least for selenite and hydrogen selenite. Be aware that Se shielding (decreasing δ_{Se}) does not occur concurrently with the increasing number of negative charges in Se^{IV} species upon successive deprotonation. That is, whereas the shielding of the Se nucleus of SeO_3^{2-} is largest (as

expected), that of HSeO_3^- is not in between the former and that of neutral H_2SeO_3 , but smallest (*cf.* Table 8). Apart from decreasing shielding due to decreasing solvent density and, concomitantly, decreasing bulk susceptibility upon increasing temperature, it is particularly the rovibrational mode changes that result in a (usually) decreased shielding [186]. Upon increasing temperature, in general the nuclei are displaced from equilibrium coordinates, resulting in both increasing mean bond lengths and angle opening, with simultaneous increased electron density distribution and, hence, reduced effective shielding.

Dividing the above shown selenium species into two groups – (i) hydrogen bond (Hb) acceptor-only species such as selenate and selenite, and (ii) Hb acceptor-and-donor species such as selenous acid and hydrogen selenite, the former two only form Hbs with water, whereas the latter two are able to form Hbs with both water and other molecules of the same kind – as already indicated for the hydrogen selenite dimer. Hence, it is certainly no coincidence that the first two exhibit significant lower temperature coefficients than the latter two. According to the sketched hydrogen selenite dimer structure in Table 8, selenous acid is as well able to form dimers, however, with $\text{Se}=\text{O}$ (instead of $\text{Se}-\text{O}^-$) as the acceptor site. Since $\text{SeO}-\text{H}$ are more acidic than $\text{HO}-\text{H}$, these donor sites likely form stronger Hbs, which is in accord with a higher temperature coefficient. Owing to the negatively charged acceptor site ($\text{Se}-\text{O}^-$) the Hbs formed by this means can also be considered to be stronger as in $\text{Se}=\text{O}$ or H_2O . Consequently, among all Se^{IV} species investigated, the hydrogen selenite ion is most suited for Hb formation in general and homo-dimerization in particular, resulting in significantly more stable Hbs. Therefore, the latter are a plausible reason for hydrogen selenite to exhibit both the largest δ_{Se} and $\Delta T\delta$, for the strong intermolecular hydrogen bonds cause elongation and angle opening for both the monomer's and dimer's intramolecular bonds. Hence, for the same reasons, temperature stability is increased, and the long maintained Hbs cause the dimer as a whole to be progressively stretched rather than dissociated.²⁶ Thus, the mean electron density responsible for Se shielding is effectively decreased.

This explanation is in agreement with the quite high asymmetric energy barrier for the dissociation of the dimer. The observed concentration-dependent exchange rate, *i.e.*, the rate by which hydrogen selenite dimerising Hbs break and form, was estimated to 10^3 s^{-1} for 1 M Se^{IV} (see p. 106). Among the temperature-dependent measurements at more diluted concentrations of $[\text{Se}^{\text{IV}}] = 0.1 \text{ M}$, just for now k_{ex} is amply assumed to be $\sim 10^6 \text{ s}^{-1}$. Finally, upon temperature increase up to 60 °C, k_{ex} is further assumed to be $\sim 10^7 \text{ s}^{-1}$. The latter value is still at least five orders of magnitude lower than Hb exchange in water [192]. This implies quite high Hb stability, or say GIBBS free energy for hydrogen selenite Hb formation upon dimerization or sorption at a suited surface. The latter would be best of acceptor-and-donor type as hydrogen selenite is itself, which might be the case at the surface's point of zero charge. For sorption to occur it is crucial that the latter is in the pH range where hydrogen selenite is the predominating species.

²⁶ To be more accurate, over an integrated time average, *i.e.*, for the duration of the life time (in terms of site exchange) the overall ensemble of observable dimers is in stretched condition instead of dissociating faster.

By means of NMR speciation changes in terms of deprotonation were not observed upon increasing temperature. IR spectroscopy is well suited to monitor changing selenium oxo species protonation states resulting in changing the molecules' symmetry, resulting in vibration mode alterations with concomitant band position shifts and band shape changes. Accordingly, 0.1 M solutions of Se^{IV} at pH 4 and 10, as well as Se^{VI} at pH 4 were investigated at 25, 40, and 60 °C, by means of IR spectroscopy with the results shown in Figure 61. As can be seen for the antisymmetric Se–O stretch of selenate in (C), the spectra remain unaffected upon heating, since the fraction of hydrogen selenate being present at pH 4 is negligible.

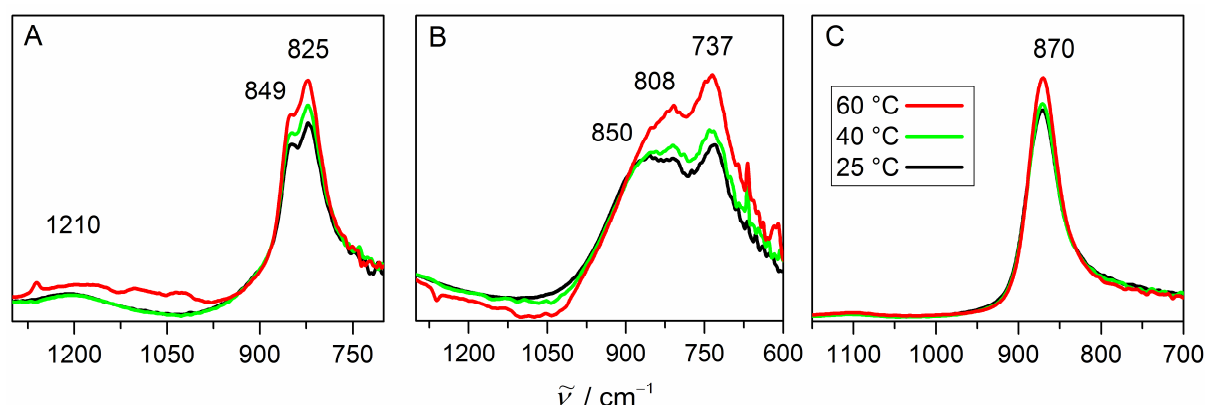


Figure 61. FT-IR spectra of 0.1 M solutions of Se^{IV} at pH 4 (A) and pH 10 (B), and Se^{VI} at pH 4 (C) at variable temperatures.

Similar to δ_{Se} , both the symmetric and antisymmetric Se–O stretching vibrations ν_{s} and ν_{as} are sensitive towards discrimination of SeO_3^{2-} and HSeO_3^- , with values found at 849 and 825 cm^{-1} , and 807 and 737 cm^{-1} , respectively (see also Fig. A44, Appendix). As can be seen in Fig. 61 A, regardless of temperature, both HSeO_3^- attributed Se–O stretching modes are found and, as evidenced by the characteristic feature at 1210 cm^{-1} , at pH 4 its dimer being present up to 60 °C. It seems that, however, as of 60 °C the dimers start to decrease in concentration, *i.e.* dissociate, as the aforesaid feature becomes vaguer. The pH 10 solution IR spectra depicted in Fig. 61 B disclose a superposition of ν_{s} and ν_{as} of both SeO_3^{2-} and HSeO_3^- , although SeO_3^{2-} is predominating under these conditions. In fact, the protonated species is present in solution to about 3% according to $\text{p}K_{\text{a}}$ values. Features attributed to the latter shrink with increasing temperature, indicating that the fraction of HSeO_3^- decreases as depicted in Fig. 61 B, however, being aware that the band intensity does not scale with concentration only – implying much higher HSeO_3^- contents – due to the much smaller electric dipole moment changes by reason of the high symmetry of the selenite ion, thus being intrinsically low in intensity.

To conclude, temperature induced $\text{p}K_{\text{a}}$ changes ($\Delta_T \text{p}K_{\text{a}}$) will have no effect on speciation at all if the solution pH is far from limiting $\text{p}K_{\text{a}}$ values. If, however, the solution pH is in the order of the $\text{p}K_{\text{a}}$ of the species under consideration, small $\Delta_T \text{p}K_{\text{a}}$ result in a significant shift of the acid-base equilibrium and, hence, changing species distribution. As

for the latter above discussed example of pH 10 solution, $\Delta_T pK_{a2}$ of Se^{IV} causes the barely present HSeO_3^- to also deprotonate, upon which its fraction further decreases from 3% to, for instance 1.5%, which means a high relative content change, however, hardly affecting overall speciation.

Consequently, both IR and NMR spectroscopy showed temperature impact on aqueous selenium speciation within the studied temperature range (23 to 60 °C) to be small, so that temperature-dependent sorption behavior (subject of related studies) is not caused by changes in the aqueous selenium speciation, but must rather be due to changes in the surface properties.

3.3.4 Interaction of Se^{IV} and Se^{VI} with Mg^{2+} and Ca^{2+}

In order to study interactions of Se^{IV} and Se^{VI} with the ubiquitous Ca^{2+} and Mg^{2+} metal ions, samples were prepared from the sodium salts of selenite and selenate and defined amounts of calcium or magnesium chloride. The samples were prepared under nitrogen atmosphere, adjusting pH_c to 5 with respect to the high ionic strength (5.6 M in total)²⁷, the latter maintained by addition of NaCl. The (constant) high ionic strength is used to mimic the high salinities occurring in salt domes or argillaceous rock, both being considered as host rock for radioactive waste repositories, and in order to rule out spectral changes solely due to ionic strength effects upon varying M^{2+} contents.

In the presence of Ca^{2+} and Mg^{2+} both the Se^{VI} and Se^{IV} NMR signals shift in comparison to the M^{2+} free sample solutions of equal total ionic strength, Figure 62. The magnitude of the M^{2+} induced signal shift correlates with the metal to selenium ratio: the higher the ratio, the stronger the shift. The observed shifts are remarkably small but significant. This agrees well with the high solubility as well as the low formation constants with $\log \beta \approx 2-3$ for selenate complexes of magnesium and calcium ions [61]. Taking account of δ_{Se} the Se^{IV} species Mg^{2+} and Ca^{2+} interact with at pH_c 5 and $I = 5.6$ M (Fig. 62 B) is the hydrogen selenite dimer. As long as Se^{VI} and Se^{IV} occur in molar excess, neither Ca^{2+} and Mg^{2+} were able to precipitate selenium since soluble ion pair complexes are formed. However, contrary to Mg^{2+} , the Se^{IV} pH_c 5 sample containing equimolar (0.1 M) Se^{IV} and Ca^{2+} concentrations showed precipitation, with the obtained solid being further analysed (*vide infra*).

²⁷ In the course of examining the high ionic strength Se^{IV} solutions it appeared that the signal attributed to the dimer shifted even further downfield (*cf.* Figs. 59 A and 62 B) by increasing ionic strength. A comment related thereto is given in the Appendix with Fig. A46.

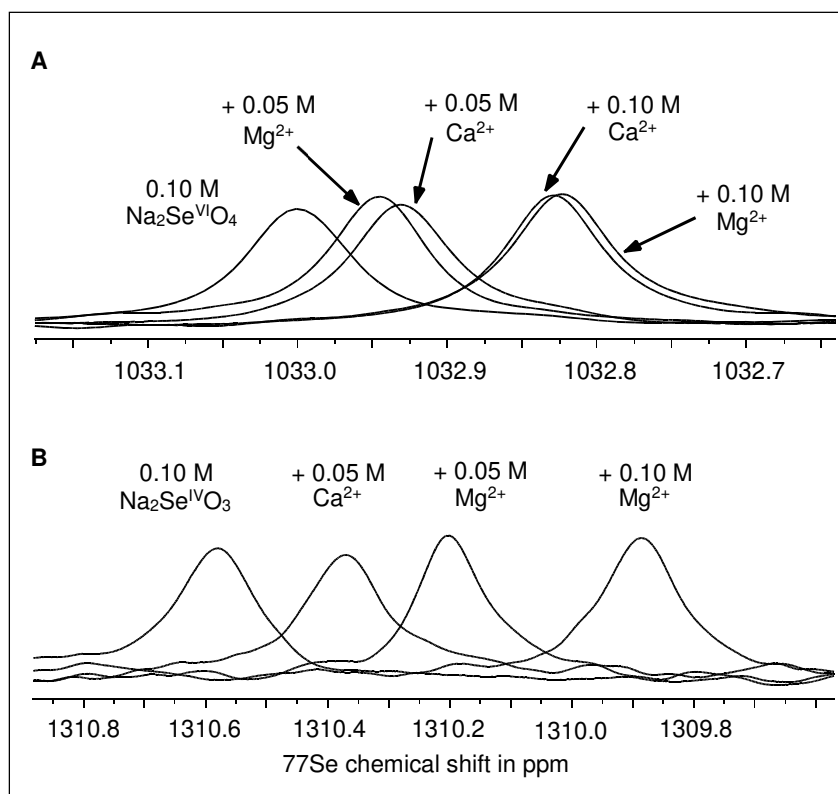


Figure 62. Superimposed ^{77}Se NMR spectra of (A) 0.1 M sodium selenate solutions at pH_c 7.5 and (B) 0.1 M sodium hydrogen selenite solutions at pH_c 5, containing different amounts of CaCl_2 or MgCl_2 , and a total ionic strength of 5.6 M. Note that for the chosen conditions Se^{IV} predominates as dimeric species in solution.

Results to compare with owing to high $[\text{Se}^{\text{IV}}]$ as well as high I are scarcely found in the literature. TORRES ET AL. report on soluble complexes of hydrogen selenite with both Mg^{2+} and Ca^{2+} with $\log \beta_{111}$ values of 9.53 and 9.4 for $I = 0.1$ M NMe_4Cl [25] as well as 11.96 and 12.25 for $I = 0.15$ M NaClO_4 [170]. The authors even recommend to consider formation of both hydrogen selenite dimer itself and M^{2+} complexes thereof, however, for concentrations in a range above their scope.

Solid-state NMR is a very powerful method in determining local molecular structures and interactions. Because of the restricted mobility, anisotropic NMR parameters will not be averaged anymore as for molecular tumbling in solution. As a tensor the chemical shift now shows directional dependencies. Magic Angle Spinning (MAS) is a technique where the sample is spun at the magic angle (54.74°) with respect to the direction of the external magnetic field. Thus, resolution is improved by narrowing the lines due to averaging the anisotropic interactions. As a typical effect in cross-polarization (CP) MAS NMR, the spectral lines are modulated by the rotational frequency the sample is spun at.²⁸ Sample spinning at different rotational frequencies is necessary to determine the isotropic chemical shift, δ_{iso} , as this particular line remains unaffected. Changes in the side band pattern are

²⁸ as long as the spinning frequency does not exceed the detected spectral range

used for chemical shift tensor analysis. Therefore, the spectrum discloses not only information on the chemical shift itself, but also on the electronic density distribution around the selenium atom as well as the morphology of the substance. MAS NMR can be combined with cross polarization (CP) to improve the sensitivity by magnetization transfer from sensitive nuclei, *e.g.* ^1H , to insensitive ones such as ^{77}Se . In this case it has to be taken into account that signal enhancement strongly depends on number and spatial proximity and mobility of ^1H nuclei.

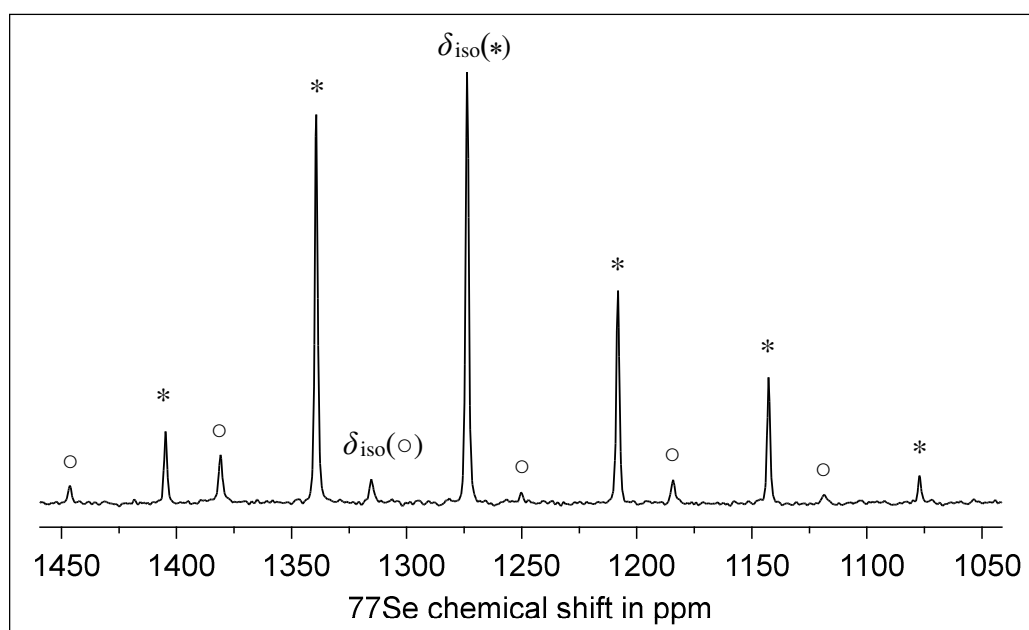


Figure 63. ^{77}Se CP/MAS NMR spectrum at 5 kHz rotational frequency of the precipitate obtained from equimolar Se^{IV} and Ca^{2+} pH_c 5 solution; δ_{iso} and corresponding spinning sidebands (*, o).

Table 9. Analysis of CP/MAS spectra according to Figure 63 of the precipitate obtained from equimolar Se^{IV} and Ca^{2+} pH_c 5 solution.

δ_{iso} in ppm	δ_{11}	δ_{22}	δ_{33}	Ω	κ	% CP	% SP
1273.7	1396.4	1321.6	1103.1	293.3	0.49	86.5	96
1315.3	1443.7	1434.0	1068.1	375.6	0.95	13.3	4

isotropic chemical shift $\delta_{\text{iso}} = \frac{1}{3} (\delta_{11} + \delta_{22} + \delta_{33})$, with δ_{11} , δ_{22} , δ_{33} as principal components of the chemical shift tensor, defined as $\delta_{11} > \delta_{22} > \delta_{33}$ | span $\Omega = \delta_{11} - \delta_{33}$ | skew $\kappa = 3(\delta_{22} - \delta_{\text{iso}})/\Omega$ | according to Ref. [193]; CP: cross polarization; SP: single pulse

^{77}Se solid-state NMR shows the occurrence of three selenium compounds, a major (96%) and a minor (4%) component with δ_{iso} at 1273.3 and 1315.3 ppm, respectively (Figure 63 and Table 9). With a content of < 1% the third component ($\delta_{\text{iso}} = 1331.3$ ppm) will not be discussed further. Though being precipitated from a pH_c 5 solution, with

(HSeO_3^-)₂ predominating, the major component can clearly be assigned to a selenite species (CaSeO_3), as compared to the chemical shift value of ≈ 1260 ppm of the SeO_3^{2-} solution (*vide supra*). The fact that the signal can be observed by CP/MAS implies that the compound must contain hydrogen, probably as water molecules included in the crystal. The minor component, however, points to a hydrogen selenite species, in solution resonating around 1305 ppm (monomer) and 1315 ppm (dimer), *cf.* Table 8. This is supported by a comparison of the cross polarization (CP) and single pulse (SP) spectra, the latter allowing quantification. CP is more efficient for the minor component, suggesting hydrogen close to selenium (Se–OH), whereas the major component is lacking these Se–OH groups. In addition, the span Ω of the chemical shift tensor is much larger for the minor component, representing a larger anisotropy in the shielding as to be expected for hydrogen selenite in comparison to selenite. Taking together these findings, the minor component is tentatively assigned a calcium hydrogen selenite species – that is, the calcium salt of either hydrogen selenite monomer, $\text{Ca}(\text{HSeO}_3)_2$, or dimer $\text{Ca}(\text{H}_2\text{Se}_2\text{O}_6)$. Moreover, solid-state NMR line width (74 Hz) reveals the precipitate may contain crystalline material. It was therefore subjected to X-ray powder diffraction and, additionally, IR spectroscopy (*cf.* Appendix), finally confirming the precipitate to be crystalline and made of calcium selenite monohydrate ($\text{CaSeO}_3 \cdot \text{H}_2\text{O}$), according to ICDD 01-077-1456 reference card. Obviously, other components present in low amount ($< 5\%$ w/w) or being amorphous would have been overlooked by this technique, once more emphasising the value of solid-state NMR spectroscopy.

Additionally, a KBr pellet of the $\text{Se}^{\text{IV}}\text{--Ca}^{2+}$ precipitate was prepared for IR spectroscopy. The IR spectrum (see Appendix) of the precipitate clearly confirms the occurrence of OH as an important structural element as concluded from stretching as well as deformation vibrations of OH, found at 3362, 3195, and 1672 cm^{-1} , respectively. The bands observed at 843 and 777 cm^{-1} as well as 752 and 704 cm^{-1} are due to $\nu_s(\text{SeO})$ and $\nu_{as}(\text{SeO})$, respectively, and that found at 633 cm^{-1} ascribed to $\rho(\text{H}_2\text{O})$, in agreement with IR frequencies observed for $\text{CaSeO}_3 \cdot \text{H}_2\text{O}$ [194], of which the crystal water gives rise to the observed OH features. The crystal water content was further confirmed by thermogravimetric analysis (*cf.* Appendix), which revealed the loss of one mole equivalent of water.

High to very high ionic strengths are used throughout these selenium studies not only to meet the requirements of comparability for the occasionally used quite high total selenium concentrations but also owed to nuclear waste disposal background with salt rock formations being taken into account. Such high salinities can have dramatic effects on chemical equilibria and related constants. For instance, at first glance it is rather unexpected and hence notable that crystalline calcium selenite forms in slightly acidic conditions ($\text{pH}_c = 5$), however, considering the total ionic strength of 5.6 M, the $\text{p}K_{a2}$ must have decreased inasmuch that aqueous Se^{IV} species distribution allowed for selenite to be present in and to be removed from equilibrium, the latter causing precipitation as the calcium salt.

4 CONCLUSIONS AND OUTLOOK

According to BERTINI ET AL. [67], when the interaction between the cation and the LEWIS base is electrostatic (ionic), the paramagnetic Ln^{III} ions with anisotropic distribution of f -electrons give rise to lanthanide-induced *pseudocontact* shift. However, when a LEWIS acid–base interaction is partly covalent, the unpaired electron spin density influences the molecular framework of the base and causes a *contact* shift. The alternating sign observed in carboxyl and α -carbon ^{13}C NMR signal shifts is therefore attributed to spin polarization effects due to *contact contribution* [68] with unpaired electron spin density distributed along the GSH/GSSG molecular framework, implying (partial) covalency in Eu^{III} bonding.

Observation of only averaged GSH/GSSG signals (NMR) confirms the facile ligand exchange at f -element centers particularly in aqueous solutions [16]. In combination with the rather small $\log K$ of 1.71 for $[\text{Eu}(\text{HGSH})]^{2+}$, complexation of Eu^{III} by both GSH and GSSG is ascertained labile and weak. For the Ln^{III} –GSH/GSSG solutions did not exhibit precipitation for the applied conditions, that is up to pD 5 in high millimolar range, the latter can yet be considered as highly mobile species.

In principle, the interactions of both GSH and GSSG with U^{VI} are stronger as compared to the Ln^{III} system. In contrast to the latter, upon formation of *net neutral* binary U^{VI} GSH/GSSG or ternary U^{VI} hydroxo GSH/GSSG complexes, both these U^{VI} systems revealed extensive precipitation owing to the low solubility of these complex species. The least U^{VI} contents remain in solution at pD ≈ 5 when the predominating GSSG species bears a net charge of -2 , whereas the largest quantities of aqueous GSH/GSSG– U^{VI} complexes are observed for pD ≈ 3.5 , with the association constant for pH 3 determined as $\log K = 4.81$ for a 1:1 GSSG– U^{VI} complex. GSH cannot compete with hydroxo ligands for U^{VI} complexation as of pD 6, while GSSG can at least partially compete with hydroxo and carbonate ligands upon formation of both mixed U^{VI} hydroxo/carbonate GSSG (poly-)anionic species of high solubility. Therefore, particularly GSSG (and, hence, other comparable oligopeptides) can facilitate both mobilization and immobilization of U^{VI} , strongly depending on the charges of the formed complexes.

The presence of GSH at near-neutral conditions allows for an immediate U^{VI} reduction to U^{IV} *in situ* with the subsequent formation of nanocrystalline UO_{2+x} . After centrifugation of the starting material and allowing the supernatant to age, the dissolved nanocrystals assemble as outstanding network-like structures. Particularly due to the cheap and simple synthesis and the resulting network-structured material, this approach surely is interesting for both fundamental and applied research purposes due to not only its potential catalytic activity, but also a much larger surface area as compared to conventional spherical uraninite nanocrystal agglomerates. Owing to unique properties on the nano-scale one may think of perspective applications for, *e.g.*, optoelectronics, energy conversion, imaging, magnetic storage, or as contrast agent or host material for further dopants [195]. The striking observation of U^{V} suggests the U^{VI} reduction to occur *via* a one-electron transfer with subsequent

disproportionation of U^V to U^{IV} and U^{VI} , the former two serving as source for nanocrystalline hyperstoichiometric UO_{2+x} phases with O/U ratio between 2 and 2.34. For the multitude of high-class publications dealing with either lab syntheses or environmental occurrence of nanocrystalline actinide oxides, network-like assembled uranium containing nanocrystals are remarkable in their significance and originality. Furthermore, in consideration of GSH's properties and role as an intracellular reductant and detoxification agent of human, animal, and plant cells, formation of water soluble Ln^{III} (and, probably, analogous An^{III}) complexes can increase bioavailability for uptake into organisms, facilitate transport and distribution *in vivo* or, to the contrary, promote excretion as part of detoxification mechanisms. Related to the latter, a significant contribution of GSH, or comparable molecules such as mycothiol and bacillithiol found in actinobacteria [196-197] and *Bacillus* species [198], respectively, on biogenic formation of uraninite is conceivable.

On the one hand, GSH may be a potential reductant and, therefore, immobilizing auxiliary not only for uranyl in particular, but also for actinyl ions in general and, apart from *f*-elements, for technetium as well. On the other hand, in consideration of both the observed Eu^{III} 4*f* hyperfine contact contribution and the much more diffuse and, hence, even more likely covalent bond forming An^{III} 5*f* orbitals, GSH may be able to provide further access to fundamental understanding of actinide bonding and covalency. In this context also the question is raised whether, for instance, Am^{III} is sufficiently "HSAB soft" to involve GSH's thiol group into complex formation. Consequently, further investigations of GSH interaction with Np, Pu, and Am, perhaps Cm, as well as Tc are of paramount interest for both basic research in actinide/radionuclide chemistry and environmental and health research with GSH bridge-building between studies *in vitro* and *in vivo*. Against the background of both possible GSH thiyl radical formation along a one-electron or hydrogen-atom transfer and unpaired 5*f* electron bearing actinides, electron paramagnetic resonance (EPR) spectroscopy would be of great advantage.

Although already investigated for decades, studies concerning the uranium–citrate system allowed further fundamental insights into the structures of the formed complexes on a molecular level. It is noteworthy that upon the multitude of papers dealing with the U^{VI} –Cit complexes neither considers the induced chirality in the Cit molecule upon complexation and the, thus, expectable formation of spectroscopically distinct isomers. On crucial consideration of the stereocenters induced in the molecules upon citrate complexation, for the first time the overall configurations of the 2:2 complex isomers, *viz.* *syn* and *anti*, were evidenced by spectroscopy in aqueous solution. In fact, the combination of ^{17}O NMR (note: at natural abundance) and quantum chemical calculations allowed an unequivocal assignment of uranyl- ^{17}O NMR signals and, thus, unambiguous decision on complex geometry and the overall configurations, with the *syn* isomer being strongly favored, but the *anti* isomer to coexist in aqueous solution and to interconvert among one another with a rate estimated to be in the order of 10^2 s $^{-1}$ at 25 °C. Apparently, the *anti* isomer crystallizes preferably owing to its higher symmetry which enables regular arrangement in the crystal lattice. The *syn* isomer can, hence, be considered more soluble. As a matter of fact, the

predominance of the *syn* isomer in solution was hitherto unnoticed, demonstrating that, particularly upon different physicochemical properties of the isomers, the solid phase does not necessarily reflect speciation and structures found in (aqueous) solution, underlining the importance of rigorous solution studies. In this context, an alternative explanatory approach is evinced for the disparity of uranyl oxygen atoms' ^{17}O chemical shifts. That is, spatially close hydrogen atoms instead of nearby oxygen atoms may impact the electronic environment of the probed nuclei. This issue deserves further investigation by both theoretical and spectroscopic methods.

Moreover, there is indication for uranium chirality as observed for U^{4+} , with the 1:1 $\text{U}^{\text{IV}}\text{-Cit}$ complexes forming two diastereomeric pairs of enantiomers (*R,R*)/(*S,S*) and (*S,R*)/(*R,S*), whereupon each of the two distinct Cit ligands possesses two different methylene groups, each with unique protons, giving rise to eight signals. For U^{4+} is spherical and thus showing no steric requirements, all isomers are equally populated, therefore all the signals are of same intensity. For chirality is not only a naturally occurring feature, but also exhibits interesting properties for both basic research, *e.g.*, optical rotation, and applied research such as chiral catalysts, further studies on uranium chirality might be a very interesting and promising project. Additionally, $\text{U}^{\text{IV}}\text{-Cit}$ complexes are candidates for both studying magneto-chiral dichroism and, particularly when succeeding (enantiopure) crystallization, synthesis of molecular magnets. The latter might be of outstanding magnetic and optical properties since a "crucial design factor expected to achieve a large boost in the magneto-chiral response is to have structural centers that support both the chirality and the magnetism" [199], with U^{IV} possessing two unpaired *f*-electrons (thus also being a chromophore), and both the metal and the ligand being chiral.

Comprehensive NMR measurements, supported by complementary UV-Vis-NIR and EXAFS experiments as well as quantum chemical calculations, shed light on the photoreaction in the uranyl-citrate system. Whereas the fate of the citrate was proven to be degradation to CO_2 , β -ketoglutarate, acetoacetate, and acetone regardless of sample conditions applied, that of U^{VI} was reduction to U^{IV} at pD 2 and U^{V} at pD 5, suggesting a two- and a one-electron transfer, respectively. Missing U^{V} evidence at pD 2 does not necessarily mean no formation at all, for its disproportionation is very fast under acidic conditions, however, is slowing down with increasing pD. Therefore, the NMR signals observed for the pD 5 samples at remarkable ^1H chemical shift values between 25 and 53 ppm, in combination with (weak) UV-Vis-NIR absorptions at 751 and 931 nm, are assigned to U^{V} complexes of citrate. With regard to reported pH-dependence on reaction rate and yield in the literature combined with observations in this work, H^+/D^+ are considered mechanistically crucial constituents. Furthermore, as evidenced by both experiment and quantum chemical calculation, the photoreaction proceeds *intermolecularly*, requiring for a citrate molecule not uranium-bound by its carboxyl groups – instead, *via* hydrogen bonding by dint of coordinating water.

For the U^{VI} –Cit 3:2 complex is considered photochemically active, light-irradiation may be an interesting route aiming at the synthesis of long-time stable U^V – and also mixed-valence uranium – containing $(U^V)(U^{VI})_2(Cit)_2$ species. Given fine-tuned conditions, the 3:2 U^{VI} precursor is the predominating species and dismutation of the formed U^V is less likely at circumneutral pH, hence sufficient amounts of obtained U^V may allow comprehensive spectroscopic or even crystallographic studies on usually short-living aqueous U^V .

In consideration of both the uranyl–citrate *photoreaction* and the uranyl–GSH *chemical* redox reaction, regardless of the respective mechanism, the process is *intermolecular*. This is not only a highly interesting, but the more a very important result, rendering the reductants not required to be bound to U^{VI} in order to reduce it. That is, in principle, or at least under certain (*e.g.*, pH) conditions, only weak or even non-binding ligands – by virtue of either unsuited speciation or functional groups – can act as reductants and, therefore, utilized for, *e.g.*, detoxification mechanisms *in vivo* or applied for focused synthesis or immobilization and remediation purposes.

For the first time spectroscopic evidence is given for hydrogen selenite dimerization in aqueous solution upon formation of homo-dimers by hydrogen bonding that are stable up to 60 °C and so are other selenium oxyanionic species. Observed temperature-induced changes in sorption behavior are, therefore, rather related to alterations in the surface properties. Additionally, the remarkably higher temperature coefficient of the hydrogen selenite dimer as compared to corresponding selenite and selenous acid was intensively discussed for it is touching both understanding of selenium speciation and the basics of (^{77}Se) NMR spectroscopy. These findings are attributed to a significant deshielding by changing rovibrational modes upon heating due to stretching the dimer as a whole instead of its dissociation into monomers owing to rather strong hydrogen bonds. Interaction of selenium oxyanions with ubiquitous alkaline earth metals, *i.e.*, Ca^{2+} and Mg^{2+} showed formation of weak complexes of Se^{VI} (selenate) and Se^{IV} (hydrogen selenite dimer) for excessive selenium, however, at high ionic strength (5.6 M) for equimolar Ca^{2+} and Se^{IV} even at pH_c 5 crystalline calcium selenite is formed, which is promising regarding Se immobilization attempts in high salinities.

Further selenium investigations, related to the current interest in biogenic zerovalent selenium nanoparticle formation, should involve Se–GSH interaction studies since in preliminary experiments indications for not only mechanistically important intermediates, *viz.* bis(glutathione)polyselenides, but also increased stability of the yielded red nanoparticles towards modification changes to elemental grey selenium were found.

Although some conditions and set-ups may seem rather academic, however, only by means of a sound understanding of the physical and chemical fundamentals determining radionuclide interaction by studying small model systems in a controlled simple environment, the influence of the various effects can be assessed individually so that robust results then can be used for safety and risk assessment or transformed into valuable applications.

5 EXPERIMENTAL DETAILS

5.1 SAMPLE PREPARATION

5.1.1 General remarks

All preparation steps were performed with safety precautions according to both radio- and chemotoxicity of natural uranium (U-nat.) and the chemotoxicity of water soluble selenium salts.

For the NMR spectra are usually recorded in deuterated solvents, that is, unless stated otherwise, throughout this work sample solutions refer to D₂O solutions, with pD adjustment achieved by accordingly deuterated reagents, as both stock solutions and dilutions thereof (deuterated water, D₂O, 99.98% D, DEUTERO or 99.8% D ALDRICH; deuteriochloric acid, DCl, 37% in D₂O with 99% D, DEUTERO, or 35% in D₂O with ≥99% D, ALDRICH; sodium deuterioxide, NaOD, 40% in D₂O with 99% D, DEUTERO or ALDRICH), and by means of $pD = pH + 0.4$, *i.e.*, addition of 0.4 units to the pH meter reading to obtain pD values, according to [200-201].

Additionally, a D₂O stock solution containing 0.01% of 4,4-dimethyl-4-silapentane-1-sulfonic acid sodium salt (DSS; ALDRICH, 97%) as ¹H and ¹³C NMR chemical shift reference was prepared and used for solution NMR sample preparation.

5.1.2 Glutathione–Lanthanide System

All samples (and blanks) contain a final [GSH] of 300 μM. Samples of varying [Ln^{III}] were prepared by admixture of appropriate aliquots of a freshly prepared GSH (ROTH, ≥98%) stock solution (intrinsically acidic) to weighed amounts of the respective Ln^{III} salts*, with continuous stirring and pD control (INOLAB WTW 720 pH meter with SCHOTT INSTRUMENTS Blue Line 16 pH electrode) and successive sample volume and pD adjustment towards the final GSH/Ln^{III} sample composition and pD (3 and 5). Since GSH is fairly stable at acidic conditions and only freshly prepared solutions were subjected to NMR measurement, samples were prepared under atmospheric conditions.

* Ln^{III} salts used: LaCl₃·7H₂O and CeCl₃·7H₂O (both 99.999%), EuCl₃·6H₂O (99.99%), YbCl₃·6H₂O and LuCl₃·6H₂O (both 99.9%), all by ALDRICH.

TRLFS samples with final [Eu^{III}] of 5.5×10^{-5} M and varying [GSH] were made from freshly prepared stock solutions of 5.5×10^{-3} M Eu^{III} and 5.5×10^{-2} M GSH in Milli-Q water, by mixture of appropriate aliquots thereof, with the final solutions containing 0.1 M NaCl (*p.a.*, Merck) for ionic strength maintenance.

5.1.3 Glutathione–Uranium System

5.1.3.1 Oxidizing conditions

Sample series of varying both pD and GSSG to U^{VI} ratio were prepared by admixture of appropriate amounts of a 100 mM U^{VI} stock solution, prepared by dissolving 1.3096 g $UO_3 \cdot 2.3H_2O$ (U-nat, $A = 25.5$ kBq/g) in 40 ml 0.5 M DCl, to aliquots of freshly prepared GSSG ($\geq 98\%$, SIGMA) stock solutions (in D_2O) under continuous stirring and pD control (XYLEM ANALYTICS WTW inoLab[®]720 pH meter with SCHOTT INSTRUMENTS Blue Line 16 pH electrode) and adjustment towards the final sample solution concentrations and pD. As both luminescence and NMR spectroscopy require different analyte concentrations, of the above mentioned stock solutions further diluted stock solutions were prepared. Since U^{VI} and GSSG are already present in their oxidized form, and studies are intended for oxidizing conditions, samples were prepared and handled under atmospheric conditions.

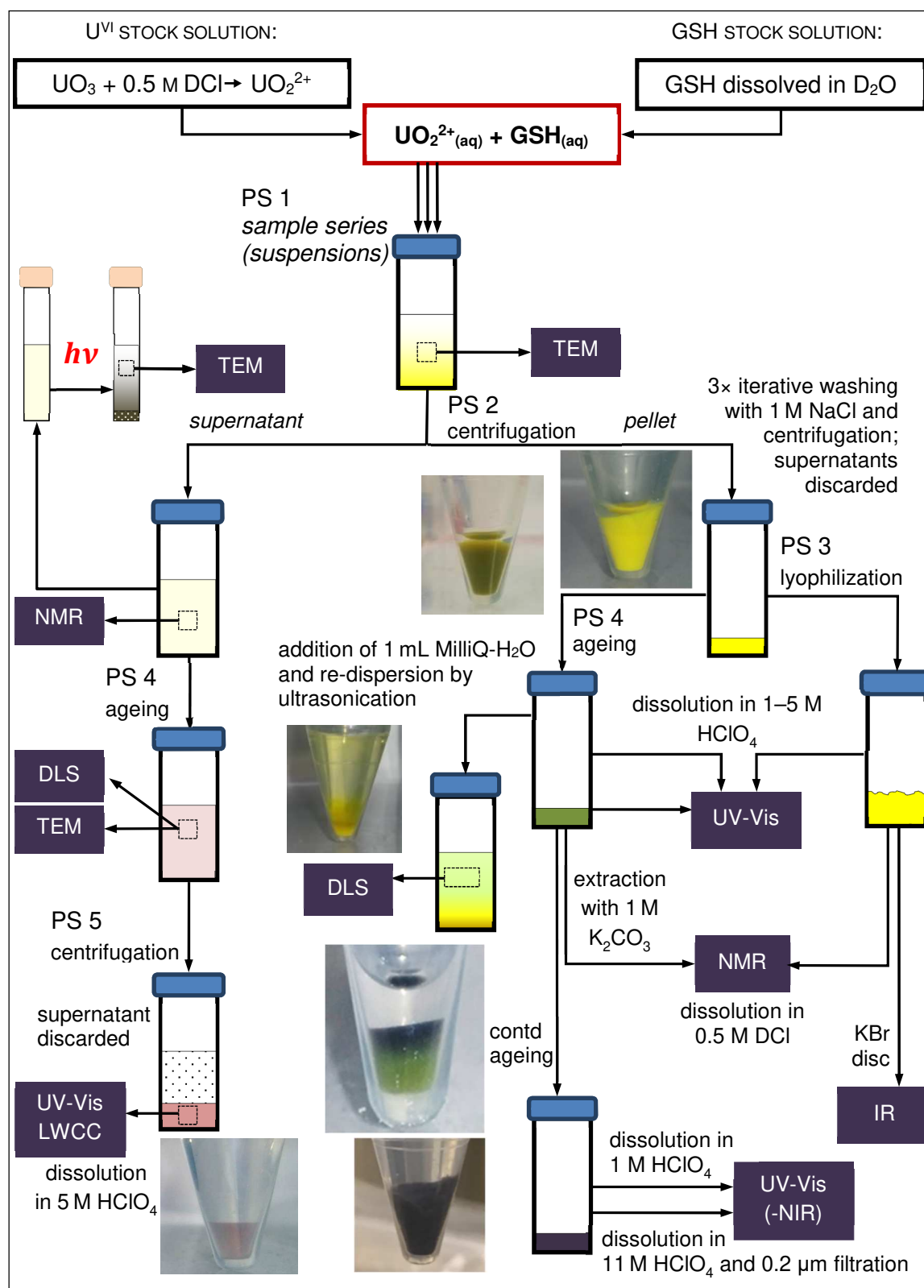
Owing to precipitate formation, after pD adjustment the suspensions were centrifuged for 1 h at $5500 \times g$ with a SIGMA 3K18 centrifuge, the obtained supernatants decanted, pD re-determined and, if necessary, adjusted to final value, prior to solution NMR spectroscopy. Selected corresponding pellets were washed three times with 1 M NaCl H_2O solution and repeatedly centrifuged, thereby discarding the accruing supernatants, and after lyophilization further analysed as KBr disc by IR spectroscopy. Upon storage (six months) of pellets in both conditions, wet-paste and lyophilized, the bright yellow appearance did not change.

Fractions of both supernatants and precipitates obtained from the GSSG– U^{VI} NMR sample preparation were used for U^{VI} luminescence spectroscopy. Therefore, the precipitates obtained after (initial) centrifugation were re-dispersed by ultrasonication, then twice iteratively washed with 1 M $NaClO_4$ solution and centrifuged, discarding the arising supernatants. Suspensions of the bright yellow precipitates dispersed in 1 M $NaClO_4$ as well as the decanted sample solutions' supernatants were transferred in a plastic cuvette, shock frozen by liquid N_2 , then subjected to luminescence spectroscopy.

Samples directly intended for TRLFS measurements were prepared using Milli-Q water (Alpha-Q, 18.2 M Ω cm). Aliquots of a 98 mM $UO_2(ClO_4)_2$ stock solution were further diluted and admixed to appropriate amounts of a 0.8 mM GSSG stock solution under continuous stirring, with 0.1 M $NaClO_4$ (*p.a.*, Merck) for total ionic strength maintenance. $HClO_4$ and NaOH were used for pH adjustment utilizing the above stated equipment by a parallel approach. That is, pH determination (with potentially chloride leaking electrodes) was performed with a parallel sample series of the same composition. Required amounts of $HClO_4$ and NaOH, respectively, were then used for adjustment of the TRLFS samples. The pH 3 ligand titration series for association constant determination applied 500 μM [U^{VI}] and the following [GSSG]: 0, 5, 10, 40, 70, 100, 150, and 200 μM .

5.1.3.2 Reducing conditions

Since very comprehensive, for this part an additional preparation scheme is given (Scheme 10), summarising all related processing steps (PS) and analyses at a glance.



Scheme 10. Preparation scheme showing the processing steps (PS) and analyses performed among the investigation of the Glutathione–Uranium^{VI} system under reducing conditions.

A 100 mM U^{VI} stock solution was prepared by dissolving 1.3096 g $UO_3 \cdot 2.3H_2O$ ($A = 24.3$ kBq) in 40 ml 0.5 M DCl. Proper aliquots of both the latter and a freshly prepared GSH (ROTH, $\geq 98\%$) stock solution were mixed by continuous stirring with pD control (XYLEM ANALYTICS WTW inoLab[®] pH Level 1 and pH 540 GLP pH meters with SCHOTT INSTRUMENTS Blue Line 16 pH electrodes) and adjustment towards final pD (2 to 10) and sample solution concentrations of 6.7 mM GSH and 0.33 through 33.3 mM U^{VI} , under N_2 atmosphere in a glovebox (PS 1). A further set of samples was prepared analogously, however, in H_2O solutions using HCl and NaOH for pH adjustment, applying 10 mM GSH and 5 mM U^{VI} , particularly intended for UV-Vis(-NIR) measurements. Of the latter series a control sample was kept dark the entire preparation and examination process, *i.e.*, right from the mixture of GSH and U^{VI} , pH adjustment, ageing, and occasional analyses, showed no differences in its reaction and, thus, spectroscopic behavior, as compared to samples handled at lab-light conditions.

Because of precipitate formation, after pH/pD adjustment and allowing the suspensions to equilibrate under continued stirring, the latter were centrifuged for 15 min at $14400 \times g$ with a BECKMAN COULTER Avanti j-20 XP centrifuge (PS 2). After decanting the obtained supernatants, pD was re-adjusted to final value, that is acidification, implying spent H^+/D^+ , respective aliquots were taken for extensive solution 1H NMR measurements. Selected corresponding pellets were washed three times with 1 M NaCl solution and repeatedly centrifuged, thereby discarding the accruing supernatants, and after lyophilization (PS 3) used as obtained for KBr disc IR spectroscopy, and after re-dissolution in 0.5 M DCl and 1 M $HClO_4$, respectively, for both NMR and UV-Vis spectroscopy.

Both remaining clear pale yellow supernatant solution and bright yellow wet paste pellet leftover from decanting were stored, *i.e. aged*, under N_2 atmosphere in the glovebox, with characteristic color changes (PS 4). Aliquots of the pale-brownish two months aged supernatant were analysed by both light microscopy and TEM, and after centrifugation (PS 5) and careful removal of the supernatant the residual brownish phase dissolved in 5 M $HClO_4$ and investigated by UV-Vis using a 250 cm LWCC. The meanwhile olive colored aged wet paste pellet (PS 4) was also analysed by NMR and UV-Vis-NIR spectroscopy after re-dissolution in 0.5 M DCl and 5 M $HClO_4$, respectively.

Samples for TEM measurements were prepared by dropping one drop of the solutions under investigation on a carbon-coated copper grid (400 mesh, S 160, Plano GmbH) and drying it under N_2 atmosphere. For TEM aliquots of 6.7 mM GSH and 3.3 mM U^{VI} samples at the following processing stages and conditions were used: (i) freshly prepared (non-centrifuged) yellow pD 7 suspension, (ii) pale brownish, two months aged decanted supernatant obtained from pD 7 suspension, and (iii) mercury lamp light-irradiated pD 2.25 solution.

5.1.4 Citrate – Uranium System

5.1.4.1 Complex structure studies

For the complexation concerns oxidized U^{VI} , samples were prepared under ambient conditions. Therefore, appropriate aliquots of 0.2 M citric acid (ROTH, *p.a.*) and 0.5 M uranyl nitrate stock solutions in D_2O were mixed accordingly to yield the desired final concentrations, with pD adjusted by DCl and NaOD, respectively. Two reference samples at pD 2 and 7 were prepared with concentrations of 0.25 M in both U^{VI} and Cit.

5.1.4.2 Photoreaction studies

Samples supposed to be photo-irradiated and extensively examined by means of NMR spectroscopy, were also investigated prior to light-irradiation; prepared under N_2 atmosphere, using D_2O as solvent, and DCl and NaOD for pD adjustment, by mixing aliquots of respective stock solutions of 200 mM Cit and 200 mM U^{VI} (prepared by dissolving 1.3096 g $UO_3 \cdot 2.3H_2O$ (U-nat, $A = 9.52$ kBq) in 20 ml 1 M DCl) to yield samples with $([U^{VI}]/[Cit]/pD)$ [in mM], and corresponding designation (UX) as follows: U1 (50/100/2), U2 (50/100/5), U3 (100/100/2), and U4 (100/100/5).

Samples studied by EXAFS were prepared analogously, however, using non-deuterated chemicals instead. For the samples of equimolar composition only half the concentrations were used as compared to the NMR samples. Accordingly, samples with $([U^{VI}]/[Cit]/pH)$ [in mM], and corresponding designation (U14-X) as follows: U14-48 (50/100/5), U14-49 (50/100/2), U14-50 (50/50/5), and U14-51 (50/50/2).

NMR U^{IV} -reference samples at pD 2 and 5, containing equimolar (50 mM) Cit and U^{IV} , were prepared under N_2 atmosphere by mixture of appropriate amounts of stock solutions of both Cit (100 mM) and U^{IV} , the latter finally being 89 mM, obtained by electrochemical reduction of a 100 mM acid U^{VI} solution. U^{IV} sample solution quality and quantity were verified by UV-Vis.

Light-irradiation was facilitated by a mercury-vapor lamp (LOT-ORIEL) for the NMR samples directly in the borosilicate glass NMR tube, for the EXAFS samples in quartz cuvettes, as long until the solutions changed their color from U^{VI} characteristic straw yellow to darker tones of yellowish/orange to olive/brownish, depending on pH, typically for reduced uranium. Whereas the NMR samples were measured immediately after light-irradiation, required amounts (≈ 2 ml) for EXAFS samples were transferred into a plastic cuvette reservoir, heat-sealed, and shock-frozen by and stored under liquid nitrogen until and during shipment to the beamline.

Note that during preparation in the lab the samples must be shielded from light, since even under these light conditions a photo-reaction is induced, albeit the fraction of degradation products is quite small.

5.1.5 Selenium

All Se^{VI} and Se^{IV} solutions were prepared by dissolving Na₂SeO₄ (SIGMA-ALDRICH, p.a.) and Na₂SeO₃ (APPLICHEM, >99%), respectively, in CO₂-free Millipore de-ionized water (Alpha-Q, 18.2 MΩ cm). All solutions were prepared in a glovebox under oxygen-free conditions (O₂ < 5 ppm). To adjust the ionic strength, dissolved NaCl (MERCK, p.a.) was used as background electrolyte. In order to avoid possible contamination of the solutions by silicate, polypropylene or polycarbonate flasks were used for all experiments. During preparation and transportation, all samples were kept under N₂ atmosphere. For NMR spectroscopy, 10 vol-% of D₂O (SIGMA-ALDRICH) were added to the aqueous solutions, thus reducing concentrations by 10%. Afterwards pH and concentration (by ICP-MS) were re-determined.

Se^{IV} dimerization related sample solutions were prepared at varying [Se^{IV}] ranging from 1 mM through 1 M at pH_c 5 and 13. To keep the ionic strength constant, samples were adjusted to *I* = 3 M by addition of NaCl if necessary, considering pH corrections due to ionic strength.

According to references [22,23], ionic-strength corrected pH, denoted pH_c, is defined as $\text{pH}_c = -\log_{10} [\text{H}^+] = \text{pH}_{\text{reading}} + A$, with *A* being a correction term applied to the pH-meter reading, depending on the respective electrolyte used:

$$A(\text{NaCl}) = -0.0988 + 0.1715 \times m(\text{NaCl}) + 0.0013 \times m(\text{NaCl})^2$$

$$A(\text{CaCl}_2) = -0.1176 + 0.4308 \times m(\text{CaCl}_2) + 0.0096 \times m(\text{CaCl}_2)^2$$

$$A(\text{MgCl}_2) = -0.0887 + 0.4549 \times m(\text{MgCl}_2) + 0.0172 \times m(\text{MgCl}_2)^2$$

with *m* denoting molality.

Investigations regarding the temperature impact on aqueous Se^{IV} and Se^{VI} speciation were carried out with 0.1 M aqueous solutions prepared at ambient temperature using NaOH and HCl for pH adjustment. Se^{IV} solutions were adjusted to pH values of 4, 10, and 13, that of Se^{VI} to pH 4 and 7.5.

To study the interaction of alkaline earth metal ions with selenium oxyanions, aqueous solutions containing 10 vol.-% of D₂O were prepared with sodium selenite or sodium selenate concentrations of 0.1 M under N₂ atmosphere in a glovebox. Appropriate amounts of CaCl₂·2H₂O or MgCl₂·6H₂O (both MERCK, p.a.) were added to yield metal concentrations of 0.05 and 0.10 M. Total ionic strength in all samples was set to 5.6 M (background electrolyte: NaCl) and pH_c was adjusted to 5 or 7.5 in the case of Se^{IV} or Se^{VI}, respectively.

The precipitate obtained from equimolar Se^{IV} and Ca²⁺ pH_c 5 solution was washed with de-ionized water, centrifuged and, after discarding the supernatant, lyophilized and then further analysed by means of IR (KBr disc) and ⁷⁷Se solid-state NMR spectroscopy, as well as thermogravimetry (SSC 5200 TG/DTA 22, SEIKO INSTRUMENTS, with 300 ml min⁻¹ argon gas flow and a heating rate of 5 K min⁻¹ up to 773 K) and X-ray powder diffraction (SIEMENS D5000 with BRAGG-BRENTANO configuration within 2θ of 5–70°, 0.02° step size and 2 s counting, using Cu-Kα, λ = 0.15406 nm).

At moderate ionic strength (< 0.5 M), pH measurements were performed with a XYLEM ANALYTICS WTW inoLab[®] 720 pH meter and a SCHOTT INSTRUMENTS Blue Line 16 pH combination glass electrode with incorporated Ag/AgCl reference electrode, whereas for samples at high ionic strength (3 and 5.6 M) WTW SenTix[®] Mic combination pH electrodes were used. Both electrodes were freshly calibrated using NIST-traceable buffer solutions, to an accuracy of ± 0.05 . The molar H⁺ concentrations in the solutions at high ionic strength were determined as described in detail elsewhere [22,23].

5.2 INSTRUMENTATION

5.2.1 Solution NMR

Measurements regarding the GSH–Ln^{III}, GSSG–U^{VI}, and Cit–U^{VI} systems (unless stated otherwise) were carried out on a VARIAN UNITY INOVA 400 spectrometer with a field strength of 9.4 T, corresponding to ¹H and ¹³C resonance frequencies of 400.1 and 100.6 MHz, respectively, using a 5 mm direct detection broadband probe. Investigations pertaining the GSH–U^{VI} (redox) samples were performed on an AGILENT DD2-600 NMR system, operating at 14.1 T with corresponding ¹H and ¹³C resonance frequencies of 599.8 and 150.8 MHz, respectively, using a 5 mm oneNMR[™] probe. ¹³C NMR spectra are ¹H-broadband decoupled. ⁷⁷Se dimerization, temperature impact, and M²⁺ complexation studies were conducted on a BRUKER DPX-400 with a corresponding ⁷⁷Se resonance frequency of 76.4 MHz, using a 10 mm broadband direct detection probe. ⁷⁷Se (repeated dimerization studies) and natural abundance-¹⁷O NMR spectra were acquired at the 14.1 T device at 114.6 and 81.4 MHz, respectively, utilising a 10 mm low-gamma broadband direct detection probe and a corresponding 80–125 MHz quarterwave switch. For all probed nuclei exact $\pi/2$ pulses were repeatedly verified. Except for ¹⁷O, and ¹H and ¹³C measurements in the presence of paramagnetic Ln^{III}, $\pi/6$ instead of $\pi/2$ pulses were applied. ¹⁷O and ⁷⁷Se as nuclei covering large frequency ranges (up to 100 and 240 kHz, respectively), sufficient excitation was assured by sweep-range partitioning. ¹H NMR spectra were in part acquired with water signal suppression by a 2 s pre-saturation pulse with offset on the water resonance, the latter depending on pD and sample composition, especially in the presence of paramagnetic Ln^{III}. ¹H and ¹³C chemical shifts are reported relative to the trimethylsilyl signal of DSS with δ_H and δ_C set to 0.0 ppm. ⁷⁷Se solution NMR spectra are referenced to $\delta_{Se}(\text{Me}_2\text{Se}) = 0$ ppm, using external sodium selenate solution as secondary reference with $\delta_{Se} = 1032$ ppm, according to Ref. [191]. ¹⁷O is referenced relative to bulk water (natural abundance ¹⁷OH₂), $\delta_O = 0$ ppm.

The DQF-COSY for the 50 mM U^{VI} and 100 mM Cit pD 2 sample was for once acquired at a 11.7 T BRUKER Avance III 500 at 0 °C, with 512 × 512 data points in F_2 and F_1 with 4 transitions per F_1 increment. Zero-filling was applied in both dimensions to obtain 2k × 2k real data points, and squared sine bell and squared cosine bell window function applied in F_2 and F_1 , respectively.

For the 250 mM U^{VI} and 250 mM Cit pD 7.5 solution correlation spectroscopy was performed on a 9.4 T AGILENT 400MR DD2 system. The H,H-COSY was acquired with 2 s pre-saturation pulse with offset on the HDO resonance, with 512 × 256 data points in F_2 and F_1 and 4 transitions per F_1 increment. In both dimensions a sine square bell multiplication and zero-filling to 2k × 1k real data points in F_2 and F_1 was applied, respectively. The corresponding H,C-HMBC spectrum was recorded using 512 × 1k data points in F_2 and F_1 and 32 acquisitions in F_1 , zero-filled to 2k × 4k real data points, applying cosine bell and sine square bell windows to F_2 and F_1 , respectively.

5.2.2 Solid-State NMR

⁷⁷Se solid-state NMR experiments were performed on a 9.4 T BRUKER Avance 400 WB, using a 4 mm CP/MAS probe and ZrO₂ rotors. The spectra are referenced externally to solid sodium selenate with $\delta_{\text{iso}} = 1049$ ppm [202].

5.2.3 UV-Vis-NIR

Apectra were acquired on a Tidas 100 UV-Vis-NIR spectrometer (J&M ANALYTIK AG) in the range between 200 and 1000 nm (for the aged wet paste pellet of a U^{VI}-GSH sample also down to 1400 nm) using a 1 cm quartz cuvette or, where required, a 250 cm liquid waveguide capillary cell (LWCC) by WORLD PRECISION INSTRUMENTS.

5.2.4 IR/Raman

GSSG-U^{VI} precipitates (KBr disc) were acquired with a PERKIN ELMER Spektrum 2000, GSH-U^{VI} precipitates (KBr disc) as well as Se^{IV} dimerization related sample solutions (using a horizontal ATR diamond crystal and blank solutions of same pH and ionic strength for background correction) were recorded on a BRUKER Vertex 80/v spectrometer, equipped with a mercury cadmium telluride (MCT) detector. Each IR spectrum recorded was an average over 256 scans at a spectral resolution of 4 cm⁻¹ using the OPUSTM software for data acquisition and evaluation.

Raman measurements of Se^{IV} dimerization related sample solutions were performed at room temperature with a dispersive HORIBA LabRam ARAMIS spectrometer equipped with a CCD detector. Three radiations, HeNe at 633 nm (output power 17 mW), Nd:YAG at 532 nm (output power 50 mW) and diode pumped solid-state laser at 473 nm (output power 20 mW) were used.

5.2.5 TRLFS

Eu^{III} luminescence spectroscopy was carried out with a pulsed flash lamp pumped Nd:YAG-OPO laser system (CONTINUUM). The solutions were stirred and both static and time-resolved europium spectra were recorded with an excitation wavelength of 394 nm, a gate width of 1 ms, a pulse energy of 2–3 mJ and an optical multichannel analyzer (spectrograph (ORIEL MS 257) and ICCD camera (ANDOR ISTAR)). Stationary spectra were recorded for a wavelength detection range of 565–650 nm, with 1200 lines per mm grating (0.2 nm resolution), and 2000 accumulations. Time-resolved spectra were recorded in the

wavelength detection range between 440 and 780 nm, with 300 lines per mm grating (0.7 nm resolution), 100 accumulations, and delay time steps of 15–40 μ s.

U^{VI} luminescence spectra were acquired by means of a Nd:YAG laser system (MINILITE laser system, CONTINUUM) pulsed with a repetition rate of 10 Hz at an excitation wavelength of 266 nm and an averaged pulse energy of 500 μ J. The luminescence emission was detected perpendicular to the direction of excitation, focused into a spectrograph and an ICCD camera system (both HORIBA JOBIN YVON) in the wavelength range 370–670 nm with a resolution of 0.3 nm by averaging 100 laser pulses using a gate width of 200 μ s. For measurements at 153 K (–120 °C) temperature maintenance was achieved by a cryostat (OERLICON LEYBOLD, Dresden, Germany). The shock frozen GSSG– U^{VI} sample precipitates and supernatants were released from the plastic cuvette and transferred as an ice cube in a specially designed sample holder (metal block with one hole to insert the sample and three windows for laser irradiation and luminescence emission detection).

5.2.6 XANES + EXAFS

EXAFS spectroscopy facilitated uranium L_{III} -edge measurements in transmission mode using a 13-element Ge detector at the Rossendorf Beamline (ROBL) BM20, ESRF, France. For energy calibration, an yttrium foil was measured simultaneously in transmission mode. The program suite EXAFSPAK [203] was used for averaging, dead-time correction, energy calibration, isolation of the EXAFS signal, and data fitting. The ionization energy (E_0) was set to 17185 eV for all spectra.

5.2.7 DLS

Particle size determination in suspensions was performed by dynamic light scattering using a Zetasizer Nano ZS (MALVERN INSTRUMENTS) device.

5.2.8 TEM

Bright-field TEM and high-resolution TEM (HRTEM) images were collected on an image-corrected TITAN 80-300 electron microscope (FEI) operating at 300 kV. Selected area electron diffraction (SAED) patterns were acquired from a specimen area of 190 nm in diameter. Energy-dispersive X-ray spectroscopy (EDXS) was performed with a Li-drifted silicon detector (EDAX).

5.2.9 Quantum Chemical Calculations

All calculations were computed with the Gaussian 09 program [160].

Regarding the Uranium–Citrate structures, the DFT method (B3LYP) [161-162] was employed through the use of the conductor-like polarizable continuum model (CPCM) [163-164]. The energy-consistent small-core effective core potential (ECP) and the corresponding basis set suggested by DOLG ET AL. [165] were used for uranium. The most diffuse basis functions on uranium with the exponent 0.005 (all s -, p -, d -, and f -type

functions) were omitted as in previous studies [125]. For carbon, oxygen, and hydrogen, valence double-zeta plus polarization basis was used [204]. The GIBBS energy correction to the electronic energy was calculated at the same level from the vibrational energy levels in aqueous phase and the molecular partition functions. The structures were confirmed to be energy minima through vibrational frequency analysis where no imaginary frequency was found to be present. Spin-orbit effect and the basis set superposition error (BSSE) corrections were neglected.

Se^{IV} dimerization related studies were performed at the MP2 level [205-206] using triple-zeta basis set including diffuse and polarization functions. Geometrical optimization as well as harmonic vibrational frequency calculations (IR) were performed in aqueous phase using the conductor-like polarizable continuum model (CPCM) [163-164] as the solvation model. The structure optimization and vibrational frequency calculations were performed for the selenite (SeO₃²⁻) and hydrogen selenite (HSeO₃⁻) ions and for two configurations of the (HSeO₃⁻)₂ dimer. Note that the optimization of these species was performed without imposing any symmetry constraint.

5.3 DATA PROCESSING AND ANALYSES

NMR data acquisition was performed with the workstation's operating software, TopSpinTM and VnmrJTM for BRUKER and VARIAN/AGILENT NMR systems, respectively. Spectra were further processed and spin simulations performed using MestReNova (version 6.0.2-5475) by MESTRELAB RESEARCH, S.L..

Electronic absorption, IR, Raman, and TRLFS spectra were drawn, and diagrams for data presentation and analyses created with OriginPro 9.1G (ORIGINLAB[®]). Applied non-linear fittings such as sigmoidal dose-response-fits or asymptotic fits were used as predefined and the corresponding fitting parameters given in the Appendix.

The GSH–Eu^{III} complex stability constant was determined from the luminescence spectra by using the factor analysis program SPECFIT [207]. Input parameters for the data fitting were the total concentrations of the metal ion and the ligand, pH, and the pK_a of GSH. A brief description of the operation mode of this program [92] and of the fitting procedure is given elsewhere [208].

PARAFAC was performed according to the description by DROBOT ET AL. [91] and related Refs. cited therein. All Toolboxes were used with MATLAB 8, R2013a.

6 REFERENCES

- [1] IAEA, Nuclear power reactors in the world. Reference data series. International Atomic Energy Agency, Vienna, (2019-02-21). <https://www.iaea.org/pris/> (retrieved 2019-02-22).
- [2] C. W. Forsberg, in *Encyclopedia of Physical Science and Technology (Third Edition)* (Ed.: R. A. Meyers), Academic Press, New York, **2003**, pp. 643-659.
- [3] D. Bodansky, *Nuclear Energy: Principles, Practices, and Prospects*, 2nd ed., Springer, New York, **2005**.
- [4] C. W. Forsberg, *Nucl. Technol.* **2000**, *131*, 337-353.
- [5] E. R. Landa, J. R. Gray, *Environ. Geol.* **1995**, *26*, 19-31.
- [6] J. R. Bargar, R. Bernier-Latmani, D. E. Giammar, B. M. Tebo, *Elements* **2008**, *4*, 407-412.
- [7] Y. Wang, M. Frutschi, E. Suvorova, V. Phrommavanh, M. Descostes, A. A. A. Osman, G. Geipel, R. Bernier-Latmani, *Nat. Commun.* **2013**, *4*.
- [8] E. J. O'Loughlin, S. D. Kelly, R. E. Cook, R. Csencsits, K. M. Kemner, *Environ. Sci. Technol.* **2003**, *37*, 721-727.
- [9] T. B. Scott, G. C. Allen, P. J. Heard, M. G. Randell, *Geochim. Cosmochim. Acta* **2005**, *69*, 5639-5646.
- [10] H. Veeramani, A. C. Scheinost, N. Monsegue, N. P. Qafoku, R. Kukkadapu, M. Newville, A. Lanzirrotti, A. Pruden, M. Murayama, M. F. Hochella, *Environ. Sci. Technol.* **2013**, *47*, 2361-2369.
- [11] M. I. Boyanov, K. E. Fletcher, M. J. Kwon, X. Rui, E. J. O'Loughlin, F. E. Löffler, K. M. Kemner, *Environ. Sci. Technol.* **2011**, *45*, 8336-8344.
- [12] J. M. Cerrato, M. N. Ashner, D. S. Alessi, J. S. Lezama-Pacheco, R. Bernier-Latmani, J. R. Bargar, D. E. Giammar, *Environ. Sci. Technol.* **2013**, *47*, 9756-9763.
- [13] S. Y. Lee, M. H. Baik, J. W. Choi, *Environ. Sci. Technol.* **2010**, *44*, 8409-8414.
- [14] D. R. Lovley, E. J. P. Phillips, Y. A. Gorby, E. R. Landa, *Nature* **1991**, *350*, 413-416.
- [15] Y. Suzuki, S. D. Kelly, K. M. Kemner, J. F. Banfield, *Nature* **2002**, *419*, 134-134.
- [16] Z. Zheng, J. E. Greedan, in *Encyclopedia of Physical Science and Technology (Third Edition)* (Ed.: R. A. Meyers), Academic Press, New York, **2003**, pp. 1-22.
- [17] K. A. Gschneidner Jr., L. Eyring, G. R. Choppin, G. H. Lander, *Handbook on the Physics and Chemistry of Rare Earths, Vol. 18: Lanthanides/Actinides: Chemistry*, Elsevier B.V., Amsterdam, **1994**.
- [18] J. R. Duffield, D. M. Taylor, in *Handbook on the Physics and Chemistry of the Actinides, Vol. 4* (Eds.: A. J. Freeman, C. Keller), Elsevier B.V., Amsterdam, **1986**.
- [19] D. S. Popplewell, G. N. Stradling, G. J. Ham, *Rad. Res.* **1975**, *62*, 513-519.
- [20] J. R. Duffield, P. M. May, D. R. Williams, *J. Inorg. Biochem.* **1984**, *20*, 199-214.
- [21] E. Rabinowitch, R. L. Belford, in *Spectroscopy and Photochemistry of Uranyl Compounds*, 1st edition ed. (Ed.: J. V. Dunworth), Pergamon, **1964**, pp. 229-334.
- [22] L. J. Heidt, K. A. Moon, *J. Am. Chem. Soc.* **1953**, *75*, 5803-5809.
- [23] H. D. Burrows, T. J. Kemp, *Chem. Soc. Rev.* **1974**, *3*, 139-165.
- [24] A. B. Yusov, V. P. Shilov, *Russ. Chem. Bull.* **2000**, *49*, 1925-1953.
- [25] J. Torres, V. Pintos, L. Gonzatto, S. Dominguez, C. Kerner, E. Kremer, *Chem. Geol.* **2011**, *288*, 32-38.
- [26] A. Fernandez-Martinez, L. Charlet, *Rev. Environ. Sci. Biotechnol.* **2009**, *8*, 81-110.

- [27] G. Jörg, R. Buhemann, S. Hollas, N. Kivel, K. Kossert, S. Van Winckel, C. L. V. Gostomski, *Appl. Radiat. Isot.* **2010**, *68*, 2339-2351.
- [28] ANDRA, Agence Nationale pour la gestion des Déchets RAdioactifs, Châtenay-Malabry, **2005**.
- [29] T. Brasser, J. Droste, I. Müller-Lyda, J. Neles, M. Sailer, G. Schmidt, M. Steinhoff, Gesellschaft für Anlagen und Reaktorsicherheit (GRS) mbH and Öko-Institut e.V., Braunschweig / Darmstadt, **2008**.
- [30] ONDRAF/NIRAS, Belgian Agency for Radioactive Waste and Enriched Fissile Materials, Brussels, **2001**.
- [31] P. H. Stauffer, P. K. Mishra, D. G. Levitt, B. A. Robinson, *Nucl. Technol.* **2014**, *187*, 294-307.
- [32] P. D'Angelo, A. Zitolo, V. Migliorati, G. Chillemi, M. Duvail, P. Vitorge, S. Abadie, R. Spezia, *Inorg. Chem.* **2011**, *50*, 4572-4579.
- [33] V. M. Sastri, J.-C. Bünzli, V. Ramachandra Rao, G. V. S. Rayudu, J. R. Perumareddi, *Modern aspects of rare earths and their complexes*, Elsevier B.V., Amsterdam, **2003**.
- [34] S. Hübener, in *Encyclopedia of Physical Science and Technology (Third Edition)* (Ed.: R. A. Meyers), Academic Press, New York, **2003**, pp. 211-236.
- [35] S. Cotton, *Lanthanide and Actinide Chemistry*, Wiley, London, **2006**.
- [36] R. G. Pearson, *J. Am. Chem. Soc.* **1963**, *85*, 3533-3539.
- [37] *EQ3/6: a software package for geochemical modeling of aqueous systems: package overview and installation guide (version 7.0)*, T. J. Wolery, Lawrence Livermore National Laboratory, Livermore, CA, **1992**.
- [38] R. Guillaumont, T. Fanghänel, J. Fuger, I. Grenthe, V. Neck, D. A. Palmer, M. H. Rand, OECD/NEA, *Update on the Chemical Thermodynamics of Uranium, Neptunium, Plutonium, Americium and Technetium*, Elsevier, Amsterdam, **2003**.
- [39] R. Dringen, *Progress in Neurobiology* **2000**, *62*, 649-671.
- [40] A. Meister, M. E. Anderson, *Annu. Rev. Biochem* **1983**, *52*, 711-760.
- [41] A. Pompella, A. Visvikis, A. Paolicchi, V. De Tata, A. F. Casini, *Biochem. Pharmacol.* **2003**, *66*, 1499-1503.
- [42] H. Sies, *Free Radical Biol. Med.* **1999**, *27*, 916-921.
- [43] J. Kretzschmar, E. Brendler, J. Wagler, A.-C. Schmidt, *J. Hazard. Mater.* **2014**, *280*, 734-740.
- [44] P. M. Kidd, *Altern. Med. Rev.* **1997**, *2*, 155-176.
- [45] A. Raha, K. D. Tew, in *Drug Resistance, Vol. 87* (Ed.: W. N. Hait), Springer US, **1996**, pp. 83-122.
- [46] B. K. Singh, *Asian J. Chem.* **2005**, *17*, 1-32.
- [47] B. Ketterer, B. Coles, D. J. Meyer, *Environ. Health Perspect.* **1983**, *49*, 59-69.
- [48] N. Vanhoudt, H. Vandenhove, K. Smeets, T. Remans, M. Van Hees, J. Wannijn, J. Vangronsveld, A. Cuypers, *Plant Physiol. Biochem.* **2008**, *46*, 987-996.
- [49] H. Vandenhove, A. Cuypers, M. Van Hees, G. Koppen, J. Wannijn, *Plant Physiol. Biochem.* **2006**, *44*, 795-805.
- [50] C. Cassier-Chauvat, F. Chauvat, *Int. J. Mol. Sci.* **2014**, *16*, 871-886.
- [51] K. Viehweger, G. Geipel, G. Bernhard, *BioMetals* **2011**, *24*, 1197-1204.
- [52] B. Noszál, Z. Szakács, *J. Phys. Chem. B* **2003**, *107*, 5074-5080.
- [53] T. N. Huckerby, A. J. Tudor, J. G. Dawber, *J. Chem. Soc., Perkin Trans. 2* **1985**, *0*, 759-763.

- [54] W. Hummel, G. Anderegg, I. Puigdomènech, L. Rao, O. Tochiyama, OECD/NEA, *Chemical Thermodynamics of Compounds and Complexes of U, Np, Pu, Am, Tc, Se, Ni and Zr with Selected Organic Ligands*, Elsevier, Amsterdam, **2005**.
- [55] D. M. Taylor, in *Handbook on the Physics and Chemistry of the Actinides*, Vol. 6 (Eds.: A. J. Freeman, C. Keller), Elsevier B.V., Amsterdam, **1991**.
- [56] F. Fordyce, *Ambio* **2007**, *36*, 94-97.
- [57] A. Kabata-Pendias, *J. Environ. Pathol., Toxicol. Oncol.* **1998**, *17*, 173-177.
- [58] A. Wessjohann Ludger, A. Schneider, M. Abbas, W. Brandt, *Biol. Chem.* **2007**, *388*, 997-1006.
- [59] T. C. Stadtman, *Science* **1974**, *183*, 915.
- [60] C. Frechou, S. Aguerre, J.-P. Degros, G. Kerlau, T. Grangeon, *Talanta* **2007**, *72*, 1166-1171.
- [61] A. Olin, B. Noläng, E. G. Osadchii, L.-O. Öhman, E. Rosén, OECD/NEA, *Chemical Thermodynamics of Selenium*, Elsevier, Amsterdam, **2005**.
- [62] J. Keeler, *Understanding NMR Spectroscopy*, Wiley, **2011**.
- [63] M. H. Levitt, *Spin Dynamics: Basics of Nuclear Magnetic Resonance*, Wiley, **2013**.
- [64] Prolate Spheroid by AugPi, 2004, Licensed to Wikimedia under GNU Free Documentation License (GFDL v. 1.3), <https://upload.wikimedia.org/wikipedia/commons/archive/8/88/20120221182303%21ProlateSpheroid.png> (retrieved 2018-04-17).
- [65] Oblate Spheroid by AugPi, 2004, Licensed to Wikimedia under GNU Free Documentation License (GFDL v. 1.3), <https://upload.wikimedia.org/wikipedia/commons/archive/b/b5/20120221182232%21OblateSpheroid.PNG> (retrieved 2018-04-17).
- [66] H. Yasuoka, G. Koutroulakis, H. Chudo, S. Richmond, D. K. Veirs, A. I. Smith, E. D. Bauer, J. D. Thompson, G. D. Jarvinen, D. L. Clark, *Science* **2012**, *336*, 901-904.
- [67] I. Bertini, C. Luchinat, G. Parigi, *Solution NMR of Paramagnetic Molecules*, Elsevier, Amsterdam, **2001**.
- [68] E. W. Stout Jr, H. S. Gutowsky, *J. Magn. Reson.* **1976**, *24*, 389-398.
- [69] B. C. Mayo, *Chem. Soc. Rev.* **1973**, *2*, 49-74.
- [70] C. C. Hinckley, *J. Am. Chem. Soc.* **1969**, *91*, 5160-5162.
- [71] J. D. Roberts, G. E. Hawkes, J. Husar, A. W. Roberts, D. W. Roberts, *Tetrahedron* **1974**, *30*, 1833-1844.
- [72] J. Schott, J. Kretzschmar, M. Acker, S. Eidner, M. U. Kumke, B. Drobot, A. Barkleit, S. Taut, V. Brendler, T. Stumpf, *Dalton Trans.* **2014**, *43*, 11516-11528.
- [73] J. Schott, J. Kretzschmar, S. Tsushima, B. Drobot, M. Acker, A. Barkleit, S. Taut, V. Brendler, T. Stumpf, *Dalton Trans.* **2015**, *44*, 11095-11108.
- [74] A. Barkleit, J. Kretzschmar, S. Tsushima, M. Acker, *Dalton Trans.* **2014**, *43*, 11221-11232.
- [75] D. Vila-Vicosa, H. A. Santos, V. H. Teixeira, M. Machuqueiro, *J. Phys. Chem. B* **2013**, *117*, 7507-7517.
- [76] H. Sigel, R. B. Martin, *Chem. Rev.* **1982**, *82*, 385-426.
- [77] J. F. Hinton, E. S. Amis, W. Mettetal, *Spectrochim. Acta, Part A* **1969**, *25*, 119-130.
- [78] M. L. D. Touche, D. R. Williams, *J. Chem. Soc., Dalton Trans.* **1976**, 1355-1359.
- [79] B. Podanyi, R. S. Reid, *J. Am. Chem. Soc.* **1988**, *110*, 3805-3810.
- [80] P. Feige, D. Mocker, R. Dreyer, R. Münze, *J. Inorg. Nucl. Chem.* **1973**, *35*, 3269-3275.
- [81] B. S. Garg, B. K. Singh, D. N. Kumar, P. K. Singh, *Indian J. Chem.* **2003**, *42A*, 79-83.

- [82] A. D. Sherry, E. Pascual, *J. Am. Chem. Soc.* **1977**, *99*, 5871-5876.
- [83] B. A. Levine, R. J. P. Williams, *Proc. R. Soc. London, Ser. A* **1975**, *345*, 5-23.
- [84] B. A. Levine, J. M. Thornton, R. J. P. Williams, *J. Chem. Soc., Chem. Commun.* **1974**, 669-670.
- [85] B. Bleaney, *J. Magn. Reson.* **1972**, *8*, 91-100.
- [86] R. M. Golding, M. P. Halton, *Aust. J. Chem.* **1972**, *25*, 2577-2581.
- [87] O. A. Gansow, P. A. Loeffler, R. E. Davis, M. R. Willcott, R. E. Lenkinski, *J. Am. Chem. Soc.* **1973**, *95*, 3389-3390.
- [88] B. Bleaney, C. M. Dobson, B. A. Levine, R. B. Martin, R. J. P. Williams, A. V. Xavier, *J. Chem. Soc., Chem. Commun.* **1972**, 791-793.
- [89] A. Strobel, Bachelor thesis, Faculty of Physical Engineering/Computer Sciences, University of Applied Sciences Zwickau / Institute of Resource Ecology, Helmholtz-Zentrum Dresden-Rossendorf **2014**.
- [90] G. Bernhard, G. Geipel, V. Brendler, H. Nitsche, *Radiochim. Acta* **1996**, *74*, 87-91.
- [91] B. Drobot, R. Steudtner, J. Raff, G. Geipel, V. Brendler, S. Tsushima, *Chem. Sci.* **2015**, *6*, 964-972.
- [92] A. Günther, R. Steudtner, K. Schmeide, G. Bernhard, *Radiochim. Acta* **2011**, *99*, 535-542.
- [93] R. Steudtner, T. Arnold, G. Geipel, G. Bernhard, *J. Radioanal. Nucl. Chem.* **2010**, *284*, 421-429.
- [94] G. Meinrath, *J. Radioanal. Nucl. Chem.* **1997**, *224*, 119-126.
- [95] Z. Wang, J. M. Zachara, W. Yantasee, P. L. Gassman, C. Liu, A. G. Joly, *Environ. Sci. Technol.* **2004**, *38*, 5591-5597.
- [96] K. Mizuoka, I. Grenthe, Y. Ikeda, *Inorg. Chem.* **2005**, *44*, 4472-4474.
- [97] K. Müller, V. Brendler, H. Foerstendorf, *Inorg. Chem.* **2008**, *47*, 10127-10134.
- [98] F. Quilès, A. Burneau, *Vib. Spectrosc.* **2000**, *23*, 231-241.
- [99] C. Lucks, A. Rossberg, S. Tsushima, H. Foerstendorf, A. C. Scheinost, G. Bernhard, *Inorg. Chem.* **2012**, *51*, 12288-12300.
- [100] K. Gückel, S. Tsushima, H. Foerstendorf, *Dalton Trans.* **2013**, *42*, 10172-10178.
- [101] H. R. Hoekstra, S. Siegel, *J. Inorg. Nucl. Chem.* **1973**, *35*, 761-779.
- [102] O. Lampela, A. H. Juffer, A. Rauk, *J. Phys. Chem. A* **2003**, *107*, 9208-9220.
- [103] M. Karplus, *J. Am. Chem. Soc.* **1963**, *85*, 2870-2871.
- [104] M. J. York, G. R. Beilharz, P. W. Kuchel, *Int. J. Pept. Protein Res.* **1987**, *29*, 638-646.
- [105] G. B. Deacon, R. J. Phillips, *Coord. Chem. Rev.* **1980**, *33*, 227-250.
- [106] M. Kakihana, T. Nagumo, M. Okamoto, H. Kakihana, *J. Phys. Chem.* **1987**, *91*, 6128-6136.
- [107] J. Kretzschmar, T. Haubitz, R. Hübner, S. Weiss, R. Husar, V. Brendler, T. Stumpf, *Chem. Commun.* **2018**, *54*, 8697-8700.
- [108] A. Ekstrom, *Inorg. Chem.* **1974**, *13*, 2237-2241.
- [109] D. M. H. Kern, E. F. Orlemann, *J. Am. Chem. Soc.* **1949**, *71*, 2102-2106.
- [110] H. Steele, R. J. Taylor, *Inorg. Chem.* **2007**, *46*, 6311-6318.
- [111] G. Leinders, R. Bes, J. Pakarinen, K. Kvashnina, M. Verwerft, *Inorg. Chem.* **2017**, *56*, 6784-6787.
- [112] D. Cohen, W. T. Carnall, *J. Phys. Chem.* **1960**, *64*, 1933-1936.
- [113] H. Wu, Y. Yang, Y. C. Cao, *J. Am. Chem. Soc.* **2006**, *128*, 16522-16523.
- [114] T. Ling, H. Yu, Z. Shen, H. Wang, J. Zhu, *Nanotechnology* **2008**, *19*, 115608.
- [115] E. J. O'Loughlin, S. D. Kelly, R. E. Cook, R. Csencsits, K. M. Kemner, *Environ. Sci. Technol.* **2003**, *37*, 721-727.

- [116] T. B. Scott, G. C. Allen, P. J. Heard, M. G. Randell, *Geochim. Cosmochim. Acta* **2005**, *69*, 5639-5646.
- [117] H. Veeramani, A. C. Scheinost, N. Monsegue, N. P. Qafoku, R. Kukkadapu, M. Newville, A. Lanzirrotti, A. Pruden, M. Murayama, M. F. Hochella, *Environ. Sci. Technol.* **2013**, *47*, 2361-2369.
- [118] M. I. Boyanov, K. E. Fletcher, M. J. Kwon, X. Rui, E. J. O'Loughlin, F. E. Löffler, K. M. Kemner, *Environ. Sci. Technol.* **2011**, *45*, 8336-8344.
- [119] J. M. Cerrato, M. N. Ashner, D. S. Alessi, J. S. Lezama-Pacheco, R. Bernier-Latmani, J. R. Bargar, D. E. Giammar, *Environ. Sci. Technol.* **2013**, *47*, 9756-9763.
- [120] S. Y. Lee, M. H. Baik, J. W. Choi, *Environ. Sci. Technol.* **2010**, *44*, 8409-8414.
- [121] F. Q. Schäfer, G. R. Buettner, *Free Radical Biol. Med.* **2001**, *30*, 1191-1212.
- [122] I. Grenthe, J. Fuger, R. J. M. Konings, R. J. Lemire, A. B. Muller, C. Nguyen-Trung, H. Wanner, *Chemical Thermodynamics of Uranium, Vol. 1*, Elsevier Science, Paris, **1992**.
- [123] K. Meng, J. Medina-Ramos, E. Yibeltal-Ashenafi, J. C. Alvarez, *Phys. Chem. Chem. Phys.* **2018**, *20*, 17666-17675.
- [124] Z. Szabó, I. Furó, I. Csöreg, *J. Am. Chem. Soc.* **2005**, *127*, 15236-15247.
- [125] S. Tsushima, *Dalton Trans.* **2011**, *40*, 6732-6737.
- [126] S. Tsushima, A. Rossberg, A. Ikeda, K. Müller, A. C. Scheinost, *Inorg. Chem.* **2007**, *46*, 10819-10826.
- [127] G. Lu, A. J. Haes, T. Z. Forbes, *Coord. Chem. Rev.* **2018**, *374*, 314-344.
- [128] V. Vallet, T. Privalov, U. Wahlgren, I. Grenthe, *J. Am. Chem. Soc.* **2004**, *126*, 7766-7767.
- [129] I. Feldman, W. F. Neuman, *J. Am. Chem. Soc.* **1951**, *73*, 2312-2315.
- [130] I. Feldman, J. R. Havill, W. F. Neuman, *J. Am. Chem. Soc.* **1954**, *76*, 4726-4732.
- [131] I. Feldman, C. A. North, H. B. Hunter, *J. Am. Chem. Soc.* **1960**, *64*, 1224-1230.
- [132] S. Berto, F. Crea, G. Daniele Pier, C. De Stefano, E. Prenesti, S. Sammartano, *Radiochim. Acta* **2012**, *100*, 13-28.
- [133] M. T. Nunes, V. M. S. Gil, *Inorg. Chim. Acta* **1987**, *129*, 283-287.
- [134] K. S. Rajan, A. E. Martell, *Inorg. Chem.* **1965**, *4*, 462-469.
- [135] S. P. Pasilis, J. E. Pemberton, *Inorg. Chem.* **2003**, *42*, 6793-6800.
- [136] C. Lucks, Ph.D. thesis, Technische Universität Dresden; Institut für Ressourcenökologie, Helmholtz-Zentrum Dresden-Rossendorf **2012**.
- [137] M. Basile, D. K. Unruh, K. Gojdas, E. Flores, L. Streicher, T. Z. Forbes, *Chem. Commun.* **2015**, *51*, 5306-5309.
- [138] P. Thuery, *CrystEngComm* **2007**, *9*, 358-360.
- [139] Y. Suzuki, T. Nankawa, T. Yoshida, T. Ozaki, T. Ohnuki, A. J. Francis, S. Tsushima, Y. Enokida, I. Yamamoto, *Radiochim. Acta* **2006**, *94*, 579-583.
- [140] P. G. Allen, D. K. Shuh, J. J. Bucher, N. M. Edelstein, T. Reich, M. A. Denecke, H. Nitsche, *Inorg. Chem.* **1996**, *35*, 784-787.
- [141] R. Meyer, Master thesis, Faculty of Mechanical Science and Engineering, University of Applied Sciences Dresden / Institute of Resource Ecology, Helmholtz-Zentrum Dresden-Rossendorf **2012**.
- [142] P. Thuery, *Inorg. Chem.* **2007**, *46*, 2307-2315.
- [143] P. Thuery, *CrystEngComm* **2008**, *10*, 79-85.
- [144] P. Thuery, *CrystEngComm* **2013**, *15*, 6533-6545.
- [145] R. Bramley, W. F. Reynolds, I. Feldman, *J. Am. Chem. Soc.* **1965**, *87*, 3329-3332.

- [146] F. Castiglione, A. Mele, G. Raos, in *Annual Reports on NMR Spectroscopy, Vol. 85* (Ed.: G. A. Webb), Academic Press, **2015**, pp. 143-193.
- [147] D. L. Clark, S. D. Conradson, R. J. Donohoe, D. W. Keogh, D. E. Morris, P. D. Palmer, R. D. Rogers, C. D. Tait, *Inorg. Chem.* **1999**, *38*, 1456-1466.
- [148] Z. Szabó, J. Glaser, I. Grenthe, *Inorg. Chem.* **1996**, *35*, 2036-2044.
- [149] W.-S. Jung, M. Harada, H. Tomiyasu, H. Fukutomi, *Bull. Chem. Soc. Jpn.* **1988**, *61*, 3895-3900.
- [150] P. G. Allen, J. J. Bucher, D. L. Clark, N. M. Edelstein, S. A. Ekberg, J. W. Gohdes, E. A. Hudson, N. Kaltsoyannis, W. W. Lukens, M. P. Neu, P. D. Palmer, T. Reich, D. K. Shuh, C. D. Tait, B. D. Zwick, *Inorg. Chem.* **1995**, *34*, 4797-4807.
- [151] H. Moll, T. Reich, C. Hennig, A. Roßberg, Z. Szabó, I. Grenthe, *Radiochim. Acta* **2000**, *88*, 559.
- [152] Z. Szabó, *J. Chem. Soc., Dalton Trans.* **2002**, *0*, 4242-4247.
- [153] T. Watanabe, Y. Ikeda, *Energy Procedia* **2013**, *39*, 81-95.
- [154] L. S. Natrajan, *Coord. Chem. Rev.* **2012**, *256*, 1583-1603.
- [155] G. E. Heckler, A. E. Taylor, C. Jensen, D. Percival, R. Jensen, P. Fung, *J. Phys. Chem.* **1963**, *67*, 1-6.
- [156] A. Adams, T. D. Smith, *J. Chem. Soc.* **1960**, 4846-4850.
- [157] A. Ohyoshi, K. Ueno, *J. Inorg. Nucl. Chem.* **1974**, *36*, 379-384.
- [158] R. Steudtner, Ph.D. thesis, Technische Universität Dresden; Institut für Radiochemie, Forschungszentrum Dresden-Rossendorf **2010**.
- [159] C. J. Dodge, A. J. Francis, *Environ. Sci. Technol.* **1994**, *28*, 1300-1306.
- [160] *Gaussian 09*, M. J. Frisch, G. W. Trucks, H. B. Schlegel, G. E. Scuseria, M. A. Robb, J. R. Cheeseman, G. Scalmani, V. Barone, B. Mennucci, G. A. Petersson, H. Nakatsuji, M. Caricato, X. Li, H. P. Hratchian, A. F. Izmaylov, J. Bloino, G. Zheng, J. L. Sonnenberg, M. Hada, M. Ehara, K. Toyota, R. Fukuda, J. Hasegawa, M. Ishida, T. Nakajima, Y. Honda, O. Kitao, H. Nakai, T. Vreven, J. A. Montgomery, Jr., J. E. Peralta, F. Ogliaro, M. Bearpark, J. J. Heyd, E. Brothers, K. N. Kudin, V. N. Staroverov, R. Kobayashi, J. Normand, K. Raghavachari, A. Rendell, J. C. Burant, S. S. Iyengar, J. Tomasi, M. Cossi, N. Rega, J. M. Millam, M. Klene, J. E. Knox, J. B. Cross, V. Bakken, C. Adamo, J. Jaramillo, R. Gomperts, R. E. Stratmann, O. Yazyev, A. J. Austin, R. Cammi, C. Pomelli, J. W. Ochterski, R. L. Martin, K. Morokuma, V. G. Zakrzewski, G. A. Voth, P. Salvador, J. J. Dannenberg, S. Dapprich, A. D. Daniels, Ö. Farkas, J. B. Foresman, J. V. Ortiz, J. Cioslowski, and D. J. Fox, *Gaussian 09, Revision A.02*, Gaussian Inc., Wallingford CT, **2009**.
- [161] A. D. Becke, *J. Chem. Phys.* **1993**, *98*, 5648-5652.
- [162] C. Lee, W. Yang, R. G. Parr, *Phys. Rev. B* **1988**, *37*, 785-789.
- [163] V. Barone, M. Cossi, *J. Phys. Chem. A* **1998**, *102*, 1995-2001.
- [164] M. Cossi, N. Rega, G. Scalmani, V. Barone, *J. Comput. Chem.* **2003**, *24*, 669-681.
- [165] W. Küchle, M. Dolg, H. Stoll, H. Preuss, *J. Chem. Phys.* **1994**, *100*, 7535-7542.
- [166] S. Tsushima, *Inorg. Chem.* **2009**, *48*, 4856-4862.
- [167] J. T. Bell, H. A. Friedman, M. R. Billings, *J. Inorg. Nucl. Chem.* **1974**, *36*, 2563-2567.
- [168] D. Cohen, *J. Inorg. Nucl. Chem.* **1970**, *32*, 3525-3530.
- [169] K. Schmeide, G. Bernhard, in *Uranium, Mining and Hydrogeology* (Eds.: B. J. Merkel, A. Hasche-Berger), Springer Berlin Heidelberg, Berlin, Heidelberg, **2008**, pp. 591-598.
- [170] J. Torres, V. Pintos, S. Dominguez, C. Kremer, E. Kremer, *J. Solution Chem.* **2010**, *39*, 1-10.

- [171] J. Janickis, H. Gutmanaitė, *Z. Anorg. Allg. Chem.* **1936**, 227, 1-16.
- [172] H. Ley, E. König, *Z. Phys. Chem., Abt. B* **1938**, 41, 365-387.
- [173] A. Rosenheim, L. Krause, *Z. Anorg. Allg. Chem.* **1921**, 118, 177-192.
- [174] A. Miolati, E. Mascetti, *Gazz. Chim. Ital.* **1901**, 31, 93-139.
- [175] L. Barcza, L. G. Sillen, *Acta Chem. Scand.* **1971**, 25, 1250-1260.
- [176] R. Sabbah, G. Carpeni, *J. Chim. Phys. Phys.-Chim. Biol.* **1966**, 63, 1549-1554.
- [177] E. S. Ganelina, V. P. Kuzmicheva, M. B. Krasnopolskaya, *Russ. J. Inorg. Chem.* **1973**, 18, 698-700.
- [178] R. Arnek, L. Barcza, *Acta Chem. Scand.* **1972**, 26, 213-217.
- [179] J. N. Cooper, M. Woods, J. C. Sullivan, E. Deutsch, *Inorg. Chem.* **1976**, 15, 2862-2864.
- [180] L. S. A. Dikshitulu, P. Vani, B. V. Kumar, *J. Indian Chem. Soc.* **1984**, 61, 385-388.
- [181] L. S. A. Dikshitulu, P. Vani, V. H. Rao, *Indian J. Chem., Sect. A: Inorg., Phys., Theor. Anal.* **1981**, 20, 36-39.
- [182] S. Nadimpalli, R. Rallabandi, D. S. A. Lanka, *Transit. Met. Chem.* **1990**, 15, 191-196.
- [183] N. Voigt, Bachelor thesis, Institute of Analytical Chemistry, TU Bergakademie Freiberg **2010**.
- [184] J. Kretzschmar, N. Jordan, E. Brendler, S. Tsushima, C. Franzen, H. Foerstendorf, M. Stockmann, K. Heim, V. Brendler, *Dalton Trans.* **2015**, 44, 10508-10515.
- [185] H. Kolshorn, H. Meier, *J. Chem. Res.* **1977**, 338-339.
- [186] C. J. Jameson, *Annu. Rev. Phys. Chem.* **1996**, 47, 135-169.
- [187] H. Duddleck, *Prog. Nucl. Magn. Reson. Spectrosc.* **1995**, 27, 1-323.
- [188] J. Milne, *Magn. Reson. Chem.* **1993**, 31, 652-655.
- [189] L. Eklund, I. Persson, *Dalton Trans.* **2014**, 43, 6315-6321.
- [190] M. Falk, P. A. Giguère, *Can. J. Chem.* **1958**, 36, 1680-1685.
- [191] W. Koch, O. Lutz, A. Nolle, *Z. Naturforsch., A: Phys. Sci.* **1978**, 33, 1025-1028.
- [192] K. A. Tay, F. Bresme, *Phys. Chem. Chem. Phys.* **2009**, 11, 409-415.
- [193] J. Mason, *Solid State Nucl. Magn. Reson.* **1993**, 2, 285-288.
- [194] M. Ebert, D. Havlicek, *Collect. Czech. Chem. Commun.* **1981**, 46, 1740-1747.
- [195] S. E. Lohse, C. J. Murphy, *J. Am. Chem. Soc.* **2012**, 134, 15607-15620.
- [196] R. C. Fahey, *Annu. Rev. Microbiol.* **2001**, 55, 333-356.
- [197] V. K. Jothivasan, C. J. Hamilton, *Nat. Prod. Rep.* **2008**, 25, 1091-1117.
- [198] G. L. Newton, M. Rawat, J. J. La Clair, V. K. Jothivasan, T. Budiarto, C. J. Hamilton, A. Claiborne, J. D. Helmann, R. C. Fahey, *Nat. Chem. Biol.* **2009**, 5, 625-627.
- [199] L. D. Barron, *Nat. Mater.* **2008**, 7, 691-692.
- [200] A. Kresge, *Pure Appl. Chem* **1964**, 8, 243-258.
- [201] K. Mikkelsen, S. O. Nielsen, *J. Phys. Chem.* **1960**, 64, 632-637.
- [202] T. F. Kemp, A. Wong, M. E. Smith, P. T. Bishop, N. Carthey, *Solid State Nucl. Magn. Reson.* **2008**, 34, 224-227.
- [203] *EXAFSPAK: A Suite of Computer Programs for Analysis of X-ray Absorption Spectra*, G. N. George, I. J. Pickering, Stanford Synchrotron Radiation Laboratory: Stanford, CA, **1995**.
- [204] R. Krishnan, J. S. Binkley, R. Seeger, J. A. Pople, *J. Chem. Phys.* **1980**, 72, 650-654.
- [205] M. Head-Gordon, T. Head-Gordon, *Chem. Phys. Lett.* **1994**, 220, 122-128.
- [206] M. Head-Gordon, J. A. Pople, M. J. Frisch, *Chem. Phys. Lett.* **1988**, 153, 503-506.
- [207] *SPECFIT Global Analysis System*, R. A. Binstead, A. D. Zuberbühler, B. Jung, Version 3.0.37, Spectrum Software Associates, Marlborough, MA, USA, **2005**.
- [208] A. Barkleit, M. Acker, G. Bernhard, *Inorg. Chim. Acta* **2013**, 394, 535-541.

-
- [209] L. Alderighi, P. Gans, A. Ienco, D. Peters, A. Sabatini, A. Vacca, *Coord. Chem. Rev.* **1999**, *184*, 311-318.
- [210] L. Frost, G. Geipel, K. Viehweger, G. Bernhard, *Proc. Radiochim. Acta* **2011**, *1*, 357-362.
- [211] A. Günther, G. Geipel, G. Bernhard, *Polyhedron* **2007**, *26*, 59-65.
- [212] J. T. Bell, R. E. Biggers, *J. Mol. Spectrosc.* **1967**, *22*, 262-271.
- [213] C. Miyake, Y. Yamana, S. Imoto, H. Ohya-Nishiguchi, *Inorg. Chim. Acta* **1984**, *95*, 17-21.
- [214] K. Mizuoka, S. Tsushima, M. Hasegawa, T. Hoshi, Y. Ikeda, *Inorg. Chem.* **2005**, *44*, 6211-6218.
- [215] H. Monjushiro, H. Hara, Y. Yokoyama, *Polyhedron* **1992**, *11*, 845-846.
- [216] I. Grenthe, J. Drożdżyński, T. Fujino, E. C. Buck, T. E. Albrecht-Schmitt, S. F. Wolf, in *The Chemistry of the Actinide and Transactinide Elements* (Eds.: L. R. Morss, N. M. Edelstein, J. Fuger), Springer Netherlands, Dordrecht, **2006**, pp. 253-698.
- [217] *Description of input and examples for PHREEQC version 3 – A computer program for speciation, batch-reaction, one-dimensional transport, and inverse geochemical calculations*, D. L. Parkhurst, C. A. J. Appelo, U.S. Geological Survey Techniques and Methods 6–A43, **2013**.

7 LIST OF FIGURES AND SCHEMES

Figure	Caption	Page
1	Aquatic speciation of 1×10^{-4} M U^{VI} in 0.1 M $NaClO_4$ medium at 25 °C under nitrogen atmosphere (top) and ambient atmosphere (bottom).	8
2	Generic structure of GSH and GSSG.	10
3	Generic structure of citric acid.	12
4	^{77}Se NMR spectra of Se species of different oxidation and protonation state.	17
5	1H NMR pD titration series of 6.7 mM GSH.	18
6	Luminescence spectra of 5.5×10^{-5} M Eu^{III} with 50-fold excess in GSH at varying pH, and at constant pH 6 for varying GSH/Eu ratios, with total ionic strength of 0.1 M.	20
7	^{13}C NMR spectra of 300 mM GSH at pD 5 without, and in the presence of 30, 60, 100, and 300 mM La^{III} .	21
8	La^{III} -induced ^{13}C chemical shift changes as a function of $[La^{III}]$ obtained from spectra of 300 mM GSH at pD 5.	22
9	1H NMR spectra of 300 mM GSH at pD 5 without, and in the presence of 30, 60, 100, and 300 mM Eu^{III} .	23
10	^{13}C NMR spectra of 300 mM GSH at pD 5 without, and in the presence of 30, 60, 100, and 300 mM Eu^{III} .	24
11	Eu^{III} -induced ^{13}C chemical shift changes as a function of $[Eu^{III}]$ obtained from spectra of 300 mM GSH at pD 3 and pD 5.	25
12	^{13}C NMR carbonyl region and 1H NMR Gly α and Glu α region of pD-dependent spectra of GSSG blanks and U^{VI} containing solutions with initial GSSG and U^{VI} concentrations of 150 mM and 75 mM, respectively.	27
13	Luminescence spectra acquired at 153 K of supernatants obtained from 150 mM GSSG and 7.5 mM U^{VI} solutions at pD 3 through pD 8.	29
14	Crystal structure representation of GSSG at pH 3.	31

15	Exemplary IR spectra (KBr disc) of the washed and lyophilized precipitate pellets obtained from pD 2 and pD 8 suspensions of 150 mM GSSG and 7.5 mM U ^{VI} .	32
16	Luminescence spectra acquired at 153 K of precipitates obtained from 150 mM GSSG and 7.5 mM U ^{VI} solutions at varying pD.	34
17	U ^{VI} fraction remaining dissolved in solution for different sample series of varying both initial GSSG concentration and GSSG/U ^{VI} ratio.	36
18	¹ H NMR spectra of 5 mM GSH and varying U ^{VI} contents at pD 2.	38
19	U ^{VI} -induced ¹ H chemical shift changes ($\Delta_U\delta_H$) as a function of M/L obtained from spectra of 5 mM GSH and varying U ^{VI} content at pD 2.	38
20	¹ H NMR spectra of 6.7 mM GSH blanks and samples with initial M/L = 2 in the pD range 2–5.	39
21	U ^{VI} -induced ¹ H chemical shift changes as a function of pD obtained from spectra of 6.7 mM GSH and initial M/L = 2.	40
22	GSH and uranium contents remaining in solution for sample series of initial 6.7 mM GSH and either 13.3 mM U ^{VI} or 3.3 mM U ^{VI} .	42
23	¹ H NMR spectra of the Cys and Glu signals of 6.7 mM GSH blank at pD 3.25 and the pD 3.25 U ^{VI} sample with M/L = 2 as well as the corresponding spin simulations.	43
24	FT-IR spectrum (KBr disc) of the washed and lyophilized precipitate (yellow powder) obtained from 6.7 mM GSH pD 5 solution of initial M/L = 5.	46
25	TEM micrographs obtained from a dried aliquot of a freshly prepared sample suspension of initial 6.7 mM GSH and M/L = 0.5 at pD 7.	47
26	Photographs of the GSH–U ^{VI} precipitates: pellet immediately after washing and centrifugation, and after ageing for 1 and 5 months.	48
27	UV-Vis spectra of the wet paste pellet obtained from 10 mM GSH and 5 mM U ^{VI} at pH 8 aged for one month, treated with either 1 M HClO ₄ or 1 M K ₂ CO ₃ , and aged for five months and treated with 1 M HClO ₄ .	49
28	UV-Vis-NIR spectrum of the aged precipitate of the initial 10 mM GSH pH 8 M/L = 0.5 sample solution precipitate re-dissolved in 11 M HClO ₄ .	49

29	^1H NMR spectra of GSH pD 2 blank, and repeatedly washed GSH- U^{VI} sample suspension precipitate promptly lyophilized or after ageing as wet paste for two months, re-dissolved in 0.5 M DCl, respectively.	50
30	Light microscope image and TEM micrographs at different magnifications obtained from aged pale brownish supernatant of the sample of initial 6.7 mM GSH M/L = 0.5 at pD 7.	52
31	Aged pale brownish supernatant of the initial 6.7 mM GSH M/L = 0.5 pD 7 sample: bright-field TEM image, STEM micrographs with yellow spearheads indicating some chain-like building blocks, and photograph of the material after centrifugation.	53
32	UV-Vis spectrum of the pale brownish material obtained from centrifugation of the aged supernatant of the initial 6.7 mM GSH M/L = 0.5 pD 7 sample re-dissolved in 5 M HClO_4 and acquired with a LWCC ($d = 250$ cm).	55
33	Bright-field TEM micrographs of dark grey precipitate obtained <i>after light-irradiation</i> of a 6.7 mM GSH and 3.3 mM U^{VI} pD 2.25 sample at different magnifications.	56
34	Calculated changes in GIBBS energy in dependence of pH for the redox reactions of GSH with U^{VI} for both redox couples $\text{U}^{\text{VI}}/\text{U}^{\text{IV}}$ and $\text{U}^{\text{VI}}/\text{U}^{\text{V}}$.	58
35	^1H and ^{13}C NMR spectra of citric acid in D_2O at pD 2, 5, and 8, together with signal assignment.	62
36	Molecular structures of U^{VI} -Cit dimeric and trimeric complexes as determined from aqueous solution and from single crystals.	64
37	Conceivable 2:2 U^{VI} -Cit complex structures for different geometries, illustrating chelate ring sizes and arrangement.	65
38	DQF-COSY spectrum of 100 mM Cit and 50 mM U^{VI} pD 2 solution at 0 °C.	69
39	^1H and ^{13}C NMR spectra of 250 mM citric acid pD 2.5 solutions without and in the presence of 250 mM U^{VI} .	71
40	^{17}O NMR of 0.5 M natural ^{17}O abundance uranyl nitrate in D_2O at pD 1.	72
41	^{17}O NMR uranyl region of natural ^{17}O abundance uranyl nitrate and citric acid, both 250 mM, in D_2O at pD 2.5, together with spectral deconvolution.	74

42	DFT-calculated structures of U ^{VI} -Cit 2:2 complex <i>syn</i> and <i>anti</i> isomer.	75
43	Visualization of close spatial proximity between one of the oxygen atoms in the uranyl entities and specific hydrogen atoms shown for uranyl-adenosine-monophosphate complex.	77
44	Generic structures of U ^{VI} -Cit 3:3 and 3:2 sub-unit of 9:6 complex.	78
45	H,C-HMBC of 250 mM U ^{VI} and 250 mM citrate at pD 7.5.	79
46	H,H-COSY of 250 mM U ^{VI} and 250 mM citrate at pD 7.5.	80
47	DFT-calculated visualization of the spin density of the lowest-lying triplet state of U ^{VI} -Cit 1:2 complex.	85
48	Depiction of DFT-calculated U ^{VI} -Cit (1:1) complex and hydrogen bonded Cit association structure as singlet ground state, and the corresponding lowest-lying triplet state after photo-excitation of the hydrogen bonded Cit, the subsequent single electron transfer to reduce U ^{VI} to U ^V , and the remaining radicalic species after decarboxylation.	85
49	¹ H NMR spectra of sample solutions U1 – U4 prior to and after light-irradiation showing signals of the degradation products β-ketoglutarate, acetoacetate, and acetone.	89
50	¹ H NMR spectrum of sample U1 immediately after light-irradiation together with expansions for the signals of interest, and signal assignment to the positions in β-ketoglutarate, acetoacetate, and acetone, as well as deconvolution of methylene and methyl group signals and their attribution to the respective isotopomers.	90
51	¹³ C, APT, and H,C-HSQC spectra acquired for the justification of ¹ H signal group ascribed to acetone isotopomers in light-irradiated U3 sample.	91
52	H,C-HSQC and H,C-HMBC spectra of the light-irradiated U4 sample.	92
53	UV-Vis-NIR absorption spectra after dilution of aliquots taken from light-irradiated solutions as prepared for EXAFS measurements.	94
54	Uranium L _{III} -edge <i>k</i> ³ -weighted EXAFS data and corresponding FOURIER transforms for samples U14-X, X = 48 – 51.	95
55	¹ H NMR low-field region of light-irradiated U1 and U3 pD 2 samples and U ^{IV} -Cit reference sample, together with photographs showing the solutions' altered color as compared to a corresponding U ^{VI} -Cit solution kept dark.	96

56	^1H NMR low-field region of light-irradiated U2 and U4 pD 5 samples and U^{IV} -Cit reference sample, together with photographs showing the solutions' altered color as compared to a corresponding U^{VI} -Cit solution kept dark.	97
57	Time-dependent ^1H NMR spectra of (repeatedly) irradiated U2 sample.	98
58	Model structures of hydrogen selenite monomers and hydrogen selenite dimer with corresponding MP2 predicted IR spectra.	103
59	^{77}Se NMR of Se^{IV} at pH_c 5 and pH 13 with concentrations ranging from 1 mM through 1 M, and constant total ionic strength (3 M), as well as graphical evaluation of dependence of linewidth and chemical shift on $[\text{Se}]$.	104
60	^{77}Se NMR spectra of 0.09 M Se^{IV} solutions at pH 4, 10, and 13 at different temperatures: 23, 35, 45, and 60 °C.	108
61	FT-IR spectra of 0.1 M solutions of Se^{IV} at pH 4 and 10, and Se^{VI} at pH 4 at variable temperatures: 25, 40, and 60 °C.	111
62	^{77}Se NMR spectra of 0.1 M sodium selenate solutions at pH_c 7.5 and 0.1 M sodium hydrogen selenite solutions at pH_c 5, respectively containing either 0.05 or 0.1 M CaCl_2 or MgCl_2 , and a total ionic strength of 5.6 M.	113
63	^{77}Se CP/MAS NMR spectrum at 5 kHz rotational frequency of the precipitate obtained from equimolar Se^{IV} and Ca^{2+} pH_c 5 solution.	114

Scheme	Caption	Page
1	NMR related properties of the rare earth elements and illustration of nuclear charge distribution related to spin quantum number I and sign of electric quadrupole moment Q .	14
2	Illustration of increase in electron density of $\text{U}-\text{O}_{\text{ax}}$ bond and its bond properties upon hydroxo ligand coordination as well as hypothetical mechanism of hydrogen-atom-transfer based reduction of U^{VI} to U^{V} by GSH <i>via</i> axially U-bound oxygen.	60
3	Generic structures of U^{VI} -Cit 2:2 complex B-type geometry, configurations of the chiral carbon atoms and an exemplary configuration change upon intramolecular site exchange, with the resulting two diastereomeric pairs of enantiomers denoted <i>syn</i> and <i>anti</i> .	67

4	Changing complex geometry, shown from A-type to B-type, upon dissociation of the U ^{VI} -bound carboxyl groups, rotation of the Cit ligand about the μ_2 -O-C _q bond, and re-binding of the carboxyl groups at the opposite uranyl.	68
5	Composition of the U ^{VI} -Cit samples U1 – U4, the respective mole fraction of free Cit at 25 °C, and the corresponding region of the ¹ H NMR spectra showing the signals of free and U ^{VI} -bound Cit at 25 °C with an expansion of the U ^{VI} -Cit signals upon cooling down to 0 °C.	69
6	Proposed reaction mechanism for the decomposition of citric acid.	84
7	DFT-calculated degradation progress of the radical obtained after initial Cit decarboxylation as well as GIBBS energies of reaction and activation barriers.	86
8	Visualization of the reactions causing partial and complete deuteration of the intermediates β -ketoglutarate, acetoacetate, and acetone.	88
9	Depiction of the asymmetric energy barrier and the corresponding chemical equilibrium between sites A and B.	106
10	Preparation scheme showing the processing steps and analyses performed among the investigation of the GSH-U ^{VI} system under reducing conditions.	122

8 LIST OF TABLES

Table Title	Page
1 pK_a values of GSH and GSSG titration sites.	11
2 pK_a values of citric acid titration sites.	12
3 Numerical evaluation of the spin simulated spectra shown in Figure 23.	45
4 ^{17}O chemical shift values for various uranyl complexes.	73
5 ^{17}O chemical shift values obtained from DFT calculation and NMR experiment.	75
6 EXAFS sample designation and composition as well as U^{IV} contents after light-irradiation as determined from X-ray absorption spectra factor analyses	93
7 Temperature-induced selenium chemical shift changes in dependence of pH for 0.09 M Se^{IV} solutions obtained from linear fitting.	108
8 Comparison of selected spectroscopic observables for Se^{VI} and Se^{IV} oxo species.	109
9 Analysis of CP/MAS spectra according to Figure 63 of the precipitate obtained from equimolar Se^{IV} and Ca^{2+} pH _c 5 solution.	114

9 APPENDIX

9.1 GLUTATHIONE/GLUTATHIONE DISULFIDE TOPIC

9.1.1 Ligand-specific information

Table A1. T_1 of GSH ^1H nuclei in dependence of pD

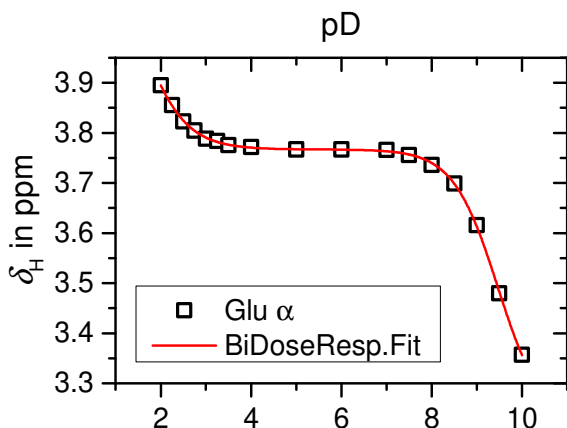
^1H	T_1 in s		
	pD 2	pD 5	pD 8
Glu β	0.73 ± 0.01	0.75 ± 0.01	0.73 ± 0.01
Glu γ	0.81 ± 0.01	0.82 ± 0.01	0.80 ± 0.04
Cys β	0.65 ± 0.01	0.67 ± 0.01	0.64 ± 0.01
Glu α	3.01 ± 0.03	2.98 ± 0.13	2.73 ± 0.07
Gly α	1.08 ± 0.01	1.37 ± 0.01	1.35 ± 0.01
Cys α	3.26 ± 0.08	3.52 ± 0.09	3.32 ± 0.07

inversion recovery sequence; $B_0 = 14.1$ T; $T = 298$ K; $[\text{GSH}] = 6.7$ mM

Table A2. GSH pK_a values obtained from sigmoidal dose-response fitting parameters.

Bi-Dose-Response Fit

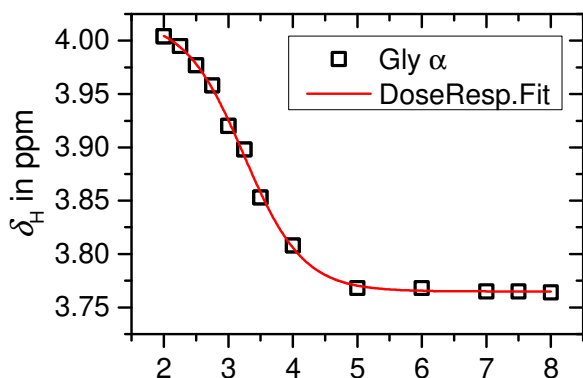
$$y = A1 + (A2 - A1) \cdot \left[\frac{h}{1 + 10^{(\log(x_{0,1} - x)) \cdot p_1}} + \frac{1 - h}{1 + 10^{(\log(x_{0,2} - x)) \cdot p_2}} \right]$$



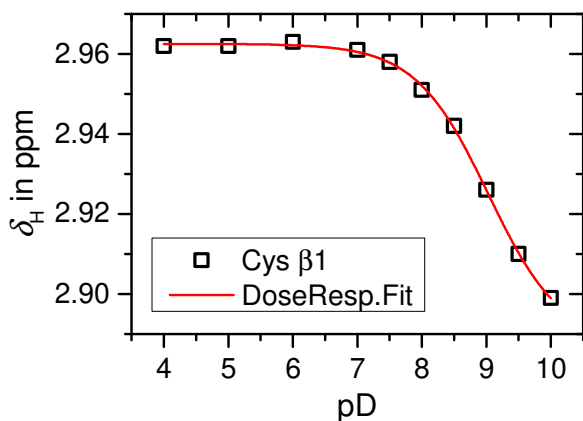
		value	σ
Glu	A1	3.216	0.015
	A2	4.317	0.378
$pK_{a,1}$	$x_{0,1}$	1.377	0.532
	$x_{0,2}$	9.467	0.031
	p_1	-0.83	0.10
	p_2	-0.88	0.03
	h	0.50	0.17
	R^2	0.99968	

Dose-Response Fit

$$y = A1 + (A2 - A1) / \left(1 + 10^{(\log(x_0 - x)) \cdot p} \right)$$



		value	σ
Gly	A1	3.765	0.002
	A2	4.021	0.006
$pK_{a,2}$	x_0	3.240	0.028
	p	-0.95	0.05
	R^2	0.99859	



		value	σ
Cys	A1	2.890	0.003
	A2	2.961	0.001
$pK_{a,3}$	x_0	9.011	0.068
	p	-0.85	0.07
	R^2	0.99913	

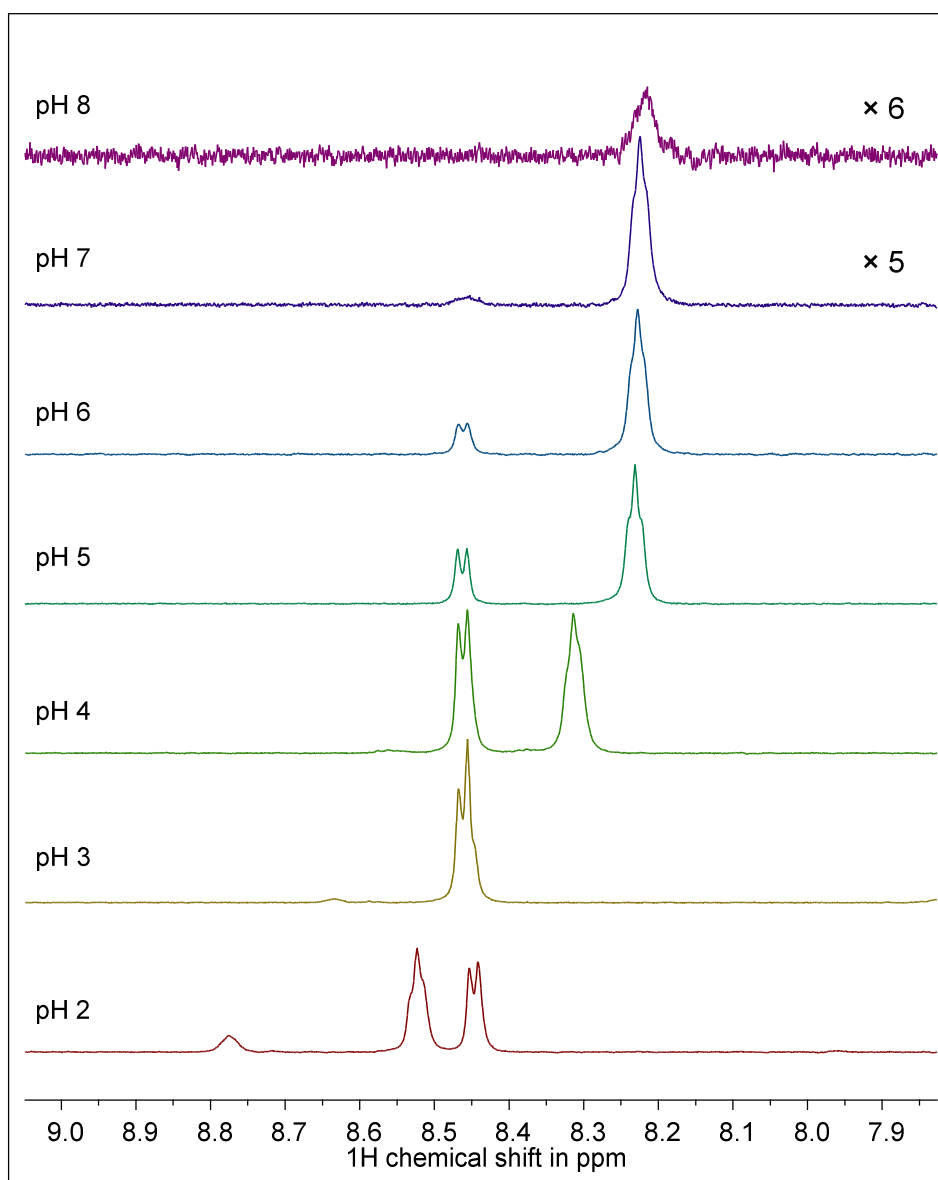


Figure A1. ^1H NMR pH-dependent spectra of $\text{C}(=\text{O})\text{NH}$ of 6.7 mM GSH $^1\text{H}_2\text{O}$ solutions.

The amide protons are found at typical chemical shifts between 6 and 9 ppm as shown in Figure A1. Notably, the amide ^1H signals also exhibit splitting due to scalar coupling to the respective α -hydrogen atoms, for example, at pH 2 the Cys NH appears as a doublet at 8.44 ppm with $^3J_{\text{NH},\alpha} = 7.2$ Hz and the Gly NH appears as a pseudo-triplet at 8.52 ppm with $^3J_{\text{NH},\alpha 1} = 6.9$ and $^3J_{\text{NH},\alpha 2} = 6.6$ Hz. By means of the pH-induced shift of the Gly NH signal even the deprotonation of the Gly carboxyl group can be comprehended. Additionally, with increasing pH the signals diminish since hydroxide ions are known to catalyse amide hydrogen exchange [76]. Note the remarkably small difference in the *vicinal* coupling constants between Gly NH and Gly α hydrogen atoms. This indicates the similarity of the magnetic environment of the latter as well as a rapid rotation about the $\text{HN}-\text{C}(\alpha)$ bond [104].

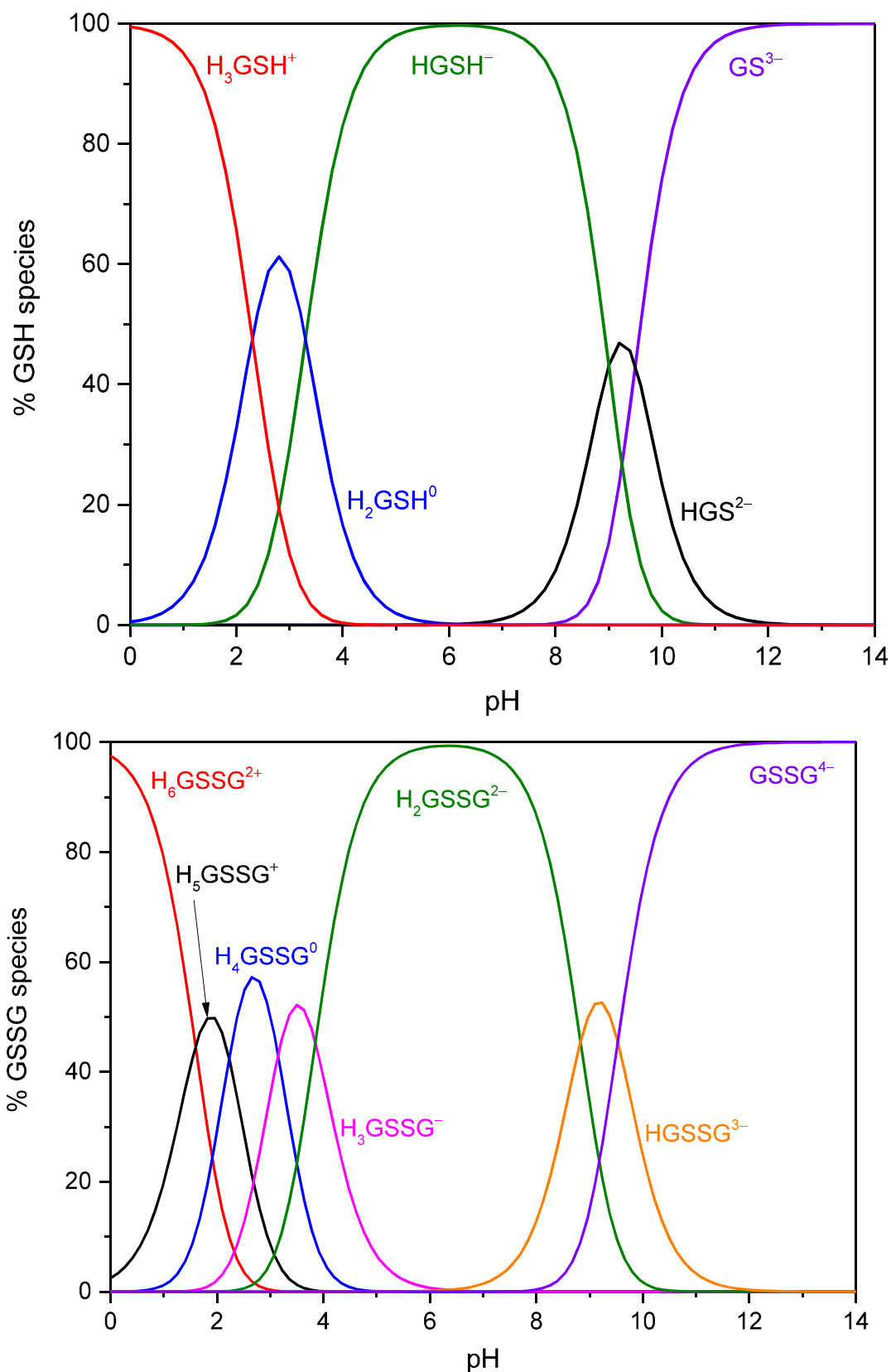


Figure A2. Speciation diagrams of GSH (top) and GSSG (bottom) depicting the fractions of the respective species in dependence on pH. Speciation calculation was performed with HySS2009 [209] using thermodynamic data from [52] (GSSG) and [53] (GSH).

9.1.2 Lanthanide-related studies

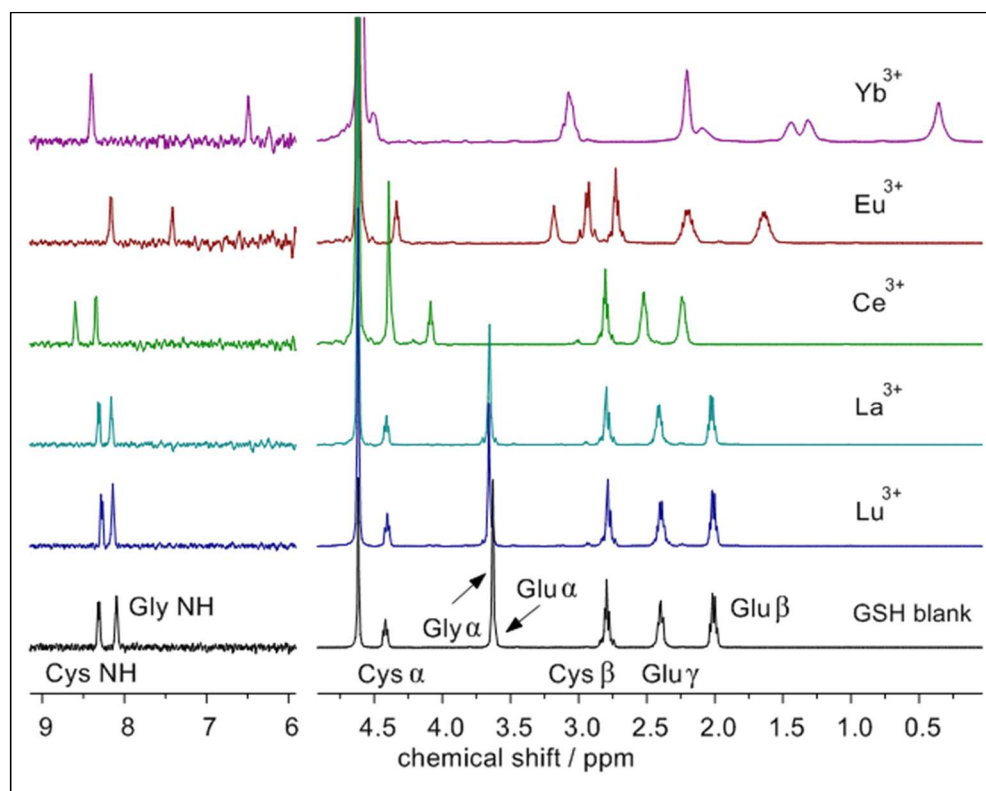


Figure A3. ^1H NMR spectra of 300 mM GSH pD 5 solutions without, and in the presence of the stated trivalent lanthanide ions (100 mM).

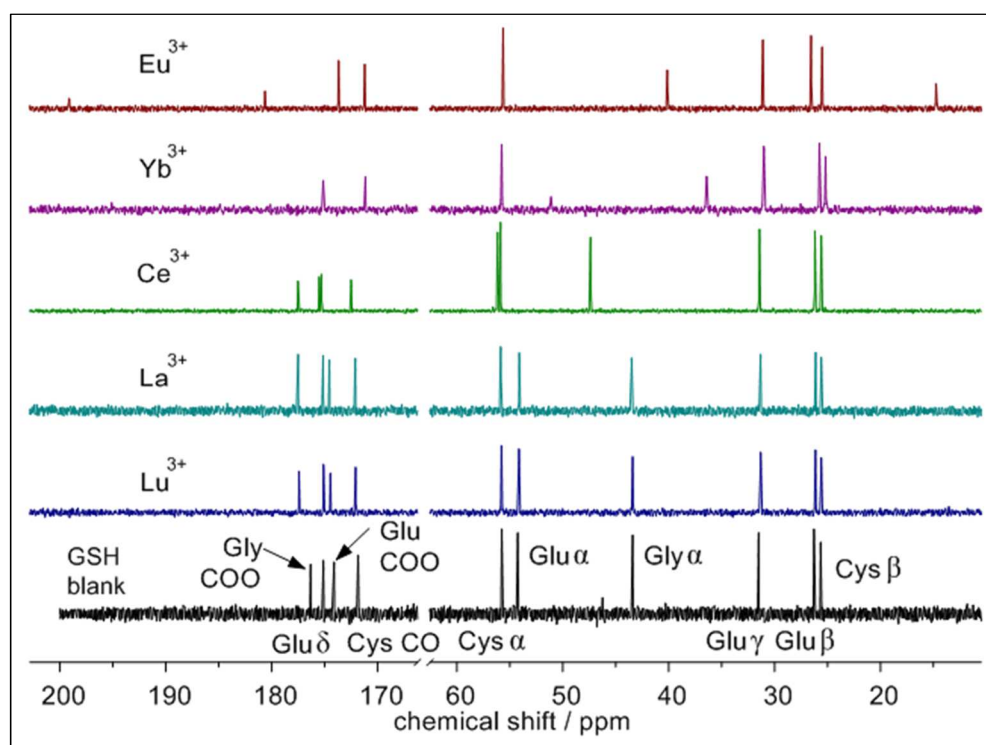


Figure A4. ^{13}C NMR spectra of 300 mM GSH pD 5 solutions without, and in the presence of the stated trivalent lanthanide ions (100 mM).

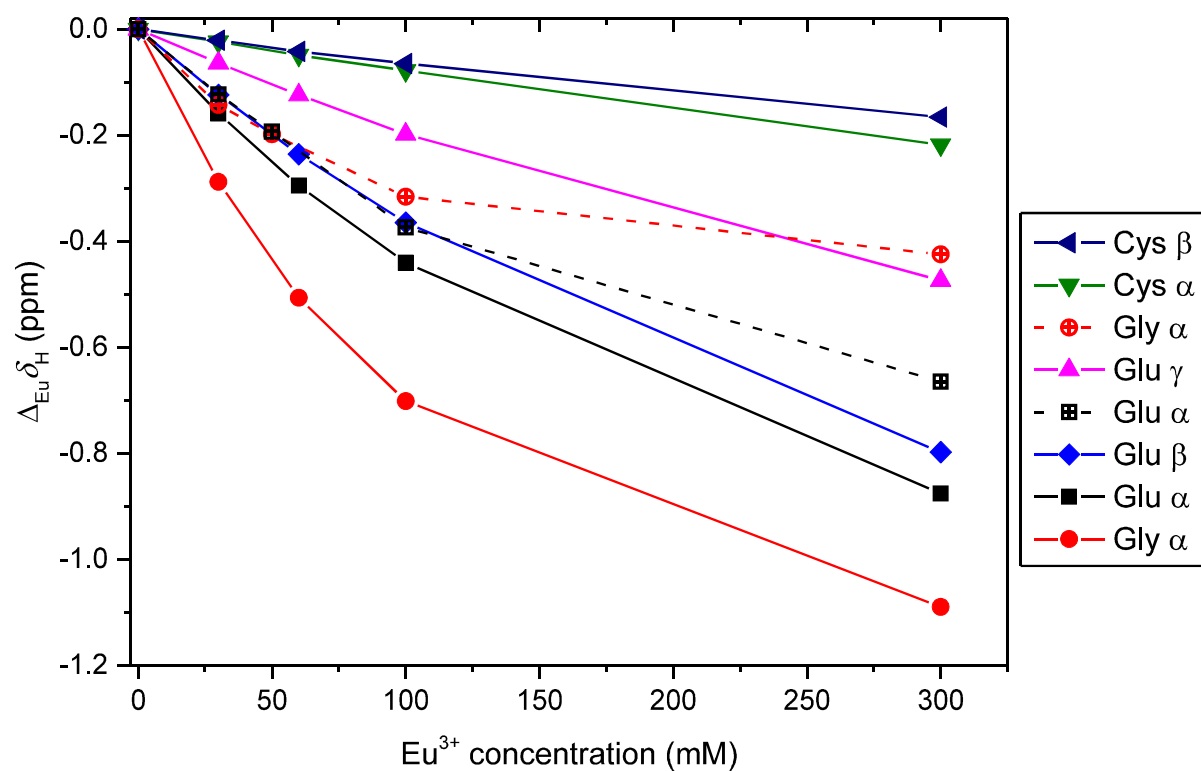


Figure A5. Eu^{III} -induced 1H chemical shift changes ($\Delta_{Eu}\delta_H$) as a function of $[Eu^{3+}]$ obtained from spectra of 300 mM GSH at pD 5 with lines drawn for better visualization. Glu α and Gly α data obtained from pD 3 solutions are shown as dashed symbols and lines.

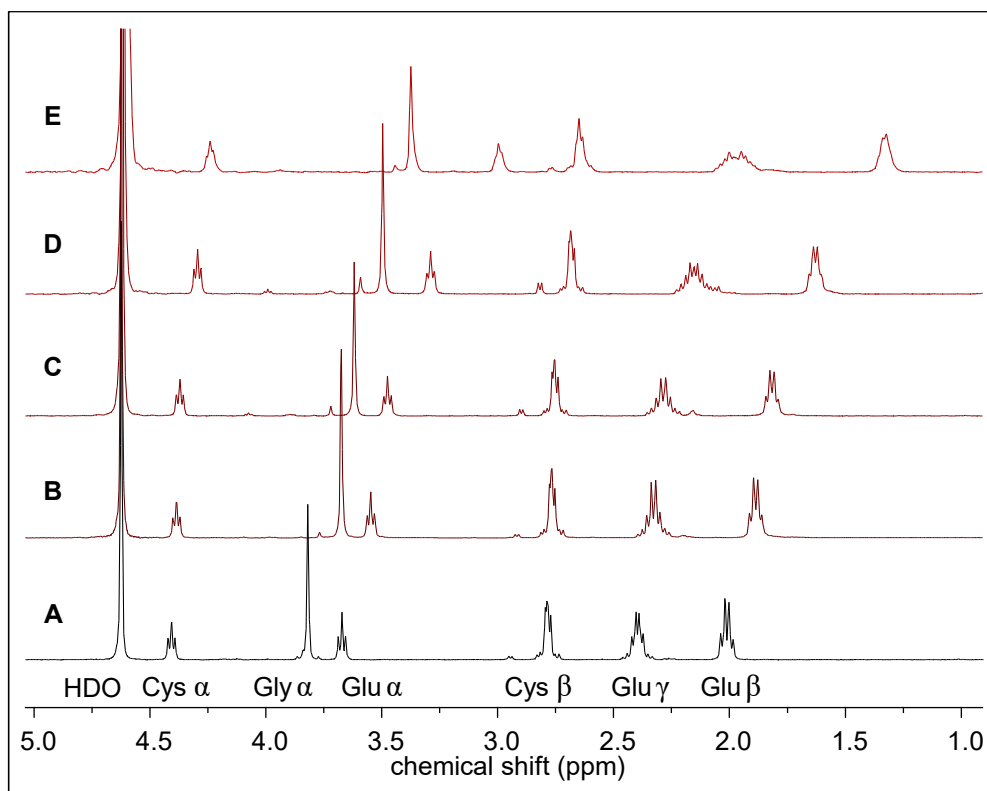


Figure A6. ^1H NMR spectra of 300 mM GSH at pH 3.0 without (A), and in the presence of (B) 30, (C) 50, (D) 100, and (E) 300 mM Eu^{III} .

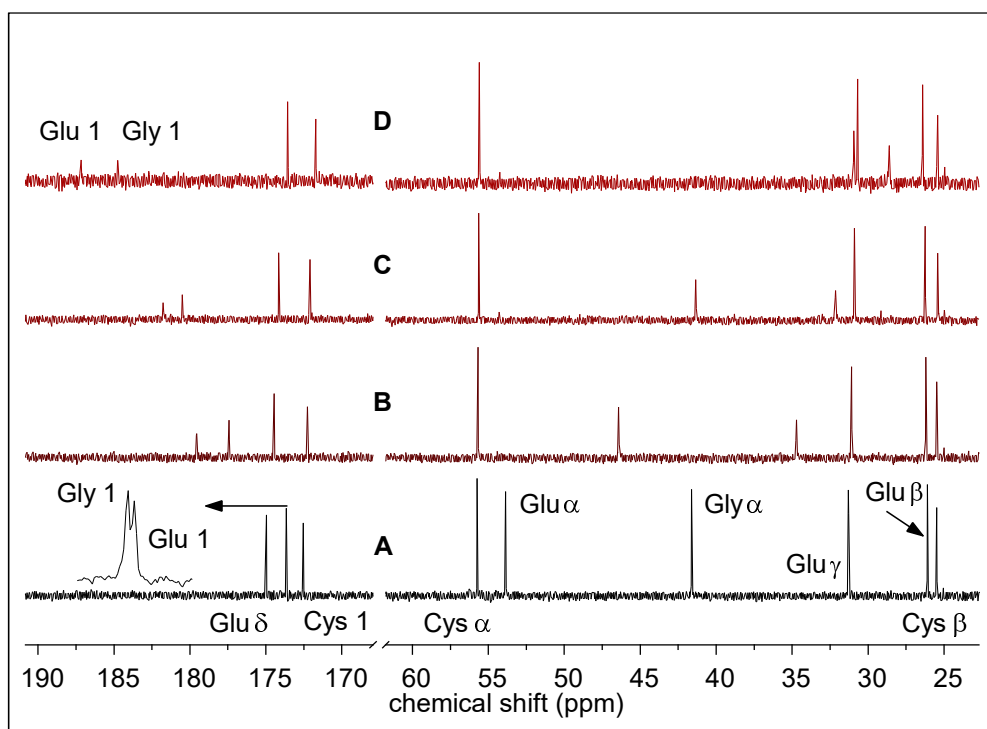


Figure A7. ^{13}C NMR spectra of 300 mM GSH at pH 3.0 without (A), and in the presence of (B) 50, (C) 100, and (D) 300 mM Eu^{III} . Note that for the blank (A) both the Glu 1 and Gly 1 ^{13}C chemical shift values differ by 0.01 ppm only.

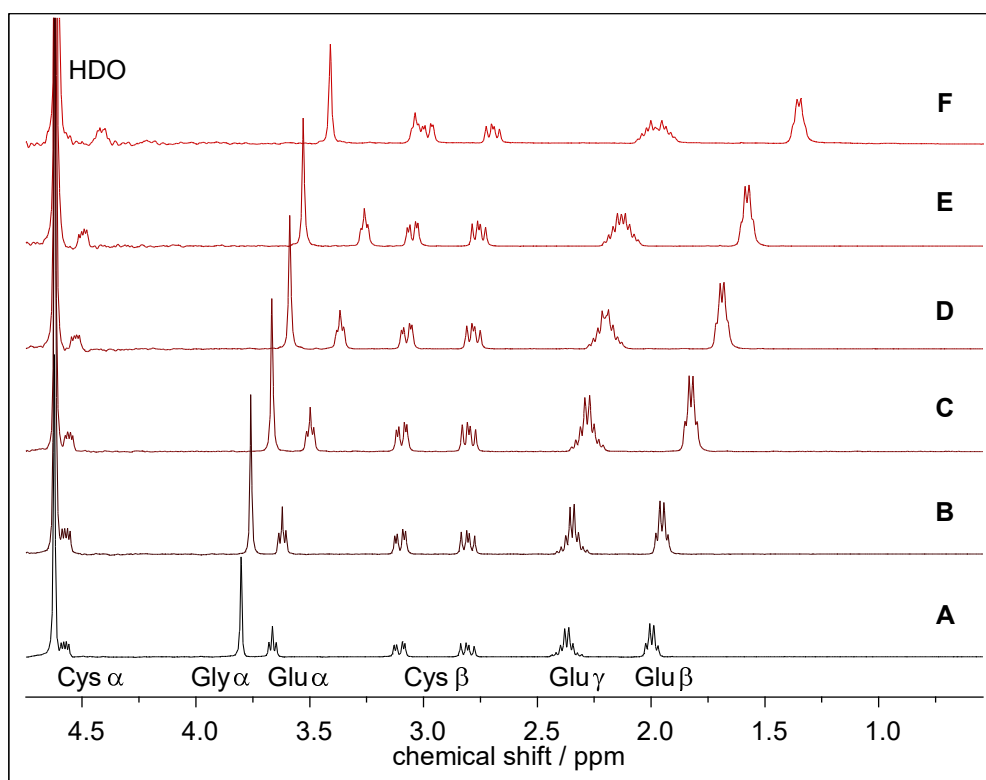


Figure A8. ^1H NMR spectra of 150 mM GSSG pD 3 solutions without (A), and in the presence of Eu^{III} at different concentrations: (B) 10, (C) 50, (D) 100, (E) 150, and (F) 300 mM.

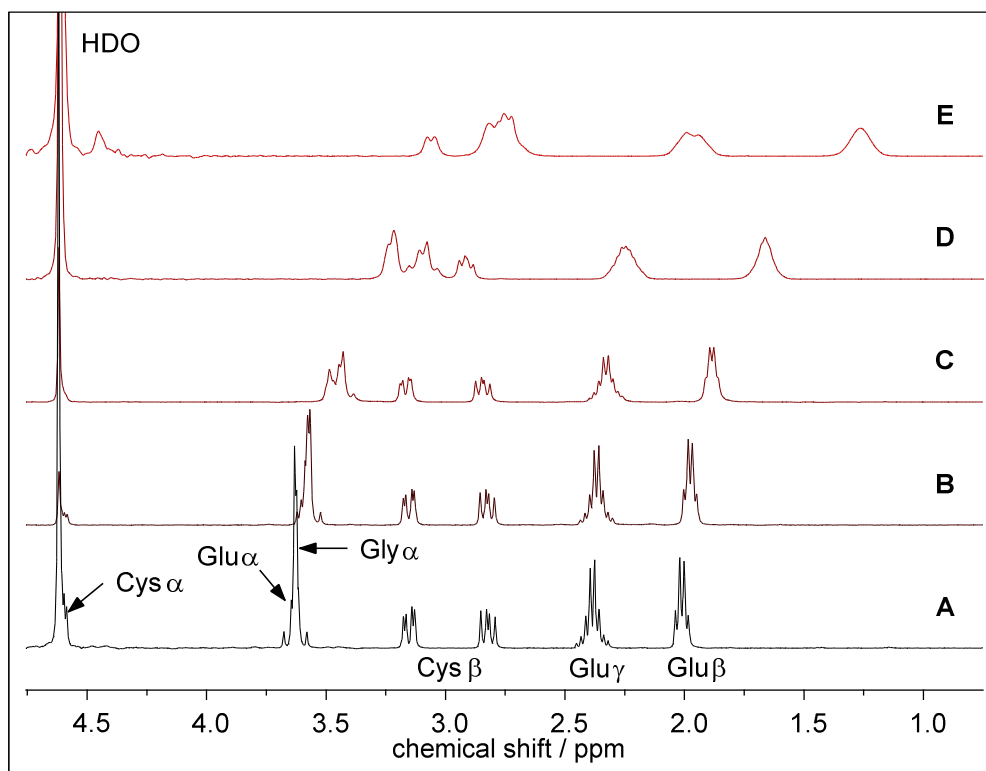


Figure A9. ^1H NMR spectra of 150 mM GSSG pD 5 solutions without (A), and in the presence of Eu^{III} at different concentrations: (B) 10, (C) 50, (D) 150, and (E) 300 mM, respectively.

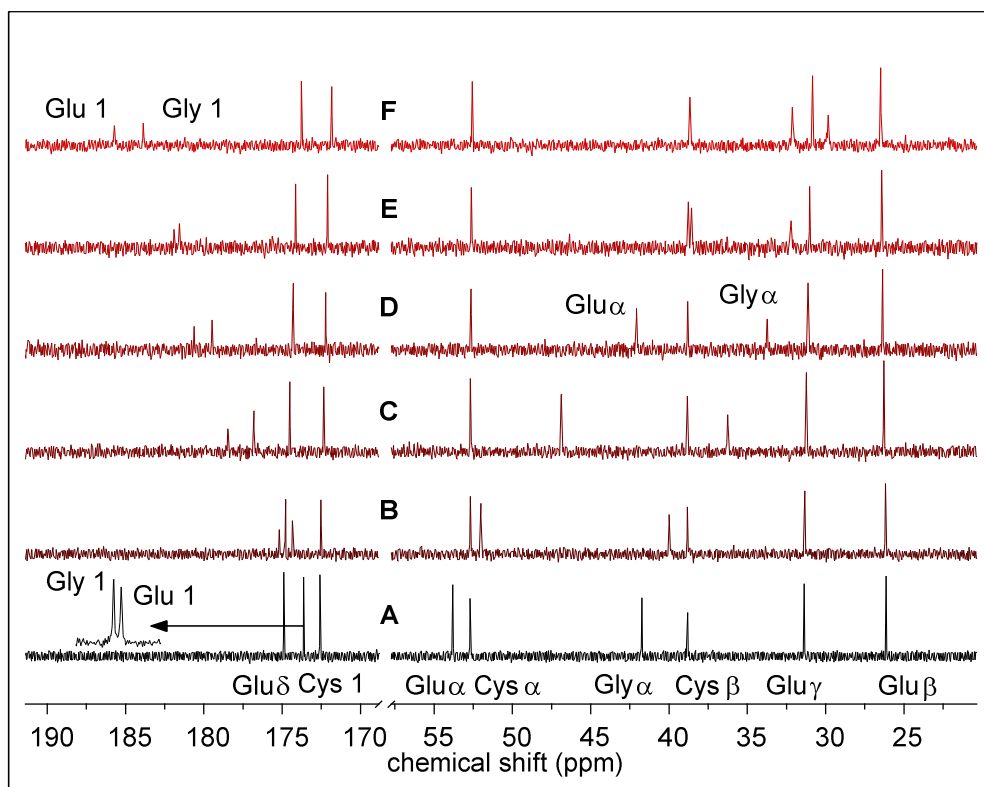


Figure A10. ^{13}C NMR spectra of 150 mM GSSG pD 3 solutions without (A), and in the presence of Eu^{III} at different concentrations: (B) 10, (C) 50, (D) 100, (E) 150, and (F) 300 mM.

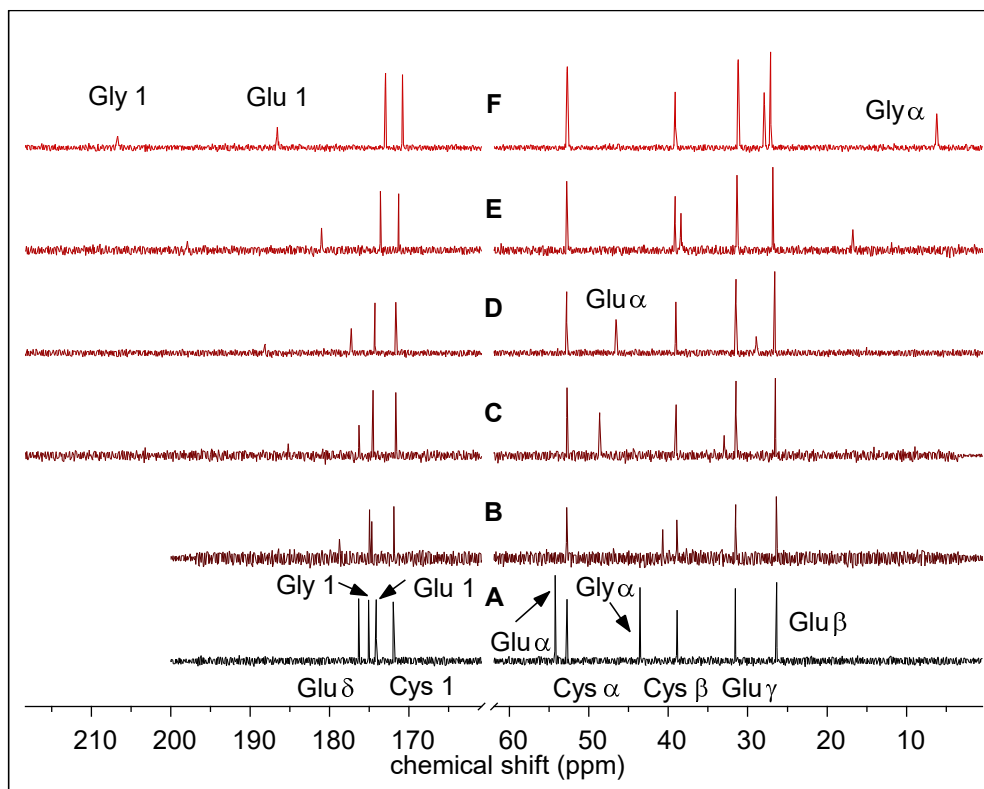


Figure A11. ^{13}C NMR spectra of 150 mM GSSG pD 5 solutions without (A), and in the presence of Eu^{III} at different concentrations: (B) 10, (C) 50, (D) 100, (E) 150, and (F) 300 mM.

9.1.3 Uranium-related studies

GSSG samples

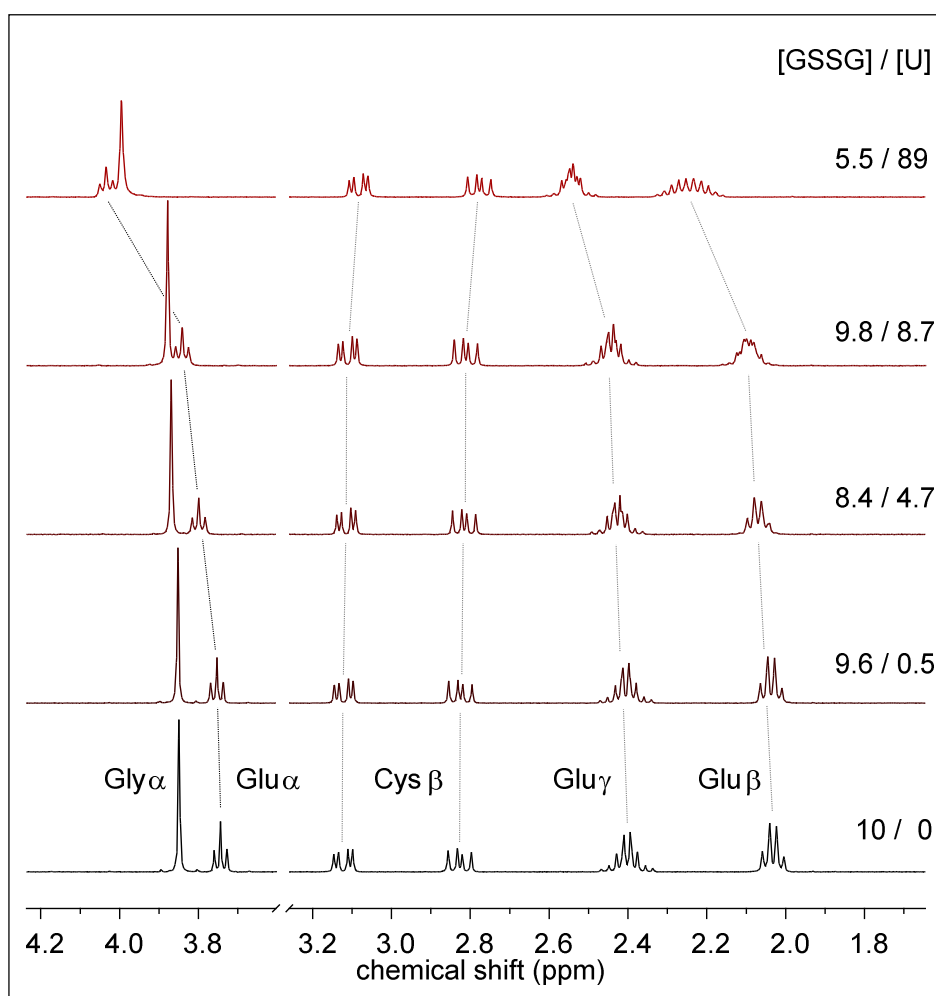


Figure A12. ^1H NMR spectra of GSSG solutions with varying U^{VI} contents at pD 2. Note, only a part of the full spectrum is shown for clarity; the initial GSSG concentration was 10 mM, the re-determined concentrations (in mM) are given.

Table A3. Complexation-induced shifts for pD 2 solutions of GSSG and U^{VI} .

[GSSG] : [U ^{VI}] (mM)	$\Delta_{\text{U}}\delta_{\text{H}}$ (ppb)			
	Gly α	Glu α	Glu β	Glu γ
9.6 : 0.5	3	9	4	3
8.4 : 4.7	20	56	37	25
9.8 : 8.7	29	97	57	39
5.5 : 89	146	290	211	145

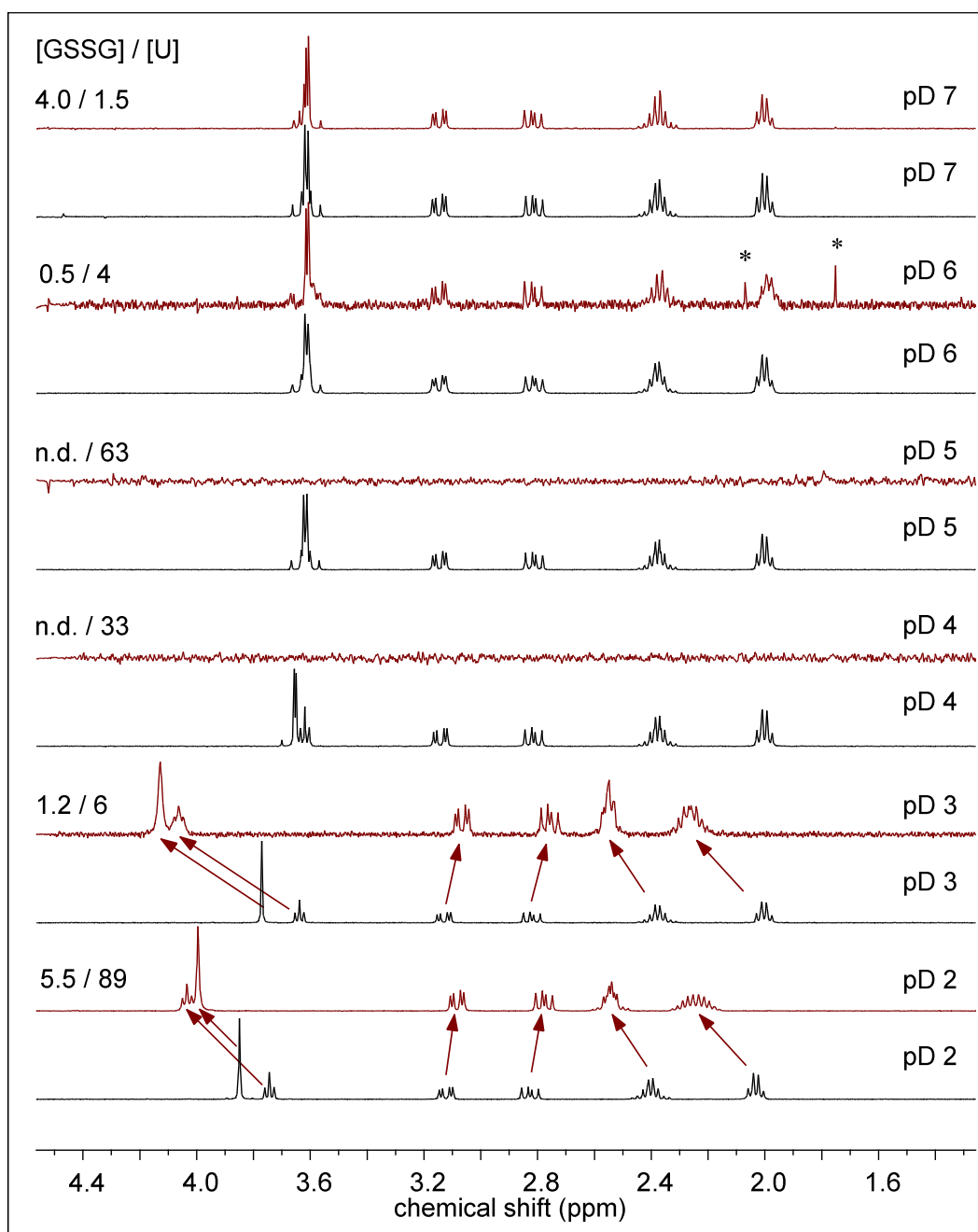


Figure A13. ^1H NMR pD-dependent spectra of GSSG blanks (black) and U^{VI} containing solutions (red). Initial concentrations for GSSG (both blank and sample) and U^{VI} were 10 and 100 mM, respectively, the re-determined concentrations are stated with the spectra; (*) denotes an impurity; n.d.: not detectable.

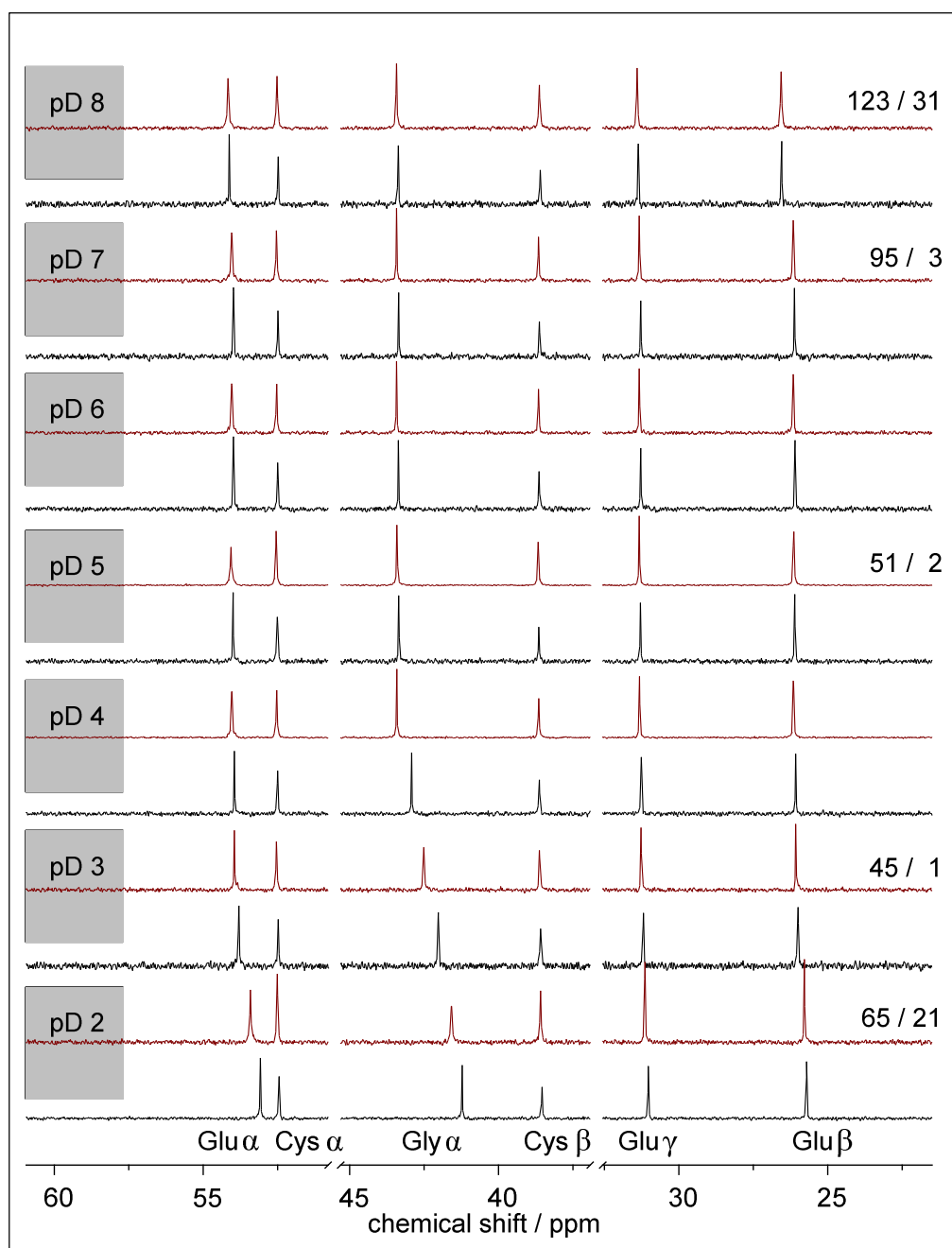


Figure A14. ^{13}C NMR aliphatic region of pD dependent spectra of GSSG blanks (black) and U^{VI} containing solutions (red) with initial $[\text{GSSG}]$ (for both blank and sample) and $[\text{U}^{\text{VI}}]$ of 150 mM and 75 mM, respectively. Note the occasionally re-determined concentrations stated with the spectra.

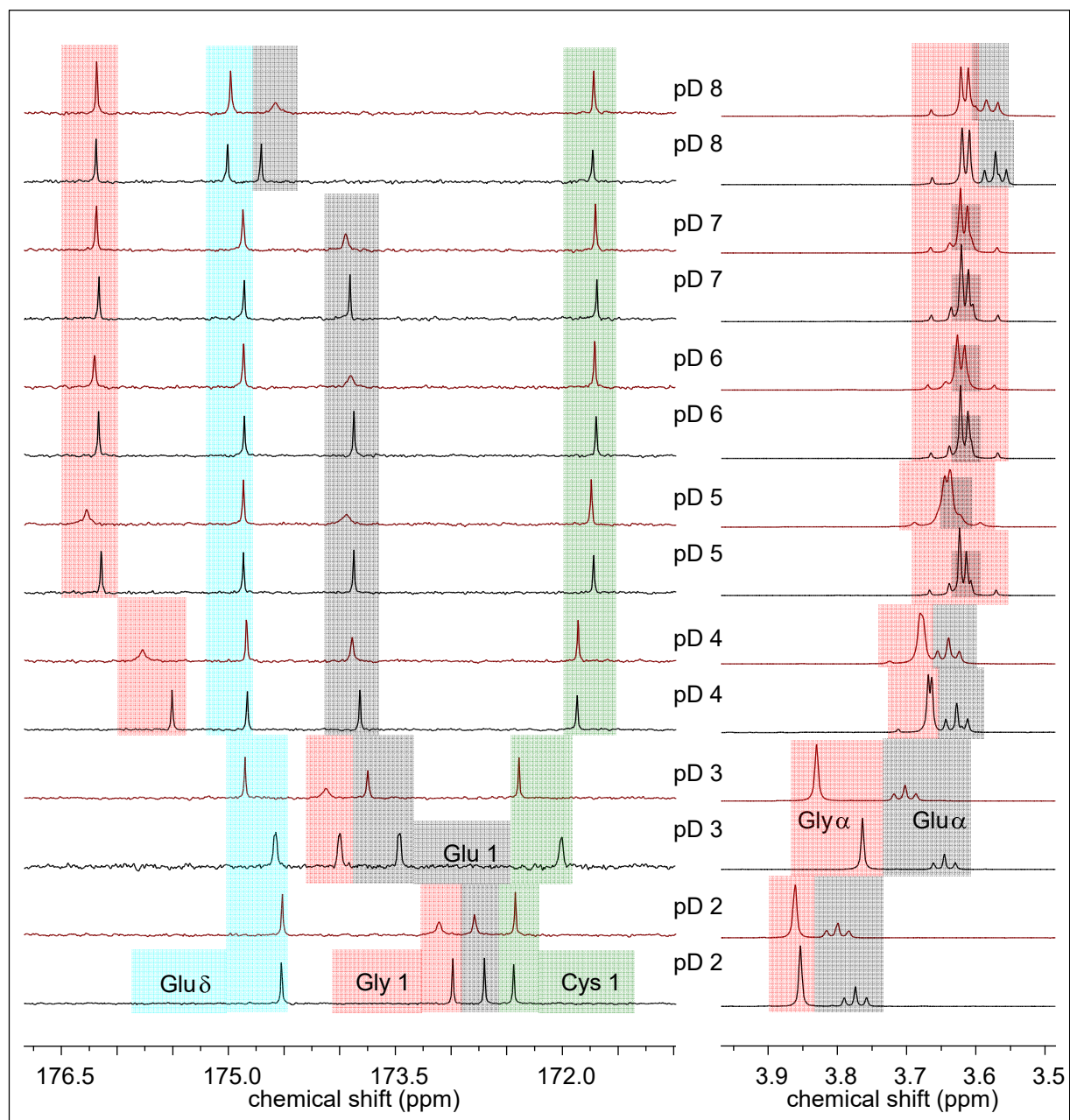


Figure A15. ^{13}C NMR carbonyl region (left) and ^1H NMR Gly α and Glu α region (right) of pD-dependent spectra of GSSG blanks (black) and U^{VI} containing solutions (red) with initial [GSSG] (for both blank and sample) and $[\text{U}^{\text{VI}}]$ of 150 mM and 7.5 mM, respectively.

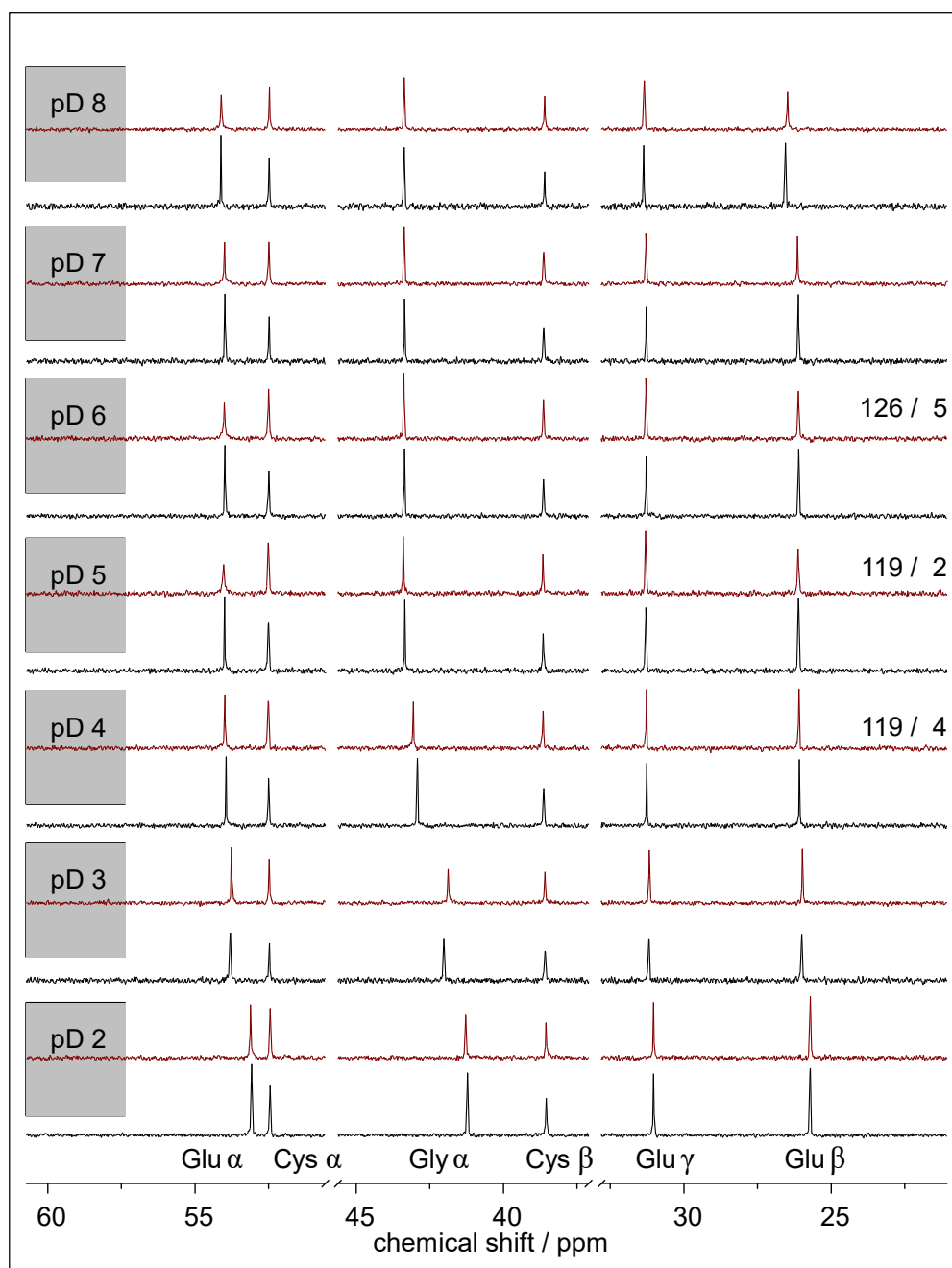


Figure A16. ^{13}C NMR aliphatic region of pD dependent spectra of GSSG blanks (black) and U^{VI} containing solutions (red) with initial [GSSG] (for both blank and sample) and [U^{VI}] of 150 mM and 7.5 mM, respectively. Note the occasional re-determined concentrations stated with the spectra.

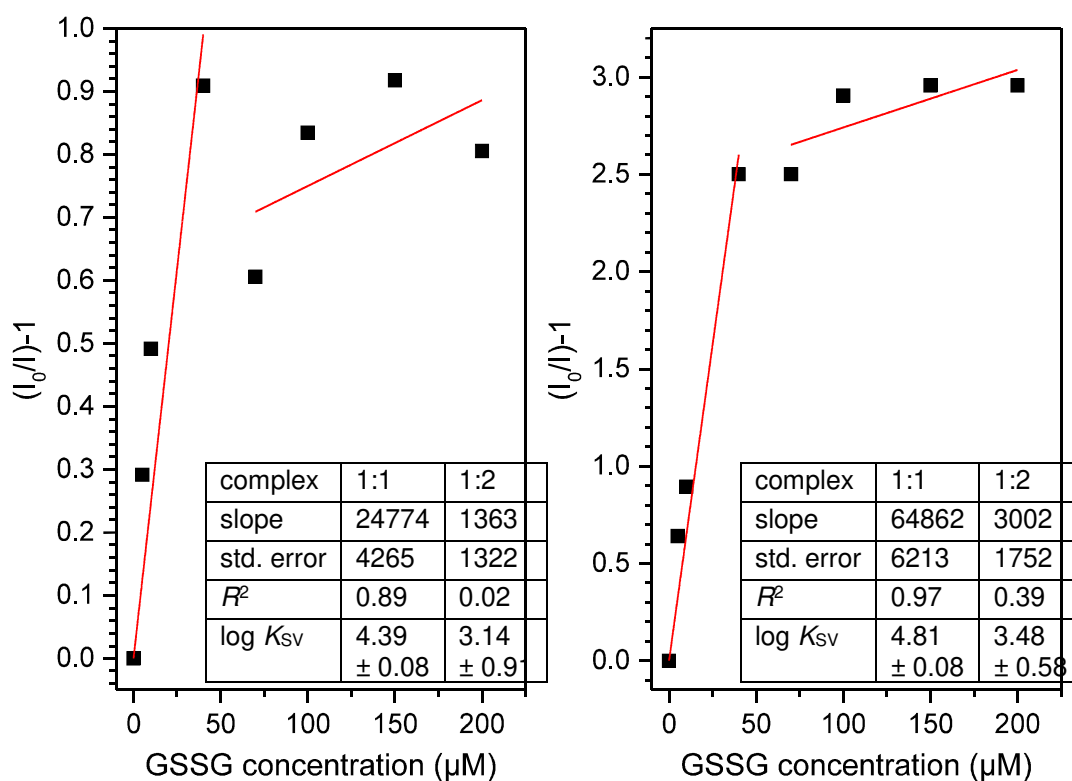


Figure A17. STERN-VOLMER-Plots of a ligand titration series for determination of the association constant at pH 3, directly obtained from TRLFS data (left) and after PARAFAC refinement (right), with the red lines representing linear fits and the tables stated with the plots reporting their analyses.

TRLFS measurements of the GSSG/ U^{VI} samples at 25 °C showed a decrease in fluorescence intensity with increasing [GSSG] lacking a shift of the emission lines accompanied with a monoexponential decay in all samples. This behavior is characteristic for static fluorescence quenching upon formation of the non-fluorescing complex and concomitant decrease of free metal ion concentration. Calculated luminescence intensities were further evaluated using the STERN-VOLMER equation, $I_0/I = 1 + K_{SV} [Q]$, where I_0 is the intensity without quencher, K_{SV} represents the STERN-VOLMER constant and $[Q]$ is the concentration of the quencher, *i.e.*, GSSG. The plot of $(I_0/I-1)$ vs. [GSSG] yields a straight line whose slope is K_{SV} , directly representing the association constant of the GSSG complex [210-211].

The data point distribution suggests grouping as two data sets. Accordingly, on account of lower and higher ligand concentrations the formation of two complexes is assumed. By means of PARAFAC the data could be significantly refined. In both cases, however, the data tentatively assigned to the 1:2 complex show a large scattering and hence a large error value. Therefore, these data were not considered.

The following respective tentative formulae are based on the assumption that only coexisting U^{VI} and GSSG species form complexes and, concomitantly, the primary U^{VI} hydrolysis and carbonate species (structures) remain intact and GSSG replaces weaker bound ligands such as coordinating water or monodentate hydroxo ligands. GSSG is considered six-basic, that is, $4 \times COOH$ and $2 \times NH_3^+$ (*cf.* Fig. A2).



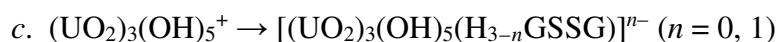
for: $n = 0$ monocationic, $n = 1$ net neutral (\downarrow), $n = 2$ monoanionic



for: $n = 0$ dicationic, $n = 1$ monocationic, $n = 2$ net neutral (\downarrow)



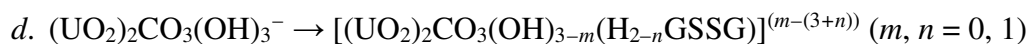
for: $m+n = 0$ dicationic, $m+n = 1$ monocationic, $m+n = 2$ net neutral (\downarrow),
 $m+n = 3$ monoanionic, $m+n = 4$ dianionic



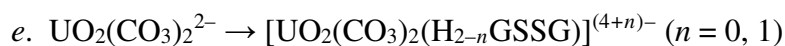
for: $n = 0$ net neutral (\downarrow), $n = 1$ monoanionic



for: $m+n = 0$ monoanionic, $m+n = 1$ dianionic, $m+n = 2$ trianionic



for: $m+n = 0, 2$ trianionic, $m = 0, n = 1$ tetraanionic, $m = 1, n = 0$ dianionic



for: $n = 0$ tetraanionic, $n = 1$ pentaanionic

For hydrolysis species, *i.e.* *a–c*, net neutral GSSG complex species can be formed which are prone to precipitation (\downarrow). Complexation by more than one GSSG ligand may be possible for polynuclear hydroxo species (cases *b* and *c*), however, by reason of steric hindrance one per uranyl unit only. Instead of a third GSSG ligand to bind in case *c*, interaction of a further carboxyl group of the same GSSG molecule with another uranyl entity of the trimeric U^{VI} hydroxo species is probable. Cases *d* and *e* yield polyanionic species regardless of stoichiometry, for which reason these species are regarded as well soluble. GSSG complexation in case *d* is plausible to release weak coordinating water and to take place at that uranyl unit bearing the smaller number of hydroxo ligands (owing to U^{VI} LEWIS acidity). If at all, presumably not more than one hydroxo ligand is replaced.

Although challenging, combination of educated guess and a multi-method approach, comprising versatile spectroscopies, potentiometry, and quantum chemical calculations seem promising for both thermodynamic data and molecular structure determination.

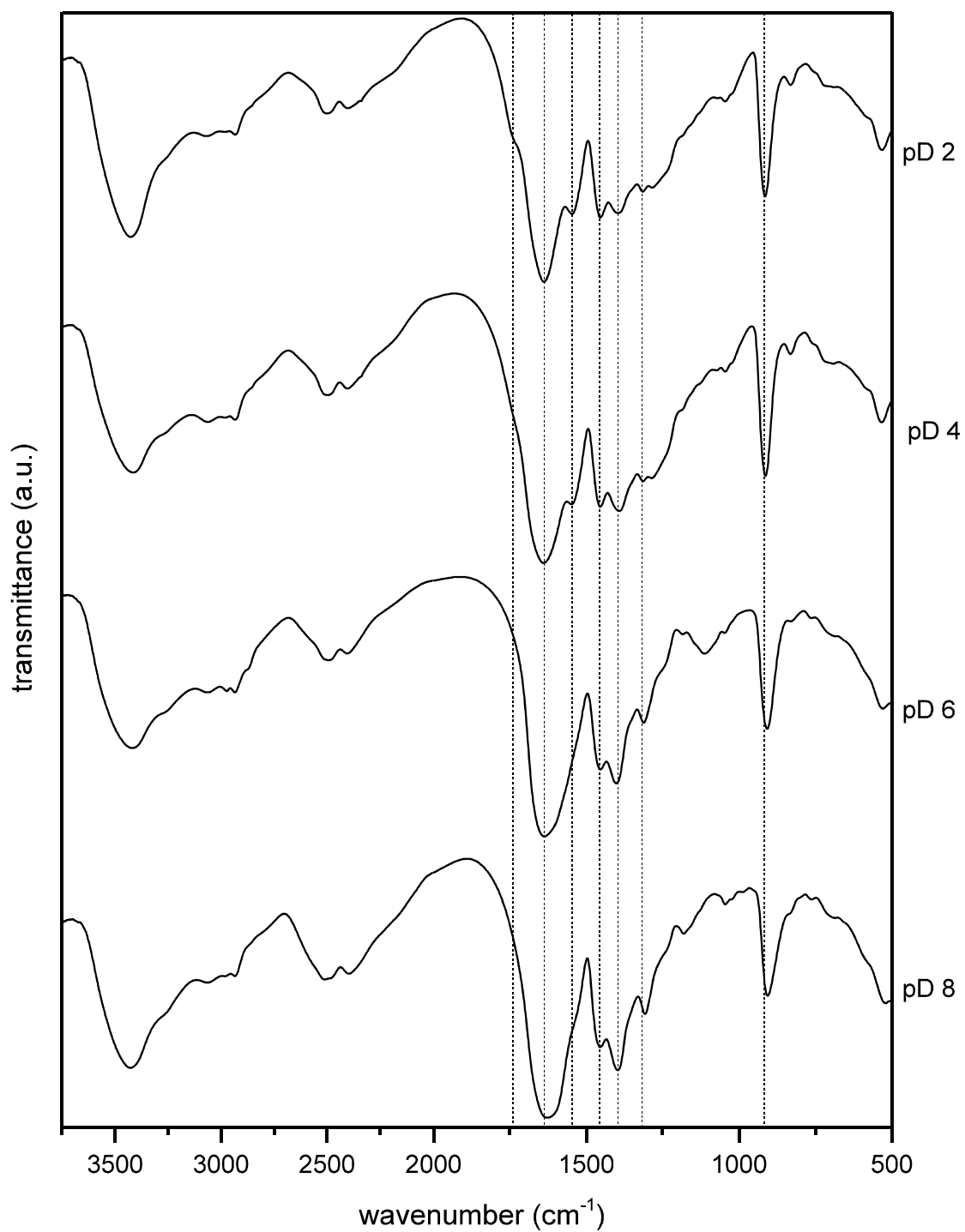


Figure A18. FT-IR spectra (KBr disc) of the washed and lyophilized pellets obtained from 150 mM GSSG and 7.5 mM U^{VI} solutions of initial pD values as stated with the spectra.

GSH samples

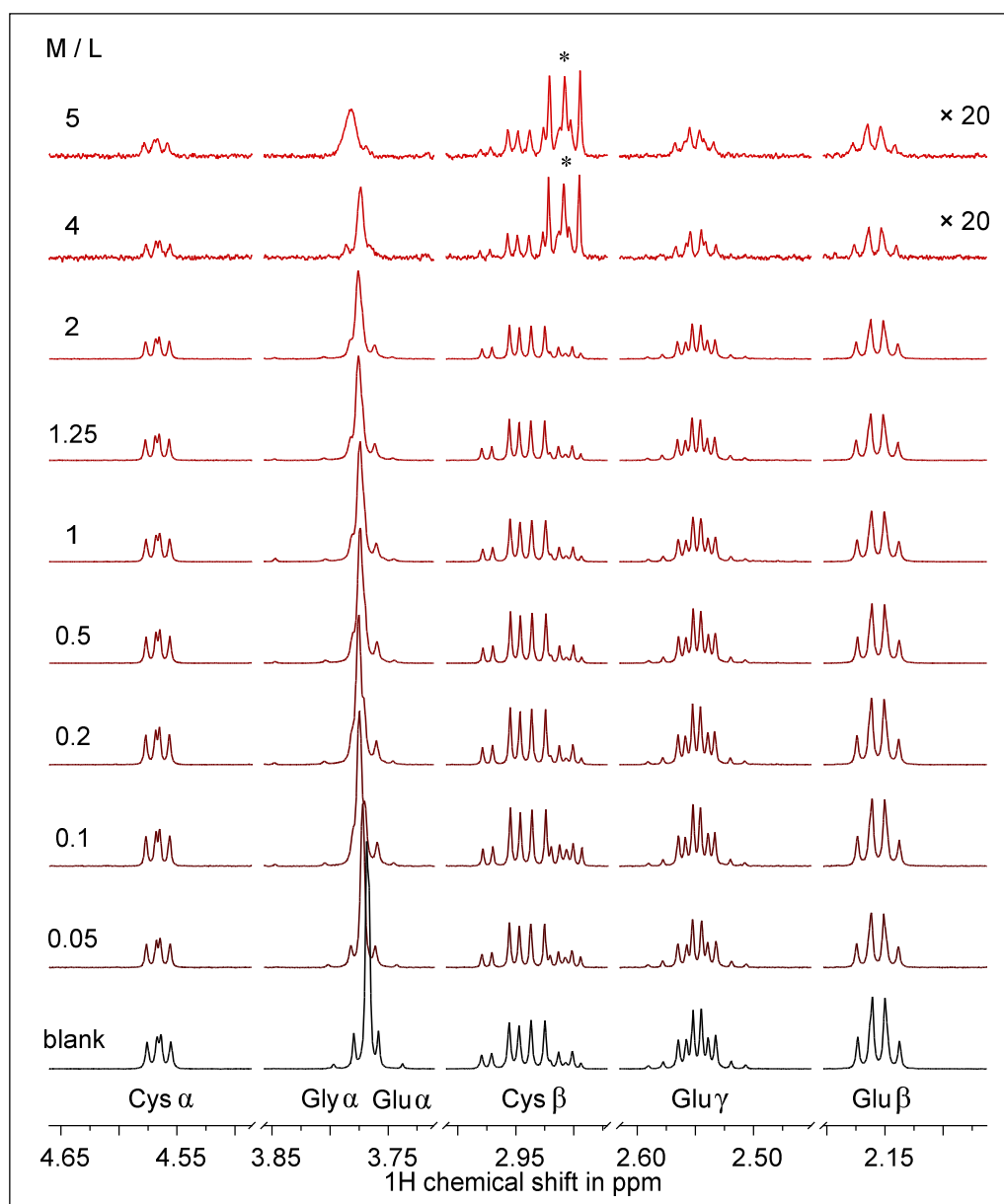


Figure A19. ^1H NMR spectra of 6.7 mM GSH and varying U^{VI} content (increasing from bottom to top) at pH 5. The initial M/L is stated with the spectra. Note that only parts of the spectra are shown for clarity; top two spectra enhanced by factor 20; * indicates the DSS ($-\text{CH}_2-\text{SO}_3^-$) signal.

The remaining GSH contents (or in other words: S/N) for the top two spectra in Fig. A19 is such low due to precipitate formation that upon enhancing the vertical scale one of DSS's signals ($-\text{CH}_2-\text{SO}_3^-$) stands out.

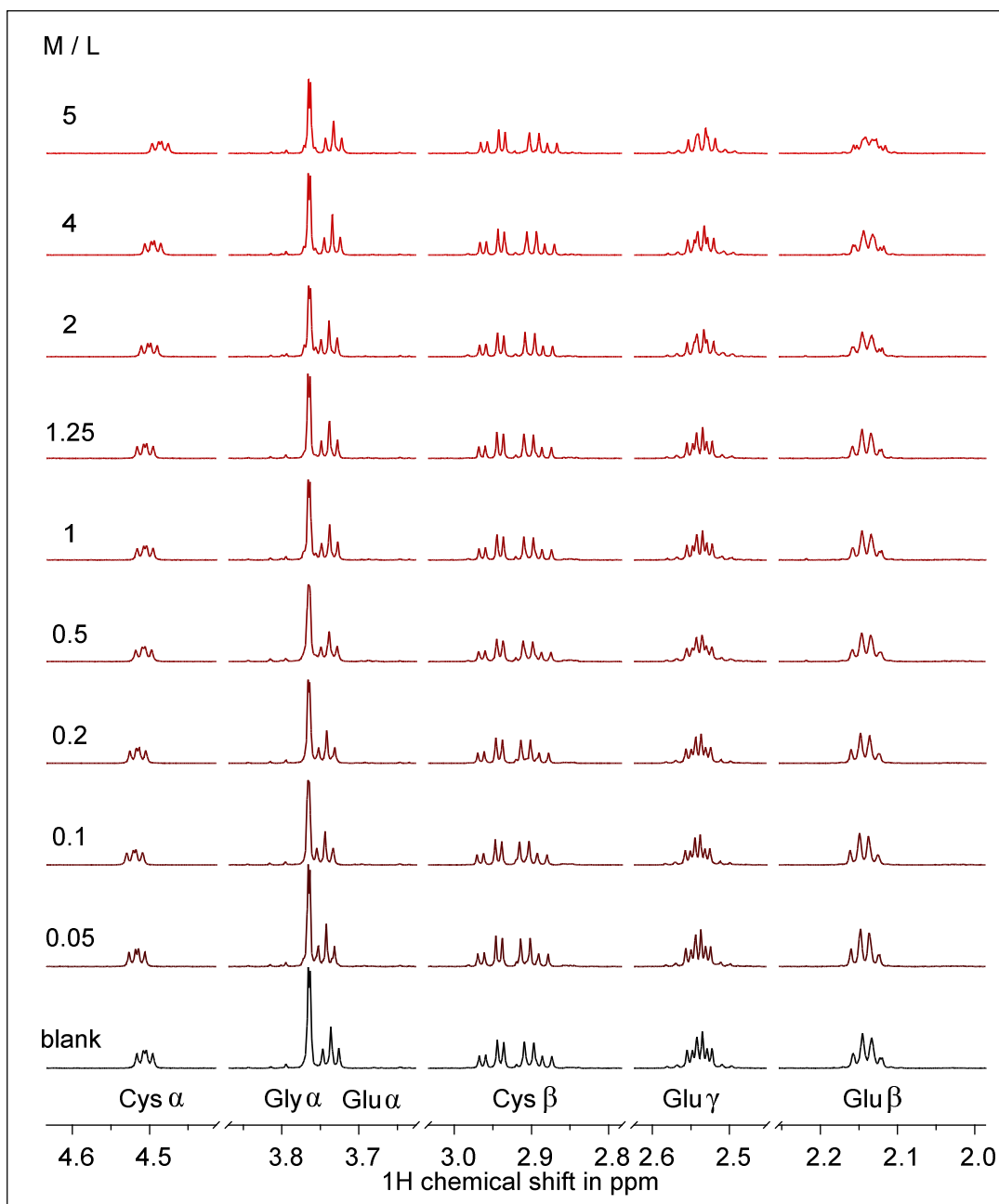


Figure A20. ^1H NMR spectra of 6.7 mM GSH and varying U^{VI} content (increasing from bottom to top) at pH 8. The initial M/L is stated with the spectra. Note that only parts of the spectra are shown for clarity.

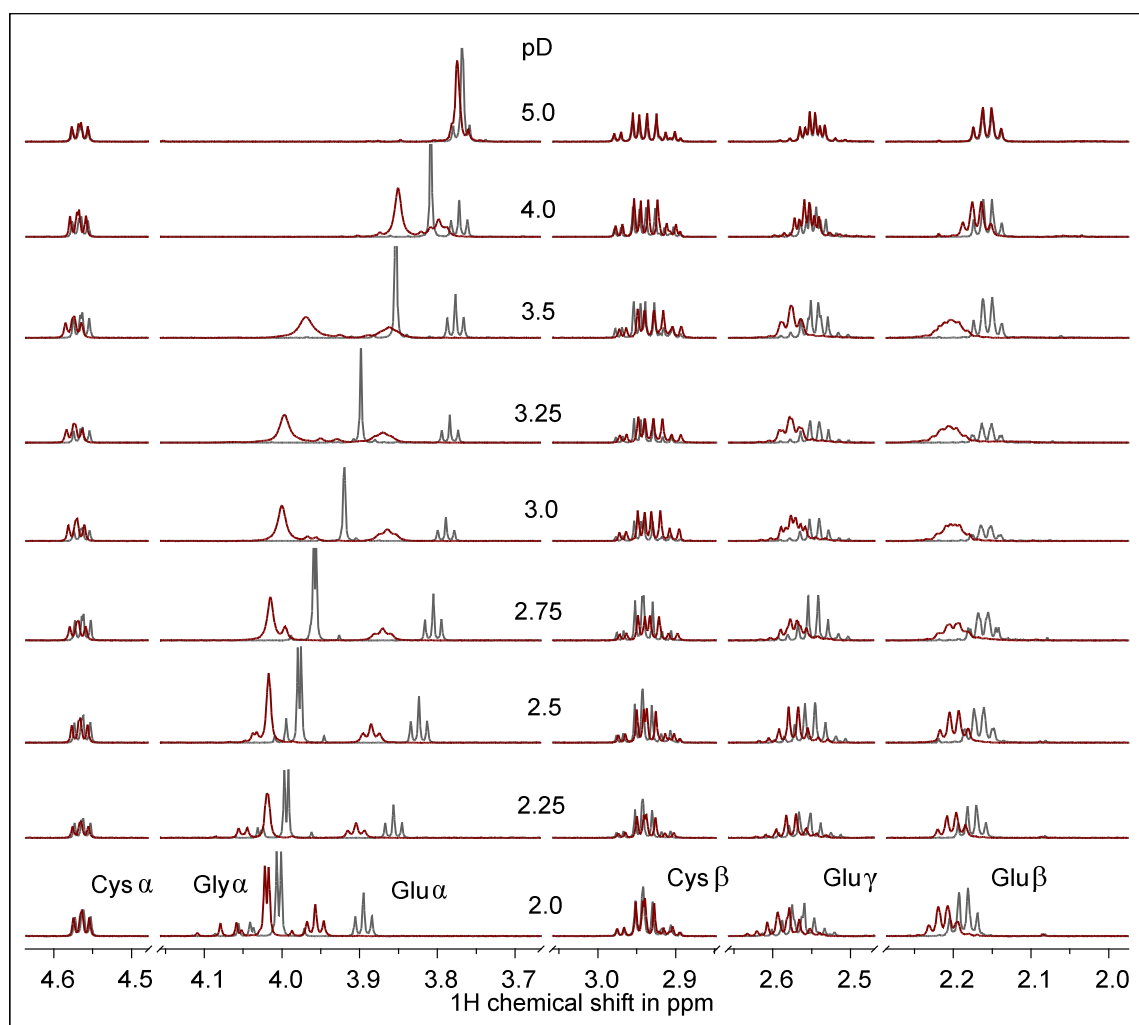


Figure A21. ^1H NMR spectra of 6.7 mM GSH blanks (grey) and samples with initial M/L = 0.5 (red) in the pD range 2–5. For clarity, only parts of the spectra are shown.

Table A4. Obtained fitting parameters for the sigmoidal dose-response-fits shown inFigure 21 according to $y = A1 + (A2 - A1) / \left(1 + 10^{(\log(x_0 - x)) \cdot p} \right)$

parameter	Glu α	Gly α
A1	50.00 \pm 7.82	4.43 \pm 17.81
A2	127.97 \pm 5.64	188.50 \pm 37.87
x_0	2.551 \pm 0.054	2.827 \pm 0.123
p	0.973 \pm 0.320	1.396 \pm 0.339
R^2	0.99485	0.99662
χ^2 red.	2.824	6.391

A1 and A2 can be seen as bottom and top asymptote,
 x_0 as the inflection point, and p as the hill slope.

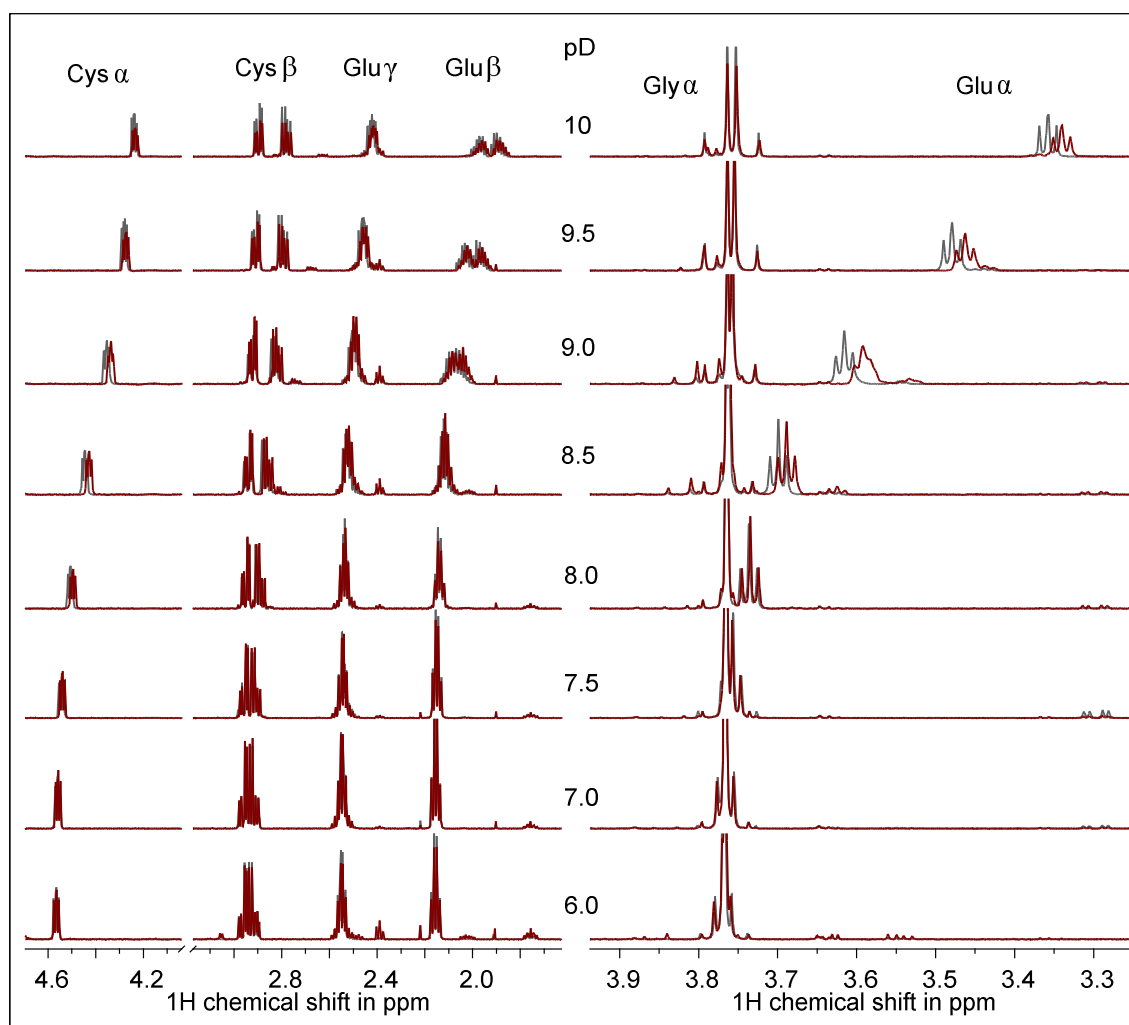


Figure A22. ^1H NMR spectra of 6.7 mM GSH blanks (grey) and samples with initial M/L = 2 (red) in the pD range 6–10. For clarity, the region between 3.3 and 3.9 ppm is omitted on the left and enlarged on the right.

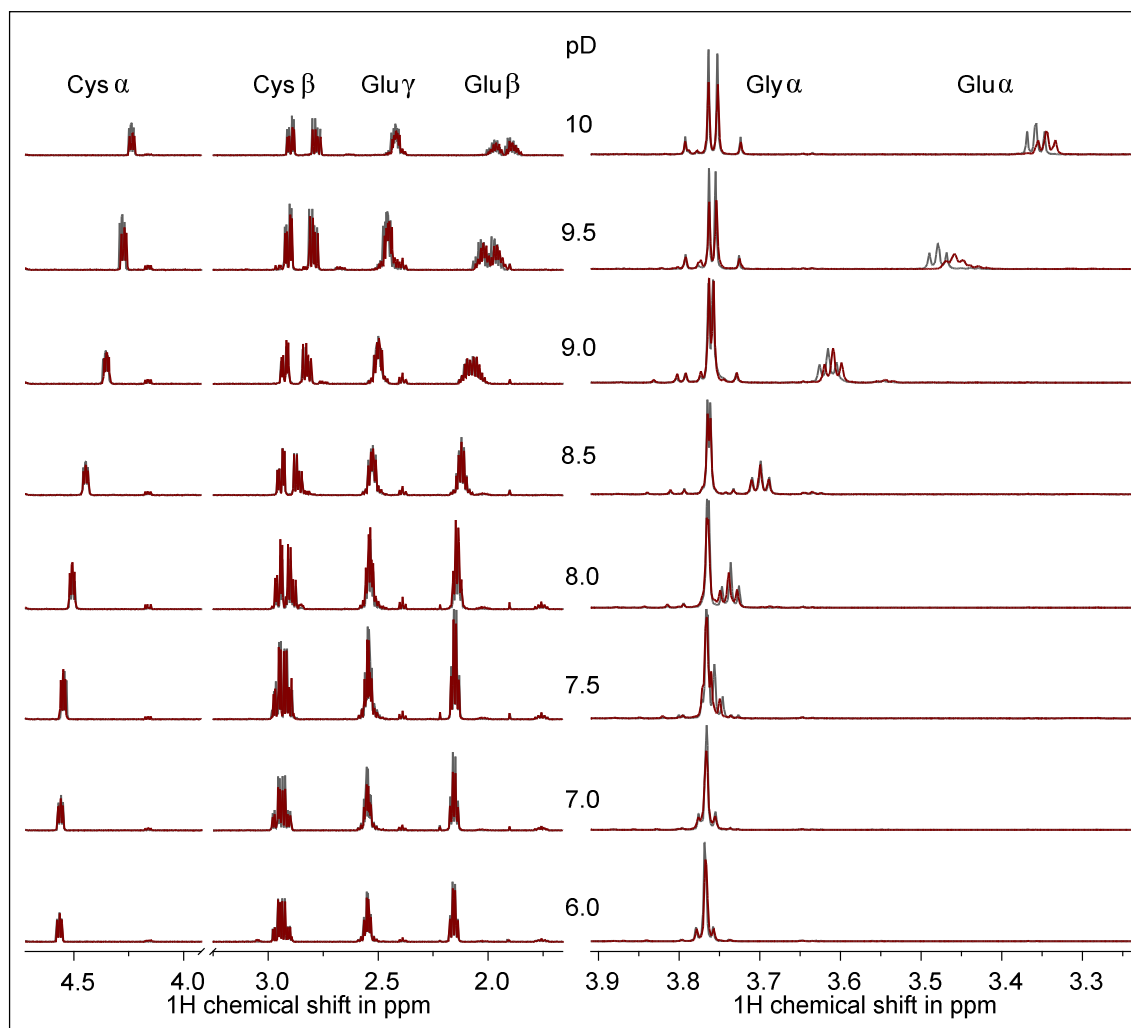


Figure A23. ^1H NMR spectra of 6.7 mM GSH blanks (grey) and samples with initial M/L = 0.5 (red) in the pD range 6–10. For clarity the region between 3.3 and 3.9 ppm is omitted on the left and enlarged on the right.

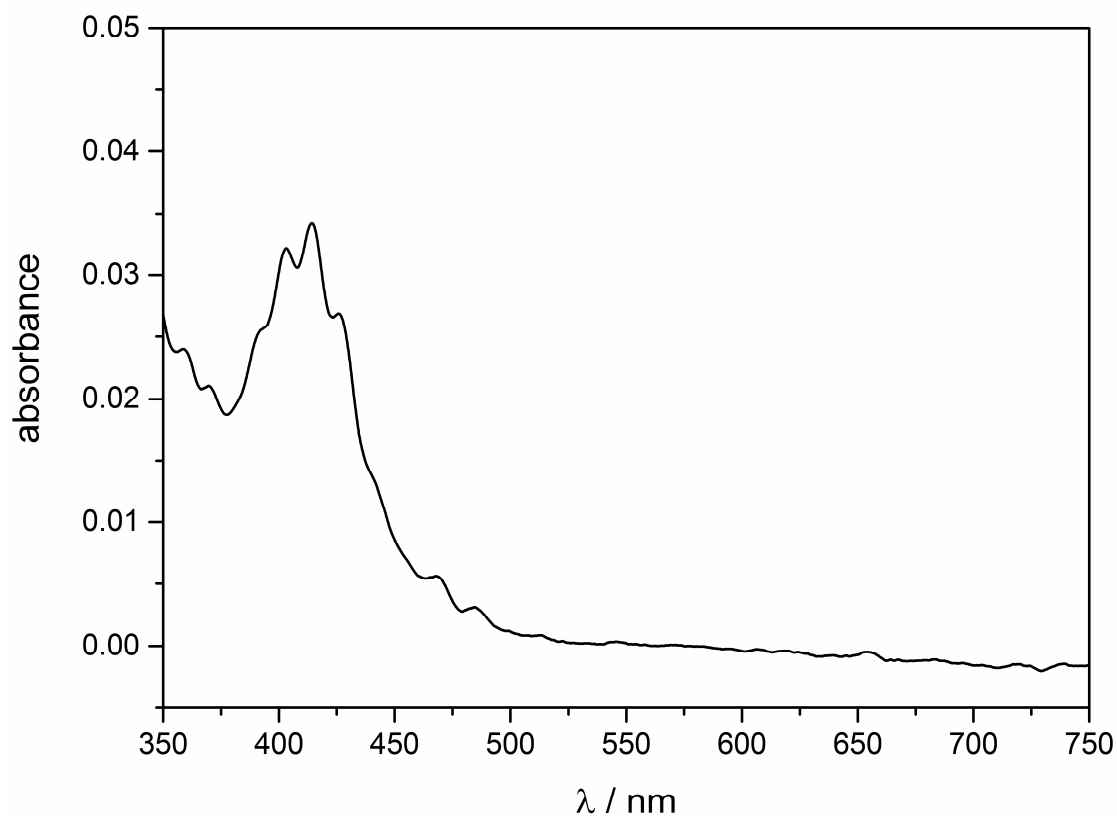


Figure A24. UV-Vis spectrum ($d = 1$ cm) of the lyophilized pellet obtained from 6.7 mM GSH and initial M/L = 5 pD 5 solution after dissolution in 5 M HClO₄.

Table A5. UV-Vis absorption maxima according to Figure A24.

absorption maxima in nm	
observed	Ref. [212]
369.5	369.9
391.0	391.6
402.9	402.7
414.2	414.5
425.9	427.0
468.1	468.8
484.6	484.6

Table A6. UV-Vis-NIR absorption maxima according to Figure 28.

observed (literature) absorption maxima in nm	assignment
369.5 (369.9) ^a	UO ₂ ²⁺
393.0 (391.6) ^a	UO ₂ ²⁺
405.3 (402.7) ^a	UO ₂ ²⁺
417.5 (414.5) ^a	UO ₂ ²⁺
429.3 (427.0) ^a / (429.4) ^b	UO ₂ ²⁺ / U ⁴⁺
470.5 (468.8) ^a	UO ₂ ²⁺
487.3 (484.6) ^a / (485.9) ^b	UO ₂ ²⁺ / U ⁴⁺
494.8 (495.3) ^b	U ⁴⁺
549.2 (549.5) ^b	U ⁴⁺
650.0 (648.5) ^b	U ⁴⁺
670.5 (671.6) ^b	U ⁴⁺
755 (738) ^c (760) ^d (770) ^e	U ^V O ₂ ⁺
878 (880) ^b	U ⁴⁺
988 (940) ^c (960) ^d (990) ^{e,f} (970) ^g	U ^V O ₂ ⁺
1073 (1069.9) ^b	U ⁴⁺
1124 (1140) ^f	U ^V O ₂ ⁺
1279	(U ^V O ₂ ⁺)*
1365	(U ^V O ₂ ⁺)*

^aRef. [212]; ^bRef. [112]; ^cRef. [167]; ^dRef. [168]; ^eRef. [213];

^fRef. [214]; ^gRef. [215]; *tentative assignment

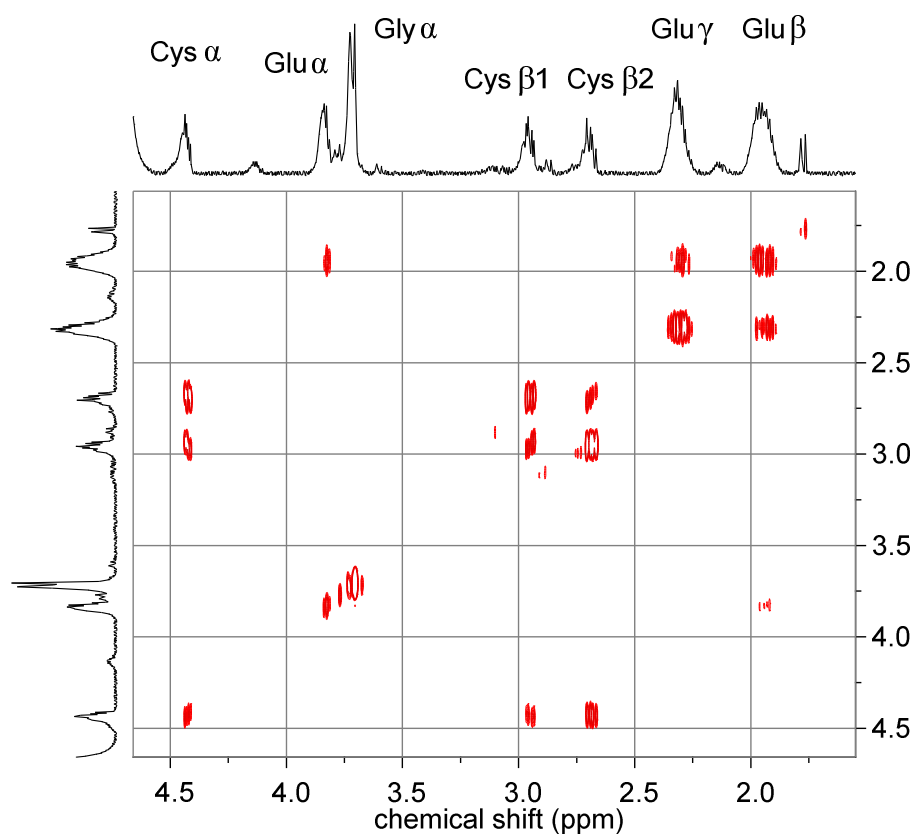


Figure A25. H,H-COSY spectrum with externally projected ^1H NMR spectra of the aged pellet of the 6.7 mM GSH pD 8 sample with initial M/L = 0.5 re-dissolved in 0.5 M DCl.

Note the considerable line broadening attributed to paramagnetic uranium ions (of valence states lower than +VI) present in the solution, affecting the relaxation time and, hence, S/N and spectral resolution.

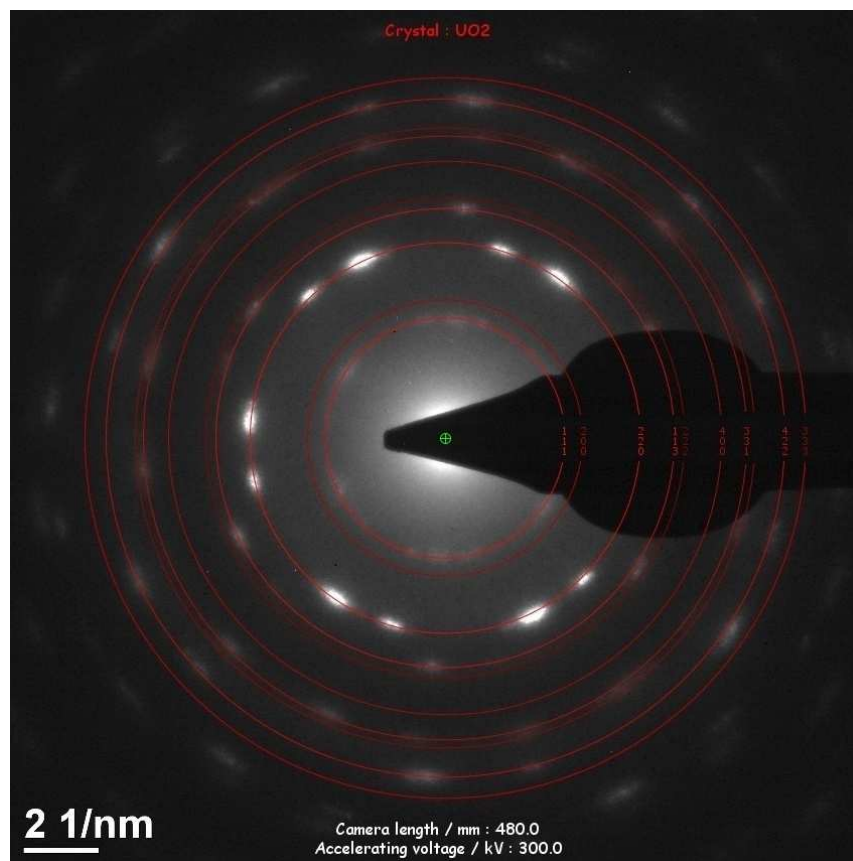


Figure A26. SAED pattern obtained from the precipitate of a freshly prepared sample suspension of initial 6.7 mM GSH and $M/L = 0.5$ at pD 7. Red rings belong to the simulated diffraction pattern based on fluorite-type UO₂ (ICSD card 24224) demonstrating that the precipitate is composed of crystalline UO₂.

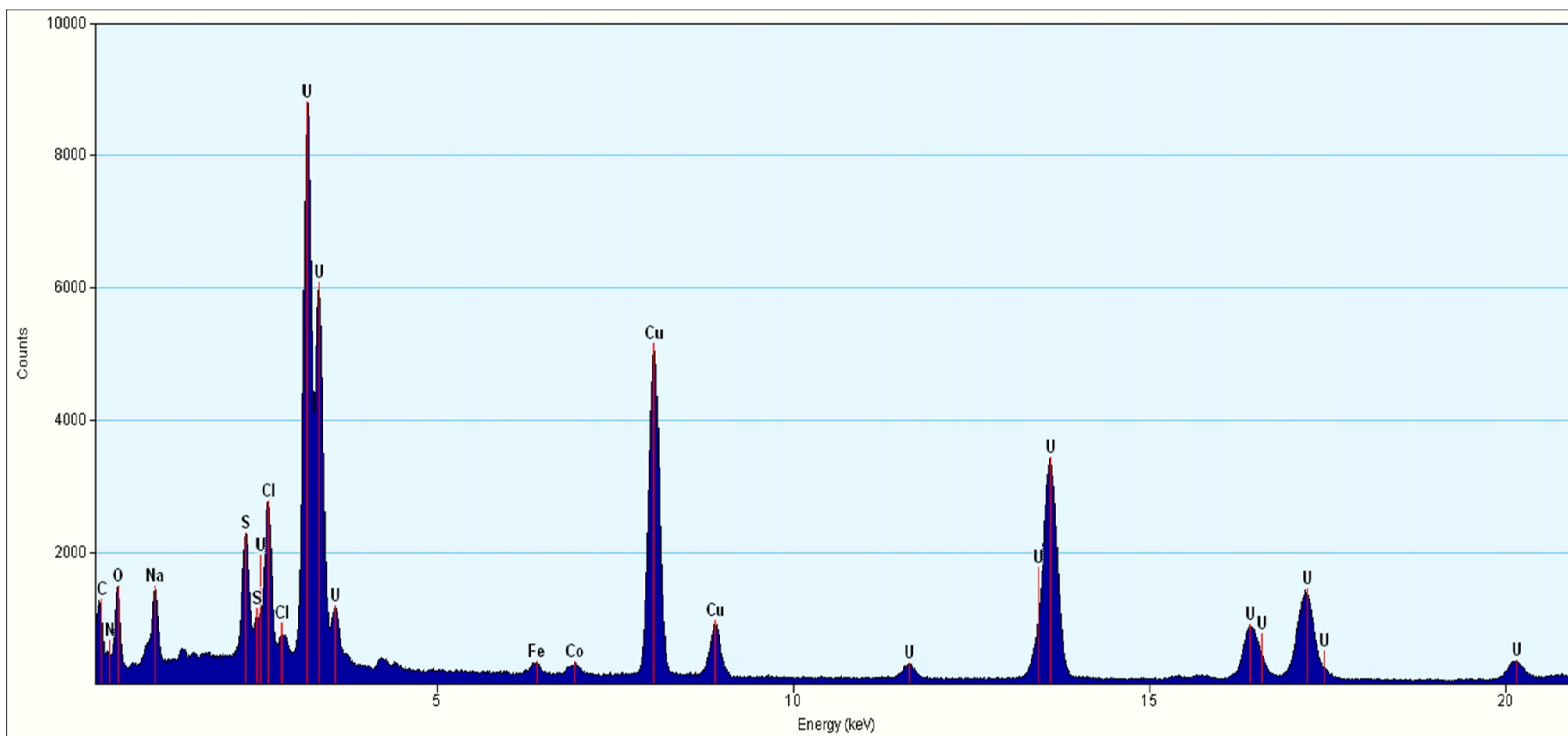


Figure A27. EDX spectrum obtained with a condensed electron beam in TEM mode of the sample of initial 6.7 mM GSH and M/L = 0.5 at pD 7. Note that the C and Cu signals are associated with the carbon-coated copper grid used for the TEM measurement. Fe and Co are fluorescence signals from the pole piece of the microscope objective lens.

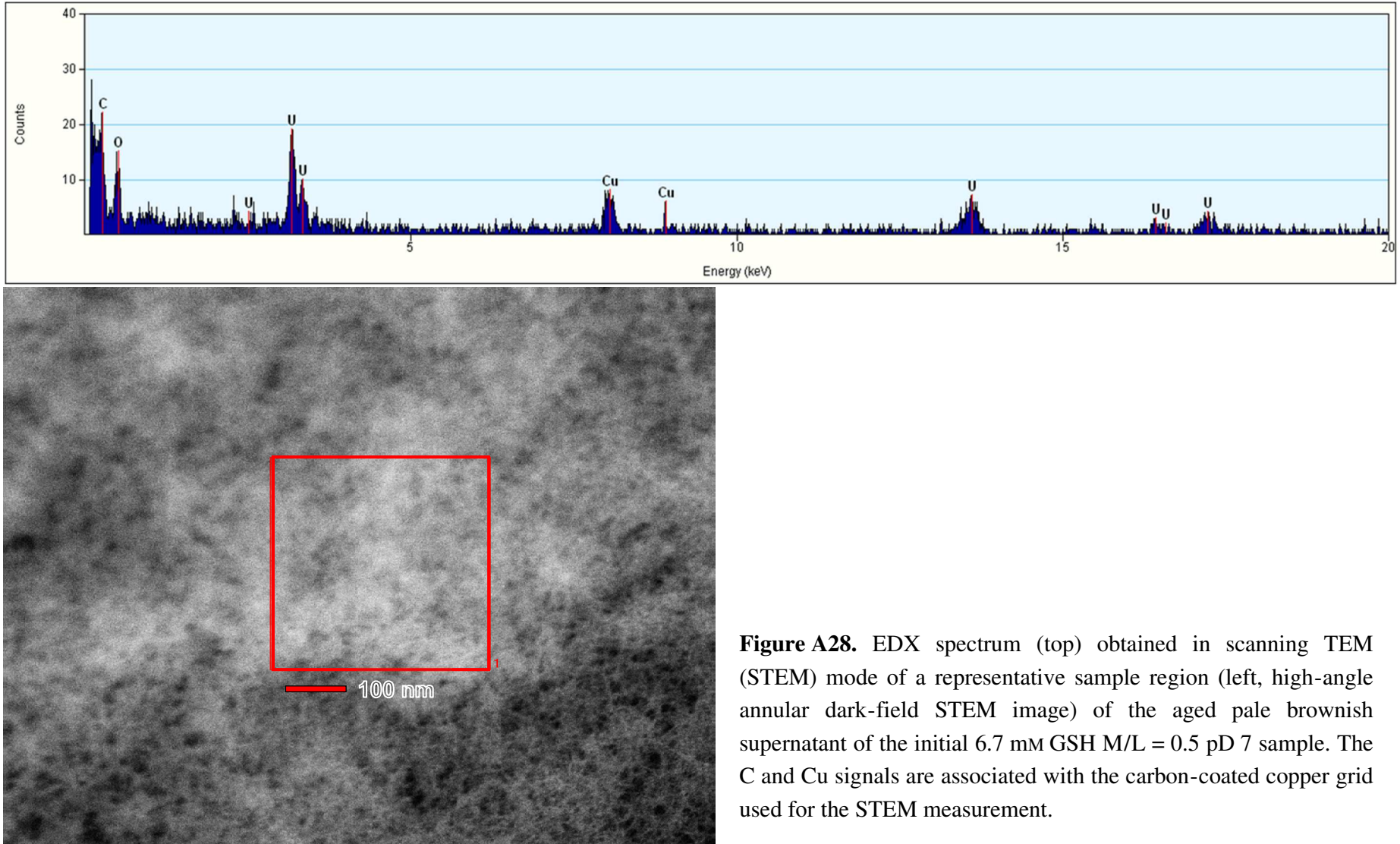


Figure A28. EDX spectrum (top) obtained in scanning TEM (STEM) mode of a representative sample region (left, high-angle annular dark-field STEM image) of the aged pale brownish supernatant of the initial 6.7 mM GSH M/L = 0.5 pD 7 sample. The C and Cu signals are associated with the carbon-coated copper grid used for the STEM measurement.

Table A7. UV-Vis absorption maxima according to Figure 32.

observed (literature) absorption maxima in nm	assignment
393.0 (391.6) ^a	UO ₂ ²⁺
408.6 (407.7) ^a	UO ₂ ²⁺
414.9 (414.5) ^a	UO ₂ ²⁺
428.3 (427.0) ^a / (429.4) ^b	UO ₂ ²⁺ / U ⁴⁺
485.2 (484.6) ^a / (485.9) ^b	UO ₂ ²⁺ / U ⁴⁺
495.1 (495.3) ^b	U ⁴⁺
548.0 (549.5) ^b	U ⁴⁺
647.5 (648.5) ^b	U ⁴⁺
671.0 (671.6) ^b	U ⁴⁺

^aRef. [212]; ^bRef. [112]

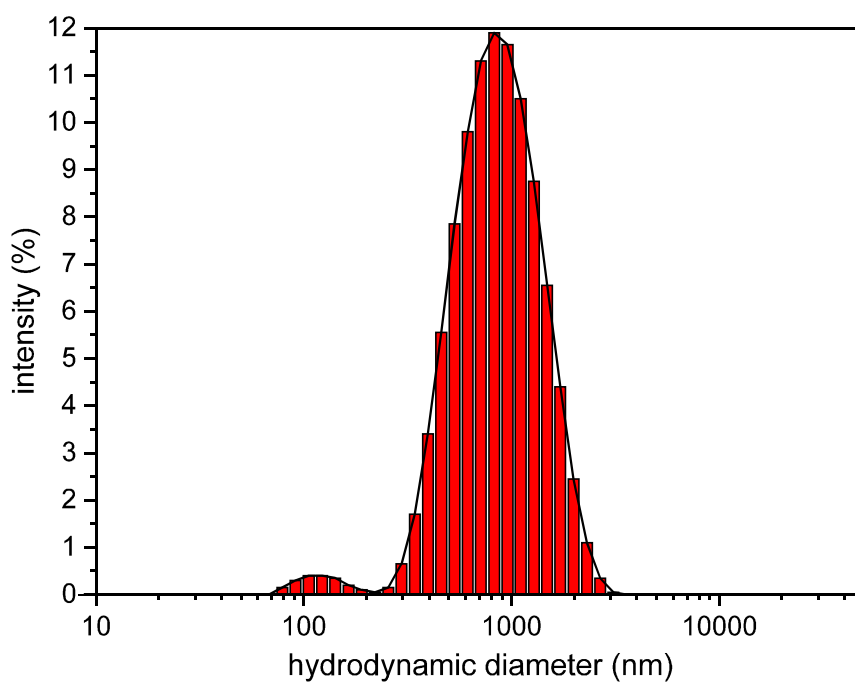


Figure 29. Particle size distribution of the pale brownish aged supernatant of the initial 6.7 mM GSH M/L = 0.5 pD 8 sample, determined by DLS. Note that the quantity of the smaller particles is potentially underestimated.

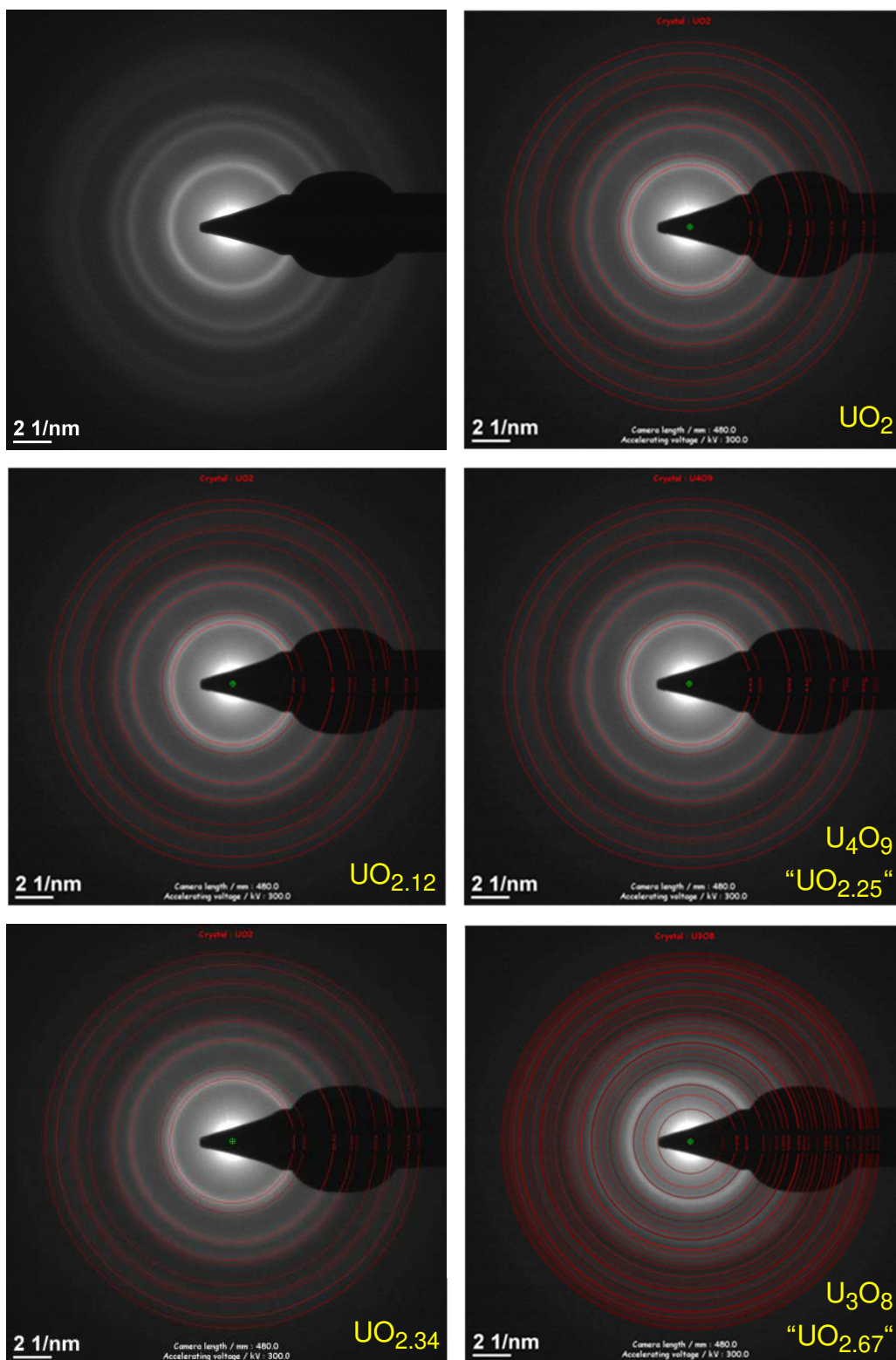


Figure A30. SAED pattern (white) of the aged pale brownish supernatant of the initial 6.7 mM GSH M/L = 0.5 pD 7 sample with trial-and-error matching attempts with simulated diffraction patterns (red rings) for different UO_x structures based on reference data: ICSD 24224 (UO_2); ICSD 1426 ($\text{UO}_{2.12}$); ICSD 15439 (U_4O_9); ICSD 29137 ($\text{UO}_{2.34}$); ICSD 246854 (U_3O_8).

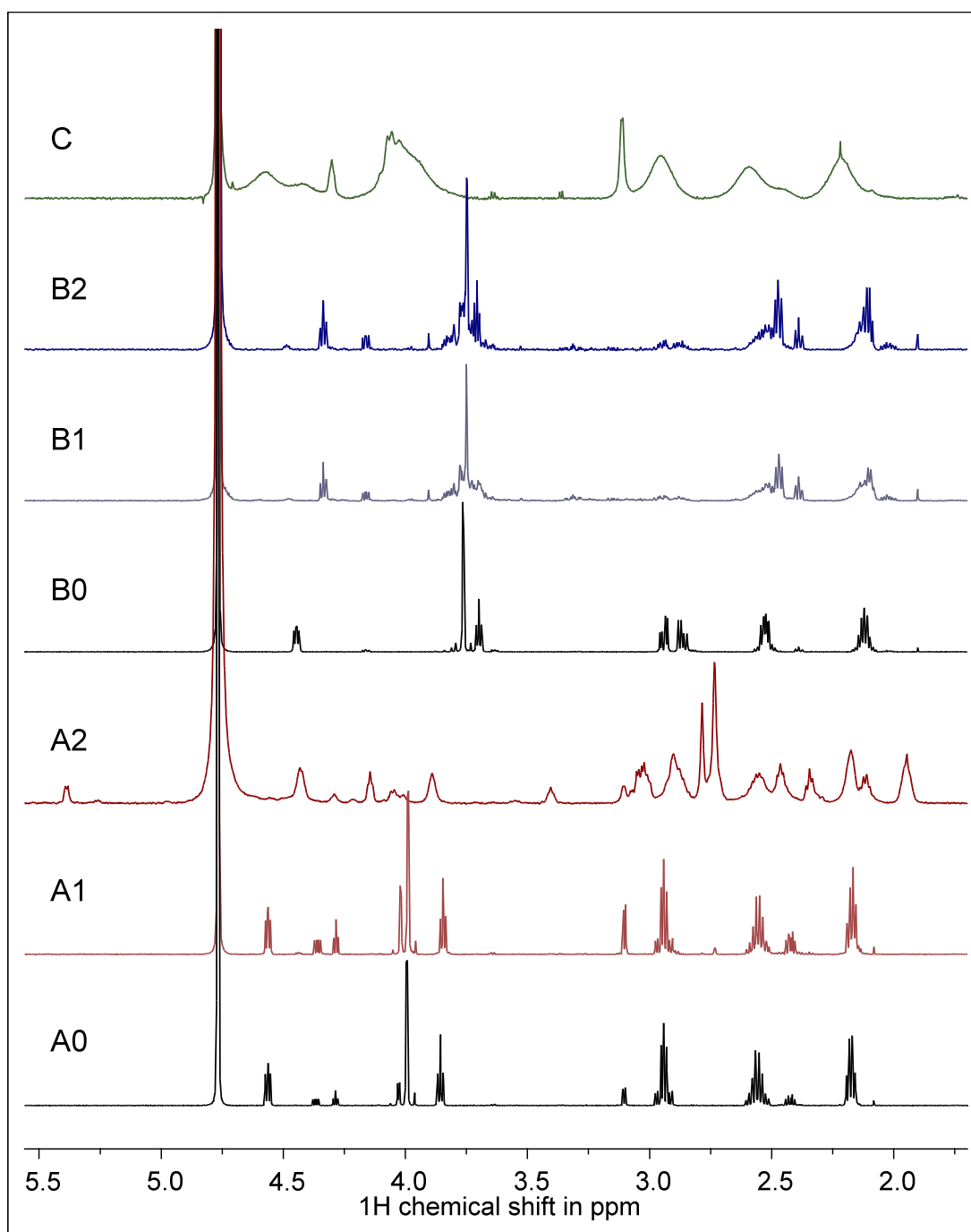


Figure A31. ¹H NMR spectra of GSH at pD 2.25 (A series) and pD 8.5 (B series), with 0: blank, 1: blank light-irradiated, 2: light-irradiated in the presence of U^{VI} with M/L = 0.5; C: GSH and U^{IV} at pD 2 with M/L = 0.5.

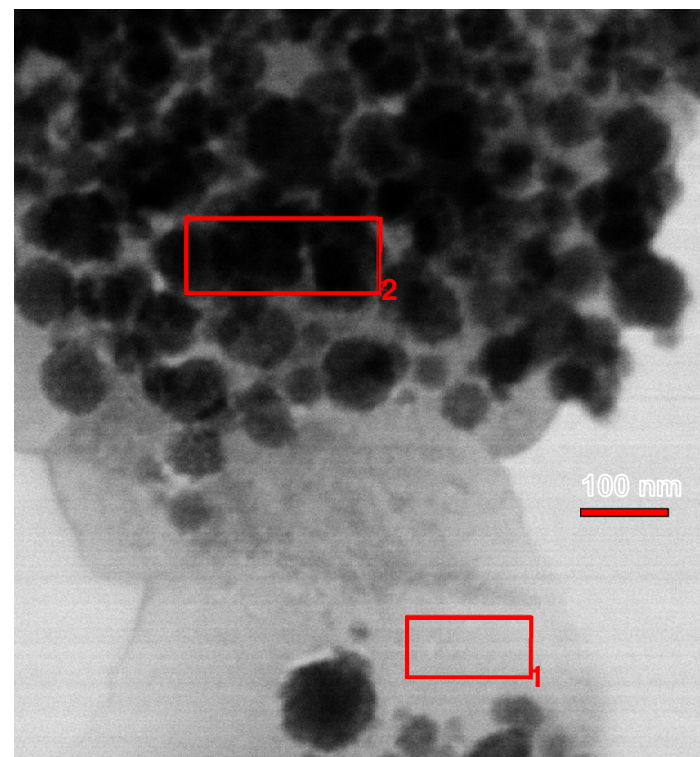
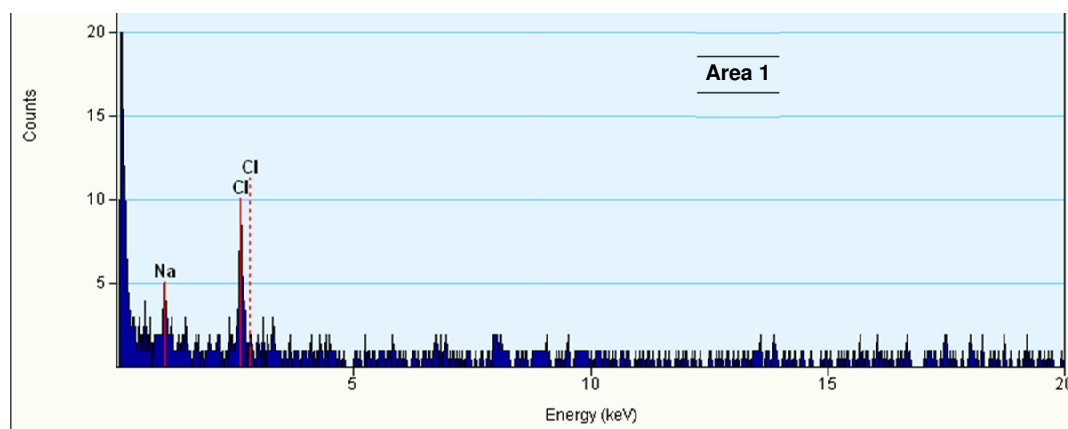
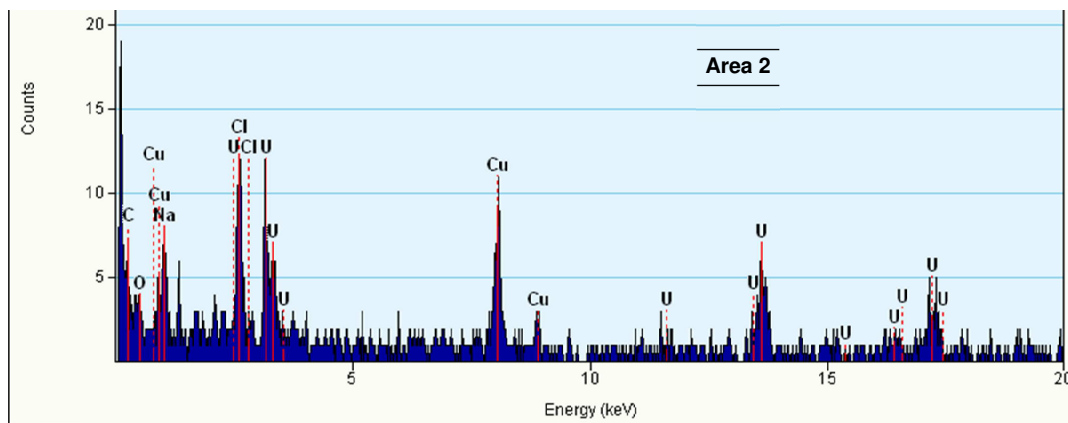


Figure A32. EDX spectra obtained in scanning TEM (STEM) mode of representative sample regions (right, high-angle annular STEM image) of the dark grey precipitate obtained after light-irradiation of a 6.7 mM GSH and 3.33 mM U^{VI}pD 2.25 sample, obtained from areas 1 and 2, respectively. Note that the C and Cu signals are associated with the carbon-coated copper grid used for the TEM measurement.

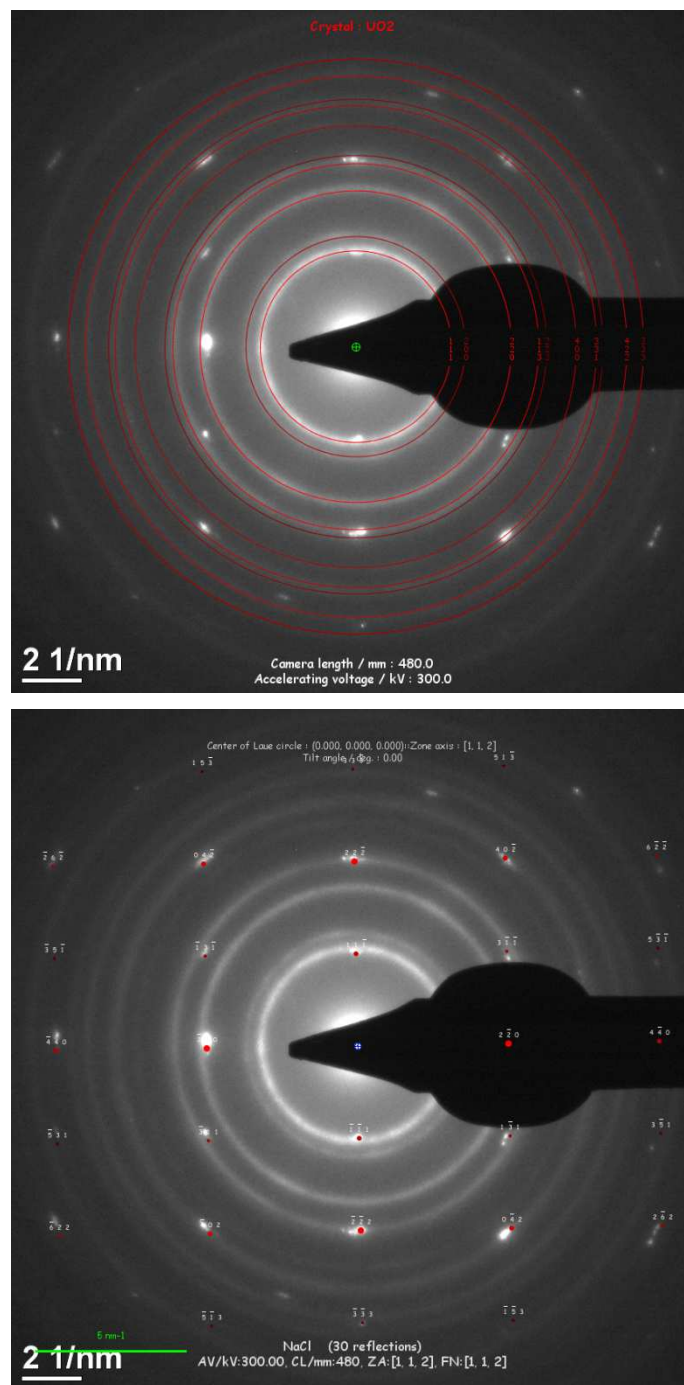


Figure A33. SAED pattern (white) of the dark grey precipitate obtained after light-irradiation of a 6.7 mM GSH and 3.3 mM U^{VI} pD 2.25 sample together with the red rings belonging to simulated diffraction pattern based on fluorite-type UO₂ (ICSD card 24224), top, and lattice reflections showing as sharp diffraction spots attributed to NaCl single crystal.

$$E = E^\circ - \frac{RT}{zF} \ln Q$$

$$\Delta G = -zF \Delta E$$

- with E half-cell potential
 E° half-cell potential for standard conditions
 R gas constant ($R = 8.31447 \text{ J K}^{-1} \text{ mol}^{-1}$)
 T temperature in K
 z number of electrons exchanged
 F FARADAY constant ($96.485 \text{ kJ V}^{-1} \text{ mol}^{-1}$)
 Q mass law quotient with numbers in brackets denoting concentrations
 ΔE electromotive force
 ΔG change in GIBBS energy

$$E(2\text{GSH}/\text{GSSG}) = E^\circ - \frac{RT}{zF} \ln \frac{[\text{GSH}]^2}{[\text{GSSG}][\text{H}^+]^2}$$

with $E^\circ(2\text{GSH}/\text{GSSG}) = +0.180 \text{ V}$ [121];

$z = 2$; $T = 298 \text{ K}$; $[\text{GSH}] = 6.7 \times 10^{-3} \text{ M}$; $[\text{H}^+] \approx 10^{-\text{pH}}$; $[\text{GSSG}] \rightarrow 0 \Rightarrow [\text{GSSG}] = 10^{-6} \text{ M}$

$$E(\text{U(VI)}/\text{U(IV)}) = E^\circ - \frac{RT}{zF} \ln \frac{[\text{U}^{4+}]^2}{[\text{UO}_2^{2+}][\text{H}^+]^4}$$

with $E^\circ(\text{U}^{\text{VI}}/\text{U}^{\text{IV}}) = +0.267 \text{ V}$ [216];

$z = 2$; $T = 298 \text{ K}$; $[\text{U}^{\text{VI}}] = 3.3 \times 10^{-3} \text{ M}$; $[\text{H}^+] \approx 10^{-\text{pH}}$; $[\text{U}^{\text{IV}}] \rightarrow 0 \Rightarrow [\text{U}^{\text{IV}}] = 10^{-10} \text{ M}$

$$E(2\text{U(VI)}/2\text{U(V)}) = E^\circ - \frac{RT}{zF} \ln \frac{[\text{UO}_2^+]^2}{[\text{UO}_2^{2+}]^2}$$

with $E^\circ(\text{U}^{\text{VI}}/\text{U}^{\text{V}}) = +0.088 \text{ V}$ [216];

$z = 2$; $T = 298 \text{ K}$; $[\text{U}^{\text{VI}}] = 3.3 \times 10^{-3} \text{ M}$; $[\text{H}^+] \approx 10^{-\text{pH}}$; $[\text{U}^{\text{V}}] \rightarrow 0 \Rightarrow [\text{U}^{\text{V}}] = 10^{-10} \text{ M}$

Note:

- i. initially there is neither GSSG nor U^{4+} nor U^{V} present, therefore, low concentrations, particularly for the latter two are assumed; for GSSG 10^{-6} M in regard of the NMR detection limit;
- ii. in order to fit the number of electrons released by the oxidation of GSH, the $\text{U}^{\text{VI}}/\text{U}^{\text{V}}$ reaction was adjusted to $z = 2$.

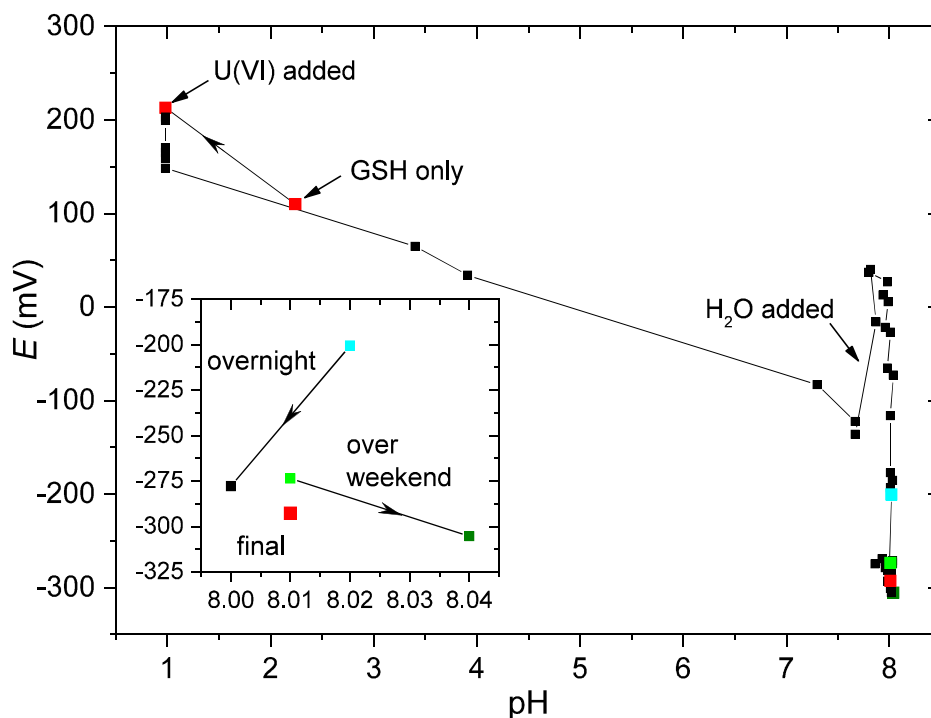


Figure A34. Redox potential E during pH adjustment of a 10 mM GSH and 5 mM U^{VI} sample in H_2O under nitrogen atmosphere with continuous stirring. Data points correspond to pH/ E values recorded after some equilibration. Note the highlighted data points.

Figure A34 shows exemplarily the redox potential E in dependence of pH for a 10 mM GSH and 5 mM U^{VI} sample under N_2 atmosphere titrated up to pH 8. Initially, that is for high $[H^+]$, the redox potential is positive for both the GSH-only solution (pH 2.3) and after admixture of an appropriate aliquot of U^{VI} stock solution (pH < 1), see correspondingly indicated data points. Upon successive addition of NaOH primarily the Gly COOH (pK_a 3.2) is titrated and U^{VI} changes its speciation from free uranyl ion to (polynuclear) hydroxo species, with concomitant formation of ternary GSH hydroxo U^{VI} complexes. The large step, *i.e.*, pH 3.91 \rightarrow 7.30, is due to totally titrated Gly COOH, thus buffering capacity is used up. As of pH 5 the redox potential becomes negative. Addition of water (for total volume adjustment; as indicated) temporarily increases E owing to dilution effects, but around pH 8 E shifts to remarkably negative values, since GSH's SH group (pK_a 9.0) starts to ionise and, therefore, develops its full pH-dependent reduction potential.

9.2 CITRATE TOPIC

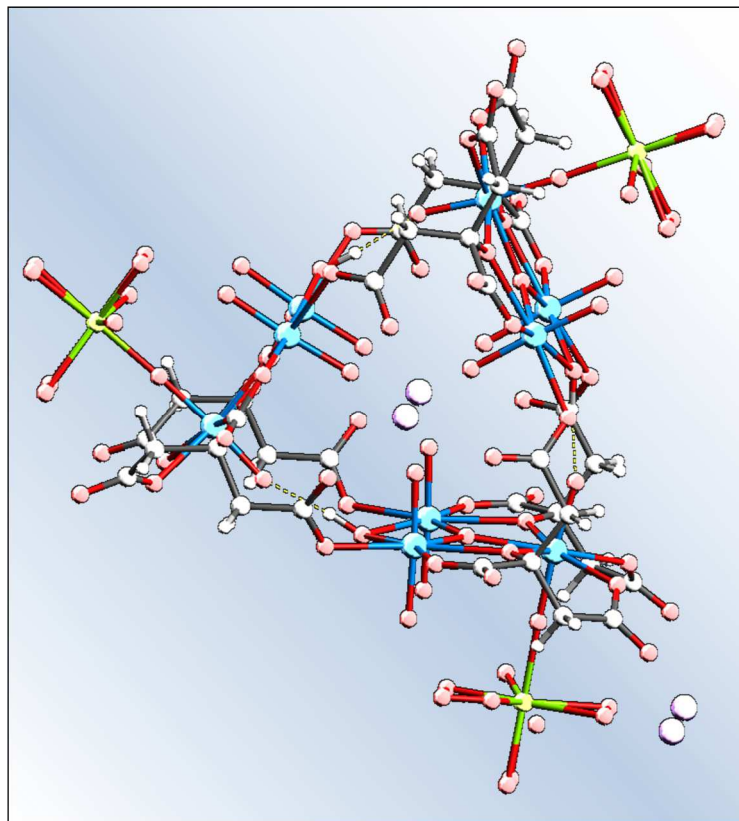


Figure A35. Crystal structure representation of the 9:6 U^{VI}-Cit macrocyclic complex, taken from [137], CCDC deposition no. 1031413.

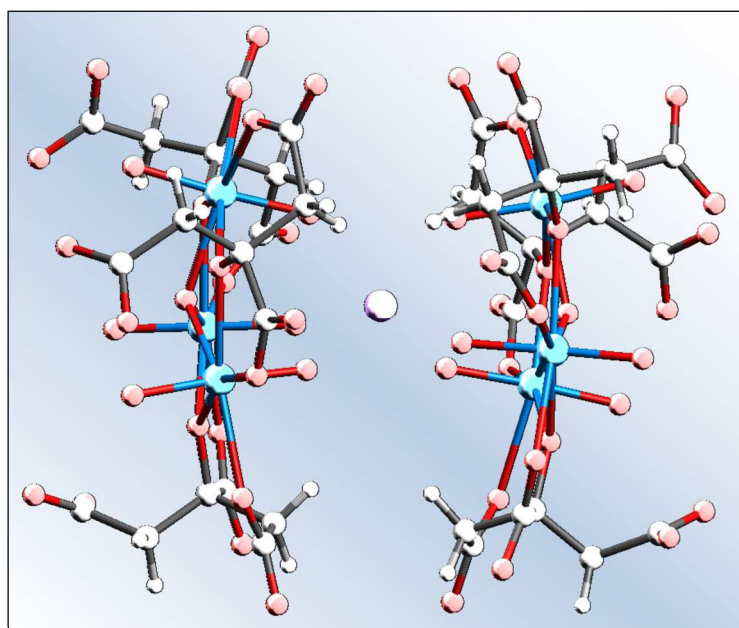


Figure A36. Crystal structure representation of the 6:6 sandwich complex formed upon bridging two 3:3 U^{VI}-Cit complexes by a Na⁺ cation, taken from [137], CCDC deposition no. 1031412.

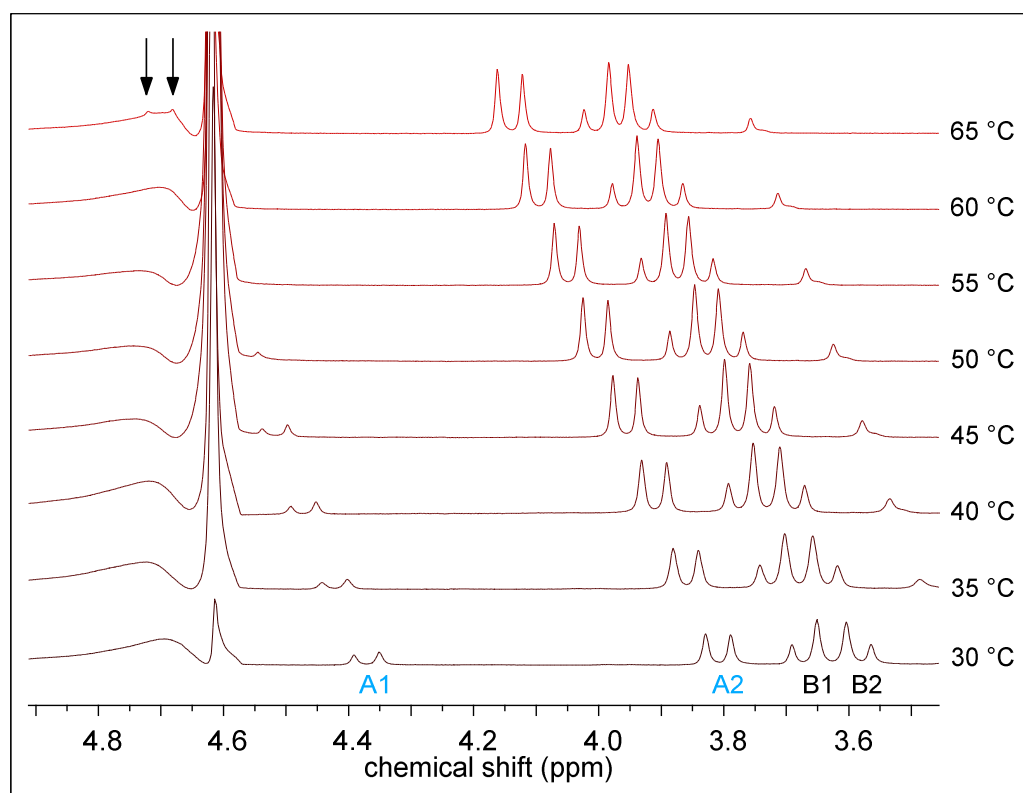


Figure A37. Temperature-dependent ^1H NMR spectra depicting the $\text{U}^{\text{VI}}\text{-Cit}$ 3:3 complex signals.

Note the presaturation sequence applied for water signal (4.65 ppm) suppression, thus also affecting signal intensity of nearby A1. Upon increasing T the 3:3 complex related signals shift unanimously by 10 ppb/K, thereby A1 is occasionally obscured by the water signal, but for sufficiently high T , it reappears (arrows).

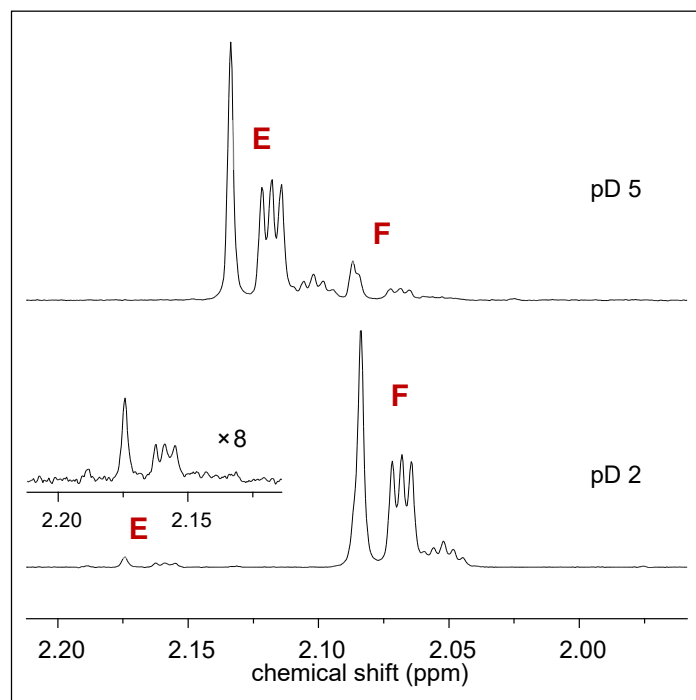


Figure A38. ^1H NMR spectra of lithium acetoacetate in D_2O solutions for pD values as indicated. Signal groups E and F correspond to (partially deuterated) methyl groups of AcAc and Ace, respectively. Note the pD-dependence of the AcAc signals because of protonation/deprotonation of the molecule's carboxyl group. The low signal intensity of E in the pD 2 sample is caused by AcAc decarboxylation yielding Ace.

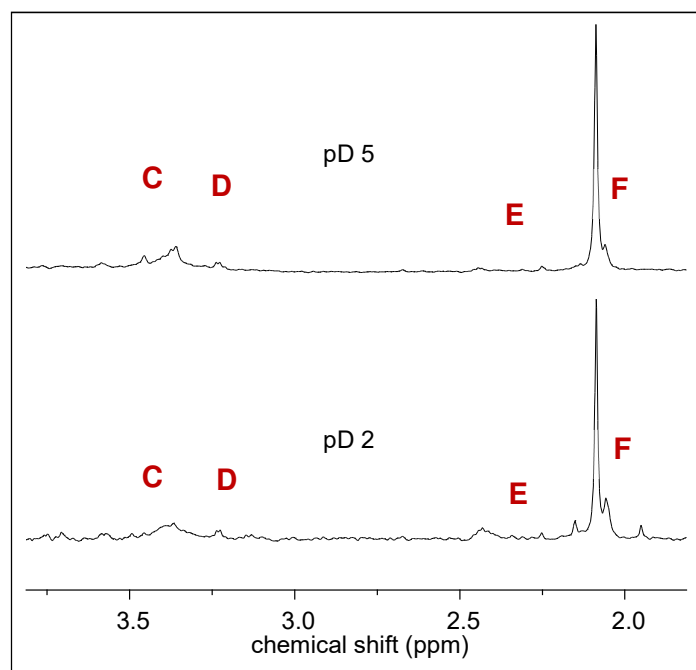


Figure A39. ^1H NMR spectra of acetonedicarboxylic acid, *i.e.*, $\beta\text{-KG}$, in D_2O solutions for pD values as indicated. Signal groups C and D, and E and F correspond to (partially deuterated) methylene and methyl groups of $\beta\text{-KG}$, AcAc and Ace, respectively. Note the low signal intensity of $\beta\text{-KG}$ (and AcAc) attributed signals due to $\beta\text{-KG}$ (and AcAc) decarboxylation yielding Ace.

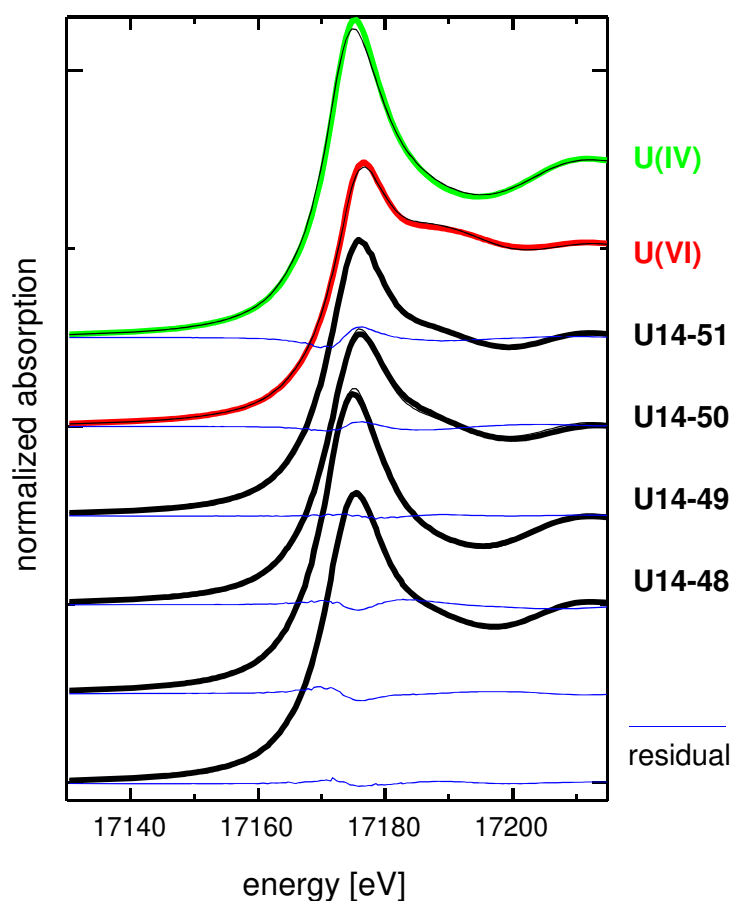


Figure A40. Uranium L_{III} X-ray absorption near-edge spectra (XANES) for samples denoted and composed as follows U14-X ([U^{VI}]/[Cit]/pH) [in mM]: 48 (50/100/5), 49 (50/100/2), 50 (50/50/5), and 51 (50/50/2).

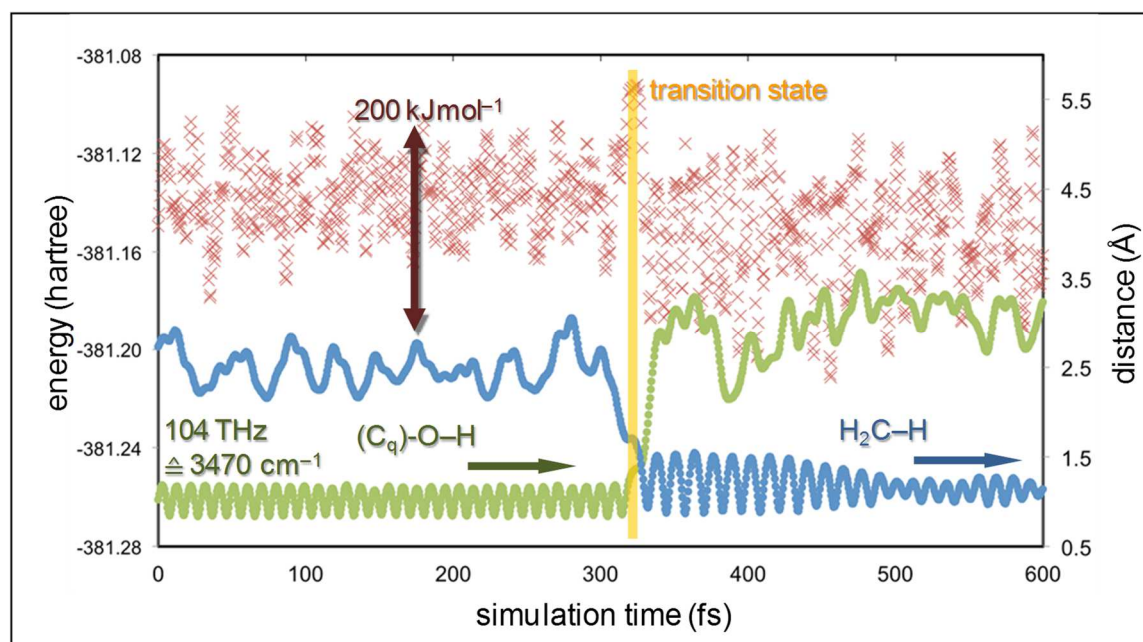


Figure A41. BORN-OPPENHEIMER molecular dynamics (BOMD) calculation illustrating hydrogen transfer during *enol-keto* re-arrangement.

9.3 SELENIUM TOPIC

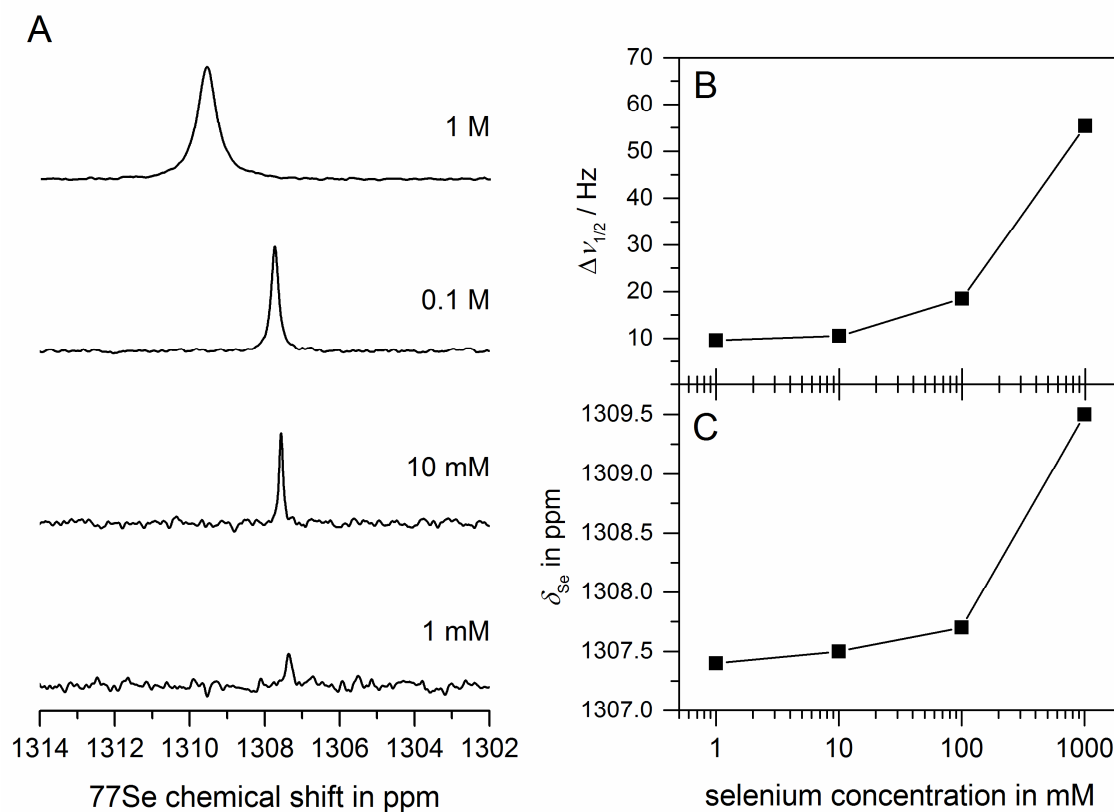


Figure A42. ^{77}Se NMR ($B_0 = 9.4$ T) pH_c 5 solutions with Se^{IV} concentrations from 1 mM through 1 M, and constant total ionic strength $I = 3$ M (A); dependence of line width (B) and chemical shift (C) on selenium concentration.

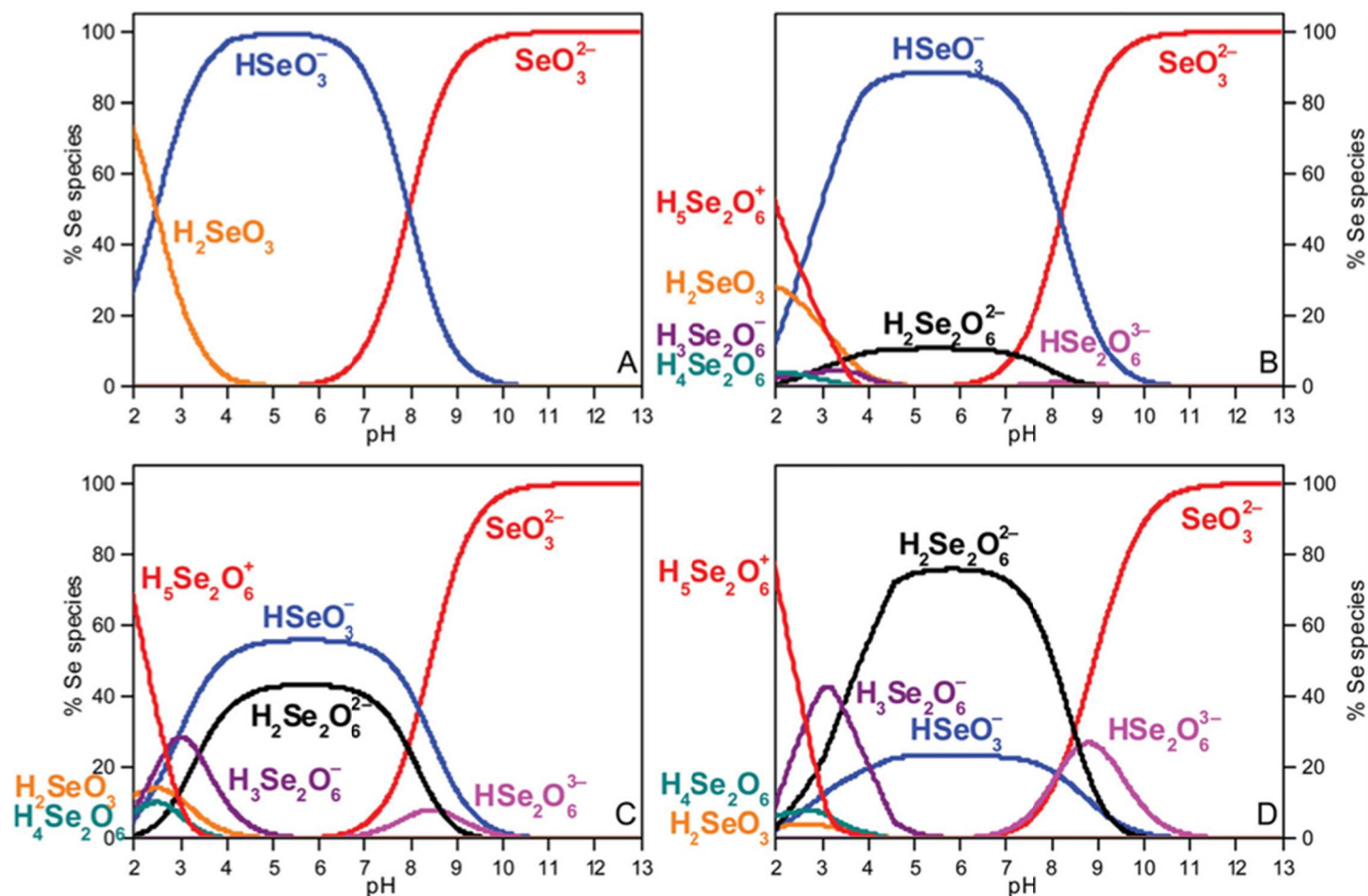


Figure A43. Se^{IV} speciation diagrams based on stability constants according to Table A8 for (A) $[\text{Se}^{\text{IV}}] = 0.1 \text{ M}$ (0.1 M NaCl) without consideration of dimeric species; (B) $[\text{Se}^{\text{IV}}] = 1 \text{ mM}$ (0.3 M NaCl), (C) $[\text{Se}^{\text{IV}}] = 10 \text{ mM}$ (0.3 M NaCl), and (D) $[\text{Se}^{\text{IV}}] = 0.1 \text{ M}$ (0.1 M NaCl) with consideration of dimeric species. Note that an increase of ionic strength from 0.35-0.58 M for pH 8-13 (A), from 0.32-0.44 M for pH 12-13 (B), from 0.31-0.46 M for pH 8-13 (C) and from 0.33-0.58 M for pH 8-13 (D) is predicted.

Table A8. Stability constants used for speciation calculations using PHREEQC [217] (with $\log K$ corrected to $I = 0$).

Aqueous Species	$\log K^a$	$\log K^b$
$\text{H}^+ + \text{SeO}_3^{2-} \rightleftharpoons \text{HSeO}_3^-$	8.36	8.60
$2 \text{H}^+ + \text{SeO}_3^{2-} \rightleftharpoons \text{H}_2\text{SeO}_3$	11.00	11.33
$\text{H}^+ + 2 \text{SeO}_3^{2-} \rightleftharpoons \text{HSe}_2\text{O}_6^{3-} (\equiv \text{H}(\text{SeO}_3)_2^{3-})$		9.55
$2 \text{H}^+ + 2 \text{SeO}_3^{2-} \rightleftharpoons \text{H}_2\text{Se}_2\text{O}_6^{2-} (\equiv \text{H}_2(\text{SeO}_3)_2^{2-})$		18.77
$3 \text{H}^+ + 2 \text{SeO}_3^{2-} \rightleftharpoons \text{H}_3\text{Se}_2\text{O}_6^- (\equiv \text{H}_3(\text{SeO}_3)_2^-)$		22.57
$4 \text{H}^+ + 2 \text{SeO}_3^{2-} \rightleftharpoons \text{H}_4\text{Se}_2\text{O}_6 (\equiv \text{H}_4(\text{SeO}_3)_2)$		25.02
$5 \text{H}^+ + 2 \text{SeO}_3^{2-} \rightleftharpoons \text{H}_5\text{Se}_2\text{O}_6^+ (\equiv \text{H}_5(\text{SeO}_3)_2^+)$		27.80

^aRef. [61]; ^bRef. [170]

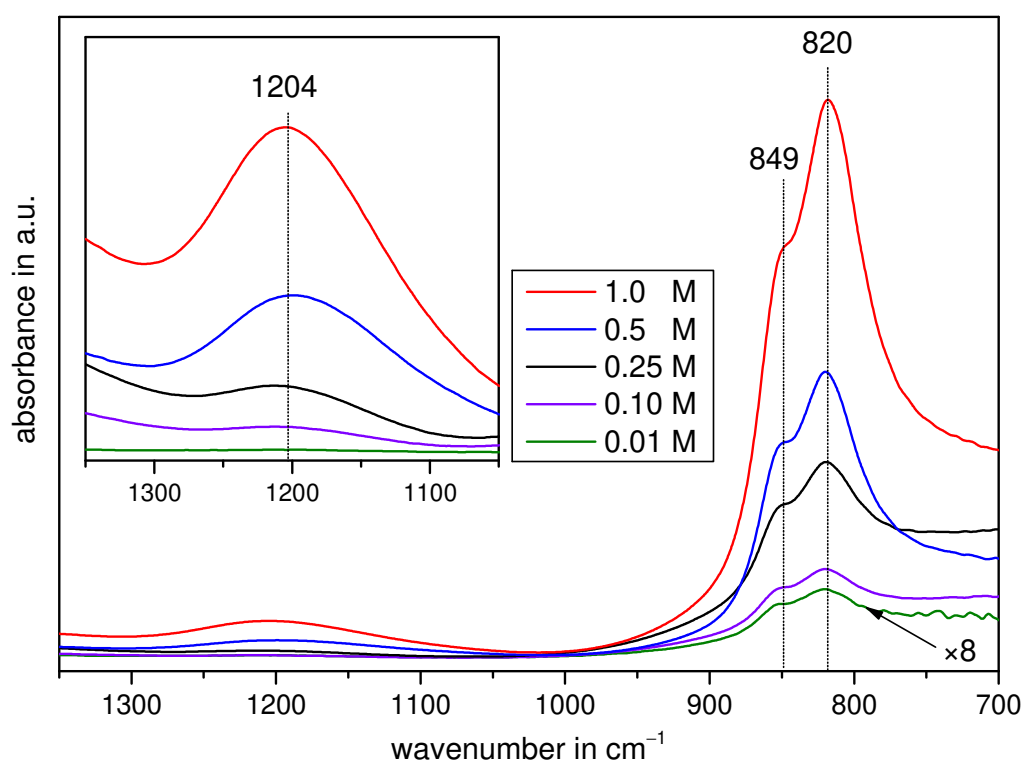


Figure A44. IR spectra of aqueous Se^{IV} pH_c 5, $I = 3$ M solutions at concentrations ranging from 0.01 through 1 M with the inset showing the dimer characteristic feature. Note the enhanced scaling of the spectrum of lowest concentration.

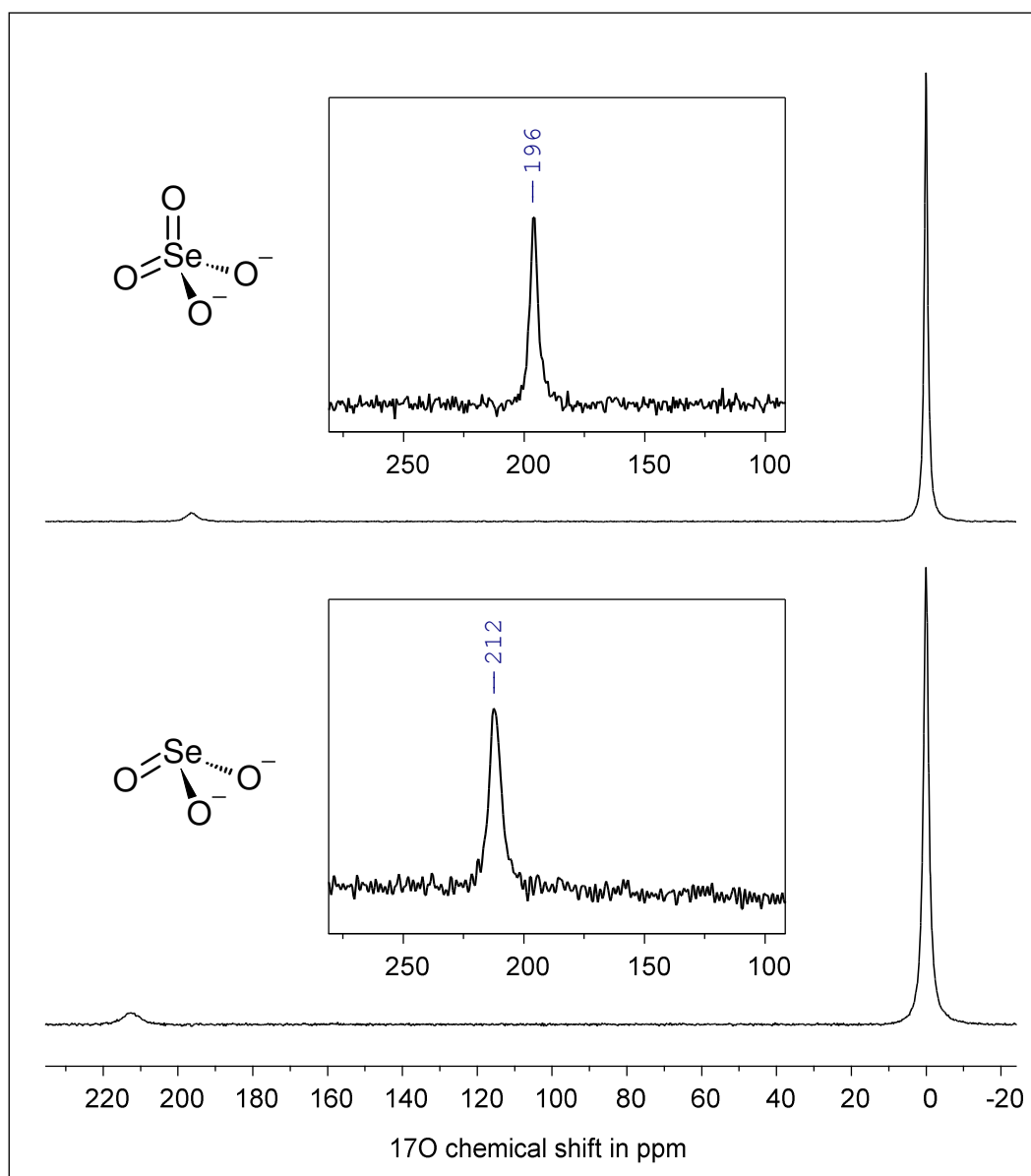


Figure A45. ^{17}O NMR of 1 M aqueous solutions of Na_2SeO_3 (bottom) and Na_2SeO_4 (top) acquired at 14.1 T using a 10 mm direct detection probe, $\pi/2$ pulse optimized to 40 μs at 60 dB, centered at 150 ppm, with 125 ms acquisition time, 1512 and 2440 transitions and interpulse delays of 2 and 1.5 s for Se^{IV} and Se^{VI} , respectively, resulting in total acquisition times of 1 h. The spectra were processed without applying a line broadening factor, by truncation of the FID after 1024, 512, and 256 pt, the latter two for the expansions of the Se^{IV} and Se^{VI} signals, respectively.

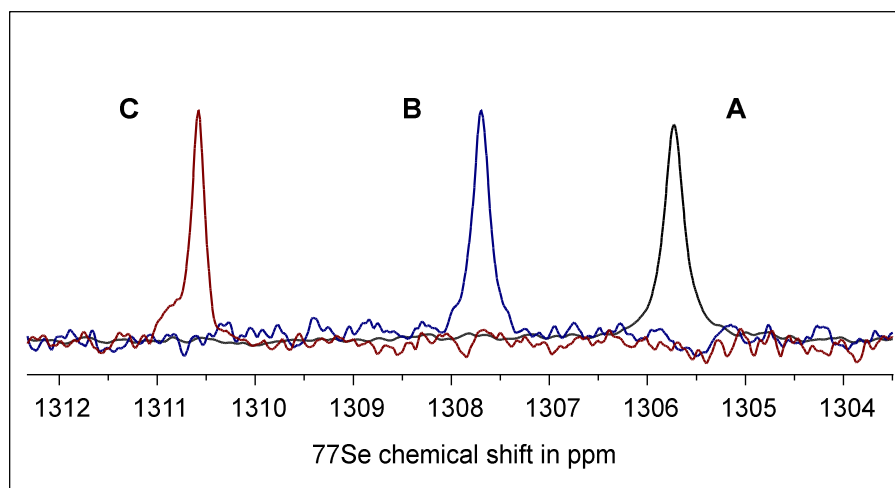


Figure A46. Superposition of ^{77}Se NMR spectra of 0.1 M Se^{IV} samples at pH_c 5 without (A), and with 2.7 M (B) and 5.3 M (C) NaCl added.

Spectra of 0.1 M Se^{IV} pH_c 5 samples containing additional NaCl in order to adjust ionic strength (I) revealed significant shifts further downfield with increasing I (Fig. A46 A to C), concluding that the monomer/dimer ratio has changed. According to the principle of LE CHÂTELIER AND BRAUN changing I establishes a new equilibrium constant K (as a function of I). The water required for solvation of additional NaCl is set free from hydrated monomers by virtue of (further) dimerization, say, decrease of effective water concentration.

Correspondingly, adjusted $K(I) = k_{\text{ass}}(I)/k_{\text{dis}}(I)$ results in changing both apparent δ_{Se} (due to altered molar fractions of monomer and dimer) and $\Delta\nu_{1/2}$ (with the signal in C being half as wide as that in A) since $k_{\text{ex}}(I)$ has increased as consequence of increased $k_{\text{ass}}(I)$.

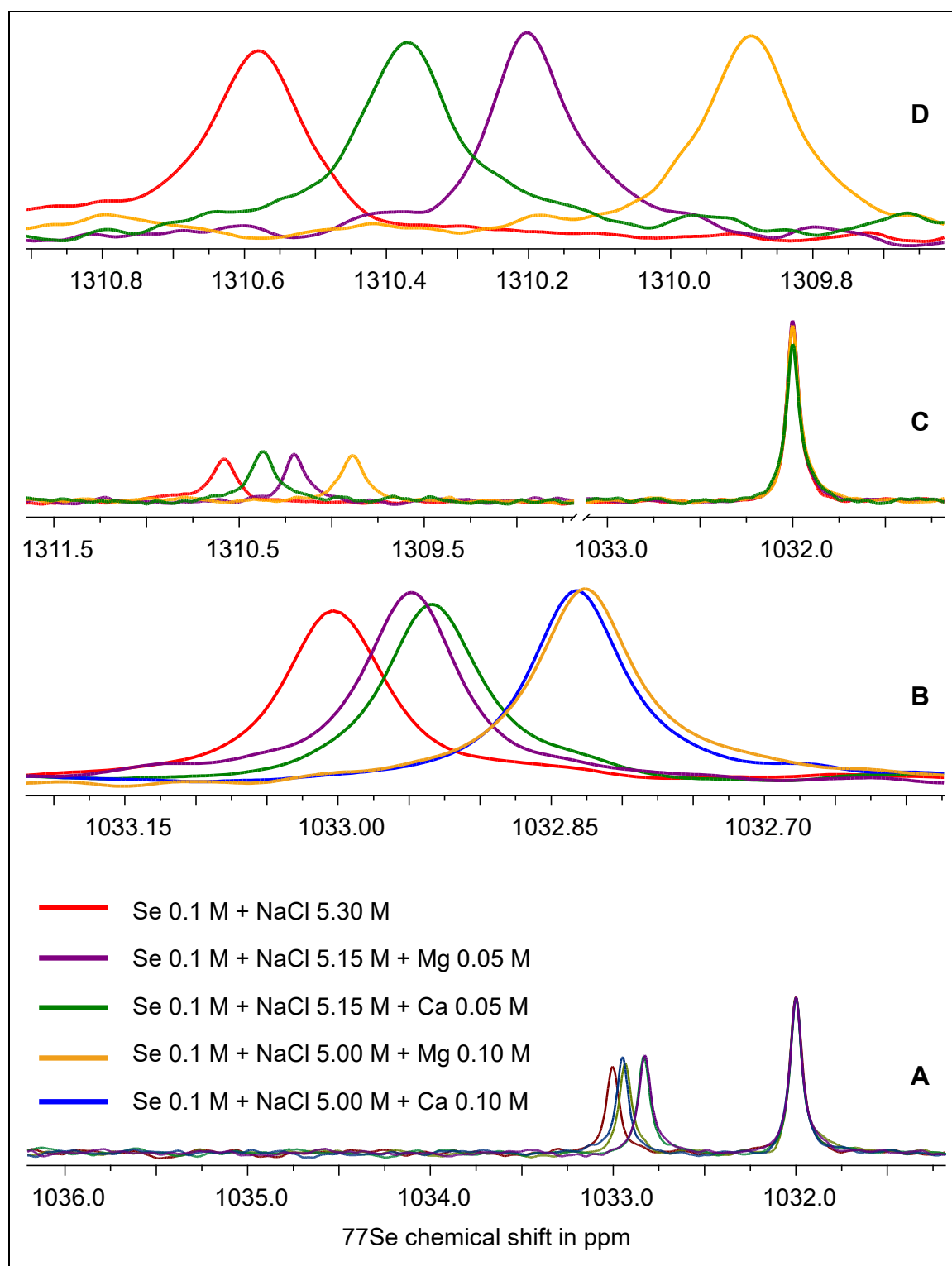


Figure A47. ^{77}Se NMR spectra of 0.1 M sodium selenate solutions at pH_c 7.5 (A, and expansion B), and 0.1 M sodium hydrogen selenite solutions at pH_c 5 (C, and expansion D), containing different amounts of CaCl_2 or MgCl_2 , and a total ionic strength of 5.6 M. Note that 0.5 M Na_2SeO_4 in 90/10 v/v $\text{H}_2\text{O}/\text{D}_2\text{O}$ was used as external reference ($\delta = 1032$ ppm); for the chosen conditions Se^{IV} predominates as dimeric species in solution.

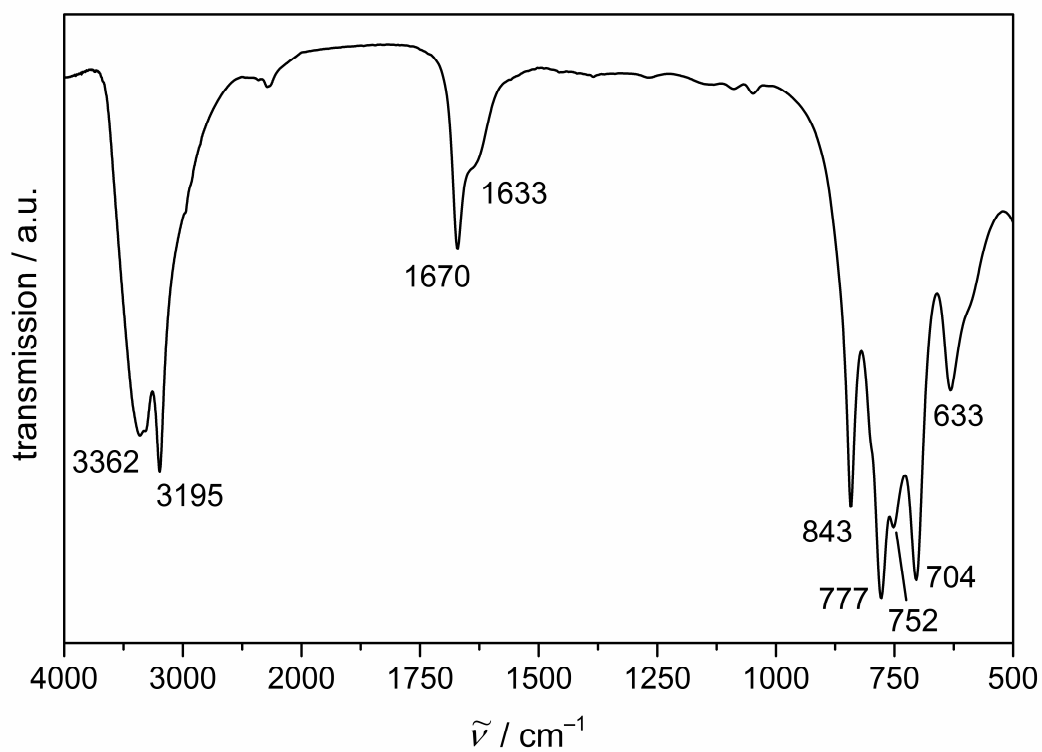


Figure A48. FT-IR (KBr) of the precipitate obtained from equimolar Se^{IV} and Ca^{2+} pH 5 solution.

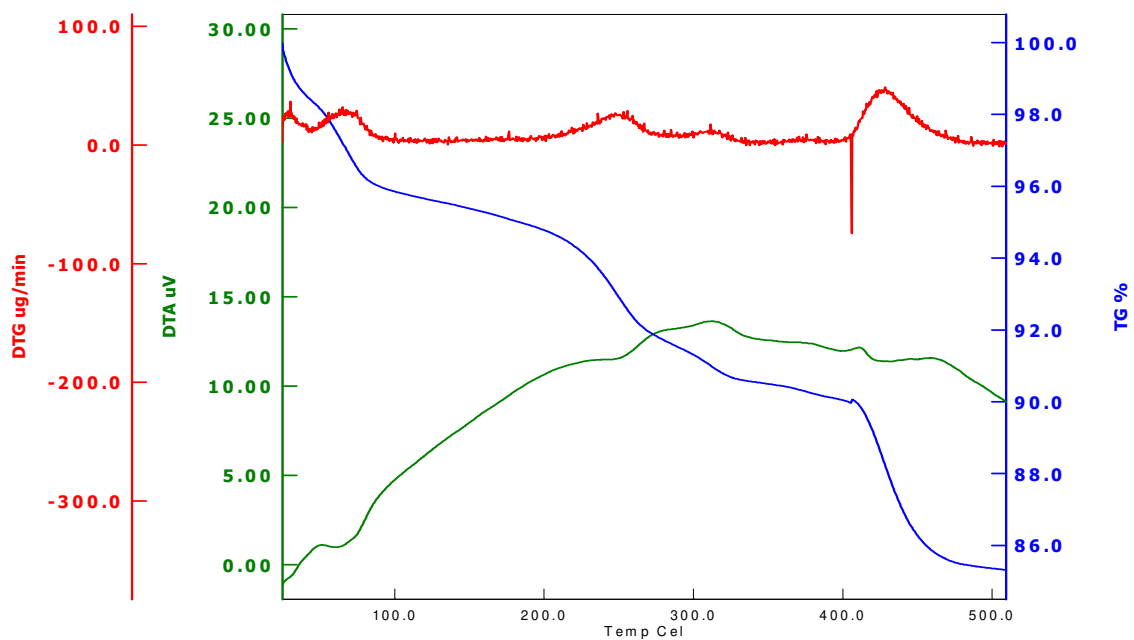


Figure A49. Thermogravimetric analysis of the precipitate obtained from equimolar Se^{IV} and Ca^{2+} pH 5 solution.

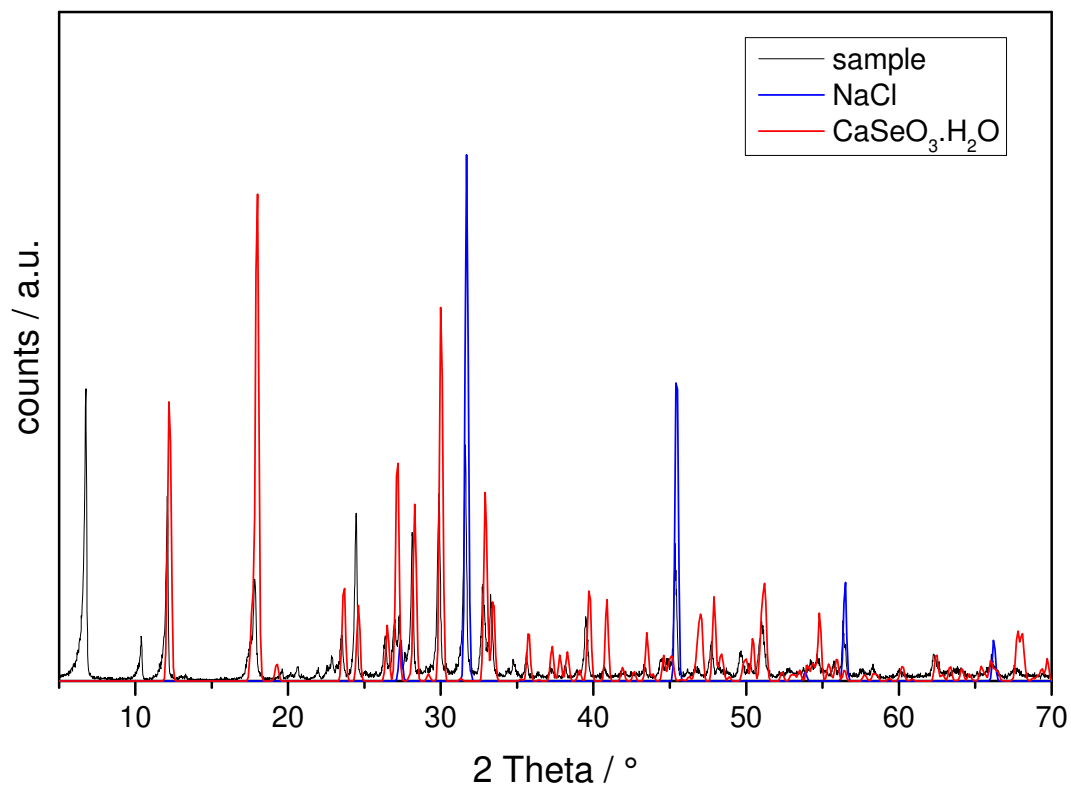


Figure A50. Powder diffractogram of the precipitate obtained from equimolar Se^{IV} and Ca²⁺ pH_c 5 solution matching the ICDD 01-077-1456 reference card. Note residual NaCl from sample preparation at high ionic strength.

Eidesstattliche Versicherung

Hiermit versichere ich, dass ich die vorliegende Arbeit ohne unzulässige Hilfe Dritter und ohne Benutzung anderer als der angegebenen Hilfsmittel angefertigt habe; die aus fremden Quellen direkt oder indirekt übernommenen Gedanken sind als solche kenntlich gemacht. Die Arbeit wurde bisher weder im Inland noch im Ausland in gleicher oder ähnlicher Form einer anderen Prüfungsbehörde vorgelegt.

Die Arbeit wurde am Institut für Ressourcenökologie des Helmholtz-Zentrums Dresden-Rossendorf in der Zeit von Oktober 2011 bis Juli 2015 unter Betreuung von Herrn Professor Dr. Thorsten Stumpf und der wissenschaftlichen Leitung von Herrn Professor Dr. Vinzenz Brendler und Frau Dr. Astrid Barkleit angefertigt.